UNIVERSITY OF CALIFORNIA SAN DIEGO

Mechanistic Electrochemical Characterization of Novel Microelectrode Arrays and Their Application in Mapping Brain Activity across Species and Humans

A dissertation submitted in partial satisfaction of
the requirements for the degree Doctor of Philosophy

in

Electrical Engineering (Nanoscale Devices and Systems)

by

Mehran Ganji

Committee in charge:

Professor Shadi A. Dayeh, Chair
Professor Gert Cauwenberghs
Professor Vikash Gilja
Professor Eric Halgren
Professor Tina Ng

2019

The Dissertation of Mehran Ganji is approved, and it is acceptable in quality and form for publication on microfilm and electronically:

_____

_____

_____

_____

_____

Chair

University of California San Diego

2019

DEDICATION

I dedicate this thesis to

my beloved parents

I can't imagine what my life would have been without their sacrifice

EPIGRAPH

"It is not the eyes that are blind, but the hearts."

Quran 22:46

TABLE OF CONTENTS

LIST OF FIGURES

LIST OF TABLES

ACKNOWLEDGEMENTS

First of all, I would like to thank Professor Shadi Dayeh for his support as my graduate advisor and the chair of my committee. I have learned and grown so much during my time working with him and I am grateful for the opportunities and resources that he has afforded me. I appreciate his inspirational guidance, timely advice, and constant encouragement throughout my time as his student. I appreciate him for being an inspiration to me of what research and life should be all about. One of the things I have really admired about Prof. Dayeh is his desire and push to always make the research more important and relevant and I hope to take that drive with me throughout the rest of my career.

I would also like to thank my doctoral committee members Professor Eric Halgren, Professor Vikash Gilja, Professor Tina Ng and Professor Gert Cauwenberghs for their advice and feedback during my exams and for their invaluable insights and discussions.

Beyond the research, working in the IEBL Lab has been a pleasure due to the intelligent, curious, talented, and generally awesome people who make up the team. Their support, friendship, guidance, and hard work have helped inspire me through my PhD program. Thank you to Atsunori Tanaka, Yun Goo Ro, Renjie Chen, Ren Liu, Sang Heon Lee, Lorraine Hossain, Ahmed Yousef, Woojin Choi and Nasim Vahidi. I would also like to express my appreciation to highly talented staff members at Nano3 for providing a stimulating environment for research and for keeping the equipment on-line and running.

Outside of the IEBL Lab, I have been fortunate to work with some truly outstanding people and research groups. My research and scientific growth have undoubtedly been advanced through

my collaboration with them, thank you to Dr. Erik Halgren, Dr. Vikash Gilja, Dr. Sydney Cash and Dr. Anna Devor research lab members.

Finally, I would like to thank my family. My parents, my brother Behnam, and my sister Behnaz who have always pushed me to be curious, open-minded, and fair. All of them have been incredibly patient in listening to me vent, supporting me when I needed it, and pushing me when I needed that instead.

My sister Behnaz has been a source of inspiration for me through her kindness and dedications to our family. I was blessed to always have her selfless support and affection. This whole process would not have been possible without her unconditional love and support.

Words cannot express the feeling I have for my best and most loyal friend, my twin brother, Mehdi. I appreciate him for his constant, unconditional love and support. Mehdi has always supported me during my most challenging moments. With his guidance, emotional support, and encouragement, I have been able to attain achievements I once thought were unattainable.

The greatest discovery I have ever found during my PhD is my soul mate, my love, Saba. I could not make it this far without her by my side and without her unconditional love and support.

Chapter 2, in full, is a reprint of material as it appears in the following publication: Uguz, M. Ganji, A. Hama, A. Tanaka, S. Inal, A. Youssef, R. M. Owens, P. P. Quilichini, A. Ghestem, C. Bernard, S. A. Dayeh G. G. Malliaras, "Autoclave sterilization of PEDOT: PSS electrophysiology devices," Advanced healthcare materials, vol. 5, pp. 3094-3098, 2016.. The dissertation author was the primary investigator and author of this material.

Chapter 3, in full, is a reprint of material as it appears in the following publication: M. Ganji, E. Kaestner, J. Hermiz, N. Rogers, A. Tanaka, D. Cleary, S. H. Lee, J. Snider, M. Halgren, G. R. Cosgrove, B. S. Carter, D. Barba, I. Uguz, G. G. Malliaras, S. S. Cash, V. Gilja, E. Halgren, S. A.

Dayeh, "Development and translation of PEDOT: PSS microelectrodes for intraoperative monitoring," Advanced Functional Materials, vol. 28, p. 1700232, 2018. The dissertation author was the primary investigator and author of this material.

Chapter 4, in full, is a reprint of material as it appears in the following publication: M. Ganji, A. T. Elthakeb, A. Tanaka, V. Gilja, E. Halgren, and S. A. Dayeh, "Scaling Effects on the Electrochemical Performance of poly (3, 4-ethylenedioxythiophene (PEDOT), Au, and Pt for Electrocorticography Recording," Advanced Functional Materials, vol. 27, p. 1703018, 2017. The dissertation author was the primary investigator and author of this material.

Chapter 5, in full, is a reprint of material as it appears in the following publication: M. Ganji, A. Tanaka, V. Gilja, E. Halgren, and S. A. Dayeh, "Scaling Effects on the Electrochemical Stimulation Performance of Au, Pt, and PEDOT: PSS Electrocorticography Arrays," Advanced Functional Materials, vol. 27, p. 1703019, 2017. The dissertation author was the primary investigator and author of this material.

Chapter 6, in full, is a reprint of material as it appears in the following publication: M. Ganji, L. Hossain, A. Tanaka, M. Thunemann, E. Halgren, V. Gilja, A. Devor, S. A. Dayeh, "Monolithic and Scalable Au Nanorod Substrates Improve PEDOT–Metal Adhesion and Stability in Neural Electrodes," Advanced healthcare materials, vol. 7, p. 1800923, 2018. The dissertation author was the primary investigator and author of this material.

Chapter 7, in full, is a reprint of material as it appears in the following submitted manuscript for publication: M. Ganji, A. C. Paulk, J. C. Yang, N. W. Vahidi, S. H. Lee, R. Liu, L. Hossain, E. M. Arneodo, M. Thunemann, M. Shigyo, A. Tanaka, S. B. Ryu, S. W. Lee, M. Marsala, A. Devor, D. Cleary, V. Gilja, T. Q. Gentner, S. I. Fried, E. Halgren, S. S. Cash, and S. A. Dayeh, " Selective Formation of Porous Pt Nanorods for Highly Electrochemically Efficient Neural Electrode

Interfaces" Submitted to Nano Letters. The dissertation author was the primary investigator and author of this material.

VITA

2014	Bachelor of Science in Electrical Engineering, University of Tehran, Iran
2014-2019	Research Assistant, University of California San Diego
2017	Master of Science, Electrical Engineering (Nanoscale devices and systems) University of California San Diego
2019	Doctor of Philosophy, Electrical Engineering (Nanoscale devices and systems) University of California San Diego

PUBLICATIONS

[1] **M. Ganji**, J. Hermiz, A. C. Paulk, J. C. Yang, N. W. Vahidi, S. H. Lee, *et al.*, " Selective Formation of Porous Pt Nanorods for Highly Electrochemically Efficient Neural Electrode Interfaces,"Submitted to *Nano Letters*.

[2] N. Rogers, J. Hermiz, **M. Ganji**, E. Kaestner, K. Kılıç, L. Hossain, *et al.*, "Correlation Structure in Micro-ECoG Recordings is Described by Spatially Coherent Components," *PLoS computational biology*, vol. 15, p. e1006769, 2019.

[3] **M. Ganji**, L. Hossain, A. Tanaka, M. Thunemann, E. Halgren, V. Gilja, *et al.*, "Monolithic and Scalable Au Nanorod Substrates Improve PEDOT–Metal Adhesion and Stability in Neural Electrodes," *Advanced healthcare materials*, vol. 7, p. 1800923, 2018.

[4] J. Hermiz, N. Rogers, E. Kaestner, **M. Ganji**, D. R. Cleary, B. S. Carter, *et al.*, "Sub-millimeter ECoG pitch in human enables higher fidelity cognitive neural state estimation," *NeuroImage*, vol. 176, pp. 454-464, 2018.

[5] **M. Ganji**, A. T. Elthakeb, A. Tanaka, V. Gilja, E. Halgren, and S. A. Dayeh, "Scaling Effects on the Electrochemical Performance of poly (3, 4-ethylenedioxythiophene (PEDOT), Au, and Pt for Electrocorticography Recording," *Advanced Functional Materials*, vol. 27, p. 1703018, 2017.

[6] **M. Ganji**, A. Tanaka, V. Gilja, E. Halgren, and S. A. Dayeh, "Scaling Effects on the Electrochemical Stimulation Performance of Au, Pt, and PEDOT: PSS Electrocorticography Arrays," *Advanced Functional Materials*, vol. 27, p. 1703019, 2017.

[7] **M. Ganji** and S. Dayeh, "Scaling Effects on the Electrophysiological Stimulation Capabilities of PEDOT: PSS, Pt, and Au," in *Meeting Abstracts*, 2017, pp. 2333-2333.

[8] **M. Ganji**, E. Kaestner, J. Hermiz, N. Rogers, A. Tanaka, D. Cleary, *et al.*, "Development and translation of PEDOT: PSS microelectrodes for intraoperative monitoring," *Advanced Functional Materials*, vol. 28, p. 1700232, 2018.

[9] K. Lee, **M. Ganji**, L. Hossain, Y. G. Ro, S. H. Lee, J.-w. Park, *et al.*, "Flexible inorganic light emitting diodes and transparent PEDOT: PSS/Parylene C for simultaneous optogenetics and electrocorticography (Conference Presentation)," in *Optogenetics and Optical Manipulation*, 2017, p. 1005208.

[10] I. Uguz, **M. Ganji**, A. Hama, A. Tanaka, S. Inal, A. Youssef, *et al.*, "Autoclave sterilization of PEDOT: PSS electrophysiology devices," *Advanced healthcare materials*, vol. 5, pp. 3094-3098, 2016.

[11] J. Hermiz, N. Rogers, E. Kaestner, M. Ganji, D. Cleary, J. Snider, *et al.*, "A clinic compatible, open source electrophysiology system," in *2016 38th Annual International Conference of the IEEE Engineering in Medicine and Biology Society (EMBC)*, 2016, pp. 4511-4514.

[12] M. Taghinejad, H. Taghinejad, **M. Ganji**, A. Rostamian, S. Mohajerzadeh, M. Abdolahad, *et al.*, "Integration of Ni 2 Si/Si Nanograss Heterojunction on n-MOSFET to Realize High-Sensitivity Phototransistors," *IEEE Transactions on Electron Devices*, vol. 61, pp. 3239-3244, 2014.

[13] H. Taghinejad, **M. Ganji,** A. Rostamian, M. Taghinejad, M. Abdolahd, S. Mohajerzadeh, *et al.*, "Direct Integration of Ni2Si/Si Nanograss Heterojunction Array on the Gate Terminal of N-MOSFET Utilizing a CMOS Compatible Top-Down Technique."

ABSTRACT OF THE DISSERTATION

Mechanistic Electrochemical Characterization of Novel Microelectrode Arrays and Their Application in Mapping Brain Activity across Species and Humans

by

Mehran Ganji

Doctor of Philosophy in Electrical Engineering (Nanoscale Devices and Systems)

University of California San Diego, 2019

Professor Shadi A. Dayeh, Chair

Electrocorticography (ECoG) arrays are used in clinical mapping for neurosurgical resection and hold the promise for less damaging brain-machine interfaces. Current clinical ECoG electrodes face physical limits to the number of contact sites, spatial resolution (centimeter scale), and contact diameter (millimeter scale), and thus cannot resolve the dynamically changing neural activity over sub-millimeter scales. In addition to these practical limitations, current clinical electrode arrays are constrained to non-conformal electrode-carriers/substrates and to less-optimal

metal electrochemical interfaces. Increasing the flexibility of clinical electrodes may lead to higher signal-to-noise ratios as well as higher spatial specificity and this also requires overcoming substantial physical barriers due to the compromised metal electrochemical interface properties. The objectives of this thesis, described in seven chapters, are to develop high performance, safe, and durable neural electrode interfaces to yield stable, high signal-to-noise ratio cortical recordings in animal models as well as in humans.

In the second chapter, we demonstrate that sterilization of PEDOT:PSS electrophysiology devices can be performed using autoclave. We find that autoclaving is a viable sterilization method, leaving morphology unaltered and causing only minor changes in electrical properties. These results pave the way for the widespread utilization of PEDOT:PSS electrophysiology devices in the clinic.

In the third chapter, we translate the use of robust PEDOT:PSS microelectrode arrays for safe intraoperative monitoring of the human brain. PEDOT:PSS micro-electrodes measured significant differential neural modulation under various clinically relevant conditions. We report the first evoked (stimulus-locked) cognitive activity with changes in amplitude across pial surface distances as small as 400 μm, potentially enabling basic neurophysiology studies at the scale of neural micro-circuitry.

In the fourth and fifth chapters, we present the first systematic study of scaling effects on the electrochemical properties of Pt and Au metallic and PEDOT:PSS organic electrodes from neural recording and stimulation perspectives. PEDOT:PSS coating reduced the impedances of metallic electrodes by up to 18X. The overall reduced noise of the PEDOT:PSS microelectrodes enable a lower noise floor for recording action-potentials with high fidelity. We observed substantial enhancement in charge injection capacity up to 9.5X for PEDOT:PSS microelectrodes

compared to metal ones and 88% lower required power for injecting the same charge density. These results permit quantitative optimization of contact material and diameter for different ECoG applications.

In the sixth chapter, We report an effective method of mechanically anchoring the PEDOT within the Au nanorod (Au-nr) structure and demonstrate that it provides enhanced adhesion and overall PEDOT layer stability under various electrochemical (charge injection) and *In vivo* stability tests.

In the seventh chapter, we report the fabrication of pure Pt nanorods (PtNRs) by utilizing low-temperature selective dealloying to develop scalable and biocompatible 1D platinum nanorod (PtNR) arrays that exhibit superb electrochemical properties at various length scales for high performance neurotechnologies. PtNR arrays record brain activity with cellular resolution from the cortical surfaces in birds, mice, and non-human primates; demonstrating the PtNR microelectrode system as a robust system for high performance and stable neural electrode interfaces.

Chapter 1

Introduction

1.1 Background and motivation

Recording neural activity during neurosurgical interventions is an invaluable tool for both improving patient outcomes and advancing our understanding of neural mechanisms and organization. Electrocorticography (ECoG) is preferred in clinical and experimental mapping of brain activity due to its higher spatial resolution and sensitivity compared to electroencephalography (EEG) and magnetoencephalography (MEG), yet retains their greater temporal resolution compared to functional magnetic resonance imaging (fMRI).[1] In the clinical context, ECoG is used for precise localization of eloquent cortex in neurosurgical cases for tumors, epileptogenic foci, and vascular abnormalities. This functional localization can be confirmed using ECoG electrodes by electrical stimulation producing a temporary, functional lesion. In the experimental context, most clinical ECoG can resolve activity to less than a millimeter with a high degree of certainty, relative to fMRI, MEG, and EEG,[2] which rely upon modeling and reconstruction techniques to estimate signal source locations. Furthermore, ECoG can measure not only field potentials (which like MEG and EEG are mainly due to currents in the apical dendrites of pyramidal cells), but also measure high-frequency power, which reflects neuronal population firing.[3] Consequently, the use of ECoG in clinical environments is critical for improving neurosurgical patient outcomes—estimated to be 111,000 patient cases per year in the US only[4]—for localizing a wide variety of cortical task-related activity, and for implementing brain machine

interfaces (BCI).[1,5] Here we focus on the development of high-SNR neural recordings to increase the spatial specificity at which neural activity can be measured. Several novel materials and strategies have been employed, focusing on increasing SNR by lowering electrode impedance. Nanostructured materials such as nanowires, carbon nanotubes and graphene[6] as well as surface-modified metallic electrodes (Pt, Au, and Ir) with porous surfaces and higher geometrical surface area are among those explored.[3b,7] Their fabrication processes are generally not monolithic and face additional challenges for translation to clinical practice than poly(3,4-ethylenedioxythiophene) (PEDOT). For metallic electrodes, their relatively high electrochemical impedances and site-to-site variability can result in significant electrophysiological recording losses. Conductive polymers (CPs) on the other hand offer excellent possibilities for advancing electrode/tissue interfaces. CPs have significantly lower microelectrode impedance than inorganic microelectrodes due to their combined ionic-electronic conductivity.[8] In addition, by minimizing the mechanical mismatch at electrode/tissue interface, they permit long-lasting functional neural interface[9] with diminished biofouling.[10] When built on thin flexible films of polyimide or parylene, they conform to the curvilinear brain tissue[11] and their transparency permits their accurate placement on the cortical surface in desired regions. In particular, PEDOT:poly(styrenesulfonate) (PSS) is considered as a forefront alternative due to its low electrochemical impedance over a wide range of frequencies of cortical activity that is of interest [8,12] its excellent chemical stability[13] and its biocompatibility.[14]

1.2 Objectives and organization of the thesis

The objectives of this thesis are to advance PEDOT:PSS microelectrode arrays for high fidelity electrophysiological recordings for use in humans and to study and optimize the relevant recording/ stimulation performances and mechanical/ electrochemical stability.

The organization of this thesis is as follows. Chapter 2 investigates effect of different sterilization techniques on PEDOT:PSS electrophysiology devices and introduces autoclave sterilization as a safe and efficient sterilization method for such devices, which is the most widely used clinical sterilization technique. Chapter 3 demonstrates advancement and utilization of PEDOT:PSS microelectrode arrays for high fidelity electrophysiological recordings and intraoperative monitoring in human subjects by thoroughly benchmarking PEDOT:PSS electrodes against clinical electrodes and by demonstrating background, functional, and pathological recordings, the complete suite of mapping that is necessary for clinical translation of PEDOT:PSS into intraoperative monitoring. Chapter 4 discusses the first systematic study of scaling effects on the electrochemical properties of metallic Pt and Au and organic poly(3,4-ethylenedioxythiophene):polystyrene sulfonate (PEDOT:PSS) electrodes; characteristics which lead to improved electrochemical performance and reduced noise at smaller electrode diameters. Chapter 5 discusses scaling effects on electrochemical charge injection characteristics of Au, Pt, poly(3,4-ethylenedioxythiophene):polystyrene sulfonate (PEDOT:PSS/Au), and PEDOT:PSS/Pt electrode arrays in the 20–2000 μm diameter range. Detailed quantitative analyses are provided, enabling optimization of charge injection capacity with potential bias and symmetric and asymmetric pulse width engineering for all diameters. These systematic analyses inform the optimal design for acute and potentially chronic implants in regards to safety and clinically effective stimulation protocols. Chapter 6 introduces an effective method of mechanically

anchoring the PEDOT:PSS within an Au nanorod (Au-nr) structure and it is demonstrated that it provides enhanced adhesion and overall PEDOT layer stability compared to traditional PEDOT:PSS film on planar Au electrodes. Chapter 7 reports the fabrication of pure Pt nanorods (PtNRs) structures by selective chemical dissolution of Ag from a co-sputtered PtAg alloy on thin and flexible parylene C substrates. These results demonstrate the biocompatibility and robustness of the PtNRs as novel microelectrode coatings with potential for chronic implants. Finally, the conclusion of this dissertation work is summarized in chapter 8.

1.3 References

[1] G. Schalk, K. Miller, N. Anderson, J. Wilson, M. Smyth, J. Ojemann, D. Moran, J. Wolpaw, E. Leuthardt, *Journal of neural engineering* **2008**, 5, 75.

[2] A. M. Dale, E. Halgren, *Current opinion in neurobiology* **2001**, 11, 202.

[3] J.-P. Lachaux, N. Axmacher, F. Mormann, E. Halgren, N. E. Crone, *Progress in neurobiology* **2012**, 98, 279.

[4] A. M. Taplin, A. de Pesters, P. Brunner, D. Hermes, J. C. Dalfino, M. A. Adamo, A. L. Ritaccio, G. Schalk, *Epilepsy & Behavior Case Reports* **2016**, 5, 46.

[5] a) N. T. Sahin, S. Pinker, S. S. Cash, D. Schomer, E. Halgren, *Science* **2009**, 326, 445; b) R. T. Canolty, E. Edwards, S. S. Dalal, M. Soltani, S. S. Nagarajan, H. E. Kirsch, M. S. Berger, N. M. Barbaro, R. T. Knight, *science* **2006**, 313, 1626; c) N. Mesgarani, C. Cheung, K. Johnson, E. F. Chang, *Science* **2014**, 343, 1006; d) M. J. Vansteensel, E. G. Pels, M. G. Bleichner, M. P. Branco, T. Denison, Z. V. Freudenburg, P. Gosselaar, S. Leinders, T. H. Ottens, M. A. Van Den Boom, *New England Journal of Medicine* **2016**, 375, 2060; e) W. Wang, J. L. Collinger, A. D. Degenhart, E. C. Tyler-Kabara, A. B. Schwartz, D. W. Moran, D. J. Weber, B. Wodlinger, R. K. Vinjamuri, R. C. Ashmore, *PloS one* **2013**, 8, e55344; f) C. A. Chestek, V. Gilja, C. H. Blabe, B. L. Foster, K. V. Shenoy, J. Parvizi, J. M. Henderson, *Journal of neural engineering* **2013**, 10, 026002.

[6] a) E. W. Keefer, B. R. Botterman, M. I. Romero, A. F. Rossi, G. W. Gross, *Nature nanotechnology* **2008**, 3, 434; b) N. A. Kotov, J. O. Winter, I. P. Clements, E. Jan, B. P. Timko, S. Campidelli, S. Pathak, A. Mazzatenta, C. M. Lieber, M. Prato, *Advanced Materials* **2009**, 21, 3970; c) E. Seker, Y. Berdichevsky, M. R. Begley, M. L. Reed, K. J. Staley, M. L. Yarmush, *Nanotechnology* **2010**, 21, 125504.

[7] a) J.-H. Kim, G. Kang, Y. Nam, Y.-K. Choi, *Nanotechnology* **2010**, 21, 085303; b) M. Heim, B. Yvert, A. Kuhn, *Journal of Physiology-Paris* **2012**, 106, 137; c) S. Park, Y. J. Song, H. Boo, T. D. Chung, *The Journal of Physical Chemistry C* **2010**, 114, 8721.

[8] J. Rivnay, S. Inal, B. A. Collins, M. Sessolo, E. Stavrinidou, X. Strakosas, C. Tassone, D. M. Delongchamp, G. G. Malliaras, *Nature communications* **2016**, 7.

[9] a) R. A. Green, N. H. Lovell, G. G. Wallace, L. A. Poole-Warren, *Biomaterials* **2008**, 29, 3393; b) M. R. Abidian, J. M. Corey, D. R. Kipke, D. C. Martin, *Small* **2010**, 6, 421; c) X. Cui, V. A. Lee, Y. Raphael, J. A. Wiler, J. F. Hetke, D. J. Anderson, D. C. Martin, *Journal of biomedical materials research* **2001**, 56, 261.

[10] a) M. R. Abidian, K. A. Ludwig, T. C. Marzullo, D. C. Martin, D. R. Kipke, *Advanced Materials* **2009**, 21, 3764; b) K. A. Ludwig, J. D. Uram, J. Yang, D. C. Martin, D. R. Kipke, *Journal of neural engineering* **2006**, 3, 59.

[11] D.-H. Kim, J. Viventi, J. J. Amsden, J. Xiao, L. Vigeland, Y.-S. Kim, J. A. Blanco, B. Panilaitis, E. S. Frechette, D. Contreras, *Nature materials* **2010**, 9, 511.

[12] M. R. Abidian, D. C. Martin, *Biomaterials* **2008**, 29, 1273.

[13] L. Groenendaal, F. Jonas, D. Freitag, H. Pielartzik, J. R. Reynolds, *Advanced Materials* **2000**, 12, 481.

[14] a) M. Asplund, E. Thaning, J. Lundberg, A. Sandberg-Nordqvist, B. Kostyszyn, O. Inganäs, H. von Holst, *Biomedical Materials* **2009**, 4, 045009; b) D.-H. Kim, J. A. Wiler, D. J. Anderson, D. R. Kipke, D. C. Martin, *Acta biomaterialia* **2010**, 6, 57.

Chapter 2

Autoclave Sterilization of PEDOT:PSS Electrophysiology Devices

2.1 Introduction

The biological applications of organic electronic materials are currently attracting a great deal of interest.[1–3] One key thematic area encompasses the development of new devices for electrophysiology—devices that interface with cells by means of electrical recording and stimulation. Historically, interest in organics stems from their soft nature, which decreases the mechanical properties mismatch with tissue.[4] Another property that makes organics attractive to electrophysiology is their mixed electronic/ionic conductivity.[5] Indeed, organic coatings are shown to decrease the electrochemical impedance at the biotic/abiotic interface and lead to better recordings and more efficient stimulation compared to traditional metal electrodes.[6] In addition to making better electrodes, mixed conductivity is leveraged to design novel devices with state-of-the-art properties. One such example is the organic electrochemical transistor (OECT), a device that uses an organic film as the transistor channel.[7] When used *in vivo*, ions from the cerebrospinal fluid, set in motion by neural firing, penetrate into the volume of the film and change its doping level. As a result of this volumetric response, OECTs act as efficient signal amplifiers and are being used to record brain activity with unprecedented signal-to-noise ratio.[8] The prototypical material used in organic-based electrophysiology devices is the conducting polymer poly(3,4-ethylenedioxythiophene) doped with polystyrene sulfonate (PEDOT:PSS). It is commercially available as an aqueous dispersion, and can be easily processed into films that are biocompatible

and show high hole and ion conductivity.[9] PEDOT:PSS electrodes and OECTs are also used in *in vitro* diagnostics to monitor the health of cultures and tissue slices,[10] and have been integrated with both rigid and flexible substrates to yield devices that interface with electrically active tissues in animal models.[11,12] Deposited on thin films of parylene, they make arrays that conform well to the surface of the brain and yield stable, high signal-to-noise ratio cortical recordings in animal models as well as in humans.[13] Finally, PEDOT:PSS has been used in the fabrication of OECTs with record-high transconductance, used for electrophysiological recordings in animal models and in humans.[8,14,15] These efforts generate a great deal of potential for the realization of high-quality neural interfaces using organic materials. Such interfaces can be used to understand the brain, treat neurological diseases including epilepsy and Parkinson's, and yield stable brain/computer interfaces. These results pave the way for the widespread utilization of PEDOT:PSS electrophysiology devices in the clinic.

2.2 Experimental Details

2.2.1 Fabrication of the PEDOT:PSS Microelectrodes

4 inch glass wafers (Specialty Glass Products) were used as a substrate carrier for the thin parylene C layers. The glass wafers were first solvent cleaned by rinsing with acetone/isopropanol (IPA)/deionized (DI) water/IPA, then were subjected to ultrasonic agitation in IPA for 5 min, and were then rinsed again with acetone/IPA/DI water/IPA. Diluted Micro-90 (0.1%) as an antiadhesion layer was spun-cast at 1500 rpm on the glass wafer to facilitate the separation of the device after the device fabrication is completed. A first parylene C layer (≈3 μm) was deposited by chemical vapor deposition using a PDS 2010 Parylene coater system. Metal lead patterns were defined and exposed using a Karl Suss MA6 mask aligner using NR9-3000 negative resist. Temescal BJD 1800 electron beam evaporator was used for the deposition of 10 nm Ti adhesion layer and 100 nm Au contact layer, and lift-off process in acetone followed. O_2 plasma (Oxford Plasmalab 80 RIE) was then applied for 2 min (150 W RF power) to activate the surface of parylene C for enhancing the adhesion of the subsequent encapsulating parylene C layer. A ≈ 3 μm parylene C layer was then deposited and followed by coating another Micro-90 anti-adhesion layer. This time, a slightly higher concentrated Micro-90 (1% as opposed to 0.1% for the first layer) was spun-cast at 650 rpm for 10s on this second parylene C layer for the ease of separation of the subsequent layers. A third parylene C layer was then deposited, followed by the spin-coating and patterning the thick 2010 SU-8 photoresist layer which developed with an SU-8 developer. O_2 plasma was used to etch the openings in the third and then second parylene C layers prior to the deposition of PEDOT:PSS. After the O_2 plasma etching step, the exposed Au surface was cleaned using moderate sonication while the device was immersed in DI water. 20 mL aqueous dispersion of PEDOT:PSS (PH 1000 from Clevios) was mixed with ethylene glycol (5 mL), dodecylbenzene

sulfonic acid (50 μL), and 1 wt% of (3-Glycidyloxypropyl)trimethoxysilane, and the solution was spun-cast at 650 rpm for 30 s and pre-baked at 95 °C for 1 min. The third parylene C layer was then mechanically peeled off in all regions except where PEDOT: PSS made contact with the Au surface on the microarray and macrodot regions. Finally, the devices were cured at 140 °C for 1 h and immersed in DI water to remove any Micro-90 residue from the PEDOT:PSS and parylene C surface.

2.2.2 Device Characterization

The devices were imaged using an FEI SFEG ultrahigh resolution SEM at 10 kV accelerating voltage and a magnification of with 4702X. To reduce electron charging in the specimen, a 15 nm thick Ti layer was deposited on the back of the device and that electrically connected to the stage of the system providing a runaway path for impinging electrons. A Veeco Scanning Probe Microscope was used to take AFM images in noncontact tapping mode. EIS was performed using a GAMRY interface 1000E in phosphate buffer saline solution, using three electrodes configuration, i.e., Ag/AgCl electrode as a reference, a large platinum electrode as a counter elelectrode, and PEDOT:PSS/Pt microarray/macrodot as the working electrode. Sinusoidal signals with 10 mV rms AC voltage and zero DC voltage were applied and the frequency was swept from 1 Hz to 10 kHz.

2.2.3 Sterilization Methods

In Gardanne, sterilization of the devices was achieved using a Tuttnauer Model 3150EL autoclave. The samples were placed into autoclave pouches and sealed prior to exposure to steam. A 20 min treatment with saturated steam at 121 °C was followed by a 15 min evaporative drying step. Some of the devices were inoculated with 200 μL pre-culture (E. coli ATCC 25922), sterilized by autoclave and placed in pre-sterilized flasks that contained Luria-Bertani media

(Sigma). The arrays were incubated for 24 h at 37 °C. The optical density of the resultant microbial population was measured at a wavelength of 600 nm using a TECAN M1000 spectrophotometer. In San Diego, autoclave sterilization was performed using a SUN series autoclave (Class B). Arrays were directly exposed to water vapor at 121 °C for 20 min. Sterrad sterilization was performed by exposing arrays to hydrogen peroxide vapor at 50 °C for 47 min, at UCSD's Thornton Hospital, while the arrays were kept in appropriate sterilization pouches.

2.3 Results and Discussions

PEDOT:PSS microelectrode and OECT arrays were fabricated using lithography, as detailed in the Experimental Section. Each array consisted of a parylene substrate, Au pads/interconnects/electrodes, PEDOT:PSS islands, and a parylene layer insulating the metal interconnects. In Gardanne, each array comprised 64 microelectrodes with sizes of 10 × 10, 20 × 20, and 40 × 40 μm^2, or 13 OECTs with a channel length of 5 μm and width of 10 μm. The thickness of the PEDOT:PSS film was 220 nm. In San Diego, each array comprised 15 microelectrodes of 15 × 15 μm^2 (**Figure 2.1**). The thickness of the PEDOT:PSS film was 280 nm. The arrays were autoclaved by exposure to steam at a temperature of 121 °C for 20 min.

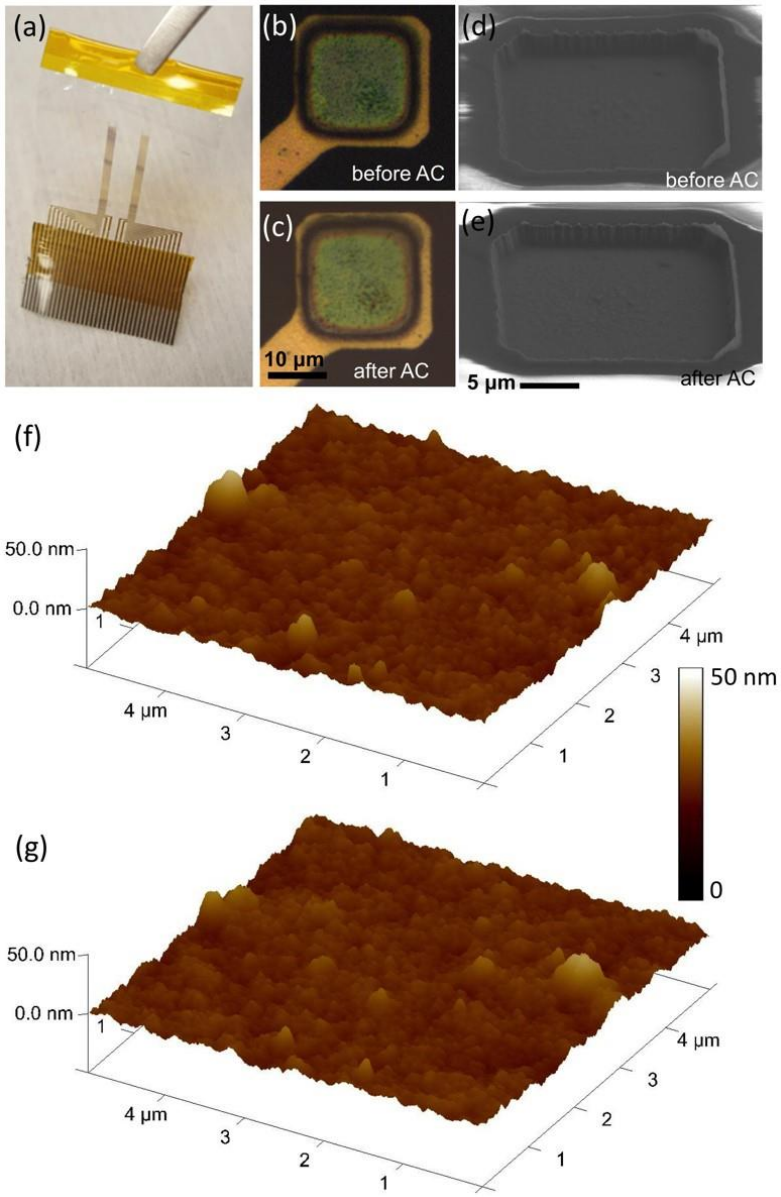

Figure 2.1 a) Picture of test geometry with two arrays, each containing 15 PEDOT:PSS microelectrodes. Optical microscopy images of the same microelectrode b) before and c) after autoclave. 45° angle view SEM images of the same microelectrode d) before and e) after autoclave. AFM topography images on a 5 × 5 μm^2 area at the same location of PEDOT:PSS f) before and g) after autoclave.

2.3.1 Efficacy of Autoclave Sterilization

We evaluated the efficacy of the sterilization process by intentionally inoculating a portion of the arrays with Escherichia coli (E. coli, ATCC 25922) before sterilization, as described in the Experimental Section. Immediately after sterilization, all arrays were incubated in culture media. After 24 h, the optical density (OD) of the media at 600 nm (OD600 is a common method for estimating the concentration of bacteria in media) was measured. We defined boundary conditions by measuring the OD of autoclaved media (reference 1—sterile) and of media containing bacteria (reference 2—non-sterile), respectively. The results are summarized in **Table 2.1**. Array 1 was neither exposed to E. coli nor sterilized. Media in which the array was incubated showed an OD above the baseline, consistent with the array being non-sterile. Array 2 was not exposed to E. coli but was sterilized, resulting into optically clear media, consistent with the array being sterile. Array 3 was exposed to E. coli but was subsequently sterilized. Media in which the array was incubated was also clear, consistent with the array being sterile. These results, therefore, show that autoclaving renders the arrays sterile.

Table 2.1 Results of the autoclave sterilization assay. N = 3 solution samples taken from each array.

	E.coli exposure	Sterilization	OD at 600nm	Sterile?
Reference 1		+	0.05±0.01	Yes
Reference 2	+		1.68±0.05	No
Array 1			0.12±0.01	No
Array 2		+	0.05±0.01	Yes
Array 3	+	+	0.05±0.01	Yes

2.3.2 Morphological Alteration upon Autoclaving

We next investigated the influence of autoclave sterilization on the morphological stability of the microelectrodes by optical microscopy, scanning electron microscopy (SEM), and atomic force microscopy (AFM). The overall structure of the arrays is shown in **Figure 2.1a**. Optical images of the same microelectrode before (**Figure 2.1b**) and after (**Figure 2.1c**) autoclaving showed no evident morphological changes (the same holds for the whole device—no visible change was observed after sterilization). Similarly, SEM images on the same PEDOT:PSS microelectrode before (**Figure 2.1d**) and after (**Figure 2.1e**) autoclaving showed no evident delamination, cuts, or other observable morphological changes. To look further at the surface topography of the PEDOT:PSS at a higher resolution, we conducted AFM topography before (**Figure 2.1f**) and after (**Figure 2.1g**) autoclaving on the same 5×5 μm^2 PEDOT:PSS location. The AFM images showed that the PEDOT:PSS morphology is generally conserved with a root mean square surface roughness of 3.41 nm before and 3.47 nm after autoclave.

2.3.3 Electrochemical Alteration upon Autoclaving

We next evaluated the impact of the sterilization process on the electrical performance of the electrodes and OECTs. For the electrodes, we measured the electrochemical impedance spectra as described in the Experimental Section. Impedance at 1 kHz is used as the benchmark for the characterization of neural electrodes, as this frequency corresponds to spiking activity.[17] **Figure 2.2a** shows a histogram of impedance values before and after sterilization, for electrodes with an area of 10×10 μm^2 made and measured in Gardanne. The data show that the distribution moves slightly to higher values, with the average value changing from 49.7 ± 3.6 kΩ before sterilization to 53.2 ± 3.4 kΩ after. Similar results were obtained in San Diego, where average impedance values at 1 kHz changed from 57.7 ± 7.2 kΩ before sterilization to 58.7 ± 7.3 kΩ after sterilization.

For the OECTs, we measured the transfer curves as described in the Experimental Section and extracted transconductance. The transconductance is the key parameter that determines the performance of OECTs in electrophysiology, as it relates to signal amplification.[18] **Figure 2.2b** shows a histogram of transconductance values before and after sterilization, for devices made and measured in Gardanne. As with impedance, the change of the transconductance was very little after sterilization, from 7.4 ± 0.2 to 7.3 ± 0.2 mS. Furthermore, the resistance of the OECT channels was found to decrease by 4% after sterilization, indicating that materials degradation, changes in mobility/doping due to changes in microstructure, and/or delamination from contacts (though not detectable in **Figure 2.1**) might be underlying the changes in impedance and transconductance. These changes are, however, small, and the devices remain functional after autoclave sterilization. The observed stability of the PEDOT:PSS electrophysiology devices to autoclaving can be attributed partly to the intrinsic thermal stability of their components and partly to the use of a cross-linker. Indeed, the devices are already baked during fabrication at 140 °C for 1 h in ambient conditions, a temperature that all components of the device can sustain. Moreover, the cross-linker 3-glycidoxypropyltrimethoxysilane (GOPS) renders the PEDOT:PSS film insoluble to water. Devices made without GOPS do not survive autoclave sterilization, as the PEDOT:PSS film falls apart.

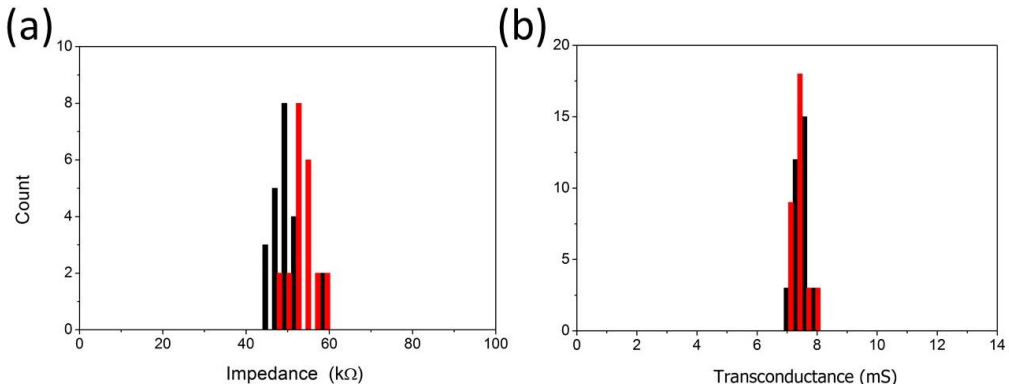

Figure 2.2 (a) Histogram showing the distribution in electrode impedance at 1 kHz before (black) and after (red) sterilization. (b) Histogram showing the distribution in OECT transconductance before (black) and after (red) sterilization.

2.3.4 Morphological and Electrochemical Alteration upon STERRAD

While autoclaving showed no significant influence in the morphology and electrical characteristics of PEDOT:PSS devices, this is not a general case for all sterilization methods. As an example to the contrary we show results from chemical sterilization using the Sterrad system. This system destroys pathogens through exposure to H_2O_2 gas plasma. Since the process does not typically exceed 50 °C, this method is particularly well-suited to heat and moisture-sensitive devices. However, Sterrad sterilization imparted extensive damage to PEDOT:PSS microelectrodes. As shown in **Figure 2.3a**, it resulted in nonfunctional devices, manifested by large impedance values. SEM and optical images in **Figure 2.3b, c**, respectively, depict severe morphological changes in the PEDOT:PSS film. By utilizing focused-ion beam (FIB) to section a PEDOT:PSS microelectrode after Sterrad sterilization (**Figure 2.3d**), we observed clear delamination of the PEDOT:PSS from the Ti/Au metal lead at the center of the microelectrode and from the parylene at the edge of the microelectrode after the Sterrad process. The reason for this delamination is currently not clear. One possibility is that exposure to peroxide plasma causes extensive cross-linking of the PEDOT:PSS film, causing it to shrink and delaminate. Regardless

of the exact mechanism of failure, the negative result points to the fact that for each sterilization method, a systematic study needs to be undertaken to ensure suitability to a particular device.

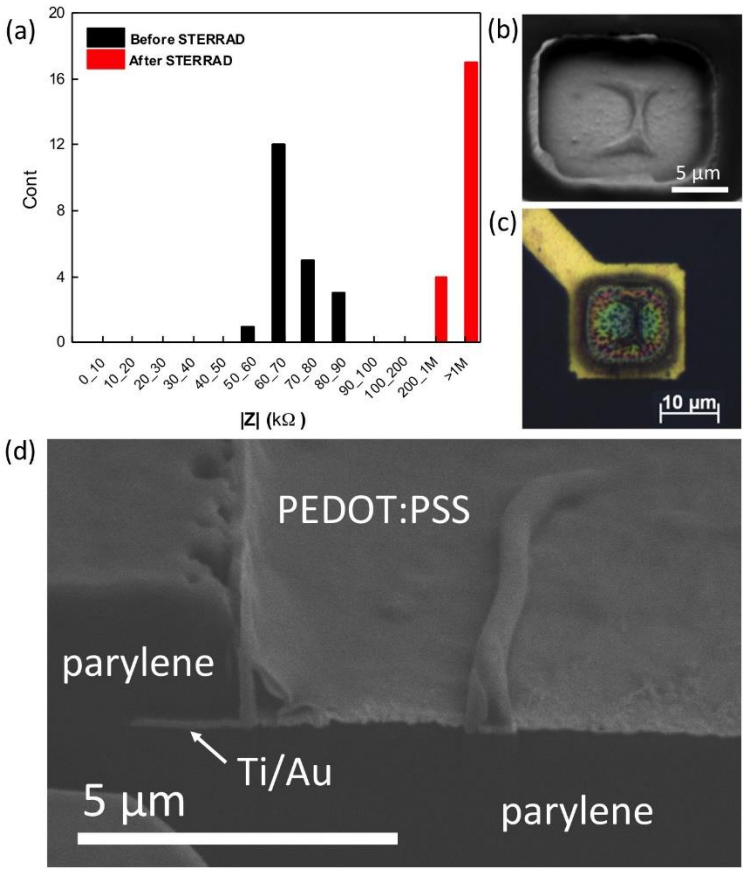

Figure 2.3 (a) Impedance histogram at 1 kHz showing mostly open circuit devices after Sterrad sterilization. (b) SEM image and (c) optical image of a typical PEDOT:PSS microelectrode after Sterrad sterilization. (d) FIB cut across showing clear delamination of PEDOT:PSS microelectrode from Ti/Au near the edge and near the center after Sterrad sterilization.

2.4 Conclusion

In conclusion, we investigated the impact of sterilization methods on PEDOT:PSS microelectrodes and electrochemical transistors integrated on thin parylene supports. We show that devices inoculated with *E. coli* are effectively sterilized using autoclaving. The process does not alter appreciably the morphology of PEDOT:PSS films, while the electrical characteristics of microelectrodes and transistors show only minor degradation after exposure to steam. Sterrad

sterilization, in contrast, causes large morphological changes in the PEDOT:PSS films and results in non-functional devices. The results show that autoclaving, which is readily available in most biological laboratories, is a viable sterilization method for PEDOT:PSS electrophysiology devices. This finding represents a significant step toward the widespread introduction of these devices to the clinic.

Chapter 2, in full, is a reprint of material as it appears in the following publication: Uguz, M. Ganji, A. Hama, A. Tanaka, S. Inal, A. Youssef, R. M. Owens, P. P. Quilichini, A. Ghestem, C. Bernard, S. A. Dayeh G. G. Malliaras, "Autoclave sterilization of PEDOT: PSS electrophysiology devices," Advanced healthcare materials, vol. 5, pp. 3094-3098, 2016.. The dissertation author was the primary investigator and author of this material.

2.5 References

[1] M. Berggren, A. Richter-Dahlfors, *Adv. Mater.* **2007**, *19*, 3201.

[2] J. Rivnay, R. M. Owens, G. G. Malliaras, *Chem. Mater.* **2014**, *26*, 679.

[3] C. Liao, M. Zhang, M. Y. Yao, T. Hua, L. Li, F. Yan, *Adv. Mater.* **2015**, *27*, 7493.

[4] D.-H. Kim, S. Richardson-Burns, L. Povlich, M. R. Abidian, S. Spanninga, J. Hendricks, D. C. Martin, in *Indwelling Neural Implants Strateg. Contend. -Vivo Environ.* (Ed.: W.M. Reichert), CRC Press, Taylon And Francis, Boca Raton, FL, **2008**, pp. 165–207.

[5] J. M. Leger, *Adv. Mater.* **2008**, *20*, 837.

[6] D. C. Martin, G. G. Malliaras, *ChemElectroChem* **2016**, *3*, 686.

[7] H. S. White, G. P. Kittlesen, M. S. Wrighton, *J. Am. Chem. Soc.* **1984**, *106*, 5375.

[8] D. Khodagholy, T. Doublet, P. Quilichini, M. Gurfinkel, P. Leleux, A. Ghestem, E. Ismailova, T. Hervé, S. Sanaur, C. Bernard, G. G. Malliaras, *Nat. Commun.* **2013**, *4*, 1575.

[9] J. Rivnay, S. Inal, B. A. Collins, M. Sessolo, E. Stavrinidou, X. Strakosas, C. Tassone, D. M. Delongchamp, G. G. Malliaras, *Nat. Commun.* **2016**, *7*, 11287.

[10] M. Sessolo, D. Khodagholy, J. Rivnay, F. Maddalena, M. Gleyzes, E. Steidl, B. Buisson, G. G. Malliaras, *Adv. Mater.* **2013**, *25*, 2135.

[11] M. D. Johnson, R. K. Franklin, M. D. Gibson, R. B. Brown, D. R. Kipke, *J. Neurosci. Methods* **2008**, *174*, 62.

[12] D. Khodagholy, T. Doublet, M. Gurfinkel, P. Quilichini, E. Ismailova, P. Leleux, T. Herve, S. Sanaur, C. Bernard, G. G. Malliaras, *Adv. Mater.* **2011**, *23*, H268.

[13] D. Khodagholy, J. N. Gelinas, T. Thesen, W. Doyle, O. Devinsky, G. G. Malliaras, G. Buzsaki, *Nat. Neurosci.* **2015**, *18*, 310.

[14] A. Campana, T. Cramer, D. T. Simon, M. Berggren, F. Biscarini, *Adv. Mater.* **2014**, *26*, 3874.

[15] J. Rivnay, P. Leleux, M. Ferro, M. Sessolo, A. Williamson, D. A. Koutsouras, D. Khodagholy, M. Ramuz, X. Strakosas, R. M. Owens, C. Benar, J.-M. Badier, C. Bernard, G. G. Malliaras, *Sci. Adv.* **2015**, *1*, e1400251.

[16] K. Kuribara, H. Wang, N. Uchiyama, K. Fukuda, T. Yokota, U. Zschieschang, C. Jaye, D. Fischer, H. Klauk, T. Yamamoto, K. Takimiya, M. Ikeda, H. Kuwabara, T. Sekitani, Y.-L. Loo, T. Someya, *Nat. Commun.* **2012**, *3*, 723.

[17] G. Buzsáki, C. A. Anastassiou, C. Koch, *Nat. Rev. Neurosci.* **2012**, *13*, 407.

[18] J. Rivnay, P. Leleux, M. Sessolo, D. Khodagholy, T. Herve, M. Fiocchi, G. G. Malliaras, *Adv. Mater.* **2013**, *25*, 7010.

Chapter 3

Development and Translation of PEDOT:PSS Microelectrodes for Intraoperative Monitoring

3.1 Introduction

Recording neural activity during neurosurgical interventions is an invaluable tool for both improving patient outcomes and advancing our understanding of neural mechanisms and organization. However, increasing clinical electrodes' signal-to-noise and spatial specificity requires overcoming substantial physical barriers due to the compromised metal electrochemical interface properties. Current clinical ECoG electrodes face physical limits to the number of electrode sites, spatial resolution (centimeter scale), and electrode diameter (millimeter scale), and thus cannot resolve neural activity that changes multiple times over the course of a millimeter.[1] This limitation has important implications for surgical tissue resection, as current surgical methodology requires high precision in identifying the boundaries between diseased and eloquent cortex. In addition to these design limitations, current clinical electrode arrays are constrained to nonconformal electrode-carriers/substrates and to less-optimal metal (e.g., PtIr) electrochemical interfaces.[2] To fully exploit the advantages of ECoG in both clinical and experimental mapping of detailed neural activity, significant advances at the electrochemical, mechanical and biocompatibility fronts of electrode/tissue interfaces must be made.[3] The needed advances includes (1) the development of a high-quality electrochemical interface with low impedance (high signal-to-noise ratio (SNR) recording), (2) high charge injection capacity (safe/ efficient stimulation),[4] (3) compliant mechanical properties for mimicking the curvilinear brain surface and to compensate

for brain micromotion in order to reduce tissue damage,[5] and (4) enhanced biocompatible electrode/tissue interfaces to minimize biofouling.[3a,6] Conductive polymers (CPs) on the other hand offer excellent possibilities for advancing electrode/tissue interfaces. CPs have significantly lower microelectrode impedance than inorganic microelectrodes due to their combined ionic-electronic conductivity.[9] In addition, by minimizing the mechanical mismatch at electrode/tissue interface, they permit long-lasting functional neural interface[10] with diminished biofouling.[11] When built on thin flexible films of polyimide or parylene, they conform to the curvilinear brain tissue[12] and their transparency permits their accurate placement on the cortical surface in desired regions. In particular, PEDOT:poly(styrenesulfonate) (PSS) is considered as a forefront alternative due to its low electrochemical impedance over a wide range of frequencies of cortical activity that is of interest,[9,13] its excellent chemical stability,[14] and its biocompatibility.[15] However, to date, there is only one group who has demostrated PEDOT:PSS utilization in intraoperative monitoring. Their pioneering work reported single units from a human brain and began to explore the spatial specificity capabilities of PEDOT:PSS devices.[16] Here we expand on these efforts by thoroughly benchmarking PEDOT:PSS electrodes against clinical electrodes and by demonstrating background, functional, and pathological recordings, the complete suite of mapping that is necessary for clinical translation of PEDOT:PSS into intraoperative monitoring. The objective of our work is to advance PEDOT:PSS microelectrode arrays for high fidelity electrophysiological recordings in human subjects. To accomplish this, we first studied the structural and surface integrity of the devices for suitability in safe intraoperative monitoring from human subjects. Here, we refined earlier fabrication procedures[17] for which we optimized the autoclave sterilization for clinical use[18] and obtained high yield with a narrow distribution of microelectrode electrochemical characteristics. We benchmark PEDOT:PSS electrodes characteristics against clinical PtIr and

pure Pt electrodes, correlate clinical recordings from PEDOT:PSS and clinical electrodes to their electrochemical properties, and present the first recording of stimulus-locked neural activity from human subjects using PEDOT:PSS microarrays. By employing high yield PEDOT:PSS microelectrode arrays, not only high SNR was obtained, but evidence of spatially modulated activity across the scale of cortical microcolumns was measured. These changes, measured in high-gamma amplitude across 400 μm pitch electrodes, demonstrate the spatial specifity afforded by the low impedance, small electrode diameter, and fine electrode pitch of the fabricated PEDOT:PSS devices.

3.2 Experimental Details

3.2.1 Device Fabrication

The fabrication of PEDOT:PSS-based electrodes followed previously discussed processes in part 2.2.1. Fabrication of the platinum microarrays followed similar procedure to that of PEDOT:PSS devices except for the PEDOT:PSS deposition which was not carried out. For the Pt devices, a 10 nm Ti adhesion layer and 100 nm Pt contact layer were deposited by sputtering (Denton Discovery 18 Sputter System).

3.2.2 Device Characterization

The devices were imaged using an FEI SFEG ultrahigh resolution SEM at 10 kV accelerating voltage and a magnification of with 4702X. To reduce electron charging in the specimen, a 15 nm thick Ti layer was deposited on the back of the device and that electrically connected to the stage of the system providing a runaway path for impinging electrons. A Veeco Scanning Probe Microscope was used to take AFM images in noncontact tapping mode. EIS was performed using a GAMRY interface 1000E in phosphate buffer saline solution, using three electrodes configuration, i.e., Ag/AgCl electrode as a reference, a large platinum electrode as a counter

electrode, and PEDOT:PSS/Pt microarray/macrodot as the working electrode. Sinusoidal signals with 10 mV rms AC voltage and zero DC voltage were applied and the frequency was swept from 1 Hz to 10 kHz.

3.2.3 Electrophysiology Methods, Acquisition

Patients S1–S3 undergoing clinical mapping of eloquent cortex provided informed consent to have the microarray placed on their pial surface and to participate in a 10 min task. The PEDOT microarray was placed on the STG: anterior STG for S2 and posterior STG for S1 and S3. UC San Diego Health Institutional Review Board (IRB) reviewed and approved study protocol. Patient S4 provided informed consent to have microarray placed on their pial while unconscious. The electrode was implanted on the lateral surface of the temporal lobe across the superior and middle temporal gyrus. The Partners Human Research Committee reviewed and approved the IRB protocol at Brigham and Women's Hospital. S2 read visual words, repeated auditory words, and named visual pictures. S3 saw a three-letter string (GUH, SEE) and then heard an auditory two-phoneme combination, making a decision whether the visual and auditory stimuli matched. Interspersed were visual control trials in which a false font was followed by a real auditory stimulus and auditory control trials in which a real letter string was followed by a six-band noise-vocoded two-phoneme combination. The clinic compatible, open source electrophysiology (ephys) system was used based on Intan technology (Los Angeles, CA) to record acutely during neurosurgery. The details of the system have been published[27] and the design files and software are freely available on https://github.com/TNEL-UCSD/nacq and are briefly discussed below. The system was capable of recording 256 channels at 20 kHz and featured 5 kV RMS power isolation. The purpose of an isolator was to protect the patient from hardware malfunctions and/or power surges. The system consisted of an adapter, amplifier and digitizer (Intan RHD2164), power isolator, and

USB buffering board (RHD2000). The adapter had switches, which could connect a subset of electrodes to reference (REF) or ground (GND). Typically, two macrodots were connected to REF while GND was connected to an external needle probe (The Electrode Store, Buckley, WA) that was inserted in the scalp near the craniotomy. The signals were then amplified and digitized by the RHD2164, passed through the power isolator, then buffered and sent via USB to a laptop. Since ephys components were within several feet of the surgical site, these components were sterilized via standard methods at each of the participating hospitals. The adapter and RHD2164 were sterilized using an electronics friendly process called Sterrad. Sterrad was a low temperature sterilization method that uses hydrogen peroxide plasma to eliminate microbes. It was found that there were no obvious effects to the hardware in the first three to five sterilization runs. The clinical recording system was an Xltek with 128 channels (Natus Neurology, Pleasanton, CA).

3.2.4 Analysis and Statistical Methods

The following software and toolboxes were used: MATLAB, EEGLAB, and the Fieldtrip, Chronux toolboxes. Power spectral densities were estimated using Welch's method (pwelch) using a Kaiser Window of length 0.75 s with $\beta = 4$. An entire time period of 10 s was used with 50% between windows. Pointwise c.i.s were computed using the Matlab pwelch function and the expression for c.i. was equation 5.3.64 on page 280 in Manolakis et al.[28] Power in the 10–50 Hz band was obtained by forward and reverse filtering the signal with a third-order IIR Butterworth filter and then the resultant was squared. To determine statistical significant, the two epochs were windows into 0.5 s nonoverlapping segments. Power was estimated for all windows across the two conditions and then run through Wilcoxon signed rank sum test to determine significance. The absolute median difference of the PSD estimate was computed over the 10–50 Hz to gauge separability across frequencies. The time–frequency plot was generated using short-time Fourier

transform method with Slepian tapers (mtspecgramc from the Chronux toolbox). The moving window was of length 400 ms and step 40 ms. A time-bandwidth product of 5 and 5 tapers were used. The power was converted to units of dB then z-scored across to highlight temporal dynamics. To remove noise, the average signal of the microdot electrodes was subtracted from each channel (average re-reference) and each channel was then band stopped around line noise and its harmonics. Next, the data were epoched to the onset of stimulus presentation (visual word/picture/auditory word onset for S2, visual word onset for S3) and for each trial the baseline from −300 to 0 ms was subtracted. Trials judged to have artifactually high amplitude or variances were removed from the data set. To investigate differences between stimulus classes in the high-frequency band, amplitude was obtained using a fourth-order Butterworth bandpass filter from 70 to 170 Hz and then taking the analytic amplitude from the Hilbert transform and smoothed with a moving window. ANOVAs were run between stimuli classes and corrected for multiple comparisons with false-discovery rate.[30] S2 had 60 trials for each condition (visual word, auditory word, visual picture). S3 had 157 trials for the human voice and 80 trials for noise-vocoded stimulus. For the time–frequency plots, epochs were transformed from the time domain to the time–frequency domain using the complex Morlet wavelet transform. For the HFB frequencies, constant temporal and frequency resolution across target frequencies were obtained by adjusting the wavelet widths according to the target frequency. The wavelet widths increased linearly from 14 to 38 resulting in a constant temporal resolution of 16 ms.

3.3 Results

3.3.1 Device Benchmarking

To realize the fully conformal, high-density PEDOT:PSS microelectrode array, we utilized parylene C as an insulating and flexible substrate carrier for the sensing electrodes and the

metallization lines. The device consisted of an array of 56 microelectrodes (arranged in an 8 × 7 grid) and 6 macrodots (arranged in a 1 × 6 strip) of which a subset was used as reference. The macrodots have the same 3 mm diameter as commonly used clinical electrodes (e.g., Ad-Tech Medical Inc.) and are arranged in the same form factor (strip shape with 1 cm spacing) as shown in Figure 1a. The microelectrodes have 50 μm diameter microdots and are spaced 400 μm center-to-center yielding an array that has a footprint of 3.25 mm × 2.85 mm. Extension to higher density and channel counts is possible with either passive wiring [16a] or active multiplexing electronics,[19] here we focus on the clinical translation of PEDOT:PSS by recording μECoG intraoperatively. We use this design to directly compare clinical recordings obtained by standard PtIr electrodes, similarly sized PEDOT:PSS macrodots, and the scaled PEDOT:PSS microdot arrays. The fabrication process on 4″ glass carrier wafers is discussed in detail in the experimental section. **Figure 3.1b–d** show optical microscope images of the microarray after Ti/Au 10 nm/100 nm evaporation, parylene C chemical vapor deposition and selective etching above the Ti/Au microdots, and definition of PEDOT:PSS only above the Ti/Au microcontacts by a spin-cast and peel-off process. The metal leads are encapsulated with ≈2.9 μm thick parylene C from each side. Therefore, the cortical surface will only be exposed to the PEDOT microcontacts and the parylene C substrate surface. **Figure 3.1e** shows a scanning electron microscope (SEM) image of one 50 μm diameter microdot. To confirm the structural integrity of the microdots and their interfaces with both parylene C and underlying metal contacts, a critical safety factor for use in clinical procedures, we performed focused-ion-beam (FIB) slicing at the edge of the microdot of **Figure 3.1e**. The parylene C layers embed the edges of the metal contact and are etched at its center where only PEDOT:PSS was deposited as shown in **Figure 3.1f**. The spin-casting approach for depositing PEDOT:PSS enables an intimate contact with the underlying metal and the sidewall of

the etched parylene C, forming a tight and fully biocompatible neural interface device. After autoclave sterilization at 121 °C for 20 min in steam, we performed atomic force microscopy (AFM) on the PEDOT:PSS surface for two purposes: (1) validate that insignificant morphological changes occur post sterilization, and (2) no nanoscale voids exist in the PEDOT itself such that the electrochemical interface is only PEDOT:PSS and not a mixed PEDOT:PSS and metal one as is the case when PEDOT:PSS is electrodeposited on metal contacts. **Figure 3.1g** shows the AFM image on PEDOT:PSS film after autoclave showing a relatively smooth and continuous surface with a root mean square surface roughness of 1.22 nm. These cumulative structural studies support the integrity of PEDOT:PSS on parylene C for safe intraoperative monitoring of brain activity.

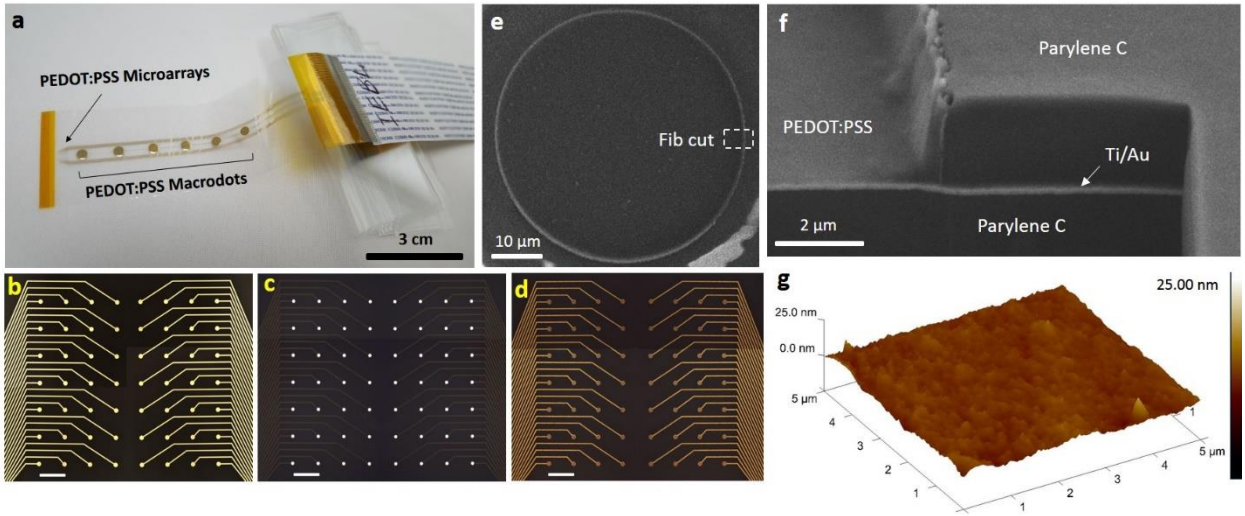

Figure 3.1 Structural and morphological characterization of PEDOT:PSS electrophysiology device. a) A picture of the fabricated electrophysiology PEDOT:PSS device on thin film parylene C layer showing the location of microarrays with 56 microdots at the top of the probe and above the 6 macro REF electrodes. Optical microscope image of the microelectrodes after b) Ti/Au deposition and lift-off process, c) selective parylene C oxygen plasma etching to expose the gold electrodes, and d) definition of PEDOT:PSS layer on top of only the metal microelectrode sites (scale bars 400 µm). e) Top view SEM image of the circular PEDOT:PSS microelectrode with 50 µm diameter. The white contrast in the lower right of the image is the result of electron charging on parylene C and does not signify a morphological detail. The dashed white box highlights the location of FIB cut. f) Slanted view SEM image showing the cross-section of the device and the stacked layers highlighting conformal and intimate contact between the different layers of the device and exposure of PEDOT:PSS as the only electrochemical interface. g) 3D AFM topography image of a 5 × 5 μm^2 scan area of PEDOT:PSS film after autoclave sterilization showing smooth and uniform morphology (compared to before sterilization, not shown) and the absence of voids in the film.

For high fidelity recordings, the yield and reproducibility in device fabrication is important. Our refined fabrication process (see the Experimental Section) resulted in a high yield of functional microelectrodes (>96% functional) and a very narrow distribution of their impedances. Specifically, as shown in **Figure 3.2a**, conventional fabrication procedures lead to a 1 kHz average impedance of 19.81 ± 6.94 kΩ whereas the refined procedure for three separate devices resulted in average impedances of 12.68 ± 0.35, 12.12 ± 0.4, and 13.1 ± 0.45 kΩ (**Figure 3.2a**). Since clinical electrodes are not manufactured with microscale electrodes, we fabricated a comparison set of Pt microarrays in a similar fashion to our PEDOT:PSS arrays to compare impedance profiles.

In contrast to PEDOT:PSS devices, Pt microelectrodes demonstrated a broader distribution of impedances with average impedance at 1 kHz of 337.52 ± 37.02, 290.23 ± 35.2, and 316.64 ± 27.18 kΩ (**Figure 3.2b**). The Bode plots of the electrochemical impedance spectroscopy (EIS) for one of these device types (MGS-112 with PEDOT:PSS contacts) and (Pt3 with platinum contacts) are depicted in the inset of **Figure 3.2a,b** respectively and demonstrate nearly identical electrochemical characteristics for all of 56 PEDOT:PSS microdots and nonuniform characteristics for Pt microdots in the array. EIS characterization of Pt and PEDOT:PSS micro/macro electrodes are shown in **Figure 3.2c,d** (clinical electrode EIS spectra are shown in Figure S2, Supporting Information). The impedance of PEDOT:PSS microarrays (50 μm diameter) displayed mostly capacitive characteristics below 100 Hz; above 100 Hz the impedance saturates at the series resistance values in a regime where the electrochemical current is impeded by edge current crowding and solution resistance. Across frequencies of interest for physiological analyses (1 Hz–10 kHz), PEDOT:PSS microelectrodes exhibited more than ten times lower impedances than those measured for Pt microelectrodes. The impedance of Pt microarrays on the other hand displayed a nearly fixed dependence on frequency with mixed capacitive and faradaic processes. For the larger 3 mm diameter macrodots, the impedances become significantly lower and are dominated by series resistances (detailed models with size dependencies will be published elsewhere[20]). These impedance values dictate the noise spectra shown in **Figure 3.2e, f**. The relatively low impedance PEDOT micro and macrodots and the Pt macrodot all exhibit noise power spectral density that is similar to that of the amplifier. The smaller Pt microelectrode with over one order of magnitude higher impedance than the PEDOT microelectrodes exhibit a larger noise floor than all other electrodes and the amplifier noise. These uniform impedances and lower noise spectra for PEDOT

microelectrodes compared to Pt microelectrodes highlight their potential for scaled ECoG microelectrodes without compromising the signal to noise ratio, as we validate in this work.

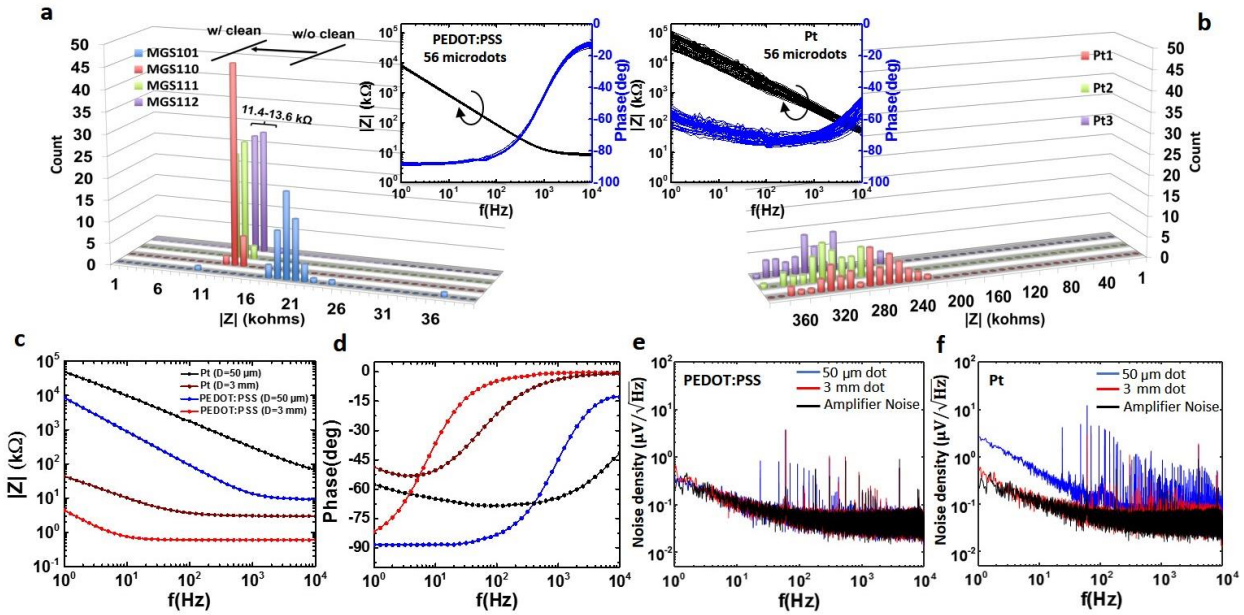

Figure 3.2 Electrochemical comparison of platinum and PEDOT:PSS electrodes. a) The 1 kHz impedance histogram for three optimized PEDOT:PSS devices, i.e., MGS 110, MGS 111, and MGS 112, with 55, 54, and 56 working channels out of 56 microdots, respectively, and for the non-optimized PEDOT:PSS (MGS 101). b) The 1 kHz impedance histogram for three Pt devices, i.e., Pt1, Pt2, and Pt3 with 52, 54, and 56 working channels out of 56 microdots, respectively. The insets of (a) and (b) show EIS spectra for all 56 microdots of MGS 112 and Pt3 displaying robust and uniform characteristics of PEDOT:PSS microdots compared to nonuniformity of Pt microdots. c) Impedance and d) phase spectra for micro and macro PEDOT:PSS and Pt electrodes showing distinctive electrochemical behavior (see the text) and lower impedances for PEDOT:PSS. e) The noise density of micro/macro PEDOT:PSS and f) Pt electrodes showing that PEDOT:PSS noise is low and is masked by the amplifier noise whereas Pt microdot noise is significantly higher, particularly in the low-frequency regime (theta, gamma, and low-frequency oscillation bands) where cognitive field potentials are located.

3.3.2 Human Electrophysiology

Having shown the favorable characteristics of our PEDOT:PSS electrodes compared to Pt electrodes, next we assessed our electrodes' ability to measure human electrophysiological activity. We performed intraoperative recordings in both anesthetized patients and patients undergoing clinical mapping of eloquent cortex during epilepsy and tumor resection surgery. The

recordings reported consist of testing with four individuals: three at UC San Diego (UCSD) Thornton Hospital (La Jolla, CA) and one at Brigham and Women's (BW) Hospital (Boston, MA). At UCSD, we performed recordings using PEDOT:PSS from Subject 1 (S1) both while awake and while unconscious, and from Subjects 2 and 3 (S2 and S3) while performing a cognitive task. At BW, Subject 4 (S4) was unconscious during the recordings. As an initial analysis, we demonstrate that PEDOT records comparable activity to current clinical electrodes (**Figure 3.3**). Here we compare electrophysiology from the macrodot Pt (clinical electrodes), versus the macrodot and microdot PEDOT:PSS electrodes during two different states for S1 when the electrodes were implanted on the anterior superior temporal gyrus (STG). The first state is awake and is engaged in an audio-visual task (see the Experimental Section for details) versus the second state of anesthesia with Propofol and Dexmedetomidine. As expected there were readily observable differences in electrophysiological recordings between the two states as illustrated in power spectral densities (PSD) (**Figure 3.3a–c**), time–frequency plots and time series (**Figure 3.3d–g**). There is markedly higher power in the anesthetized condition and in particular in the 12–17 Hz range, indicative of spindle-like activity (**Figure 3.3a–c**). Spindling has been reported in deeply anesthetized patients under the drug Dexmedetomidine.[21] Time–frequency plots also appear to show spindling and other dynamic neural activity (**Figure 3.3d, e**). Clinical ECoG using standard of care electrodes (3 mm Pt) were recorded alongside PEDOT ECoG. A PSD of a clinical electrode shows comparable effects to those measured by the PEDOT electrodes: (1) increased power during the anesthetized condition and (2) a prominent peak around the alpha range for the task condition. Each electrode showed a significant difference in power in the 10–50 Hz band (**Figure 3.3a–c**). However, there is variation in the PSD difference magnitude between the clinical and PEDOT for these measurements. The absolute median difference across 10–50 Hz frequencies is 2.4, 6.2, and

7.8 dB for clinical-, macro-, and microelectrode, respectively. Furthermore, the 95% pointwise confidence intervals (c.i.s) for the two PSD conditions begin to overlap at successively high frequencies: 30, 42, and 44 Hz, for a clinical, macro, and microelectrode, respectively (**Figure 3.3a–c**); it is important to note that these simultaneous recordings were made from different cortical sites, centimeters apart, which is likely a source of variation in the measured physiological response across electrode types. The critical observation is that the expected physiological modulation observed in the clinical ECoG is also seen in micro PEDOT electrode.

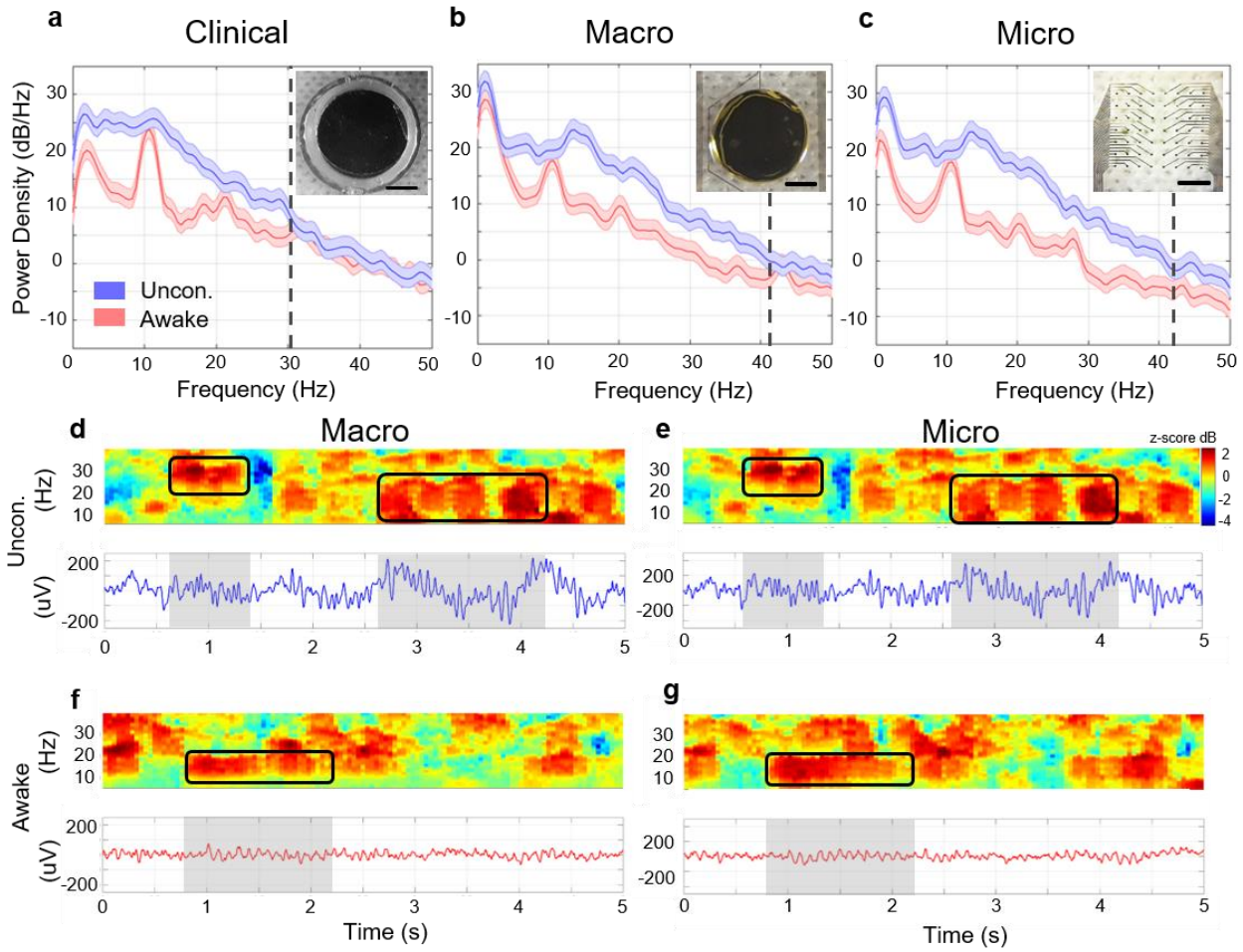

Figure 3.3 Awake versus unconscious ECoG differences in clinical, PEDOT macro, and micro electrodes. Power spectral densities (PSDs) between the two conditions (awake vs unconscious) for a) clinical electrode, b) PEDOT macro, and c) microdot. Inset of (a) shows optical image of clinical Pt macrodot and panels (b) and (c) show optical image of PEDOT:PSS macrodot and an array of 56 microdots (scale bars 1 mm). The dark blue and red lines are average PSD estimates from overlapping time windows and the lightly colored shaded regions are the 95% pointwise c.i. (see the Experimental Section). Power over the 10–50 Hz band shows significant differences between the two conditions for all electrodes: 8.9 × 10−5 (clinical), 1 × 10−4 (macro), and 8.9 × 10−5 (micro) (Wilcoxon signed rank test). The absolute median difference between 10–50 Hz of the estimate power density is 2.4, 6.2, and 7.8 dB for clinical-, macro-, and microelectrode, respectively. The dashed black line at 30, 42, and 44 Hz for (a)–(c) mark the frequency at which the c.i.s start to overlap for frequencies >15 Hz. Time–frequency and corresponding time series are shown for a sample 5 s window for the unconscious (d and e) and awake condition (f and g). The rectangles highlight increases in beta (20–30 Hz) and spindling activity (12–17 Hz). Color axis represents standard deviations away from the mean for each frequency. The time window per condition for macro and micro are nearly identical.

Another example of consistent physiological effects observed across electrode types is shown in **Figure 3.4**. S4 was undergoing a standard nondominant temporal lobe resection. Prior to removal, clinical and PEDOT electrodes were placed on the lateral surface of the temporal lobe across the superior and middle temporal gyrus. After recording under usual anesthetic conditions, a dose of Methohexital (Brevital) was administrated with the intention of increasing epileptiform activity.[22] As expected, this caused a noticable increase in epileptiform activity after several minutes as illustrated in the time traces across the electrode types (**Figure 3.4a, b**). The time traces are taken over two windows: T1 which was shortly after the Methohexital dose and T2 which occurred 200 s after T1. PSDs for T1 and T2 are plotted for clinical, PEDOT macro, and micro (**Figure 3.4c–e**, respectively) showing the same trend: more activity in T2. However, when computing the difference in power for the 10–50 Hz band, only the PEDOT electrodes showed a significant difference. Again, the measured variation can also be explained by differences in neural activity across several centimeters of cortex. As with the previous subject, the PEDOT microelectrode shows a significant difference between baseline and increased epileptiform activity demonstrating their potential clinical utility.

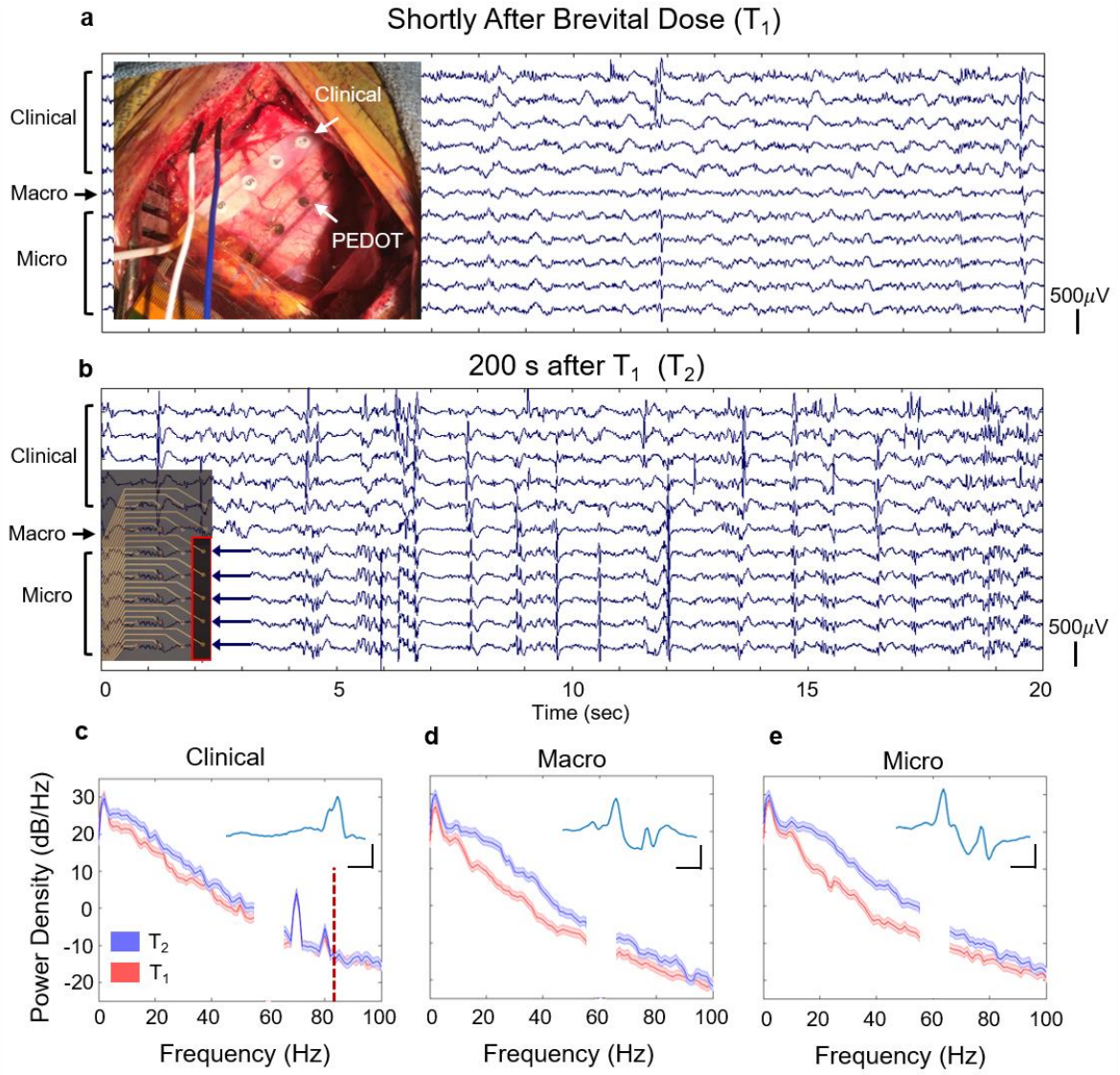

Figure 3.4 Methohexital (Brevital) induced differences in clinical, PEDOT macro, and micro electrodes. a) Simultaneously captured ECoG traces from clinical, PEDOT macro, and micro electrodes shortly after Methohexital dose (T1) and b) 200 s after T1, (T2). Inset in (a) shows the clinical and PEDOT ECoG probes implanted over the superior and middle temporal gyrus. Inset in (b) shows which microelectrodes are plotted for (a) and (b). Power spectral densities of a c) clinical, d) macro, and e) micro electrode taken from T1 (red) and T2 (blue). The dark blue and red lines are average PSD estimates from overlapping time windows and the lightly colored shaded regions are the 95% pointwise c.i. (see the Experimental Section). Power in the 10–50 Hz band show significant differences only for PEDOT electrodes: 0.010 (clinical), 5.5 × 10−6 (macro), and 4.3 × 10−6 (mirco) (Wilcoxon signed rank test). The noise spectra around 60 Hz frequency was filtered out with a notch filter for all devices. The dashed red vertical line in (c) indicates the upper passband cutoff frequency for the clinical system. Insets from (c)–(e) show an interictal epileptic discharge (IED) captured concurrently across the three electrode types. Scale bars are 200 μV (vertical) and 50 ms (horizontal).

To further examine spatial specificity, we analyzed stimuluslocked cognitive activity in two patients. Recordings were made from the anterior STG for S2 (**Figure 3.5a**) and from the posterior STG for S3 (**Figure 3.5d**) while each was awake for the clinical mapping of eloquent cortex. While awake, each also performed a short task (see the Experimental Section). S2 verbally responded on >95% of naming trials and S3 made a correct match/mismatch decision on 98% of trials. Spectrograms demonstrated increases in high-frequency power specific to certain stimuli classes: auditory words for S2 (**Figure 3.5c**) and noise-vocoded stimuli for S3 (**Figure 3.5f**).[23] The most consistent difference across electrodes was in the frequency ranges commonly referred to as "high-gamma," here defined as 70–170 Hz (**Figure 3.5c, f** shows the responses for three neighboring example channels from each subject). This high-frequency band amplitude (HFB) is highly correlated with population neuronal firing rates.[24] To better assess this HFB response, we looked at the response averages across electrodes. Of the 56 microcontacts, 42 in S2 and 34 in S3 were functional, as determined by impedance <60 000 ohms. While reference autoclave experiments here and in ref. [18] showed negligible influence on the microarray impedances (**Figure 3.2**), some of the microarray dots displayed higher impedances after transportation and autoclave by hospital personal as determined by impedance measurements just prior to the recordings and is attributed to issues in handling the arrays rather than the autoclave process itself. In S2, 16 of 42 good electrodes demonstrated a significant ($p < 0.05$ false-discovery rate corrected) increase to auditory words relative to visual words and pictures (38% of electrodes). In S3, 31 of 34 electrodes demonstrated a significant increase ($p < 0.05$ false-discovery rate corrected) to auditory noise-vocoded trials relative to human voice trials (91% of electrodes). S3 also saw a visual bigram prior to the auditory stimulus, but showed no significant response across electrodes to visual stimuli. **Figure 3.5b,e** shows the HFB of the six example electrodes chosen from a 3 × 2 portion of the

grid, demonstrating that the presence of an effect and the variability of the effect size can vary across distances as small as 400 μm.

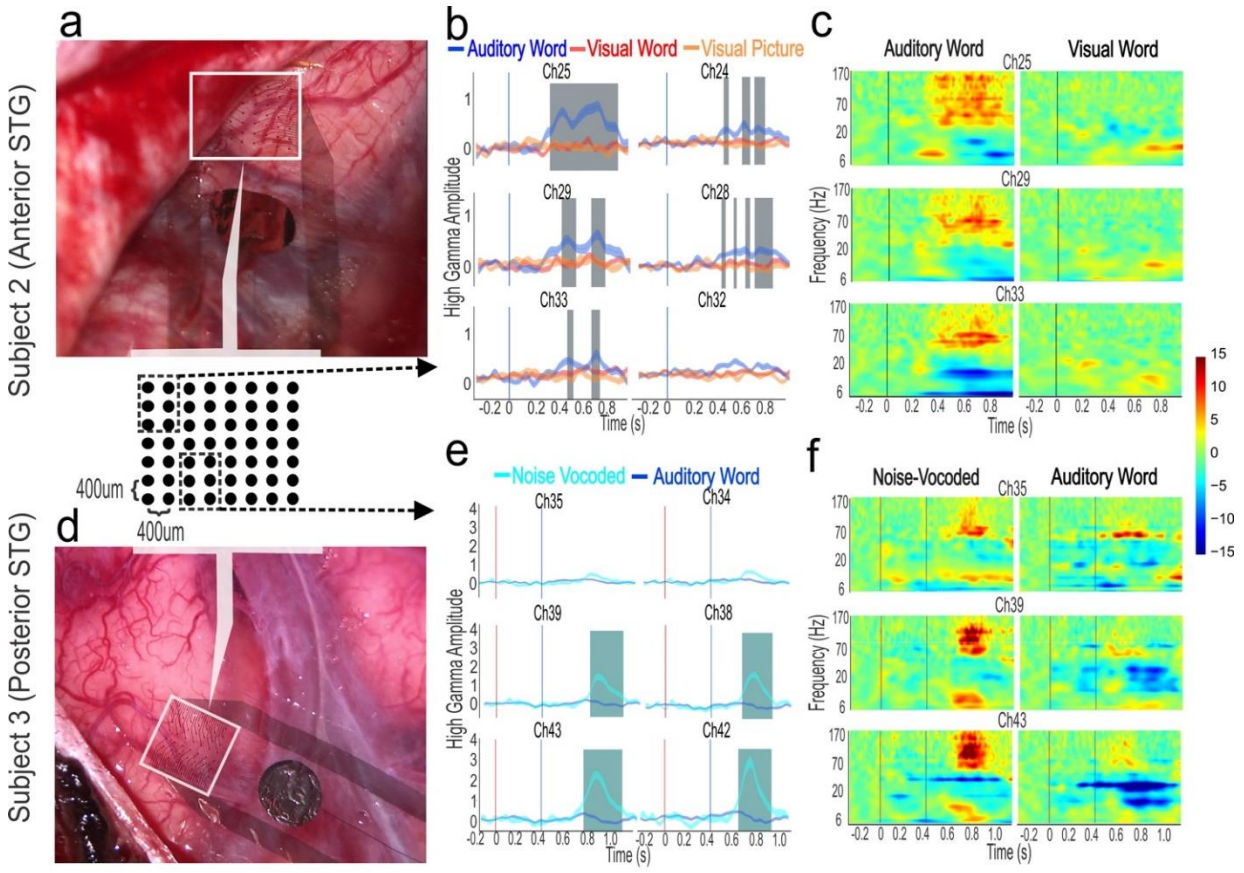

Figure 3.5 Neural activity varies across distances as small 400um (a & d) Electrode placement from the two subjects who performed cognitive tasks. Activity from six neighboring electrodes (3x2 electrodes) from the 8x7 electrode array are displayed to illustrate high-frequency amplitude variation. The white box highlights device placement (device partially obscured in subject 1 by the dural flap). (b & e) High-frequency amplitude for the 3x2 channels confirming significant differences in Hilbert analytic amplitude from 70-170Hz between stimuli classes (shaded regions are anova fdr-corrected significant differences). For subject 2, the blue vertical line indicates stimulus onset. For subject 3, the red vertical line indicates visual stimuli onset (to which no response was found across the electrodes) and blue line indicates auditory stimulus onset. (c & f) Time-frequency plots from three of the example channels (3x1) in response to different stimuli classes demonstrating strong differences in higher frequencies. Displayed is trial-averaged power determined by wavelets.

3.4 Discussion

Here we report the fabrication of a highly reproducible, high-yield PEDOT:PSS microarray, demonstrate PEDOT:PSS possesses superior impedance characteristics compared to Pt clinical electrodes, and show the first PEDOT:PSS recorded stimulus-locked human cognitive activity. A variety of structural studies confim PEDOT:PSS is safe for implantation and our microaray had a high yield of functional microelectrodes (>96% functional) with a very narrow distribution of impedances. Microelectrodes measured similar electrophysiological phenomena as macrodots made of either PEDOT:PSS or Pt across anesthesized, awake, and pathological states despite the microelectrode's 4 orders of mangitude smaller area. The PEDOT micro-electrode exhibited significant differential power among various conditions (**Figure 3.3** and **3.4**) demonstrating their clinical viability. Finally, we demonstrated that the PEDOT:PSS microelectrode array was capable of resolving differences in cognitive responses across cortical tissue over distances as small as 400μm.

In other cases, especially when considering the broad-band (1Hz to Nyquist frequency) signals, PEDOT micro-electrodes had highly similar signals as compared to the clinical electrodes as shown in **Figure 3.4a** and **3.4b**. This can partly be attributed to referencing schemes (bi-polar vs uni-polar, see methods), but is primarly a result of sensing signals much closer to each other (400μm – 3mm vs 1 – 5 cm) [25]. Recent work by Kellis et. al., have shown that pairwise correlation from μEcoG electrodes are approximately 0.5 with electrodes spaced 5 mm [25]. Since the maximum distance between any pair of microelectrodes in this work is 4.2 mm, the observed signal similarity is consistent with Kellis et. al.[25]

Measuring highly similar signals has advantages and disadvantages, which change depending on use case. An advantage for measuring highly similar or redundant signals is that they

may help denoise a collective signal or feature when combined intelligently. For example, interictal epileptic discharges, IEDs, are difficult to detect using automated algorithms and even challenging for trained electrophyiologists. IED detection might be improved if there were multiple redundant views of the signal which could increase detection confidence. This concept has been used by electrophysiologists to better detect action potentials from single units (eg. tetrode designs). This potential motivates investigation of high density or mixed density surface probe designs, even if sensed signals appear to be highly similar.[16b]

As electrode development pushes towards decreasing contact size to increase spatial specificity, PEDOT:PSS contacts facilitate high SNR recordings and have a number of favorable characteristics. The spin-casting approach used in our fabrication provides a consistent electrochemical interface and insignificant morphological changes post-sterilization.[18] This approach leads to a very high yield of functioning electrodes (>96%) with a narrow range of impedances. The EIS impedances for PEDOT:PSS are smaller than those for Pt which in turn results in lower noise power spectral density than those of Pt (**Figure 3.2e-f**). This difference is significant because cognitive processes that are generally observed at low frequencies (theta, gamma, and low frequency oscillations) need to be measured with the lowest possible electrode noise. Additionally, important information about neuronal firing in the high-frequency bands has a very low amplitude, making it critical to maximize SNR.

Combining these reliably low impedances with several other favorable characteristics makes PEDOT:PSS a strong contender for leading the next generation of neural electrochemical interfaces. These additional characteristics include high charge injection capacity (safe/efficient stimulation)[4], compliant mechanical properties for mimicking the curvilinear brain tissue and to compensate brain micromotion in order to reduce tissue damage[5], and enhanced biocompatible

electrode/tissue interfaces to minimize biofouling.[3a,6] With higher channel counts being achievable via passive wiring or active multiplexing, PEDOT:PSS presents a great opportunity to achieve high-density, high-SNR arrays, with greatly increased spatial specificity.

Despite the promise of PEDOT:PSS for neural recording, we are only aware of one group which displayed human neural recordings from a PEDOT:PSS device.[16] They demonstrated that PEDOT:PSS electrodes with an area of 10 x 10 μm^2 can sense a wide variety of neurophysiological activity including low frequency oscillations (beta, delta and spindle activity) and high frequency action potentials. They validated these neurophysiological signals by showing they are modulated by other neurophysiological signals and coarse conditions such as awake or under a variety of anesthesia, similar to our results in **Figure 3.3**. However, they have not demonstrated how the sensed neurophysiology is modulated by sensory stimulus or cognitive processing, which is one of the main contributions of this work. Interestingly, we did not detect action potentials, which may have been caused by excessive CSF between the pial surface and probe, which acts as a spatial low pass filter. In[16b], they suggest adding openings homogenously throughout the probe to allow CSF to flow over the probe as well as minimizing the amount of CSF near the probe.[16b] Additionally, the device presented in our study has a larger electrode size (50 μm diameter vs 10 μm diameter), which may have prevented the electrodes from sensing action potentials. Finally, the neurogrid device makes use of a tetrode-like design, concentrating 4 electrodes every 2000μm as opposed to our grid placing 1 electrode every 400μm. Future studies will need to determine optimal electrode design, which will undoubtedly vary for different clinical and experimental questions.

Finally, we examined the ability of PEDOT:PSS microgrid arrays to measure stimulus-locked cognitive responses to audiovisual stimuli. Neural responses to stimuli showed increases in

power in high frequencies, likely related to neuronal firing.[24] These increases proved to reliably discriminate different stimuli, both between language modalities (S2) and within a single language modality (S3). Further, the high-frequency amplitude and effects differed within a displacement of 400 μm, demonstrating the great spatial specificity possible with PEDOT:PSS microelectrodes.

3.5 Conclusion

The utility of high-density, high-SNR arrays with high spatial resolution is straightforward within the context of basic science. PEDOT:PSS micro-arrays can extend the ability of intracranial research to identify precisely the borders of functional regions and tease apart the information processing micro-circuitry operations within these regions. Perhaps more important is the great potential for PEDOT:PSS clinical applications as well and the potential for higher SNR and higher spatial resolution ECoG to improve patient outcomes for surgical brain resections. The current gold standard for sparing eloquent, motor, and sensory cortex during resections is direct cortical stimulation to map brain function. In addition to this gold standard, recent work demonstrates the potential use of recorded HFB activity as a complementary method for functional mapping.[26] The surgeon often faces a very difficult tradeoff of maximizing resection extent to remove pathological tissue and thus improve the patient's health, while preserving as much function as possible. The coarse spacing, limited channel count, and non-conformability of the currently used electrode substrate constrain the resolution of the information available to make a decision about this tradeoff. PEDOT:PSS electrodes provide safe and efficient stimulation in addition to their high-SNR recording ability and conformable characteristics. Using future arrays combining the excellent stimulation and recording capabilities of PEDOT:PSS, neurosurgeons would be more confident in the functional boundaries of the exposed cortex, and thus be able to make a more informed decision of which tissue to resect. Development of these arrays is facilitated by the fact

that PEDOT:PSS electrode fabrication allows quickly iterated designs. Eventually, working together, surgeons and researchers will be able to develop arrays that are effective for optimizing post-surgical outcomes.[8–10]

Chapter 3, in full, is a reprint of material as it appears in the following publication: M. Ganji, E. Kaestner, J. Hermiz, N. Rogers, A. Tanaka, D. Cleary, S. H. Lee, J. Snider, M. Halgren, G. R. Cosgrove, B. S. Carter, D. Barba, I. Uguz, G. G. Malliaras, S. S. Cash, V. Gilja, E. Halgren, S. A. Dayeh, "Development and translation of PEDOT: PSS microelectrodes for intraoperative monitoring," Advanced Functional Materials, vol. 28, p. 1700232, 2018. The dissertation author was the primary investigator and author of this material.

3.6 References

[1] J. C. Horton, D. L. Adams, *Philosophical Transactions of the Royal Society of London B: Biological Sciences* **2005**, 360, 837.

[2] B. Rubehn, C. Bosman, R. Oostenveld, P. Fries, T. Stieglitz, *Journal of neural engineering* **2009**, 6, 036003.

[3] a) R. J. Vetter, J. C. Williams, J. F. Hetke, E. A. Nunamaker, D. R. Kipke, *IEEE transactions on biomedical engineering* **2004**, 51, 896; b) G. Buzsáki, *Nature neuroscience* **2004**, 7, 446; c) P. A. House, J. D. MacDonald, P. A. Tresco, R. A. Normann, *Neurosurgical focus* **2006**, 20, 1.

[4] a) S. F. Cogan, *Annu. Rev. Biomed. Eng.* **2008**, 10, 275; b) D. R. Merrill, M. Bikson, J. G. Jefferys, *Journal of neuroscience methods* **2005**, 141, 171; c) V. S. Polikov, P. A. Tresco, W. M. Reichert, *Journal of neuroscience methods* **2005**, 148, 1.

[5] a) R. A. Green, R. T. Hassarati, J. A. Goding, S. Baek, N. H. Lovell, P. J. Martens, L. A. Poole-Warren, *Macromolecular bioscience* **2012**, 12, 494; b) M. R. Abidian, D. C. Martin, *Advanced Functional Materials* **2009**, 19, 573; c) S. F. Cogan, K. A. Ludwig, C. G. Welle, P. Takmakov, *Journal of neural engineering* **2016**, 13, 021001.

[6] a) N. G. Hatsopoulos, J. P. Donoghue, *Annual review of neuroscience* **2009**, 32, 249; b) C. E. Lagoa, J. Bartels, A. Baratt, G. Tseng, G. Clermont, M. P. Fink, T. R. Billiar, Y. Vodovotz, *Shock* **2006**, 26, 592.

[7] a) E. W. Keefer, B. R. Botterman, M. I. Romero, A. F. Rossi, G. W. Gross, *Nature nanotechnology* **2008**, 3, 434; b) N. A. Kotov, J. O. Winter, I. P. Clements, E. Jan, B. P. Timko, S. Campidelli, S. Pathak, A. Mazzatenta, C. M. Lieber, M. Prato, *Advanced Materials* **2009**, 21, 3970; c) E. Seker, Y. Berdichevsky, M. R. Begley, M. L. Reed, K. J. Staley, M. L. Yarmush, *Nanotechnology* **2010**, 21, 125504.

[8] a) J.-H. Kim, G. Kang, Y. Nam, Y.-K. Choi, *Nanotechnology* **2010**, 21, 085303; b) M. Heim, B. Yvert, A. Kuhn, *Journal of Physiology-Paris* **2012**, 106, 137; c) S. Park, Y. J. Song, H. Boo, T. D. Chung, *The Journal of Physical Chemistry C* **2010**, 114, 8721.

[9] J. Rivnay, S. Inal, B. A. Collins, M. Sessolo, E. Stavrinidou, X. Strakosas, C. Tassone, D. M. Delongchamp, G. G. Malliaras, *Nature communications* **2016**, 7.

[10] a) R. A. Green, N. H. Lovell, G. G. Wallace, L. A. Poole-Warren, *Biomaterials* **2008**, 29, 3393; b) M. R. Abidian, J. M. Corey, D. R. Kipke, D. C. Martin, *Small* **2010**, 6, 421; c) X. Cui, V. A. Lee, Y. Raphael, J. A. Wiler, J. F. Hetke, D. J. Anderson, D. C. Martin, *Journal of biomedical materials research* **2001**, 56, 261.

[11] a) M. R. Abidian, K. A. Ludwig, T. C. Marzullo, D. C. Martin, D. R. Kipke, *Advanced Materials* **2009**, 21, 3764; b) K. A. Ludwig, J. D. Uram, J. Yang, D. C. Martin, D. R. Kipke, *Journal of neural engineering* **2006**, 3, 59.

[12] D.-H. Kim, J. Viventi, J. J. Amsden, J. Xiao, L. Vigeland, Y.-S. Kim, J. A. Blanco, B. Panilaitis, E. S. Frechette, D. Contreras, *Nature materials* **2010**, 9, 511.

[13] M. R. Abidian, D. C. Martin, *Biomaterials* **2008**, 29, 1273.

[14] L. Groenendaal, F. Jonas, D. Freitag, H. Pielartzik, J. R. Reynolds, *Advanced Materials* **2000**, 12, 481.

[15] a) M. Asplund, E. Thaning, J. Lundberg, A. Sandberg-Nordqvist, B. Kostyszyn, O. Inganäs, H. von Holst, *Biomedical Materials* **2009**, 4, 045009; b) D.-H. Kim, J. A. Wiler, D. J. Anderson, D. R. Kipke, D. C. Martin, *Acta biomaterialia* **2010**, 6, 57.

[16] a) D. Khodagholy, J. N. Gelinas, T. Thesen, W. Doyle, O. Devinsky, G. G. Malliaras, G. Buzsáki, *Nature neuroscience* **2015**, 18, 310; b) D. Khodagholy, J. N. Gelinas, Z. Zhao, M. Yeh, M. Long, J. D. Greenlee, W. Doyle, O. Devinsky, G. Buzsáki, *Science Advances* **2016**, 2, e1601027.

[17] a) M. Sessolo, D. Khodagholy, J. Rivnay, F. Maddalena, M. Gleyzes, E. Steidl, B. Buisson, G. G. Malliaras, *Advanced Materials* **2013**, 25, 2135; b) D. Khodagholy, T. Doublet, M. Gurfinkel, P. Quilichini, E. Ismailova, P. Leleux, T. Herve, S. Sanaur, C. Bernard, G. G. Malliaras, *Advanced Materials* **2011**, 23.

[18] I. Uguz, M. Ganji, A. Hama, A. Tanaka, S. Inal, A. Youssef, R. M. Owens, P. P. Quilichini, A. Ghestem, C. Bernard, *Advanced Healthcare Materials* **2016**.

[19] J. Viventi, D.-H. Kim, L. Vigeland, E. S. Frechette, J. A. Blanco, Y.-S. Kim, A. E. Avrin, V. R. Tiruvadi, S.-W. Hwang, A. C. Vanleer, *Nature neuroscience* **2011**, 14, 1599.
[20] M. Ganji, **2016**.

[21] E. Huupponen, A. Maksimow, P. Lapinlampi, M. Särkelä, A. Saastamoinen, A. Snapir, H. Scheinin, M. Scheinin, P. Meriläinen, S. L. HIMANEN, *Acta anaesthesiologica Scandinavica* **2008**, 52, 289.

[22] a) W. A. Kofke, R. Tempelhoff, R. M. Dasheiff, *Journal of neurosurgical anesthesiology* **1997**, 9, 349; b) A. R. Wyler, E. Richey, R. A. Atkinson, B. P. Hermann, *Epilepsia* **1987**, 28, 490.

[23] P. Souza, S. Rosen, *The Journal of the Acoustical Society of America* **2009**, 126, 792.

[24] S. Ray, N. E. Crone, E. Niebur, P. J. Franaszczuk, S. S. Hsiao, *The Journal of Neuroscience* **2008**, 28, 11526.

[25] a) M. W. Slutzky, L. R. Jordan, T. Krieg, M. Chen, D. J. Mogul, L. E. Miller, *Journal of neural engineering* **2010**, 7, 026004; b) D. T. Bundy, E. Zellmer, C. M. Gaona, M. Sharma, N. Szrama, C. Hacker, Z. V. Freudenburg, A. Daitch, D. W. Moran, E. C. Leuthardt, *Journal of neural engineering* **2014**, 11, 016006.

[26] F. Darvas, R. Scherer, J. G. Ojemann, R. Rao, K. J. Miller, L. B. Sorensen, *Neuroimage* **2010**, 49, 930.

[27] J. Hermiz, N. Rogers, E. Kaestner, M. Ganji, D. Cleary, J. Snider, D. Barba, S. Dayeh, E. Halgren, V. Gilja, presented at Engineering in Medicine and Biology Society (EMBC), 2016 IEEE 38th Annual International Conference of the **2016**.

[28] D. G. Manolakis, V. K. Ingle, S. M. Kogon, *Statistical and adaptive signal processing: spectral estimation, signal modeling, adaptive filtering, and array processing*, Artech House Norwood, **2005**.

[29] R. Oostenveld, P. Fries, E. Maris, J.-M. Schoffelen, *Computational intelligence and neuroscience* **2010**, 2011.

[30] Y. Benjamini, Y. Hochberg, *Journal of the royal statistical society. Series B (Methodological)* **1995**, 289.

Chapter 4

Scaling Effects on the Electrochemical Performance of poly(3,4-ethylenedioxythiophene (PEDOT), Au, and Pt for Electrocorticography Recording

4.1 Introduction

The high selectivity, sensitivity and longevity of neuronal interface devices are dependent upon design considerations such as size, shape, and morphology of the applied materials.[1] The specific electrochemical, physical (mechanical), and biological characteristics of electrophysiology devices play a direct role in achieving advanced neuronal interface standards. In particular, for neuronal probes in the form of microelectrode arrays and neuroprosthetic devices, recording quality is inversely proportional to electrode impedance at the tissue interface.[2] For large scale recording of neuronal and field activities, sampling at a high spatiotemporal resolution[1b, 3] calls for smaller microelectrode sites in order to support higher channel count while increasing spatial specificity and in maintaining the electrode/electrolyte interface at low impedance. However, decreasing electrode dimensions reduces the device's electrochemically active area and increases the electrochemical impedance, which in turn can compromise the recording quality. This compromise is mostly attributed to the rise of noise voltage at the electrode/ electrolyte interface that is directly proportional to the electrode impedance.[4]

Given the low magnitude of neuronal potentials, their content can be screened by a high noise floor due to the random ion fluctuations in an electrophysiological medium.[2b] The mixed electronic/ionic conductivity of conducting polymers, particularly of poly(3,4-ethylenedioxythiophene):polystyrene sulfonate (PEDOT:PSS),[5] readily reduces the

electrochemical impedance enabling smaller geometrical design with possibly uncompromised signal quality.[6] Despite several decades of research in neuronal interface technologies, the scaling laws of the electrochemical characteristics of neuronal probes (i.e., their functional dependencies on size) have not been systematically determined. Here, we conducted a parametric study to evaluate scaling effects on the electrochemical performance of PEDOT:PSS on Au, PEDOT:PSS on Pt, pure Au and pure Pt electrodes with diameters ranging from 20 to 2000 μm. We quantify series resistance in its electrochemical and electrode lead components, as well as the capacitive and faradaic components of the overall electrode impedance. Equations are derived to predict these values as a function of diameter for each electrode material, thus permitting calculation of how their performance scales at smaller diameters. We also show that the electrochemical component that dominates electrode impedance varies across the frequency bands commonly sampled in clinical and functional studies. We then benchmark the impedances as a function of diameter in the different brain-wave frequency bands and illustrate performance gains for PEDOT:PSS coated electrodes in these different frequency regimes. Finally, we characterize the three-terminal noise performance and depict their diameter and frequency dependencies for all electrode materials. These results provide new insight into electrochemical coupling with these different electrode materials.

4.2 Experimental Details

4.2.1 Device Fabrication

The fabrication of PEDOT:PSS-based electrodes followed previously discussed processes in part 2.2.1. Fabrication of the platinum microarrays followed similar procedure to that of PEDOT:PSS devices except for the PEDOT:PSS deposition which was not carried out. For the Pt

devices, a 10 nm Ti adhesion layer and 100 nm Pt contact layer were deposited by sputtering (Denton Discovery 18 Sputter System).

4.2.2 Device Characterization

The devices were imaged using an FEI SFEG ultra high resolution SEM at 10 kV accelerating voltage. To reduce electron charging in the specimen, a 15 nm thick Ti layer was deposited on the back of the device and was electrically connected to the stage of the system providing a runaway path for impnging electrons. EIS was performed using a GAMRY interface 1000E in phosphate buffer saline (PBS) solution, using three electrodes configuration, i.e., Ag/AgCl electrode as a reference electrode, a large platinum electrode as a counter electrode, and target microarray/macrodot arrays as the working electrode. Sinusoidal signals with 10 mV RMS AC voltage and zero DC bias were applied and the frequency was swept from 1 Hz to 10 kHz. Noise measurement was performed using TDT acquisition system (RZ2 BioAmp Processor), whereas the electrode arrays were immersed in PBS solution, and 120 s duration multiplexed measurements were carried out on different channels with 24 kHz sampling rate per channel. RMS noise values were obtained by taking the standard deviation of each channel's voltage–time trace after filtering from 1 Hz to 10 kHz with a third order Butterworth filter (no additional notch filter was applied). The NSD was obtained from the raw data using the Welch periodogram estimation method. After filtering from 1 Hz to 10 kHz, RMS noise values were obtained from each electrode's PSD.

4.2.3 Electrochemical Impedance Fitting

A custom-made fitting algorithm was developed to fit using Matlab both the Nyquist and Bode plots of each measured EIS to equivalent impedance of the circuit configurations shown in **Figure 4.3a**. The input to the fitting algorithm is initial guess for the expected range of respective

electrochemical component of the equivalent circuits in **Figure 4.3a**. The code runs to minimize the error between the model's impedance and the experimental impedance of the electrodes resulting in best-match parameter values at the minimum error for the proposed circuit model. The fits for the extracted EIS electrochemical components were carried out using built-in Power functions in Origin software package.

4.3 Results and Discussions

4.3.1 Macro and Microelectrodes layout design

Microelectrodes with different interface materials including Au, PEDOT:PSS/Au, Pt, and PEDOT:PSS/Pt were fabricated on ultrathin (3.8 μm) flexible parylene C substrates as shown in **Figure 4.1a**. The details of the fabrication are described in the Experimental Section following previously published procedures.[5a] The thin parylene C layers were used as a substrate- carrier and passivation layers, each is 1.9 μm thick, to enable a microelectrode array that conforms to the cortical surface when used *in vivo*—for better coupling of brain activity and higher signal to noise ratio (SNR) recordings.[7] Electrode contacts were connected to the external characterization circuitry via 20 μm wide and 10/100 nm thick Ti/Au wire leads, with Au being on top of Ti, and an ACF/ribbon cable (**Figure 4.1a**). To assess the scaling of the microelectrodes' electrochemical properties, 16 different electrode diameters ranging from 2000 (macrodot) down to 20 μm (microdot) were studied. The cross-sectional scanning electron microscope (SEM) image in **Figure 4.1b** where the electrode edge was sliced by focused ion beam (FIB) shows full encapsulation of the metal leads with parylene C and exposure of the evaporated surface in the microdot electrode contact.

This also applies for the PEDOT:PSS devices except that the microdot areas displayed negligible surface roughness of ≈5 nm, measured also by AFM. Also, PEDOT:PSS coated the edge

of the parylene C sidewalls as shown in **Figure 4.1c**. **Figure 4.1d–g** show top view SEMs of different PEDOT:PSS/Au electrodes with 20, 30, 40, and 50 μm diameters. In general, we observed no significant morphological differences for dots with different diameters. As can be observed in **Figure 4.1c**, there is a larger thickness of the PEDOT:PSS at the edge of the parylene C than at the surface of the Au layer. Using a surface profilometer, we observed that the thickness of the PEDOT:PSS does not change with diameter and that the edge thickness remains invariant for all studied diameters.

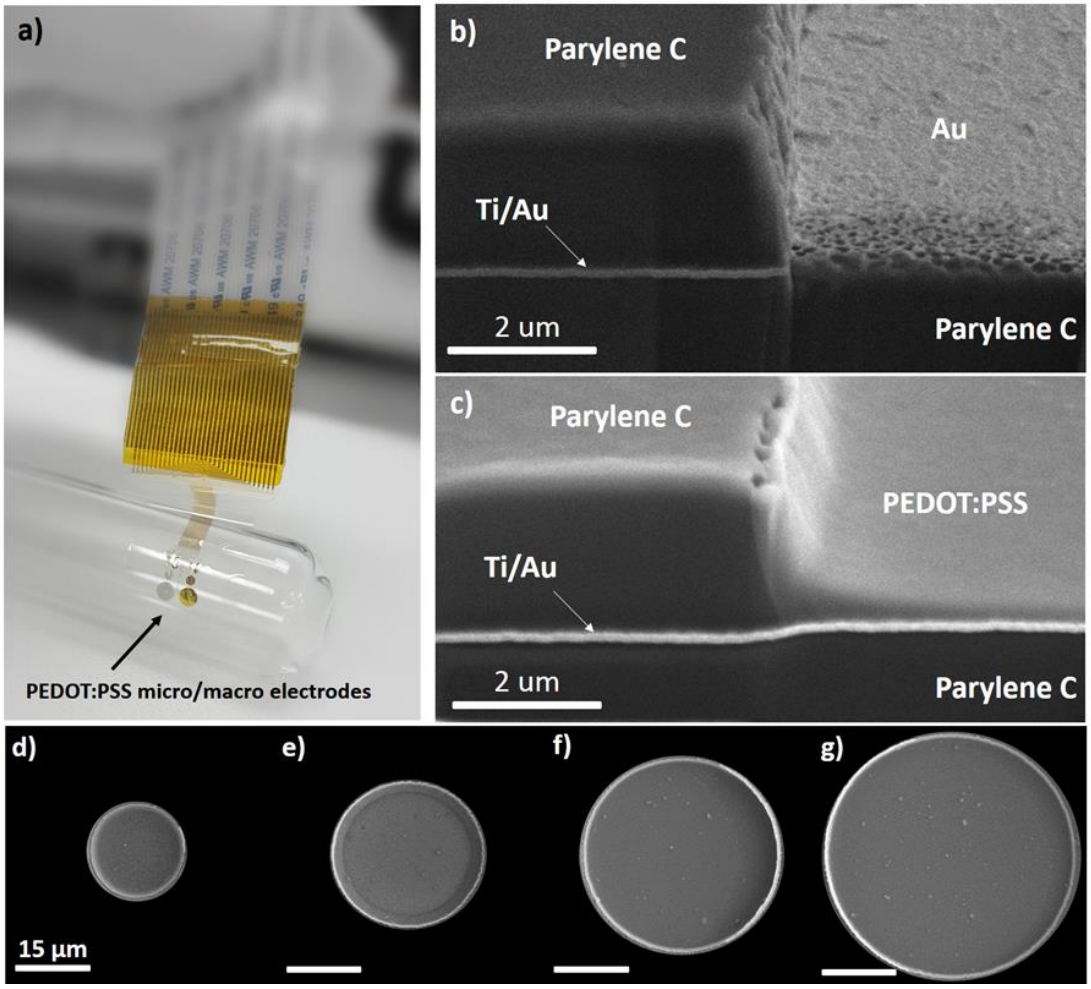

Figure 4.1 Structure and morphology of studied ECoG devices. (a) A picture of the fabricated PEDOT:PSS/Au ECoG electrodes on 6 µm thick parylene C substrate that were bonded using anisotropic conductive filament (ACF) to ribbon cables for characterization. 16 different diameters ranging from 2000 µm to 20 µm were included in each device. (b) 45° angle view of a cross-sectional SEM image after FIB slicing of an Au microelectrode edge and showing parylene C encapsulating the metal leads, and an exposed Au interface layer that is ~ 2.9 µm below the parylene C external surface. (c) 45° angle view of a cross-sectional SEM image after FIB slicing of a PEDOT:PSS/Au microelectrode displaying a uniform coating of the PEDOT:PSS layer on top of the underlying exposed Au contact. (d-g) Top view SEM images of the 20 µm (d), 30 µm (e), 40 µm (f) and 50 µm (g) PEDOT:PSS/Au electrodes.

4.3.2 Electrochemical impedance spectra

The analysis performed in this work is centered around the electrochemical impedance spectroscopy (EIS) that was performed in a three-electrode configuration in the frequency range of 1 Hz to 10^4 Hz (see Eperimental Section). **Figure 4.2a** and **4.2b** show the impedance magnitude and phase spectra of Au electrodes. As expected, by decreasing the electrode diameter and therefore decreasing the effective surface area, the electrochemical impedance values are increased. The impedance values at 1 kHz (commonly used to infer impedances at the frequency of an action potential [8]) varied from sub 1 kΩ to above 1 MΩ for diameters of 2000 µm to 20 µm, respectively. For diameters smaller than 100 µm, the Au electrodes showed capacitive-like behavior with phase spectra close to 90 degrees across the whole frequency range. For diameters larger than 100 µm, a transition to ohmic-like characteristics is observed at higher frequencies where the overall impedance is dominated by series resistances. **Figure 4.2c**, **d** show the impedance magnitude and phase spectra of PEDOT:PSS/Au electrodes. It is evident that using the PEDOT:PSS organic coating, the magnitude spectra are lower than those of the Au electrodes for the overall frequency range. For all studied diameters (down to 20 µm), the impedance values at 1 kHz were lower than 100 kΩ. Due to the overall lower impedance of PEDOT:PSS with respect to that of Au, the transition from the capacitive regime to the series-resistance dominant regime occurs at lower frequencies for PEDOT:PSS. Pt exhibited a similar impedance trend (**Figure 4.2e**) but slightly lower impedances than that of Au and the phase spectra showed a mixed capacitive-ohmic like characteristics (**Figure 4.2f**) as discussed below. When PEDOT:PSS was coated on Pt, similar impedance spectra (**Figure 4.2g**) and phase (**Figure 4.2h**) were obtained to that of PEDOT:PSS on Au with a series resistance saturation floor on Pt that is higher than that on Au.

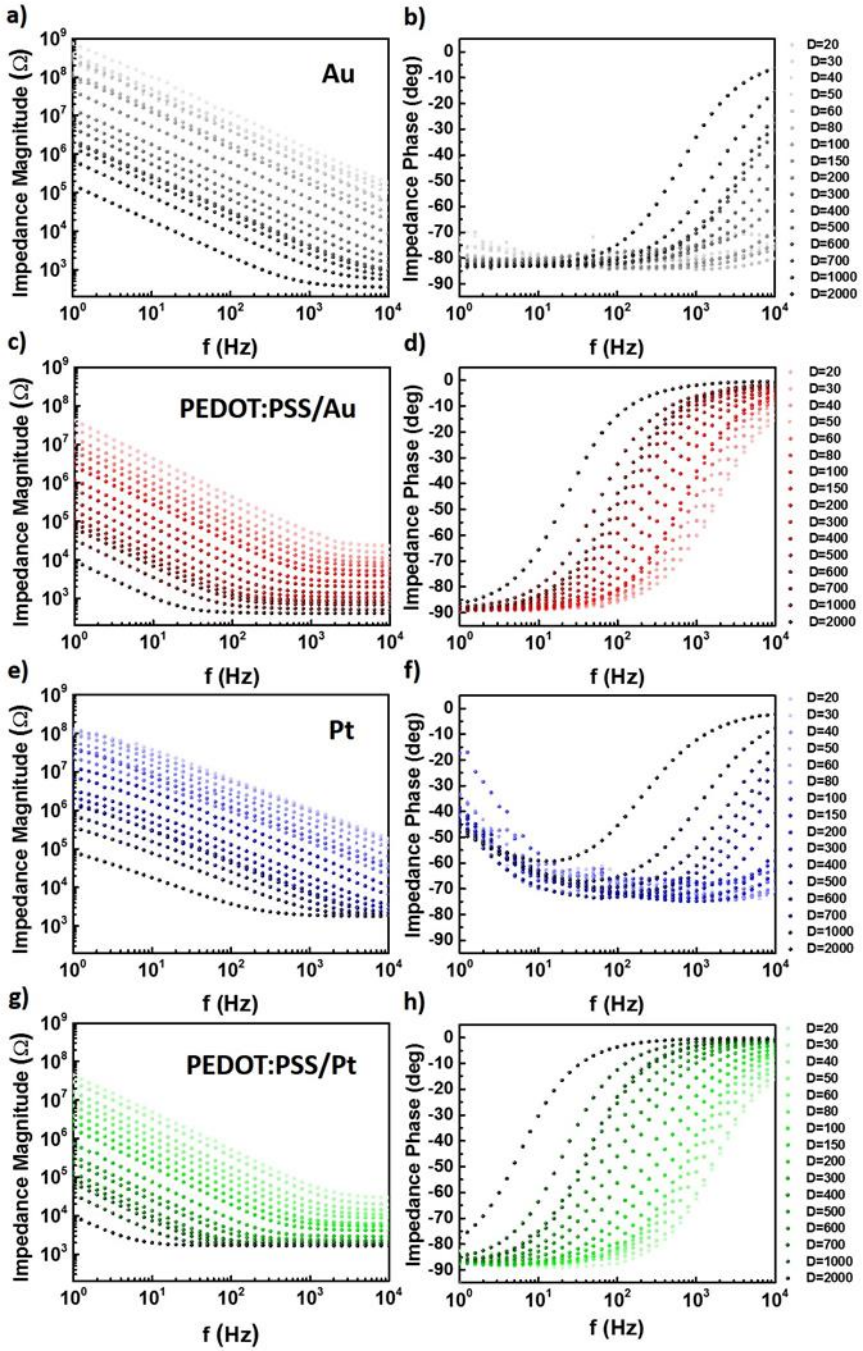

Figure 4.2 Electrochemical impedance spectra (EIS) of Au, PEDOT:PSS/Au, Pt, and PEDOT:PSS/Pt, with diameters ranging from 20 µm to 2000 µm. Magnitude and phase spectra of Au ((a) and (b)), PEDOT:PSS/Au ((c) and (d)), Pt ((d) and (e)) and PEDOT:PSS/Pt ((f) and (g)) electrodes. The graded light to dark colors denote spectra at increasing diameters.

4.3.3 Fitting EIS and Nyquist plots

These data were used to model the electrochemical characteristics of the studied materials using the circuits shown in **Figure 4.3a** for Au and PEDOT:PSS and in **Figure 4.3b** for Pt, by simultaneously fitting the impedance spectra and Nyquist plots. The models comprise a constant phase element (CPE) that accounts for the double layer capacitance, which is a non-ideal capacitor with reactance $|X|_{CPE} = \frac{1}{((2\pi f)^n C)}$. The non-ideal frequency dependence (i.e. n < 1) as opposed to that of ideal capacitors (n=1) is often associated with inhomogeneities in the electrode surface roughness.[2b,9] The redox reaction resistance, R_{ct}, accounts for the resistance to the direct charge transfer from solution to the electrode material through redox reactions, also commonly known as faradaic reactions. C_{ad} represents the adsorption capacitance, which accounts for the adsorption of the transferred species through the double layer on the electrode surface, which then participate in a redox reaction. R_s represents the series resistance that is composed of a solution resistance between the electrode surface and the counter electrode, the current crowding resistance near the electrode, usually at its edges,[2b] and the metal lead series resistances. Consistent with previous studies[2b] we did not use an adsorption capacitance for Pt because the faradaic impedance, Z_f, is usually much higher than the reactance of the capacitive branch, $|X|_{CPE}$ as discussed below. This high impedance suggests weak redox reactions and negligible adsorption of ion species occur at the surface of Pt electrodes. Indeed, the variability observed in the impedances of 50μm diameter Pt microelectrodes[1] supports the weak and variable adsorption of ion species to the surface of Pt. These models fit the impedance spectra and the Nyquist plots for all diameters within an average error of ± 3% for Au, ± 5.2% for PEDOT:PSS/Au, ± 6.9% for Pt, and ± 9.2% for PEDOT:PSS/Pt. The accuracy of the models in capturing the electrochemical characteristic of devices with different

diameters is reflected in the good fits shown for three different diameters (60, 300 and 1000 µm) in **Figure 4.3c-p** for all studied materials.

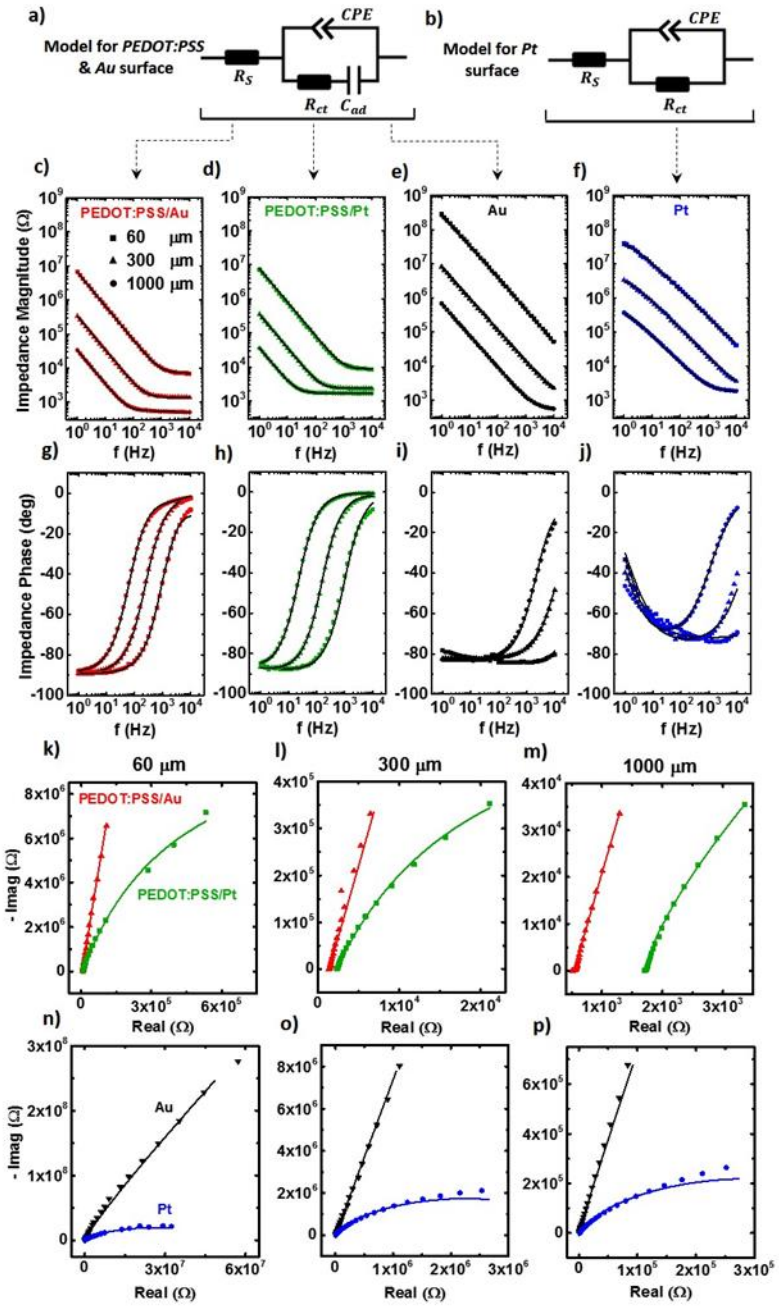

Figure 4.3 Fitting EIS and Nyquist plots of different scaled electrode materials using equivalent electrochemical circuit models. (a) Equivalent circuit model for scaled PEDOT:PSS/Au, PEDOT:PSS/Pt and Au electrodes (b) Equivalent circuit model for scaled Pt electrodes. (c-f) Measured and fitted impedance magnitude spectra of 60, 300 and 1000 µm PEDOT:PSS/Au (red), PEDOT:PSS/Pt (green), Au (black) and Pt (blue) electrodes . (g-j) Measured and fitted impedance phase spectra of 60, 300 and 1000 µm PEDOT:PSS/Au (red), PEDOT:PSS/Pt (green), Au (black) and Pt (blue) electrodes. Measured and fitted Nyquist plots of 60, 300 and 1000 µm PEDOT:PSS/Au (red), PEDOT:PSS/Pt (blue) (k, l, m), Au (black) and Pt (blue) electrodes (n, o, p).

4.3.4 Electrochemical Components

With these EIS spectra and the model, we can now study the influence of scaling on each component of the electrochemical interface. The extracted values for material-specific series resistance (R_s) are plotted versus diameter in semilog (**Figure 4.4a**) and log scales (**Figure 4.4b**), together with the best fit for their diameter dependence. The PEDOT:PSS coating did not influence R_s. The functional dependence and the lowest Rs value at larger diameters were merely determined by the underlying metal electrode. This is not surprising as the ion-permeability of PEDOT facilitates the interaction with underlying metal lead when other processes (capacitive and faradaic) are not limiting particularly at larger diameters. The Rs exhibited a 1/D dependence for Au and PEDOT:PSS/Au microelectrodes originating from current crowding at the edges of the dots with increased diameter, i.e. the electrochemical current transport occurs at the edge of the dots. Similarly, R_s for PEDOT:PSS/Pt and Pt exhibited a 1/D dependence for D < 300μm above which R_s nearly saturates at ~ 2 kΩ, the metal lead series resistance. Therefore, the overall diameter dependence for R_s of Pt and PEDOT:PSS/Pt can be fitted with $1/D^{1.75}$ masked by a diameter-independent series resistance. Since the larger contacts were more distant than the smaller contacts, the metal lead resistance is larger than those of larger contacts. Therefore, we conclude that the electrochemical component of the series resistance scales as a function of 1/D. As the diameter-independent series resistance of the metal leads becomes larger than this electrochemical series resistance, the functional dependence deviates to larger power exponent for D as we observed for the case of PEDOT:PSS/Pt and Pt.

The scaling of the capacitive coupling embodied in CPE is shown in **Figure 4.4c** (semilog) and **Figure 4.4d** (log scale). Here, the reactance, $|X|_{CPE} = \frac{1}{((2\pi f)^{0.9}\, C)}$ was calculated at 1 kHz and exhibit an areal dependence of $1/D^2$ for Au and PEDOT:PSS/Au and slightly

weaker/inhomogeneous areal dependence for Pt and PEDOT:PSS/Pt that exhibited $1/D^{1.75}$ and $1/D^{1.5}$, respectively. PEDOT:PSS/Au exhibited the largest capacitive coupling characteristics (smallest $|X|_{CPE}$), whereas PEDOT:PSS/Pt exhibited the smallest capacitive coupling characteristics (largest $|X|_{CPE}$) at 1kHz. The adsorption capacitance, C_{ad}, exhibited nearly two orders of magnitude larger value for PEDOT:PSS on both Au and Pt compared to that of Au across all diameters as shown in **Figure 4.4e**, where a nearly area-dependent scaling of $1/D^2$ was observed. To assess the impedance of the whole Faradaic branch (the serial combination of R_{ct} and $|X|_{Cad}$ except for Pt), we calculated and plotted Z_f at 1 kHz in **Figure 4.4g** and **Figure 4.4h**. Z_f is the largest for Pt, and is reduced by ~ 1000X with PEDOT:PSS coating for all diameters. The high Z_f value is consistent with the higher R_s for Pt. The Faradaic impedance of PEDOT:PSS is lowest on Au and Pt, highlighting the facilitation of the redox reaction by PEDOT:PSS coating. For a given electrode diameter, Au exhibited ~ 100X higher Z_f than Pt and ~ 10,000X larger than that of PEDOT:PSS on either Au or Pt.

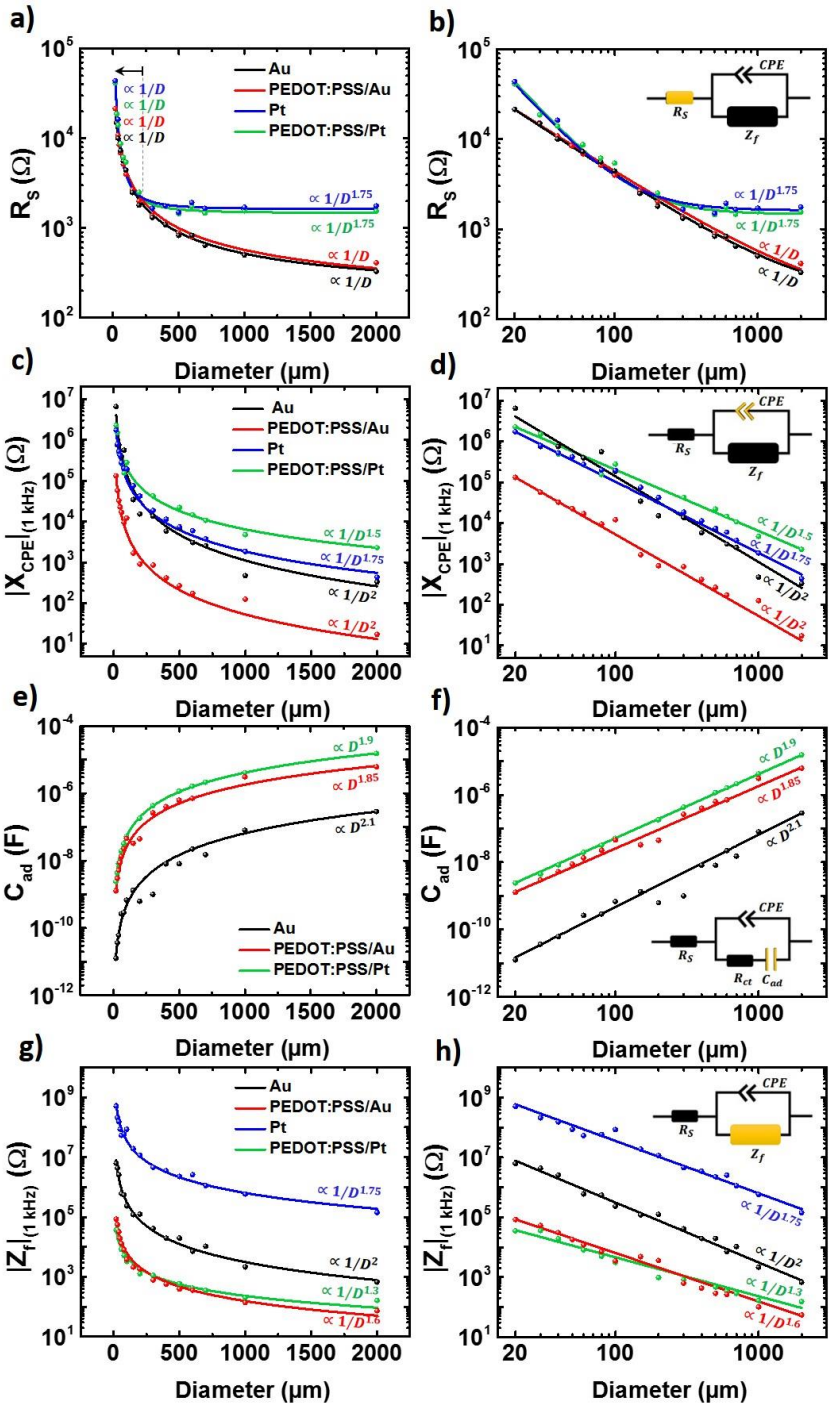

Figure 4.4 Effects of electrode diameter on specific electrochemical components of the electrode interface. (a, b) Series resistance is greater for large diameter Pt electrodes (blue and green lines compared to red and black), independent of PEDOT:PSS coating (red vs. black, green vs. blue lines). (c, d) CPE reactance at 1 kHz is least for PEDOT:PSS/Au electrodes at all diameters. (e, f) Adsorption capacitance is increased in PEDOT:PSS coated contacts. (g, h) Faradaic branch impedance (at 1 kHz) capacitance is decreased in PEDOT:PSS coated contacts. Extracted and fitted values are shown in semilog (a, c, e, g) and log (b, d, f, h) scales.

4.3.5 1 kHz impedance size dependency

To highlight the differences in the net electrochemical impedance, we plotted in **Figure 4.5a** and **Figure 4.5b** the 1 kHz magnitude of the impedance as a function of electrode diameter for all studied materials. For smaller diameters, the PEDOT:PSS coating reduces the impedance by over 10X and the impedance for the larger diameter dots converges to that of the underlying metal as the diameter increases to millimeter scales. For larger diameters, the electrochemical limiting factor is the series resistance, R_s, which we found to be dominated by the underlying metal contact in **Figure 4.4a** and **Figure 4.4b**. The PEDOT:PSS coated electrodes exhibited a combined perimeter/area dependency of $1/D^{1.5}$, whereas the metal ones showed mostly area dependency of $1/D^2$ for Au and $1/D^{1.7}$ for Pt. The independent electrochemical coupling effects for faradaic, capacitive, and those of series resistance at 1 kHz are benchmarked against the overall impedance for each material in **Figure 4.5c-4.5f**. For Au, at small diameters, the overall impedance is determined by the capacitive coupling (Z_f is highest and overall $|Z|$ is equivalent to nearly $|X|_{CPE}$) until $|X|_{CPE}$ becomes lower than R_s at larger diameters where the overall impedance becomes limited by R_s. For PEDOT:PSS on Au and Pt, and at 1 kHz, the series resistance becomes larger than the parallel combination of the capacitive and faradaic impedances at about 108 µm for PEDOT:PSS/Au and 106 µm for PEDOT:PSS/Pt and the overall impedance becomes dominated by R_s. The faradaic component for electrochemical coupling for Pt, embodied in a large R_{ct} is ineffective at 1 kHz and capacitive coupling is efficient for all diameters.

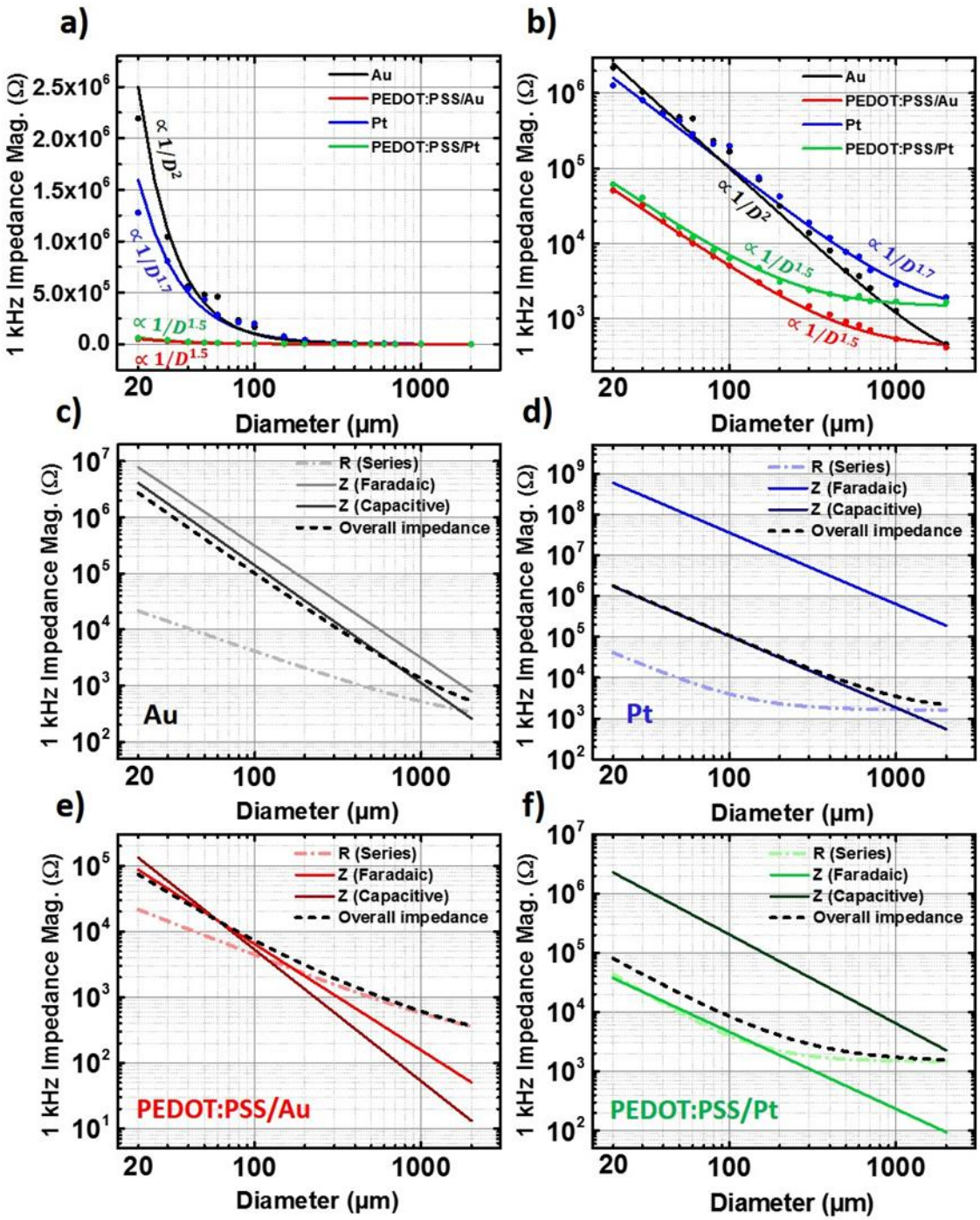

Figure 4.5 Contributions of each electrochemical element to the 1 kHz impedance as a function of contact size and material. Measured and fitted values of 1 kHz electrochemical impedances of scaled PEDOT:PSS/Au, PEDOT:PSS/Pt, Au and Pt electrodes in semilog (a) and log (b) scale. Size dependence of each component of the electrochemical impedance plotted together with the overall 1 kHz impedance for Au (c), Pt (d), PEDOT:PSS/Au (e) and PEDOT:PSS/Pt (f).

4.3.6 Impedance Spectra vs. ECoG Brain Signals

For neural activity embodied in low frequency field potentials, it is important to analyze the size-dependent impedance at frequencies lower than 1 kHz. To do this, we extracted the impedance from the spectra of **Figure 4.2** and plotted it at 1, 4, 8, 12, 40, 100, 500 and 1000 Hz in **Figure 4.6** as a function of diameter. The intermediate frequency bands between these limits are knows as the delta (Δ), theta (θ), alpha (α), beta (β), gamma (γ), high frequency oscillation (HFO), and single unit (SU). At lower frequencies, PEDOT:PSS on Au lead to over 18.4X lower impedances for all sizes compared to Au electrodes and about 4.8X lower impedances for PEDOT:PSS on Pt compared to Pt electrodes. Since the lower frequencies exhibit mainly a capacitive behavior for all diameters, a nearly $1/D^{1.75}$ dependence of the overall impedance was observed for PEDOT:PSS/Au and PEDOT:PSS/Pt. At higher frequencies, and as the diameter increases and the R_s starts to dominate, a slower dependence of $1/D^{1.5}$ for PEDOT:PSS/Au and $1/D^2$ for PEDOT:PSS/Pt was observed as noted in **Figure 4.5**. The phase spectra in **Figure 4.5b-h** demonstrate the relevant electrochemical coupling mechanism. For Au, the phase at all frequency bands is nearly capacitive and started to become a combination of capacitive/ohmic for diameters > 1000 μm and at the higher frequencies. Lower frequency signals are coupled capacitively. For PEDOT:PSS/Au and PEDOT:PSS/Pt, smaller diameters exhibited capacitive coupling up to ~ 100 μm, beyond which a mixed capacitive/ohmic coupling regime prevailed, becoming mostly ohmic at higher frequencies and larger diameters. This dependence is nearly reversed for Pt where the lower frequencies and smaller diameters exhibit mostly ohmic behavior and the larger diameter and larger frequencies exhibit a similar trend to Au, PEDOT:PSS/Au and PEDOT:PSS/Pt where mixed capacitive/ohmic characteristics were observed.

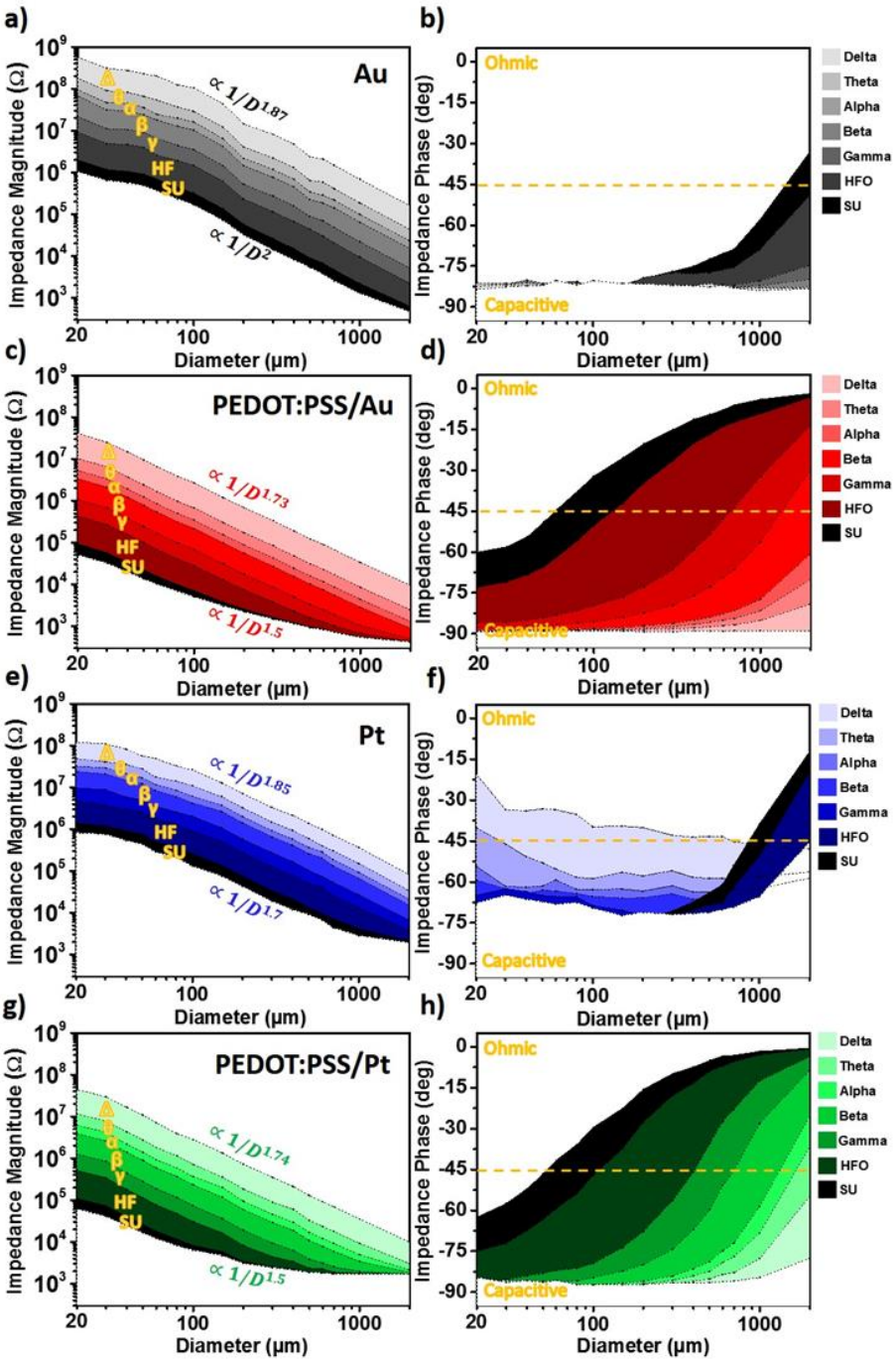

Figure 4.6 Electrochemical impedance spectra in different frequency bands relevant to ECoG brain signals plotted at 1-4 Hz, (Δ, delta), 4-8 Hz (θ, theta), 8-12 Hz (α, alpha), 12-40 Hz (β, beta), 40-100 Hz (γ, gamma), 100-500 Hz (HF, high frequency) and 500-1000 Hz (SU, single units). Impedance magnitude and phase diagrams as a function of diameter for Au electrodes ((a) and (b)), PEDOT:PSS/Au electrodes ((c) and (d)), Pt electrodes ((e) and (f)) and PEDOT:PSS/Pt electrodes ((g) and (h)).

4.3.7 Noise Performance of Scaled Electrodes

The above discussion delineates the electrochemical interface properties which underlie the recording of brain waves using ECoG electrodes. An important consequence of electrode impedance associated with electrode size is the consequent noise level. Naturally, the lower impedance PEDOT:PSS electrodes exhibit low noise voltages that are limited to that of the amplifier (Tucker Davis Technologies) background noise voltage (**Figure 4.7a**). The macroscale Au and Pt electrodes also exhibit smaller noise voltages but as the diameter is reduced at or below 100 μm, the noise voltage rapidly increases above the amplifier background noise (**Figure 4.7a**). The root-mean-square (rms) for the noise spectral density in the 1 Hz to 10 kHz frequency band exhibited a $1/D^2$ dependence at smaller diameter for Pt and a $1/D^{1.7}$ dependence of Au, whereas for PEDOT:PSS/Au and PEDOT/Pt, the noise density scaled with $1/D^{0.9}$ and 1/D, respectively as illustrated in **Figure 4.7c**. The noise power spectral density for five different diameters (20 μm, 60 μm, 200 μm, 500 μm, and 1000 μm) as a function of frequency is plotted in **Figure 4.7b**. For all diameters, the noise spectra are limited to the amplifier noise with a slight 1/f noise component below 100 Hz. The Au noise power spectra also exhibited similar noise spectra to the amplifier for diameters larger than 500 μm. For diameters below 200 μm, the $1/f^{\alpha}$ noise power increases as the diameter decreases where α, the Hooge coefficient,[11] was found to be equal to 1.6, 1.65, 2 for diameter of 200 μm, 60 μm, and 20 μm, respectively. Also, the corner frequency, fc, which its shift denotes a change in the total noise construction from 1/f noise to the frequency independent thermal/white noise, increases for smaller diameters which was found to be 92 Hz for the 200 μm, 102 Hz for the 60 μm, and 115 Hz for the 20 μm. For Pt, a similar trend was observed such that both α and f_c increase as the diameter decreases. α was found to be equal to 1.65, 1.7, 2.4 and f_c equal to 103 Hz, 111 Hz, 125 Hz for D=200 μm, 60 μm, and 20 μm, respectively. The ion transport

in porous membranes was found to exhibit Hooge coefficients that are greater than or equal to ~ 1.5.[12] We speculate that since the adsorption sites for ions on the Pt surface is nonhomogeneous[13] and the 20 μm suggesting that PEDOT:PSS has the highest potential for high spatiotemporal resolution among all ECoG microelectrode materials studied here.

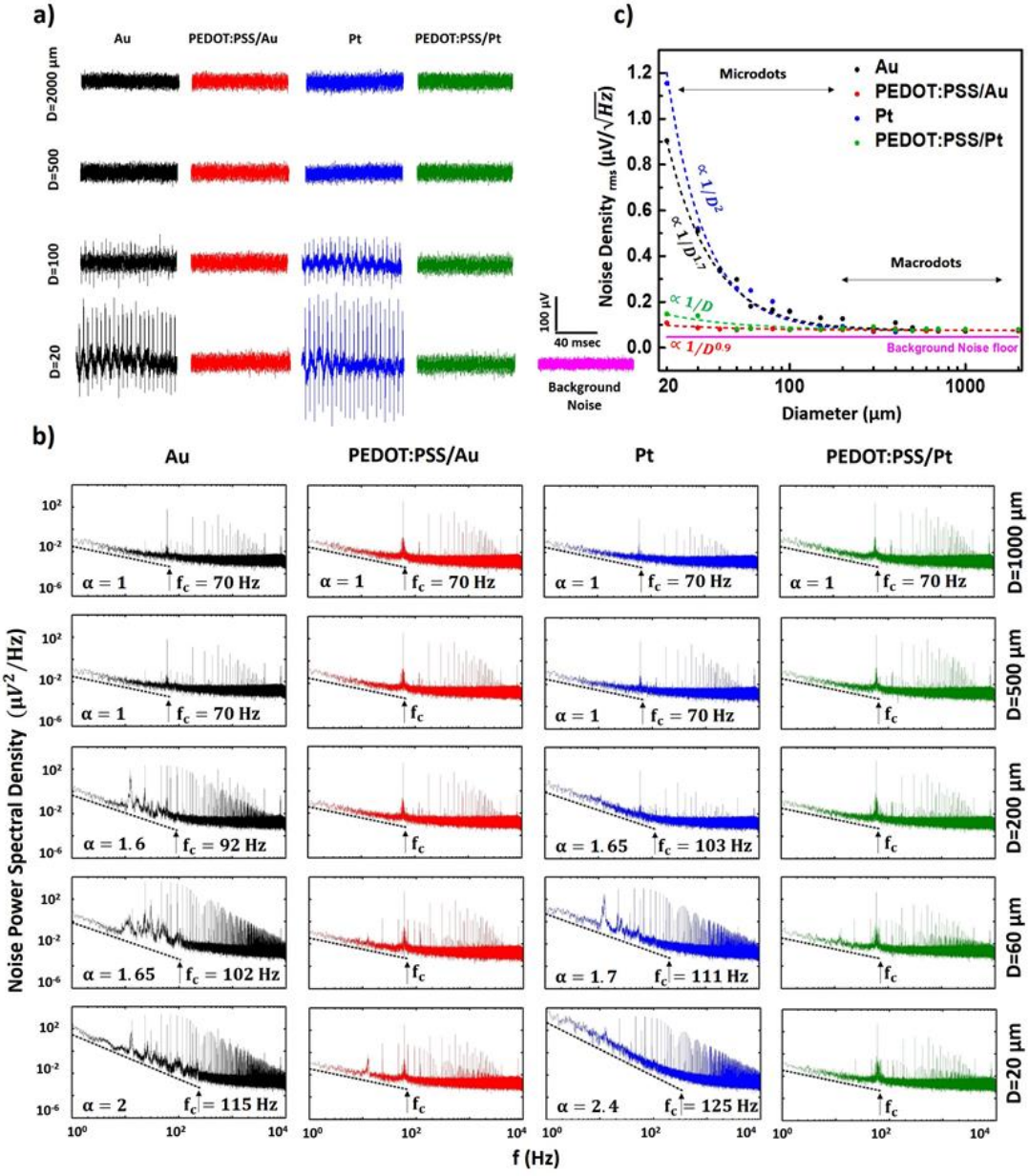

Figure 4.7 Effects of electrode diameter on noise performance for different electrode materials. (a) Noise voltage-time traces (for a time duration of 100 msec) for Au (black), PEDOT:PSS/Au (red), Pt (blue) and PEDOT:PSS/Pt (green) with 20, 100, 500 and 2000 µm diameters. Purple color voltage-time trace is the amplifier noise. (b) Noise power spectral densities for 20, 100, 500 and 1000 µm diameters. (c) Calculated and fitted root-mean-square values of PSD in the 1 Hz- 10 kHz frequency band as a function of diameter.

4.4 Conclusion

In conclusion, we presented a systematic study of the scaling effects on the electrochemical properties of Pt and Au metallic and PEDOT:PSS organic electrodes. PEDOT:PSS electrodes exhibit better faradaic charge transfer and capacitive charge coupling than metal electrodes, and these characteristics lead to improved electrochemical performance and reduced noise at smaller electrode diameters. We found that PEDOT:PSS reduced the metal electrode impedances by up to 18X for electrodes with diameters < 200 μm and the impedances became identical at millimeter scale due to dominance of series resistances particularly at higher frequencies. Therefore, the performance gains are especially significant at lower frequencies where cognitive and clinical activities are usually observed in neuronal recordings. Additionally, the overall reduced noise of the PEDOT:PSS electrodes enables a lower noise floor for single unit activity recording. We believe that the detailed understanding of the electrochemical characteristics of these different materials and their scaling properties is of critical importance for the optimization of ECoG electrodes.

Chapter 4, in full, is a reprint of material as it appears in the following publication: M. Ganji, A. T. Elthakeb, A. Tanaka, V. Gilja, E. Halgren, and S. A. Dayeh, "Scaling Effects on the Electrochemical Performance of poly (3, 4-ethylenedioxythiophene (PEDOT), Au, and Pt for Electrocorticography Recording," Advanced Functional Materials, vol. 27, p. 1703018, 2017. The dissertation author was the primary investigator and author of this material.

4.5 References

[1] a) D. R. Kipke, W. Shain, G. Buzsáki, E. Fetz, J. M. Henderson, J. F. Hetke, G. Schalk, *Journal of Neuroscience* **2008**, 28, 11830; b) G. Buzsáki, *Nature neuroscience* **2004**, 7, 446.

[2] a) S. F. Cogan, *Annu. Rev. Biomed. Eng.* **2008**, 10, 275; b) W. Franks, I. Schenker, P. Schmutz, A. Hierlemann, *IEEE Transactions on Biomedical Engineering* **2005**, 52, 1295.

[3] N. G. Hatsopoulos, J. P. Donoghue, *Annual review of neuroscience* **2009**, 32, 249.

[4] a) K. Najafi, J. Ji, K. Wise, *IEEE Transactions on Biomedical Engineering* **1990**, 37, 1; b) K. A. Ludwig, N. B. Langhals, M. D. Joseph, S. M. Richardson-Burns, J. L. Hendricks, D. R. Kipke, *Journal of neural engineering* **2011**, 8, 014001.

[5] a) M. Sessolo, D. Khodagholy, J. Rivnay, F. Maddalena, M. Gleyzes, E. Steidl, B. Buisson, G. G. Malliaras, *Advanced Materials* **2013**, 25, 2135; b) D. Khodagholy, T. Doublet, M. Gurfinkel, P. Quilichini, E. Ismailova, P. Leleux, T. Herve, S. Sanaur, C. Bernard, G. G. Malliaras, *Advanced Materials* **2011**, 23; c) D. Khodagholy, J. N. Gelinas, T. Thesen, W. Doyle, O. Devinsky, G. G. Malliaras, G. Buzsáki, *Nature neuroscience* **2015**, 18, 310; d) D. Khodagholy, J. N. Gelinas, Z. Zhao, M. Yeh, M. Long, J. D. Greenlee, W. Doyle, O. Devinsky, G. Buzsáki, *Science Advances* **2016**, 2, e1601027; e) J. Hermiz, N. Rogers, E. Kaestner, M. Ganji, D. Cleary, J. Snider, D. Barba, S. Dayeh, E. Halgren, V. Gilja, presented at Engineering in Medicine and Biology Society (EMBC), 2016 IEEE 38th Annual International Conference of the **2016**; f) I. Uguz, M. Ganji, A. Hama, A. Tanaka, S. Inal, A. Youssef, R. M. Owens, P. P. Quilichini, A. Ghestem, C. Bernard, *Advanced Healthcare Materials* **2016**.

[6] J. Rivnay, S. Inal, B. A. Collins, M. Sessolo, E. Stavrinidou, X. Strakosas, C. Tassone, D. M. Delongchamp, G. G. Malliaras, *Nature communications* **2016**, 7.

[7] J.-W. Jeong, G. Shin, S. I. Park, K. J. Yu, L. Xu, J. A. Rogers, *Neuron* **2015**, 86, 175.

[8] G. Buzsáki, C. A. Anastassiou, C. Koch, *Nature reviews neuroscience* **2012**, 13, 407.

[9] X.-Z. R. Yuan, C. Song, H. Wang, J. Zhang, *Electrochemical impedance spectroscopy in PEM fuel cells: fundamentals and applications*, Springer Science & Business Media, **2009**.

[10] M. Ganji, E. Kaestner, J. Hermiz, N. Rogers, A. Tanaka, D. Cleary, S. H. Lee, J. Snider, M. Halgren, G. R. Cosgrove, *Advanced Functional Materials* **2017**.

[11] F. Hooge, *Physics Letters A* **1970**, 33, 169.

[12] E. Frehland, *Biophysical chemistry* **1978**, 8, 255.

[13] M. Ganji, E. Kaestner, J. Hermiz, N. Rogers, A. Tanaka, D. Cleary, S. H. Lee, J. Snider, M. Halgren, G. R. Cosgrove, B. S. Carter, D. Barba, I. Uguz, G. G. Malliaras, S. S. Cash, V. Gilja, E. Halgren, and S. A. Dayeh*, in press, Advanced Functional Materials, 2017.

Chapter 5

Scaling Effects on the Electrochemical Stimulation Performance of Au, Pt, and PEDOT:PSS Electrocorticography Arrays

5.1 Introduction

Therapeutic electrical stimulation is witnessing an explosion of interest due to the success of recent neuromodulation devices such as cochlear implants, deep brain stimulation (DBS), and spinal cord stimulation for the treatment of neurological disease and disorders.[1–10] Critical for the success of these devices is to maintain the desired functional response through injection of a safe amount of charge using capacitive and reversible faradaic mechanisms without causing any deleterious effects on either the electrodes or the surrounding tissue.[11,12] Previous pioneering work has shown that a variety of factors contribute to safe, efficient, and functional electrical stimulation; factors range from material choices and electrode geometries to stimulation methodology, i.e., controlling stimulation parameters such as pulse width, charge density, interpulse potentials, and bias.[13,14] The assessment of micro/macroneuronal electrodes for functional and safe therapeutic stimulation of physiological tissue and excitable cells hinges on the details of charge injection reactions at the electrode–tissue interface.[15] In most clinical applications, electrical stimulation is injected through a biphasic charge-balanced stimulus waveform, which are identified by charge per phase or charge density.[12,16] These stimulus pulse parameters are important factors that are usually correlated with thresholds for tissue damage and are traditionally described by the Shannon equation.[17,18] Although the precise relation between tissue damage and stimulation biproduct and polarization remains unclear, in practice, in vivo charge-injection limits are typically deduced from in vitro charge injection measurements in a

buffered physiological saline (PBS) solution to predict potential tissue damage of neuronal electrodes. The maximum in vitro charge-injection capacity limit isdescribed as the maximum charge delivered through capacitive or reversible faradaic reaction without polarizing the electrode potential beyond the water window limit (reduction and oxidation of water).[13,19] Noble metal electrodes, such as Pt and Pt alloys that are presently employed in clinical stimulation and recording (e.g., deep brain stimulation and cochlear implants), possess large electrode areas with limited charge injection limits of 0.3 $mC.cm^{-2}$.[20] However, for some therapeutic stimulation purposes such as an intracortical microstimulation prosthesis (ICMS), the electrode sizes are chosen to be at microscale dimensions to permit localized stimulation of small neuronal populations. Typically, these prosthesis applications require charge injection densities above 0.5 $mC.cm^{-2}$, which might exceed the charge injection limits of noble metal electrodes, resulting in electrode degradation and tissue damage.[6,21,22] To provide higher levels of charge injection, different novel coating materials such as IrOx, TiN, and poly(3,4-ethylenedioxythiophene):polystyrene sulfonate (PEDOT:PSS) have been employed. Iridium oxide and its derivatives, such as activated iridium oxide films (AIROF) that is formed by electrochemical activation of iridium metal, or sputtered iridium oxide films (SIROF) that is deposited by reactive sputtering from iridium metal in an oxidizing plasma, hold great promise as coating materials for next-generation nerve electrodes. These materials are well characterized and optimized for higher charge injection limits (3.8 $mC.cm^{-2}$ for AIROF and 5 $mC.cm^{-2}$ for SIROF with the application of positive interpulse bias) enabled by a fast and reversible faradaic reaction involving reduction and oxidation between the Ir3+ and Ir4+ states of the oxide.[23–25] In addition to metal oxides, conducting polymers (CPs) have also emerged as prospective coating materials for next-generation stimulating and recording electrodes. Particularly, PEDOT:PSS organic coating

has been used extensively in neural interface applications.[26–32] It is argued that PEDOT:PSS reduces the electrochemical mismatch at the electrode/electrolyte interface due to its mixed electronic/ionic conductivity, and that it helps reduce the mechanical mismatch between electrode and tissue due to its soft nature. Therefore, these organic polymer-coated electrodes are viewed as a serious alternative for metal and metal oxide electrodes.[33–35] From a stimulation perspective, PEDOT:PSS coating has also shown a long-term electrochemical stability under in vitro and chronic in vivo conditions with higher charge injection limits compared to metal (PtIr) or metal oxides (IrOx).[19] With the growing interest in PEDOT:PSS electrophysiology devices and to facilitate their advancement, a thorough and systematic investigation of their charge injection and storage capacities and how these limits are influenced by the scaling of the electrode size is necessary. PEDOT:PSS is commonly deposited by electrodeposition.[19,26,27,34,36,37] This work focuses on PEDOT:PSS that is deposited from solution by spin-casting and patterned peel-off and followed by thermochemical polymerization, developed by Malliaras and co-workers [28,29,33] as described in detail below. This method provides a smooth PEDOT:PSS surface, and a uniform and identical coating of all electrodes for a given array geometry.[32] Here, we investigated and optimized the charge injection of PEDOT:PSS-coated micro/macroelectrodes (PEDOT:PSS on Au and PEDOT:PSS on Pt) and quantified their superiority to uncoated Au and Pt electrodes at different electrode diameters for the first time. Given the wide range of electrode geometry choices for different clinical purposes,[13] we studied the scaling effects on charge injection capacity (CIC) and charge storage capacity (CSC) for these materials. Additionally, we studied the effect of positive interpulse potential (bias voltage) on the CIC of PEDOT:PSS/Au electrodes and determined a 0.4 V as an optimal interpulse bias. Furthermore, we determined the influence of asymmetric pulse engineering (with different anodal/ cathodal pulse width ratios) on CIC of

PEDOT:PSS electrodes. Finally, the frequency dependency and the possible correlation of CIC with charge storage capacity are presented and discussed.

5.2 Experimental Details

5.2.1 Device Fabrication

The fabrication of PEDOT:PSS-based electrodes followed previously discussed processes in part 2.2.1. Fabrication of the platinum microarrays followed similar procedure to that of PEDOT:PSS devices except for the PEDOT:PSS deposition which was not carried out. For the Pt devices, a 10 nm Ti adhesion layer and 100 nm Pt contact layer were deposited by sputtering (Denton Discovery 18 Sputter System).

5.2.2 Device Characterization

The devices were imaged using an FEI SFEG ultra high resolution (UHR) scanning electron microscope (SEM) at 10 kV accelerating voltage. To reduce electron charging in the specimen, a 15 nm thick Ti layer was deposited on the back of the device and that electrically connected the devices to the stage of the system providing a runaway path for impinging electrons. A Veeco Scanning Probe Microscope was used to perform atomic force microscopy (AFM) in a non-contact tapping mode. Electrochemical current pulse injection (chronopotentiometry mode) and cyclic voltammetry (CV) were performed using a GAMRY interface 1000E in phosphate buffer saline (PBS) solution, using three electrodes configuration, i.e., Ag/AgCl electrode as a reference, a large platinum electrode as a counter electrode, and target micro/macro electrodes as the working electrode. To calculate the charge injection capacity, cathodal-first, bi-phasic, charge-balanced current pulse were injected across working electrode and counter electrode while measuring working electrode's polarization potential with respect to Ag/AgCl reference electrode. E_{mc} and E_{ma} were calculated as electrode potential versus Ag/AgCl (reference electrode) 10 µs after

cathodal and anodal pulses ended. Charge injection capacity (CIC) was calculated as the injected charge (by multiplying stimulation current and pulse width) at which either E_{mc} reaches water reduction potential (cathodal limit) and/or E_{ma} reaches water oxidation potential (anodal limit). Water window limits are considered between -0.6 to 0.8 for metallic electrodes (Pt and Au) and -0.9 to 0.6 for organic electrodes (PEDOT:PSS/Au and PEDOT:PSS/Pt).[4] To maintain different inter-pulse potential (E_{ipp}) bias for each electrode materials, a net current flowed across the electrode/ electrolyte interface with minute current magnitude (typically <10 nA) even for millimeter scale electrodes. Cyclic voltammetry (CV) was performed under low current density, near equilibrium conditions in PBS solution, whereas tested electrode potential was swept cyclically versus Ag/AgCl reference electrode's potential between water window limits for each electrode material at constant scan rate of 200 mV/s with 10 mV potential steps. The CSC_C and CSC_A were calculated by time integral of the cathodal and anodal current (or current density) over a potential range of water electrolysis window for each material.

5.3 Results and Discussions

5.3.1 Device Structural Properties and Electrochemical Characterization Methodology

Neural probes with different electrode materials including Au, PEDOT:PSS/Au, Pt and PEDOT:PSS/Pt were fabricated on 4-5 um thick parylene C substrate. The details of the fabrication procedure were described previously. The form factor and electrode layout of PEDOT:PSS/Au electrophysiology device are shown in **Figure 5.1a** which consists of 16 different electrode diameters ranging from 20 µm to 2000 µm. Each set of the studies presented in this work consisted of four independent devices, where each device comprised all diameters for a given material (Au, Pt, PEDOT:PSS/Au and PEDOT:PSS/Pt) fabricated side by side as shown in **Figure 5.1a**, to minimize process variations and to permit fair and accurate assessment of the scaling effects across

all diameters. Each data point for each diameter is obtained from a single electrode (N=1). Two layers of 2-2.5 µm thick parylene C film were used to serve as the substrate and passivation layers to form conformal contact to either tissue or electrolyte as shown in **Figure 5.1a**. A 10 nm thick Ti adhesion layer followed by a 100 nm thick Au or Pt layers were used as the electrode leads. Anisotropic conductive film (ACF) bonding was used to connect the device to commercial off the shelf ribbon cables that fit in the external characterization circuitry. Solution-based processing was used to pattern the PEDOT:PSS on top of the metal contacts (Au and Pt); **Figures 5.1d, f** and **h** show the top view SEM images of patterned PEDOT:PSS on Au, Pt and Au contacts with 150 µm diameter.

To evaluate the morphological characteristics of different films, atomic force microscopy (AFM) was utilized. Surface roughness root-mean-square (rms) values of different electrodes in a 5×5 μm^2 area reveal that Au (11.8 rms) and Pt (12.1 rms) metal contacts possess rougher surfaces compared to the spin-cast PEDOT:PSS film with 4.81 rms value (**Figure 5.1e, g** and **i**). The relatively smooth surface of PEDOT:PSS film is attributed to its monolithic solution-based coating technique that is used for device fabrication. These values however are directly dependent on the surface preparation of the sample and the deposition conditions.

To assess and compare the stimulation capabilities for the different scaled materials, voltage transient and cyclic voltammetry (CV) were used to measure CIC and CSC, the two major contributing factors to in vivo electrical stimulation performance. **Figure 5.1b** shows an example of injected bi-phasic, cathodal first, symmetric current and the measured corresponding voltage transient on a PEDOT:PSS/Au electrode with 500 µm diameter. In the current pulse configuration, i_c and i_a denote the cathodal and anodal phase currents, respectively. Parameters t_c, t_a and t_{ip} denote the cathodal, anodal pulse widths and inter-pulse delay, respectively. In most of our investigations,

the applied pulse width was 650 µs and the inter-pulse delay was 20 µs, unless otherwise specified. In the voltage transient configuration, the inter-pulse potential E_{ipp}, the access voltage, V_a and electrode polarization, ΔE_p, are highlighted. The maximum cathodal excursion potential, E_{mc}, and the maximum anodal excursion potential, E_{ma}, parameters which are used to determine CIC, are marked in the voltage transient curve of **Figure 5.1b** (all highlighted electrochemical variables and parameters in Figure **5.1b**, **c** are defined in **Table 5.1** in Methods section). Following the published experimental protocols 10b, E_{mc} and E_{ma} are the electrode potentials versus Ag/AgCl (reference electrode) evaluated 10 µs after the cathodal and anodal pulses end. This period of inter-pulse delay (10µs of 20 µs) is used to account for the voltage drop across the electrolyte and metal lead series resistance (instantaneous potential drop within 10 µs), resulting in an absolute polarized potential across electrode/electrolyte interface versus Ag/AgCl. CIC was calculated as the injected charge (stimulation current multiplied by pulse width) at which either E_{mc} reaches water reduction potential (cathodal limit) and/or E_{ma} reaches water oxidation potential (anodal limit). The water window limits are considered between -0.6 to 0.8 V for metallic electrodes (Pt and Au) and -0.9 to 0.6 V for organic electrodes (PEDOT:PSS/Au and PEDOT:PSS/Pt).[4] To evaluate and benchmark the CSCs of different scaled materials, cyclic voltammetry (CV) has been used within the -0.6 to 0.6 V limit (intersection of two water windows) with 200 mV/s scan rate. An example of CV plot for 500 µm PEDOT:PSS/Au diameter is displayed in **Figure 5.1c** within the PEDOT:PSS/Au water window (-0.9 to 0.6 V). The cathodal CSC (CSCc) and anodal CSC (CSCa) are calculated by the time integral of the cathodal and anodal currents over the potential range of water electrolysis window for each material.

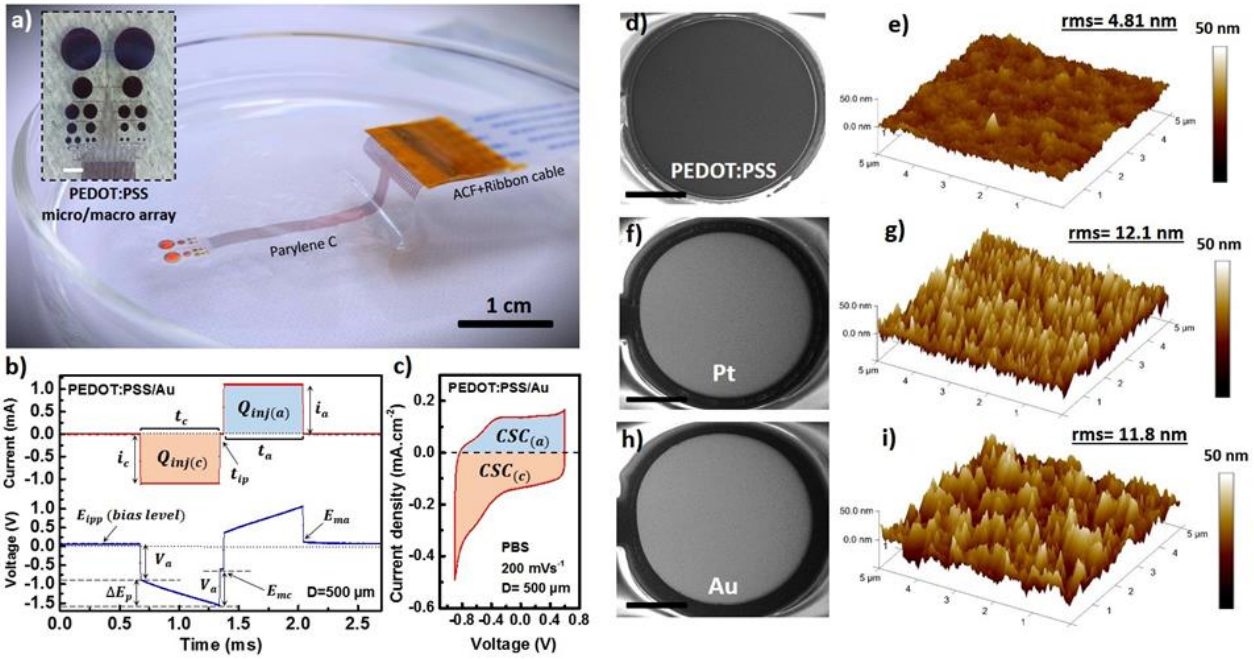

Figure 5.1 Device structural properties and electrochemical characterization methodology for ECoG devices. (a) A picture of the fabricated PEDOT:PSS/Au ECoG electrodes on conformal 4-5 µm thick parylene C substrate. 16 different electrode diameters ranging from macroscale (2000 µm) to microscale (20 µm) were included in the device layout (inset). (b) An example of injected charge-balanced, cathodal first and bi-phasic current and corresponding voltage transient with highlighted electrochemical parameters on 500 µm PEDOT:PSS/Au electrode. (c) An example of cyclic voltammetry (CV) with 200 mV/s scan rate and denoted cathodal and anodal charge storage capacity calculation. (d, f, h) Top view SEM images of PEDOT:PSS/Au, Pt and Au with 150 µm diameter. (e, g, i) atomic force microscopy (AFM) images and roughness root-mean-square values of 5×5 μm^2 scanned area of PEDOT:PSS/Au (e), Pt (g) and Au (i) electrode surfaces.

Table 5.1 Electrochemical parameters used to extract and calculate the electrochemical quantities with their corresponding sample units and technical/ theoretical definitions.

	Parameter	Unit	Description
1	t_c	ms	Cathodal phase current duration.
2	t_a	ms	Anodal phase current duration.
3	i_c	μA	Cathodal phase current magnitude.
4	i_a	μA	Anodal phase current magnitude.
5	t_{ip}	μs	Inter-pulse delay between cathodal and anodal phases to facilitate measurement of the access voltage (V_a) related to the ohmic drop across the series resistive elements of the electrochemical circuit model.
6	D	μm	Diameter of the electrode.
7	GSA	mm^2	Geometric surface area = $(\pi \times D^2)/4$
8	V_a	V	Access voltage which is associated with ohmic drop across the resistive elements of the circuit and electrochemical cell. V_a is calculated as the difference between the bias voltage and the voltage transient (10 μs) after the onset of the current pulse.
9	E_{mc}	V	Maximum cathodally electrochemical potential excursions calculated by subtracting V_a from the maximum negative voltage transients or the electrode potential immediately, i.e. 10 μs after the end of the cathodic current pulse when V_a is zero.
10	E_{ma}	V	Maximum anodally electrochemical potential excursions calculated by subtracting V_a from the maximum positive voltage transients or the electrode potential immediately, i.e. 10 μs, after the end of the anodic current pulse when V_a is zero.
11	OCP	V	Equilibrium potential of working electrode (without bias voltage) versus reference electrode (Ag/AgCl) at which the net current flow between the working and the counter electrode is zero (the anodic and cathodic reactions are kept in balance).
12	E_{ipp}	V	The inter-pulse potential (bias voltage) of the working electrode relative to a non-current carrying reference electrode (Ag/AgCl).
13	ΔE_p	V	polarization potential across the electrode/electrolyte interface, $\Delta E_p = \Delta V - V_a$, where ΔV is the voltage transient.
14	$\mathbf{Current - injection}_{(Limit)}$	μA	Maximum delivered (injected) current where $\|i_c\| = \|i_a\|$ in charge-balanced symmetric bi-phasic current pulse at which either E_{mc} reaches the water reduction potential (cathodal limit) and/or E_{ma} reaches water oxidation potential (anodal limit).
15	$Q_{inj(c)}$	mC	Total delivered (injected) charge in cathodal phase which is the time integral of the current pulse, i.e. $i_c \times t_c$ for a cathodal constant-current pulse.
16	$Q_{inj(a)}$	mC	Total delivered (injected) charge in anodal phase which is the time integral of the current pulse i.e. $i_a \times t_a$ for a anodal constant-current pulse.
17	Q_{inj}	mC	$Q_{inj(c)} + Q_{inj(a)}$
18	CIC	mC/cm^2	The total charge density at which either E_{mc} reaches water reduction potential (cathodal limit) and/or E_{ma} reaches water oxidation potential (anodal limit). $CIC = Q_{inj}/GSA$.

Table 5.1 Electrochemical parameters used to extract and calculate the electrochemical quantities with their corresponding sample units and technical/ theoretical definitions (Continued).

	Parameter	Unit	Description
19	$Q_{storage(c)}$	mC	Cathodic charge storage calculated from the time integral of the cathodic (negative) current in cyclic voltammetry at a specific sweep rate over a potential range within the water window and is related to the total amount of charge that is available for a stimulation pulse to be delivered in a cathodal current pulse without exceeding the water reduction potential.
20	$Q_{storage(a)}$	mC	Anodic charge storage calculated from the time integral of the anodic (positive) current in cyclic voltammetry at a specific sweep rate over a potential range within the water window and is related to the total amount of charge that is available for a stimulation pulse to be delivered in an anodal current pulse without exceeding the water oxidation potential.
21	$Q_{storage(Total)}$	mC	$Q_{storage(c)} + Q_{storage(a)}$
22	$CSC_{(c)}$	mC/cm^2	$Q_{storage(c)}/GSA$
23	$CSC_{(a)}$	mC/cm^2	$Q_{storage(a)}/GSA$
24	$CSC_{(Total)}$	mC/cm^2	$CSC_{(c)} + CSC_{(a)}$

5.3.2 Micro and Macro Current Injection Limits and Charge Injection Capacities

To compare the CIC for the materials investigated here, the electrodes were divided into two groups; macro electrodes with 200 µm to 2000 µm diameters and microelectrodes with diameters ranging from 20 µm to 150 µm. **Figure 5.2** shows the CIC analyses of microelectrodes for different materials. The current injection limit (µA) and charge injection capacity (mC/cm^2) of different microelectrode materials are plotted in **Figure 5.2a** and **Figure 5.2b**. The histogram indicates that by increasing the electrode size, the current injection limit is increased. Among all scaled materials, PEDOT:PSS/Pt exhibited the largest and Au the smallest current injection limit and CIC for all diameters ranging from 20 µm to 150 µm. Examples of the corresponding voltage transients at the limiting values for Pt, PEDOT:PSS/Pt, Au and PEDOT:PSS/Au with 50 µm diameter are displayed in **Figure 5.2c**. It should be noted that appropriate inter-pulse bias voltage were applied for each electrode to reach its respective water electrolysis window from both cathodal and anodal limits at the current injection limit (i.e. -0.9 to 0.6 V for PEDOTs and -0.6 to 0.8 V for metal contacts; see

Figure 5.4). To evaluate the scaling effect on current injection limit and CIC, measured values were fitted versus diameter using allometric power functions ($y = a + b/D^n$) where a and b are constants, D is the electrode diameter, and n is an exponent that varies between ±1 (perimeter dependence) and ±2 (area dependence). The microelectrode data and fits are shown in **Figure 5.2d** and **5.2e**. Based on fitting trends, the current injection of all microelectrode materials are almost a function of D^2. Therefore, by dividing the corresponding injected charge by the electrode area, CICs (mC/cm^2) become nearly constant and independent of diameter. CIC of PEDOT:PSS/Pt is about 2.71 mC/cm^2 which is 3.2 times larger than its underlying metal contact (Pt) with 0.83 (mC/cm^2) charge injection capacity. Also, PEDOT:PSS/Au demonstrates 9.5 times larger CIC values (1.9 mC/cm^2) compared to its underlying metal contact (Au) with 0.2 (mC/cm^2) charge injection capacity.

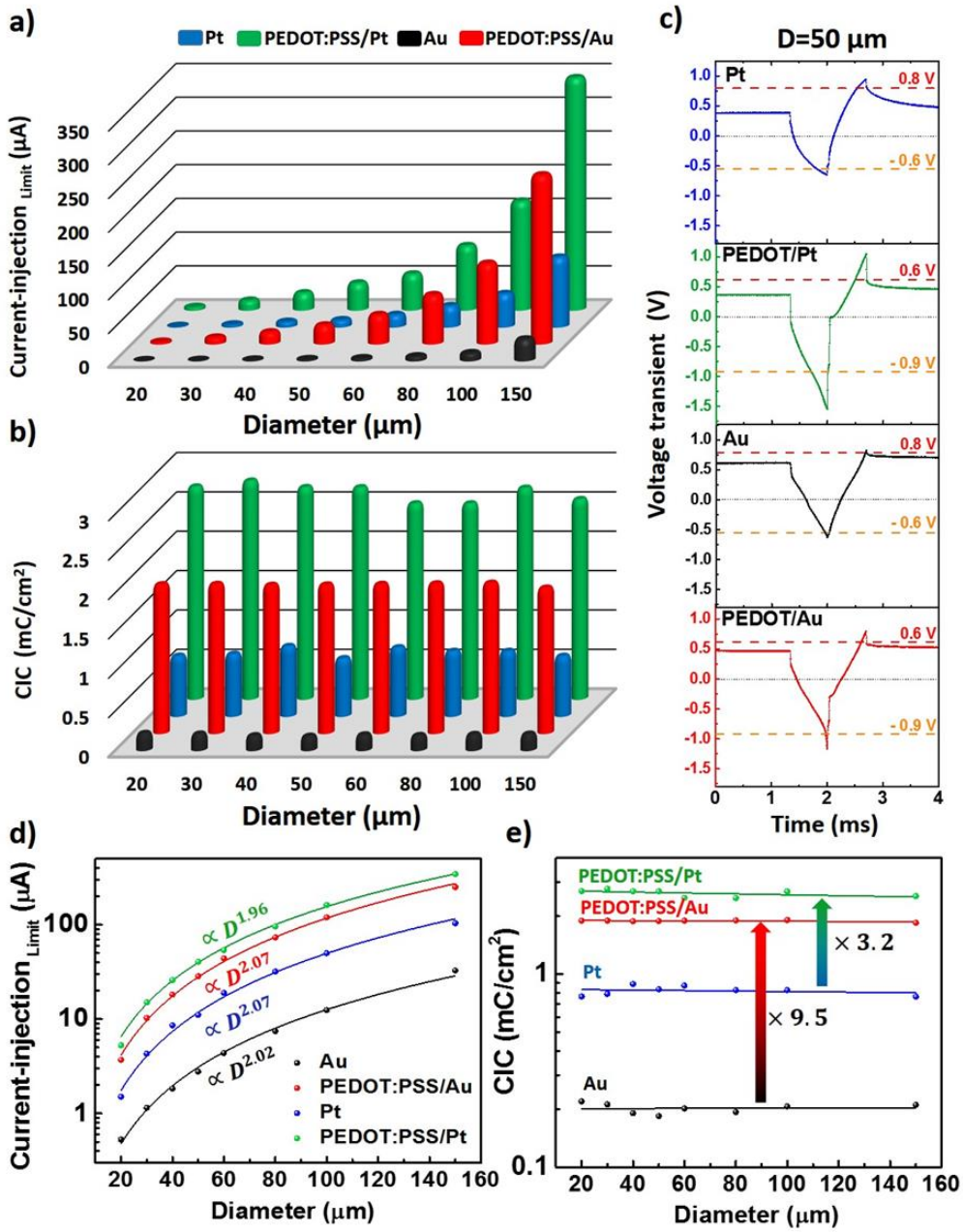

Figure 5.2 Microelectrode current injection limits and charge injection capacities. (a) Current injection limit (µA) and (b) charge injection capacity (mC/cm^2) histograms of different materials including Pt (blue), PEDOT:PSS/Pt (green), Au (black) and PEDOT:PSS/Au (red) with diameters ranging from 20 µm to 150 µm. (c) Examples of corresponding voltage transients to injected current limits for Pt, PEDOT:PSS/Pt, Au and PEDOT:PSS/Au with 50 µm diameter, limited at their respective water electrolysis window, at both the cathodal and the anodal limits, under application of appropriate inter-pulse potential bias. Measured and fitted values of current injection limits (d) and charge injection capacities (e) of different scaled materials as a function of diameter, highlighting the current injection limit and CIC scaling dependencies of each electrode material.

Figure 5.3 shows the CIC analyses of macroelectrodes (200 µm to 2000 µm) for different scaled materials. Similar to microelectrodes, the current injection limit (µA) histogram (**Figure 5.3a**) specifies larger values for larger electrodes. Among all studied materials, in contrast to the microelectrodes, PEDOT:PSS/Au exhibited the largest and Au the smallest current injection limit and CIC (**Figure 5.3b**) in the diameter range of 300 µm to 1000 µm. Examples of corresponding voltage transients to injected current limits for Pt, PEDOT:PSS/Pt, Au and PEDOT:PSS/Au with 500 µm diameters are displayed in **Figure 5.3c**. Based on fitting trends, the current injection limit of PEDOT:PSS/Au and Au macroelectrodes are scaled by almost D^2 factor (area dependency), whereas PEDOT:PSS/Pt and Pt display D and $D^{1.3}$ size dependency. Calculated and fitted CICs (mC/cm^2) values in **Figure 5.3e**, showed larger size dependency of PEDOT:PSS/Pt ($1/D^{1.03}$) and Pt ($1/D^{0.72}$) compared to non-dependency (constant value) of Au and weak dependency ($1/D^{0.34}$) of PEDOT:PSS/Au macroelectrodes. We attribute this result to edge effects that are prominent in PEDOT:PSS/Pt and Pt electrodes. For PEDOT:PSS microelectrodes with diameters smaller than ~ 150µm, the whole area of the PEDOT:PSS microelectrode contributes to the electrochemical current or charge exchange between the microelectrode and the solution. As the diameter increases beyond 150µm, the electrochemical charge exchange happens near the edge of the electrode. Therefore, the charge that is injected from the PEDOT:PSS sites near the edge of the electrode builds up a potential that is equivalent to the redox limits without the contribution of the overall GSA near the center of the dot in charge injection. Therefore, if one normalizes the injected charge by the total GSA for macroscale electrodes, an inactive portion of the electrode area that is not contributing to the electrochemical charge exchange is being included. As such, the calculation results in a reduced CIC for macroscale electrodes. By accounting for this CIC degradation at

larger electrode diameters, one is able to calculate the fraction of the electrode surface area that is contributing to the electrochemical activity. This analysis is presented in the in **Figure 5.4**.

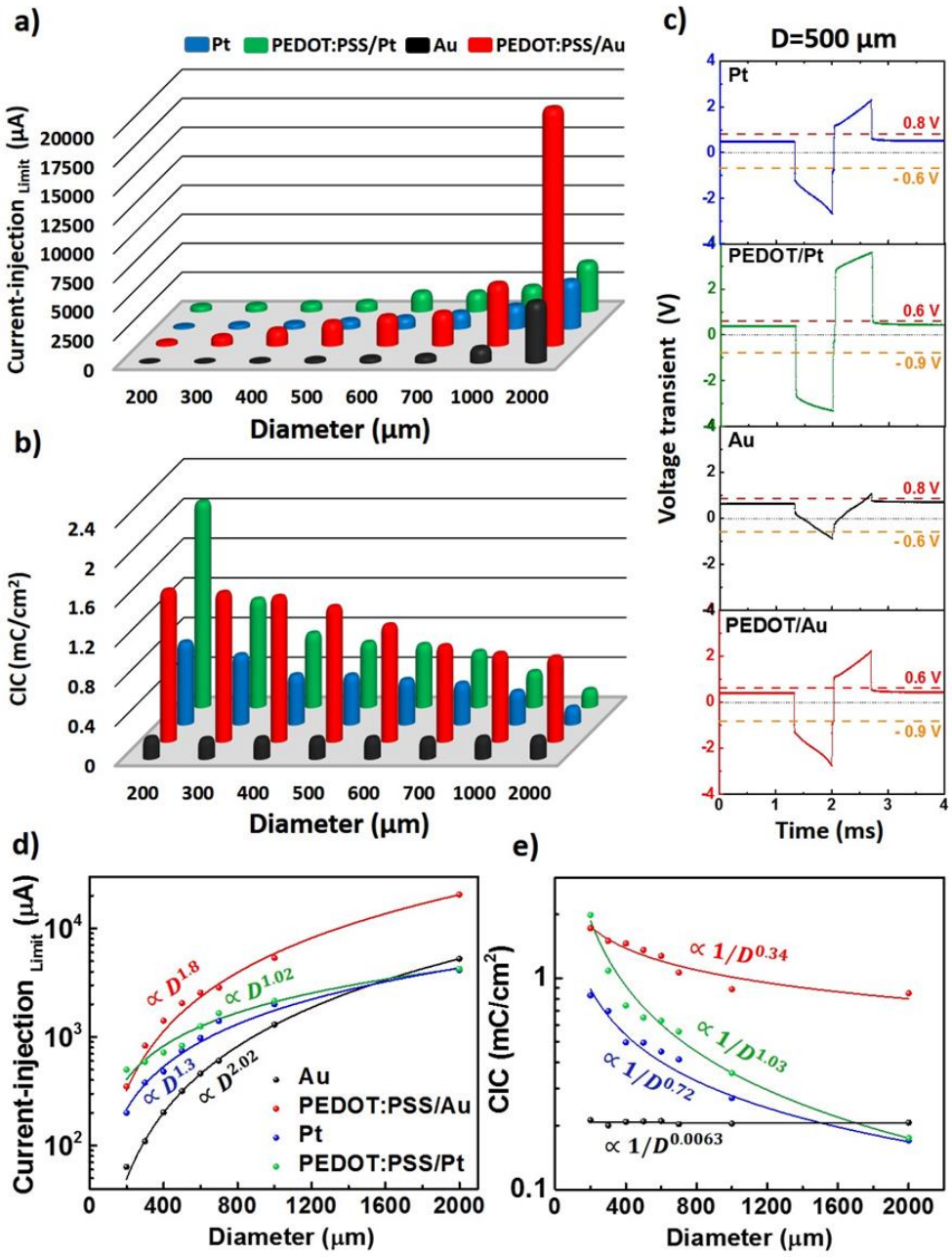

Figure 5.3 Macroelectrodes current injection limits and charge injection capacities. (a) Current injection limit (µA) and (b) charge injection capacity (mC/cm^2) histograms of different scaled materials including Pt (blue), PEDOT:PSS/Pt (green), Au (black) and PEDOT:PSS/Au (red) with diameters ranging from 200 µm to 2000 µm. (c) Examples of corresponding voltage transients to injected current limits for Pt, PEDOT:PSS/Pt, Au and PEDOT:PSS/Au with 500 µm diameter, limited at their respective water electrolysis window, at both the cathodal and the anodal limits, under application of appropriate inter-pulse potential bias. Measured and fitting values of current injection limits (d) and charge injection capacities (e) of different scaled materials as a function of diameter, highlighting the current injection limit and CIC scaling dependencies of each electrode material.

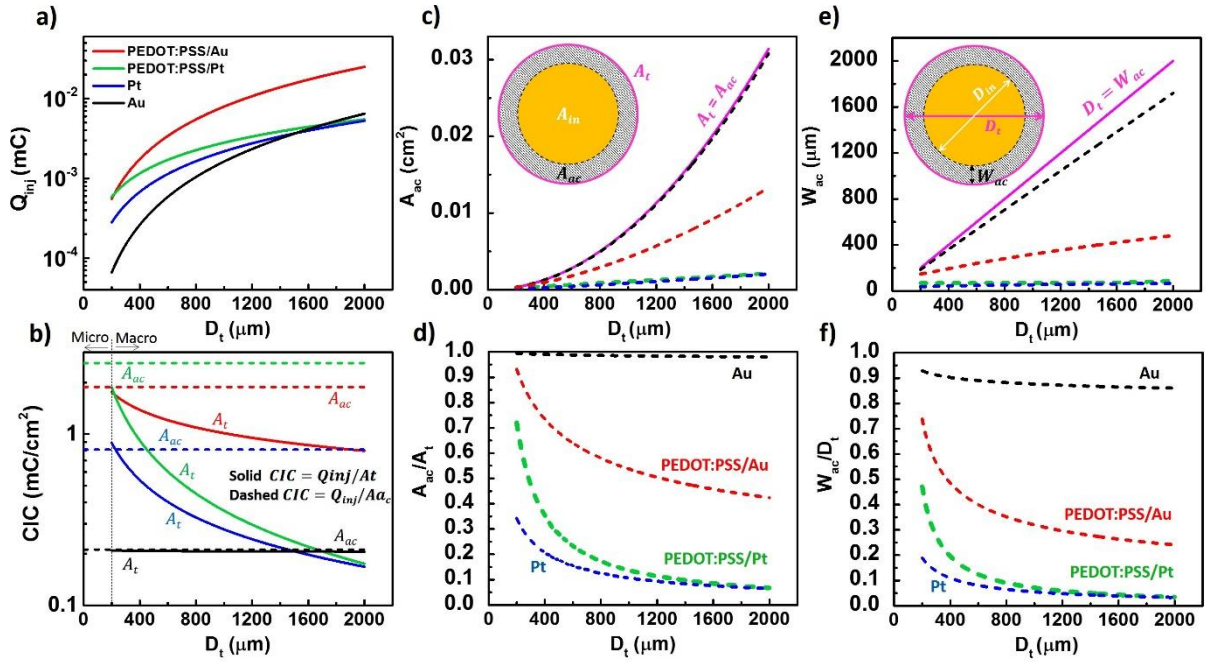

Figure 5.4 Edge effect on CICs of different macroelectrode materials. (a) The injection charge limits of different scaled materials. (b) Charge injection capacities (CICs) of different scaled materials calculated in two methods; (1) using total electrode area (A_t) shown with solid lines, (2) using active (rings around the edge) electrode area (A_ac) shown with dashed line and are constant by extrapolation from the CICs of microscale electrodes. (c) Active area that produces a constant CIC as a function of total electrode diameter; Au seems to have the most active area and Pt and PEDOT:PSS/Pt the lowest. (d) Ratio of active area over total area as a function of diameter. As the diameter increases, the active area in the electrochemical exchange decreases. (e) The width, distance from dot edge, of active region in the electrochemical interaction as a function of total diameter. (f) Ratio of active width over total diameter as a function of electrode diameter.

5.3.3 Inter-pulse potential (E_{ipp}) effect

Earlier work by Cogan et al. has shown that charge injection capacity depends on ineter-pulse potential values where appropriate bias voltage can further increase the CIC.[4b, 10b] To obtain the optimal bias voltage, current injection limits and CICs of scaled Pt and PEDOT:PSS/Au were measured as a function of E_{ipp} (bias voltage) as shown in **Figure 5.5** for microdots (blue, 20 μm to 150 μm) and macrodots (red, 200 μm to 2000 μm). Measured current injection limits of Pt and PEDOT:PSS/Au microdots are plotted as a function of E_{ipp} in linear (**Figure 5.5a** and **5.5b**) and semilog scale (**Figure 5.5c** and **5.5d**), respectively. Data represented by filled circles indicate a

cathodal limited current injection limit/CIC at respective bias voltage, whereas data represented by open circles indicate the anodal limitation. For concurrent cathodal/anodal limitation state, the data is represented by filled triangles. It is evident that by enlarging electrode diameter (darker color), more current injection is allowed with respect to anodal and cathodal threshold potentials (i.e., a larger current injection limit) for both PEDOT:PSS/Au and Pt microelectrodes (**Figure 5.5c** and **5.5d**). It is important to note that maximum current injection limits (or CICs) have been measured at 0.4 V (optimal E_{ipp} bias) in cathodal limited state for PEDOT:PSS/Au and simultaneous cathodal and anodal limits for Pt microdots. All calculated CIC values from current injection limits are depicted as general lines for both PEDOT:PSS/Au (**Figure 5.5e**) and Pt (**Figure 5.5f**) microdots. Maximum CIC of all PEDOT:PSS/Au microdots with averaged value of ~ 1.9 mC/cm^2 were calculated at 0.4 V bias voltage with cathodal limited state whereas Pt microdots show 2 to 3 times lower CIC values across different E_{ipp} biases. Similar to microdots, current injection limits of Pt and PEDOT:PSS/Au macrodots (200 µm to 2000 µm) were measured and plotted as a function of E_{ipp} in linear (**Figure 5.5g** and **5.5h**) and semilog scale (**Figure 5.5i** and **5.5j**) respectively. In a similar behavior as microdots, larger macroelectrodes (darker color), possess larger current injection limit for both PEDOT:PSS/Au and Pt macroelectrodes (**Figure 5.5i** and **5.5j**) that were also measured at 0.4 V (optimal E_{ipp} bias) for PEDOT:PSS/Au (cathodal limit) and Pt (cathodal/anodal limit) macrodots. Calculated CIC values of PEDOT:PSS/Au and Pt macrodots are shown in **Figure 5.5k** and **5.5l** respectively where PEDOT:PSS/Au macrodots showed up to ~5 times larger CIC compared to the same Pt macrodot. The CICs of PEDOT:PSS/Au and Pt electrodes decreased by transitioning from microscale to macroscale across the whole E_{ipp} biases (**Figure 5 e-f** and **k-l**).

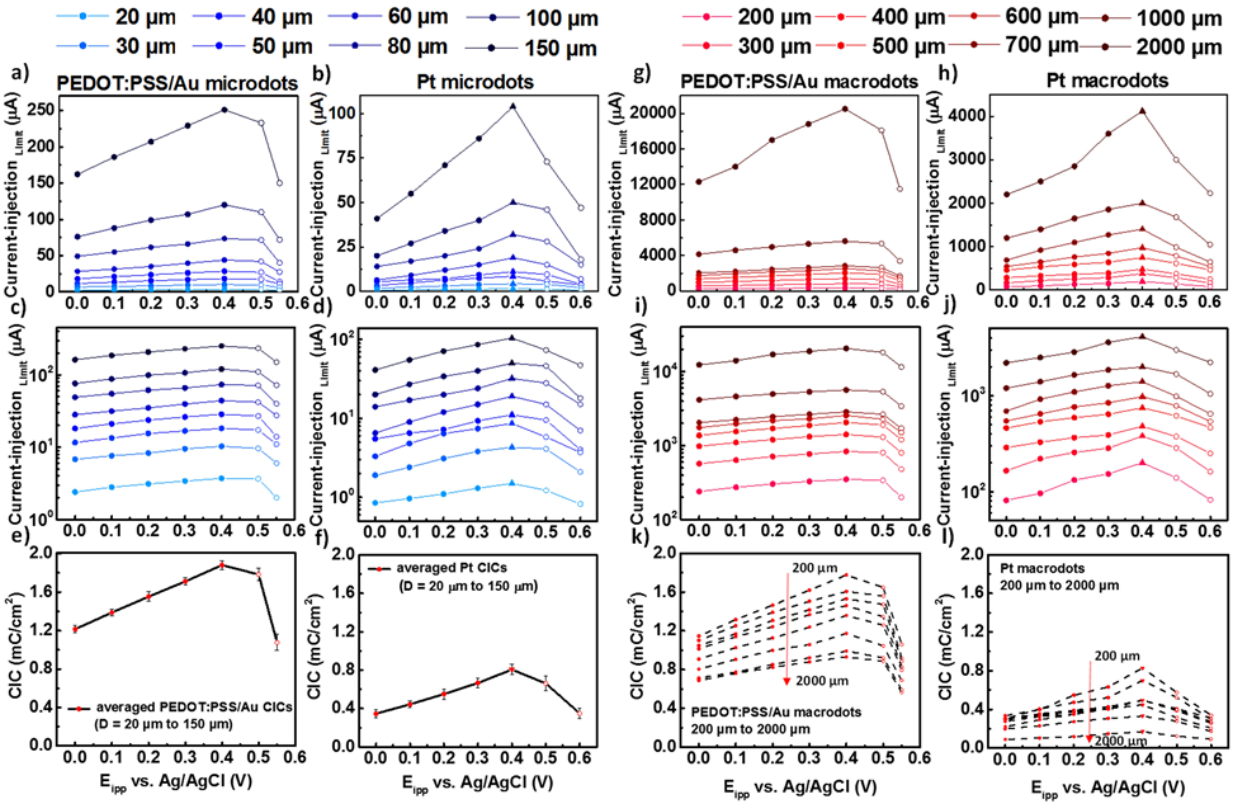

Figure 5.5 Inter-pulse potential (E_{ipp}) effect on scaled PEDOT:PSS/Au and Pt electrodes. Current injection limits of PEDOT:PSS/Au (a and c) and Pt (b and d) microelectrodes as a function of Eipp or bias voltage in linear and semilog scale respectively (darker colors indicate larger electrode sizes). Averaged CIC values of PEDOT:PSS/Au (e) and Pt (f) microdots as a function of Eipp or bias voltage. Current injection limits of PEDOT:PSS/Au (g and i) and Pt (h and j) macroelectrodes as a function of E_{ipp} or bias voltage in linear and semilog scale respectively (darker colors indicate larger electrode sizes). CIC values of PEDOT:PSS/Au (k) and Pt (l) macrodots as a function of E_{ipp} or bias voltage. Filled and open circles indicate the measured cathodal and anodal current injection limits, respectively, and filled triangles correspond to simultaneous anodal and cathodal limits.

5.3.4 Pulse Width Engineering for Boosting CIC

Asymmetric current pulses can also be employed to surpass the anodal CIC limitation, a technique referred to as pulse engineering. These asymmetric pulses include 1 to 2 (1:2), 1 to 4 (1:4) and 1 to 8 (1:8) cathodal/anodal pulse width ratios which are applied to macro/micro PEDOT:PSS/Au electrodes at 0.5 V E_{ipp} bias whereas current injection limits/ CICs were limited with anodal threshold potential (0.8 V for Pt and 0.6 V for PEDOT:PSS electrodes). The optimized current injection limits (and the their fitted lines) for PEDOT:PSS/Au micro and macro electrodes

are shown in **Figure 5.6a** and **5.6b** respectively, as a function of diameter. Open circles (black) denote the measured current injection limits before pulse engineering with anodal limit at 0.5 V E_{ipp} (**Figure 5.5**). The filled triangles in **Figure 5.6a** and **5.6b** indicate the optimized current injection limits that have been measured with specific asymmetric pulse injection ratio, for each diameter, which resulted in reaching water electrolysis limits from both anodal and cathodal sides at 0.5V bias voltage. Different types of injected asymmetric current pulses are shown in **Figure 5.6c** with their corresponding voltage transient for different PEDOT:PSS/Au electrodes with 40 µm, 150 µm and 400 µm diameters. To maintain a charge-neutral injected pulse, the anodal phase current should be divided by the respective pulse width ratio as shown in **Figure 5.6c**. Overall, pulse width engineering boosted the current injection limit of PEDOT:PSS/Au by 13.6 % for microdots and 14.6 % for macrodots.

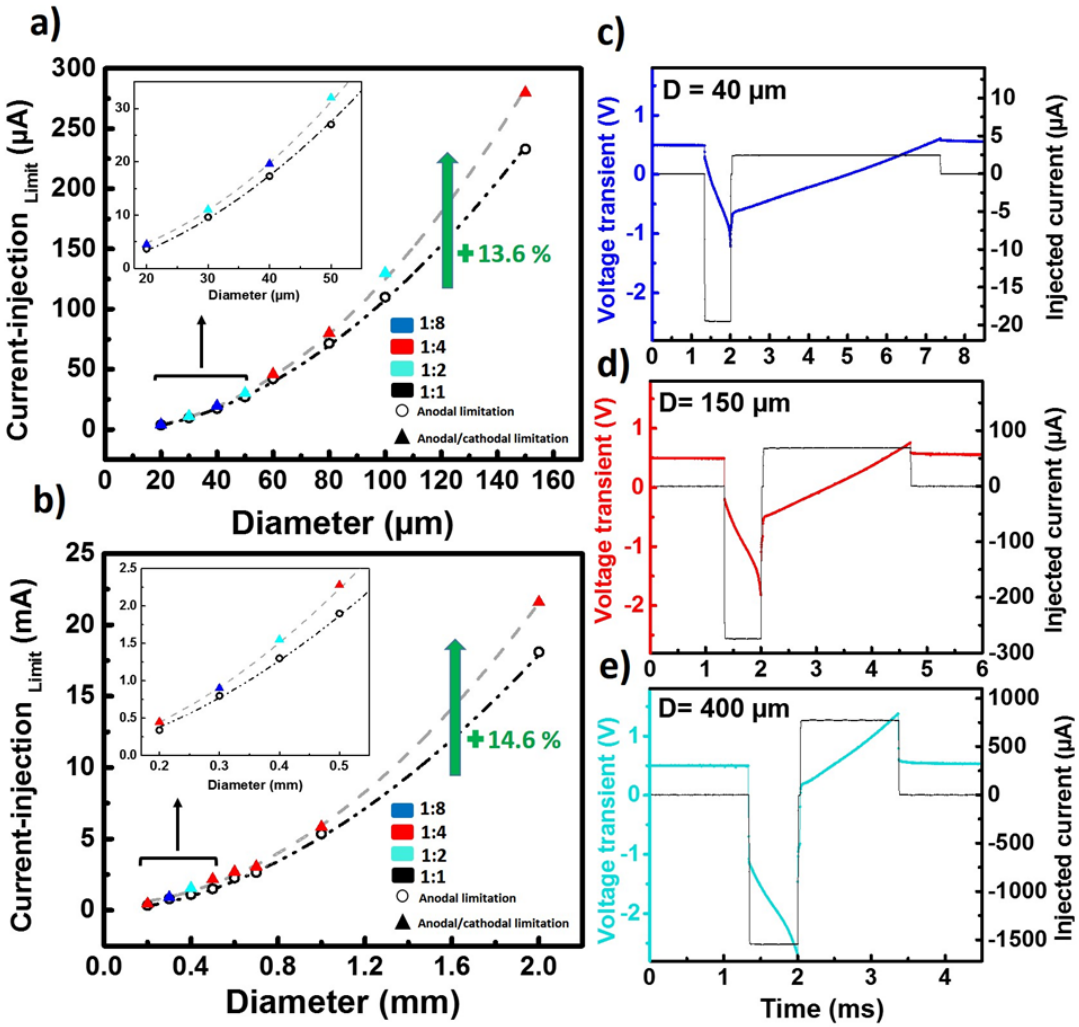

Figure 5.6 Pulse width engineering for boosting PEDOT:PSS/Au current injection limits. Measured optimized current injection limits (filled triangles) using asymmetric pulse injection and non-optimized current injection limits (open circles) using symmetric pulse injection at 0.5 V E_{ipp} bias for PEDOT:PSS microdots (a) and macrodots (b) as a function of electrode diameter. Open circles indicate the measured current injection limit at anodal limitation and filled triangles correspond to anodal/cathodal limits after pulse engineering in which resulted in 13.6% enhancement of PEDOT:PSS/Au microdots and 14.6 % enhancement of macrodots current injection limit. Colors denote the asymmetric pulse ratios (cathodal/anodal pulse width ratio; cyan 1:2, red 1:4, blue 1:8). The inset shows the close view of first 4 data points per each plot (20, 30, 40 and 50 μm in (a) and 200, 300, 400 and 500 μm in (b) diameter sizes). (c) Examples of different injected asymmetric pulses and the corresponding voltage transients for 40 μm (blue 1:8), 150 μm (red 1:4) and 400 μm (cyan 1:2) diameters.

5.3.5 Pulse Width Dependency of CIC

We also investigated the effect of pulse width on charge injection limit for safe electrochemical stimulation. CICs of two PEDOT:PSS/Au electrodes with 50 μm (microdot) and

500 µm (macrodot) diameters were measured under various pulse widths including 0.35, 0.65, 1, 1.3 and 1.65 ms as shown as a function of diameter in **Figure 5.7**. Measured current injection limits and calculated CICs are plotted as a function of pulse width in **Figure 5.7a** for PEDOT:PSS/Au microdot with 50 µm diameter and **Figure 5.7c** for 500 µm diameter macrodot (fitting lines for current injection limits (black) and CICs (blue) are included). The corresponding voltage transients of each injected current limits with varying pulse widths (frequencies) are shown in **Figure 5.7b** and **5.7d** for 50 µm microdot and 500 µm macrodot respectively. According to **Figure 5.7a** and **5.7b**, we observed that by choosing a longer pulse width (lower frequency), the limiting current values for microdots are reduced with $1/t_c^{0.88}$ ($f^{0.88}$) dependency. The amount of injected charge (or CIC) are increased by applying longer pulse widths (lower frequency). CIC improved by ~40 % by increasing the pulse width from 200 µs to 2000 µs. Similarly, the macrodot with a 500 µm diameter displayed lower current injection limit (proportional to $1/tc^{0.93}$ or $f^{0.93}$) and higher CIC (mC/cm^2) for longer pulse widths (lower frequency). A ~21% increase in CIC was calculated by increasing the pulse duration from 200 µs duration to 2000 µs (**Figure 5.7c**). Based on this result, we conclude that clinical stimulation protocols that require long pulse durations (e.g. epi-retinal stimulation with 2000 µs pulse width) have a higher CIC allowance. However, clinical stimulation protocols that require shorter pulse widths (e.g. cortical stimulation for vision application with 200 µs pulse width) have a lower CIC allowance. In other words, there is a tradeoff between initiative electrical stimulation (higher frequency) and safe stimulation (higher CIC), and these values scale with different diameters. Generally, smaller diameters provide higher CIC allowances.

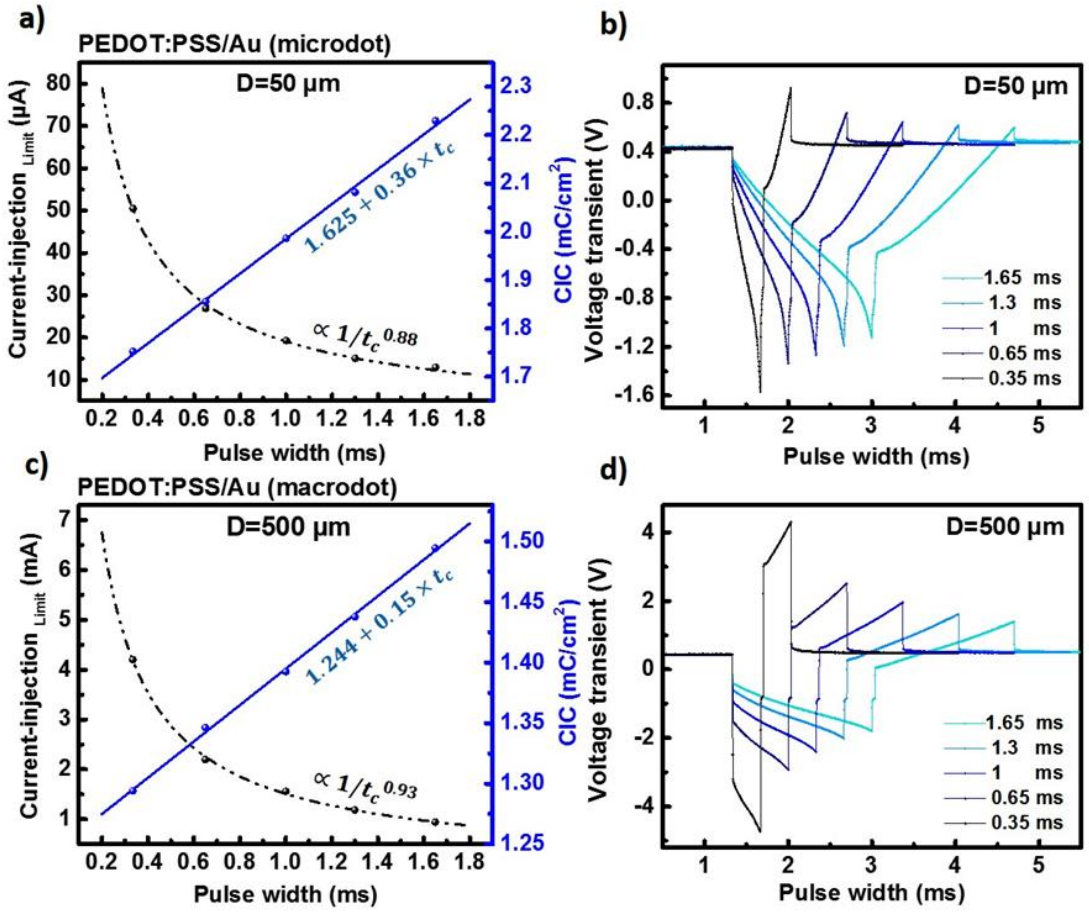

Figure 5.7 Effect of pulse width on current injection limit and CIC of PEDOT:PSS/Au micro and macrodot. (a) Measured current injection limit (black) and calculated CIC (blue) as a function of pulse width for 50 µm diameter size PEDOT:PSS/Au micro dot (a) and 500 µm diameter size macro dot (c). Pulse width dependencies are highlighted according to fitting line of current injection limit (dashed black line) and CIC (solid blue line) versus pulse duration. Corresponding voltage transients of injected current pulses with different pulse widths including 0.35, 0.65, 1, 1.3 and 1.65 ms, measured at anodal/cathodal limits (with optimal E_{ipp} bias voltage), for 50 µm diameter size PEDOT:PSS/Au microdot (b) and 500 µm diameter size macrodot (d).

5.3.6 Size-Dependent Charge Storage Capacity

The last metric relevant to stimulation is the charge storage capacity, CSC, which is evaluated and compared for different materials using cyclic voltammetry. Given different water electrolysis windows of metallic (Pt and Au, -0.6 to 0.8 V) and organic (PEDOT:PSS, -0.9 to 0.6 V) materials, and for a fair comparison, both cathodal and anodal CSCs were considered through cyclic sweep of tested electrode potential versus Ag/AgCl reference electrode between -0.6 and

0.6 V at constant scan rate of 200 mV/s as shown in **Figure 5.8**. Four examples of measured CVs for different electrode materials including Pt, PEDOT:PSS/Pt, Au and PEDOT:PSS/Au are shown in **Figure 5.8a** for electrodes with 40 and 100 µm diameters and **Figure 5.8b** for electrodes with 0.4 mm and 1 mm diameters. According to different CV responses, larger electrodes resulted in larger current response through cyclic voltammetry with larger hysteresis loop area, whereas Pt and Au electrodes show the largest and smallest current response, respectively. To evaluate the scaling effect on charge storage (µC) quantitatively, the time integral of both cathodal and anodal currents over a potential range of -0.6 to 0.6 V were calculated. Charge storage values extracted from CV responses of different electrode materials are plotted as a function of diameter in **Figure 5.8c** for microscale (20 µm to 150 µm diameters) and **Figure 5.8d** for macroscale (200 µm to 200 µm diameters) electrodes. Pt electrodes exhibited larger charge storage (µC) and dependency to scaling ($1/D^{1.91}$ for micro and $1/D^{1.61}$ for macroscale electrodes) compared to other electrode materials whereas PEDOT:PSS/Pt displayed larger charge storage than PEDOT:PSS/Au and Au with smallest charge storage for the whole tested electrode sizes. For further analysis, charge storage capacity (mC/cm^2) for all electrode materials were calculated; two examples of CV responses of 40 µm and 100 µm diameters are shown in **Figure 5.8e** and for different electrodes with 0.4 mm and 1 mm diameter sizes in **Figure 5.8f**. Charge storage capacities (CSC) for all scaled electrode materials are plotted as a function of diameter for microscale and macroscale electrodes in **Figure 5.8g** and **5.8h**, respectively as a function of diameter. Large electrodes (macro) present lower charge storage capacity (mC/cm^2) compared to small electrode sizes (micro) as demonstrated by smaller hysteresis loops in **Figure 5.8f** than the microscale ones of **Figure 5.8e**. Although the CSC is associated with total amount of charge available for a stimulation pulse, there isn't a well-established experimental relationship between the CSC, obtained under low-

current-density, and charge-injection capacity for neural stimulation. The CV response of any electrode material, depends on the different electrochemical and also physical properties such as geometrical area and the roughness of the electrodes surface which were depicted in **Figure 5.1**. In our earlier recording study[15], we found that PEDOT:PSS coated electrodes have more facile reversible faradaic (redox) reactions. It is possible that this facile redox capability prevents excess charge storage for PEDOT:PSS while enabling it to possess the highest CIC. Given the different capability of electrode materials for delivering CSC to injected current pulse without exceeding water window, our results indicate higher CIC/CSC ratio of PEDOT:PSS/Au microelectrodes for such charge delivery compared to Au, Pt and PEDOT:PSS/Pt according to CIC values reported in **Figures 5.2**, **5.3** and CSCs presented in **Figure 5.8**.

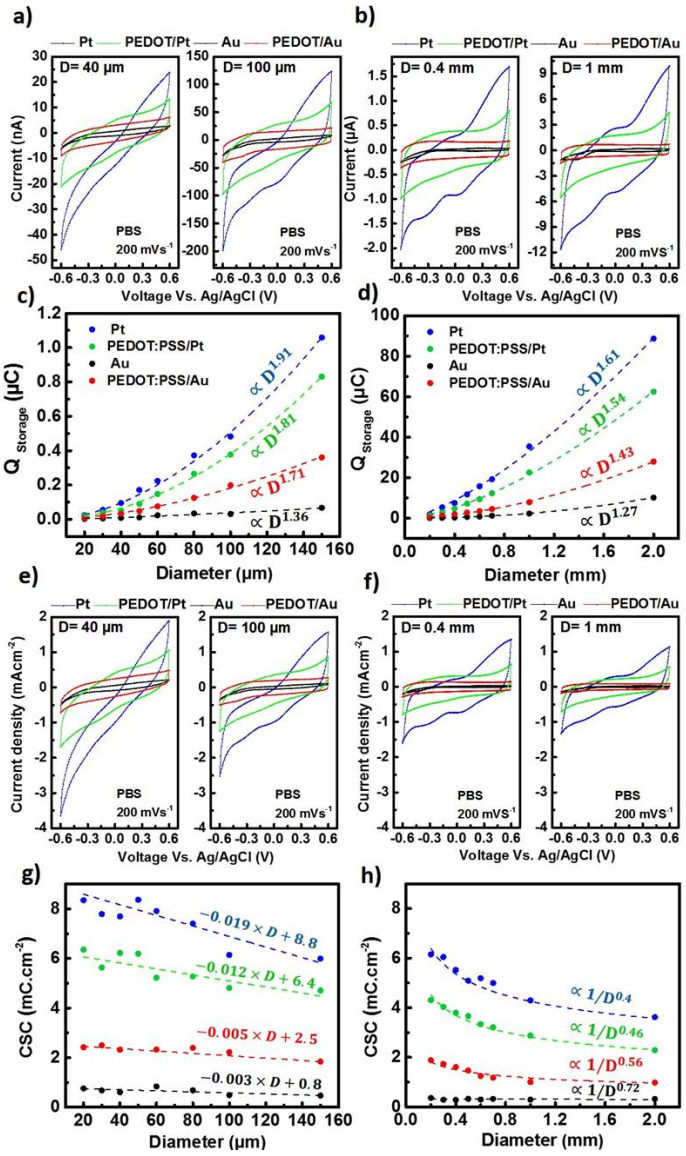

Figure 5.8 Assessment of charge storage capacities (CSC) for different scaled materials. Examples of CV characteristics of two microscale electrodes with 40 and 100 µm diameters (a) and two macroscale electrodes with 0.4 mm and 1 mm diameters (b) for all electrode materials including Pt (blue), PEDOT:PSS/Pt (green), Au (black) and PEDOT:PSS/Au (red). CVs have been performed in PBS within -0.6 and 0.6 V sweep window with constant scan rate of 200 mV/s. Charge storages (µC) of different materials plotted as a function of electrode diameter size for microscale (c) and macroscale electrodes (d). To show the scaling effect on charge storage values, fitting lines are included with corresponding geometrical dependencies. Examples of CV responses (current densities) of two microscale electrodes with 40 and 100 µm diameters (e) and two macroscale electrodes with 0.4 mm and 1 mm diameter sizes (f) for all electrode materials. Charge storage capacities (mC/cm^2) of different materials plotted as a function of electrode diameter for microscale (g) and macroscale electrodes (h) with included fitting lines with corresponding scaling dependencies.

5.3.7 Power Consumption for Charge Injection

Finally, to put these results in perspective of power needed to inject similar charge density for each materials, we measured the voltage transients under bi-phasic current injection and computed the corresponding absolute power (P=I×V). We applied bi-phasic square waves with a 0.65 ms pulse width and different amplitudes (noted in **Figure 5.9**) into all diameters for all different scaled materials and calculated the corresponding power required for that particular charge injection. **Figure 5.9a** and **Figure 5.9b** show representative measured voltage transients and corresponding absolute power plots for 40 µm and 400 µm diameter electrodes, respectively. The calculated power consumption per cycle are plotted in Figure 8c for microelectrodes and **Figure 5.9d** for macroscale electrodes. For further comparison, the fraction of power consumption for PEDOT:PSS divided by that required for same charge injection but using the metal electrodes only are plotted as a function of diameter in **Figure 5.9e**. Significant power reduction is observed at the smaller electrode diameters when PEDOT:PSS is used as opposed to metal electrodes. The 20 µm diameter dots of PEDOT:PSS/Au and PEDOT:PSS/Pt require nearly one tenth and one third of the power for injection of the same charge density compared to Au and Pt contacts. The reduction in power requirement can be significantly beneficial for extending the battery life of implanted neuroprosthetic devices. It is important to note that earlier work on electrodeposited PEDOT:PSS observed mechanical failure and delamination that is directly proportional to the film thickness.[14b] Evaluation of the PEDOT:PSS ECoG arrays prepared using our fabrication method for the purpose of chronic implantation in terms of stability and biocompatibility will be systematically investigated in future work.

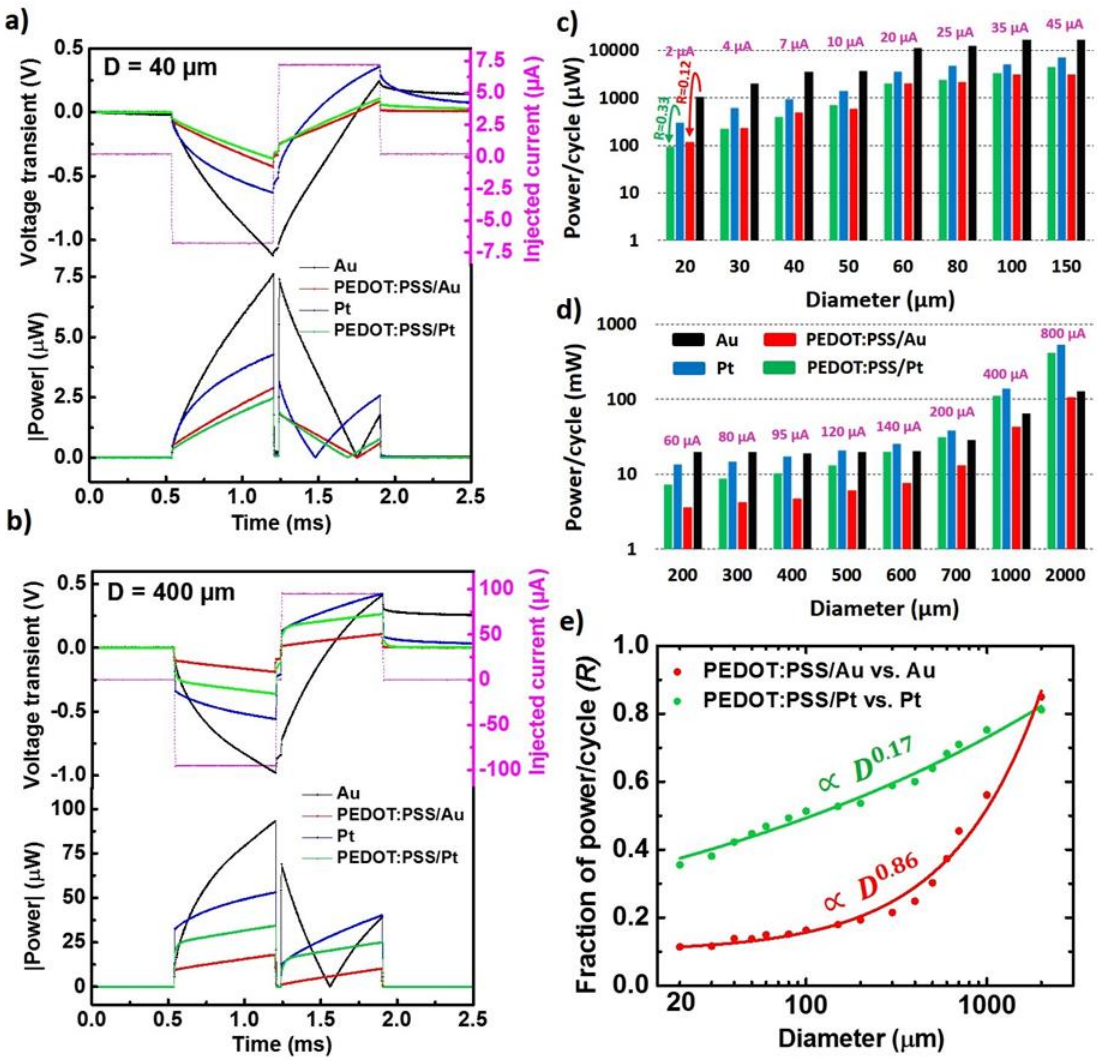

Figure 5.9 Power consumption of current injection through PEDOT:PSS/Au, Au, PEDOT:PSS/Pt and Pt micro and macrodots. Measured voltage transients and power absolute values of (a) 40 µm and (b) 400 µm diameter dots with injection of bi-phasic, cathodal first 7 µA and 95 µA current pulse respectively. (c) Calculated power consumptions per cycle of Au, PEDOT:PSS/Au, Pt and PEDOT:PSS/Pt microelectrodes and (d) macroelectrodes under the same charge injection with injected current amplitudes highlighted with purple color above each electrode diameter. (e) The ratio of power consumption/cycle of PEDOT:PSS/Pt to Pt (green) and PEDOT:PSS/Au to Au electrodes (red). The circles represent experimental measurements and the lines are fits. The largest power reduction of 67% for PEDOT:PSS/Pt compared to Pt and 88% for PEDOT:PSS/Au compared to Au electrodes were observed at 20 µm diameter.

5.4 Conclusion

To summarize, we investigated the size-dependent electrical stimulation capabilities of Au, Pt, and PEDOT:PSS electrode materials through systematic studies of charge injection capacity

(CIC) and charge storage capacity (CSC). PEDOT:PSS/Au exhibited ~9.5X larger CIC than Au microelectrodes and PEDOT:PSS/Pt exhibited ~3.2X larger CIC than Pt microelectrodes for diameters in the range of 20 µm - 150 µm. This enhancement is less prominent at macroscale (200 µm - 2000 µm diameter) where PEDOT:PSS/Au outperformed other materials by a slight margin that narrows down with diameter. We observed optimal E_{ipp} bias at 0.4 V for both PEDOT:PSS/Au and Pt micro/macro electrodes where CICs of microelectrodes experienced ~55% and ~135% enhancement compared to zero bias voltage, resulting in a maximum 1.88 mC/cm^2 and 0.8 mC/cm^2 CIC for PEDOT:PSS/Au and Pt microelectrodes, respectively. CICs of PEDOT:PSS/Au micro/macro electrodes boosted ~ 13-14% further at 0.5 V E_{ipp} bias by pulse engineering (asymmetric pulse injection). Increased pulse width from 200 µs to 2 ms duration resulted in 40% and 21% larger CIC for PEDOT:PSS/Au microdots and macrodots, respectively. This highlights the importance of accurate regulation of stimulation methodology parameters such as pulse width to make proper balance between safety (higher CIC) and efficacy for neuronal stimulation (higher current and frequency). CSC evaluation revealed the largest CSC for Pt micro/macro electrodes compared to other electrode materials, whereas PEDOT:PSS/Au micro/macro electrodes offered higher capability to convert those available stored charges into an injected electrical pulse (higher CIC/ CSC ratio). The required power to deliver the same amount of charge is 88% lower for 20 µm diameter PEDOT:PSS/Au electrodes compared to Au microelectrodes and 67% lower for 20 µm diameter PEDOT:PSS/Pt compared to Pt electrodes.

Overall, our results provide guidance that addresses considerations with regard to next generation chronic stimulation devices through (1) the evaluation of critical parameters for optimized pulse design that could be safely employed in a chronic scenario and outlining design flexibility that might be useful for finding therapeutic stimulation protocols for each individual

patient, (2) ensuring that safe stimulation is also important for electrode longevity, and (3) demonstrating that the material choices and pulse design can lead to more energy efficient stimulation which is a crucial design consideration for fully implanted devices.

Chapter 5, in full, is a reprint of material as it appears in the following publication: M. Ganji, A. Tanaka, V. Gilja, E. Halgren, and S. A. Dayeh, "Scaling Effects on the Electrochemical Stimulation Performance of Au, Pt, and PEDOT: PSS Electrocorticography Arrays," Advanced Functional Materials, vol. 27, p. 1703019, 2017. The dissertation author was the primary investigator and author of this material.

5.5 References

[1] K. Kumar, R. S. Taylor, L. Jacques, S. Eldabe, M. Meglio, J. Molet, "Spinal cord stimulation versus conventional medical management for neuropathic pain: a multicentre randomised controlled trial in patients with failed back surgery syndrome," *Pain*, vol. 132, pp. 179-188, 2007.

[2] J. S. Perlmutter and J. W. Mink, "Deep brain stimulation," *Annu. Rev. Neurosci.*, vol. 29, pp. 229-257, 2006.

[3] B. S. Wilson and C. C. Finley, "Better speech recognition with cochlear implants," *Nature*, vol. 352, p. 236, 1991.

[4] M. A. Svirsky, A. M. Robbins, K. I. Kirk, D. B. Pisoni, and R. T. Miyamoto, "Language development in profoundly deaf children with cochlear implants," *Psychological science*, vol. 11, pp. 153-158, 2000.

[5] D. R. Kipke, W. Shain, G. Buzsáki, E. Fetz, J. M. Henderson, J. F. Hetke, "Advanced neurotechnologies for chronic neural interfaces: new horizons and clinical opportunities," *Journal of Neuroscience*, vol. 28, pp. 11830-11838, 2008.

[6] E. Schmidt, M. Bak, F. Hambrecht, C. Kufta, D. O'rourke, and P. Vallabhanath, "Feasibility of a visual prosthesis for the blind based on intracortical micro stimulation of the visual cortex," *Brain*, vol. 119, pp. 507-522, 1996.

[7] V. Gilja, C. A. Chestek, I. Diester, J. M. Henderson, K. Deisseroth, and K. V. Shenoy, "Challenges and opportunities for next-generation intracortically based neural prostheses," *IEEE Transactions on Biomedical Engineering*, vol. 58, pp. 1891-1899, 2011.

[8] A. Prochazka, V. K. Mushahwar, and D. B. McCreery, "Neural prostheses," *The Journal of physiology,* vol. 533, pp. 99-109, 2001.

[9] T. W. Berger, R. E. Hampson, D. Song, A. Goonawardena, V. Z. Marmarelis, and S. A. Deadwyler, "A cortical neural prosthesis for restoring and enhancing memory," *Journal of neural engineering,* vol. 8, p. 046017, 2011.

[10] A. B. Schwartz, "Cortical neural prosthetics," *Annu. Rev. Neurosci.,* vol. 27, pp. 487-507, 2004.

[11] S. R. Kane, S. F. Cogan, J. Ehrlich, T. D. Plante, D. B. McCreery, and P. R. Troyk, "Electrical performance of penetrating microelectrodes chronically implanted in cat cortex," *IEEE Transactions on Biomedical Engineering,* vol. 60, pp. 2153-2160, 2013.

[12] D. R. Merrill, M. Bikson, and J. G. Jefferys, "Electrical stimulation of excitable tissue: design of efficacious and safe protocols," *Journal of neuroscience methods,* vol. 141, pp. 171-198, 2005.

[13] S. F. Cogan, "Neural stimulation and recording electrodes," *Annu. Rev. Biomed. Eng.,* vol. 10, pp. 275-309, 2008.

[14] S. F. Cogan, D. J. Garrett, and R. A. Green, "Electrochemical Principles of Safe Charge Injection," *Neurobionics: The Biomedical Engineering of Neural Prostheses: The Biomedical Engineering of Neural Prostheses,* pp. 55-88, 2016.

[15] S. F. Cogan, J. Ehrlich, and T. D. Plante, "The effect of electrode geometry on electrochemical properties measured in saline," in *Engineering in Medicine and Biology Society (EMBC), 2014 36th Annual International Conference of the IEEE*, 2014, pp. 6850-6853.

[16] P. H. Gorman and J. T. Mortimer, "The effect of stimulus parameters on the recruitment characteristics of direct nerve stimulation," *IEEE Transactions on Biomedical Engineering*, pp. 407-414, 1983.

[17] R. V. Shannon, "A model of safe levels for electrical stimulation," *IEEE Transactions on Biomedical Engineering*, vol. 39, pp. 424-426, 1992.

[18] S. F. Cogan, K. A. Ludwig, C. G. Welle, and P. Takmakov, "Tissue damage thresholds during therapeutic electrical stimulation," *Journal of neural engineering,* vol. 13, p. 021001, 2016.

[19] S. Venkatraman, J. Hendricks, Z. A. King, A. J. Sereno, S. Richardson-Burns, D. Martin, "In vitro and in vivo evaluation of PEDOT microelectrodes for neural stimulation and recording," *IEEE Transactions on Neural Systems and Rehabilitation Engineering,* vol. 19, pp. 307-316, 2011.

[20] J. D. Weiland, D. J. Anderson, and M. S. Humayun, "In vitro electrical properties for iridium oxide versus titanium nitride stimulating electrodes," *IEEE transactions on biomedical engineering,* vol. 49, pp. 1574-1579, 2002.

[21] D. McCreery, L. Bullara, and W. Agnew, "Neuronal activity evoked by chronically implanted intracortical microelectrodes," *Experimental neurology,* vol. 92, pp. 147-161, 1986.

[22] S. F. Cogan, P. R. Troyk, J. Ehrlich, T. D. Plante, and D. E. Detlefsen, "Potential-biased, asymmetric waveforms for charge-injection with activated iridium oxide (AIROF) neural stimulation electrodes," *IEEE Transactions on Biomedical Engineering,* vol. 53, pp. 327-332, 2006.

[23] S. Negi, R. Bhandari, L. Rieth, and F. Solzbacher, "In vitro comparison of sputtered iridium oxide and platinum-coated neural implantable microelectrode arrays," *Biomedical materials,* vol. 5, p. 015007, 2010.

[24] S. F. Cogan, T. Plante, and J. Ehrlich, "Sputtered iridium oxide films (SIROFs) for low-impedance neural stimulation and recording electrodes," in *Engineering in Medicine and Biology Society, 2004. IEMBS'04. 26th Annual International Conference of the IEEE,* 2004, pp. 4153-4156.

[25] S. F. Cogan, P. R. Troyk, J. Ehrlich, and T. D. Plante, "In vitro comparison of the charge-injection limits of activated iridium oxide (AIROF) and platinum-iridium microelectrodes," *IEEE Transactions on Biomedical Engineering,* vol. 52, pp. 1612-1614, 2005.

[26] R. A. Green, N. H. Lovell, G. G. Wallace, and L. A. Poole-Warren, "Conducting polymers for neural interfaces: challenges in developing an effective long-term implant," *Biomaterials,* vol. 29, pp. 3393-3399, 2008.

[27] M. R. Abidian, J. M. Corey, D. R. Kipke, and D. C. Martin, "Conducting-Polymer Nanotubes Improve Electrical Properties, Mechanical Adhesion, Neural Attachment, and Neurite Outgrowth of Neural Electrodes," *small,* vol. 6, pp. 421-429, 2010.

[28] M. Sessolo, D. Khodagholy, J. Rivnay, F. Maddalena, M. Gleyzes, E. Steidl, "Easy-to-Fabricate Conducting Polymer Microelectrode Arrays," *Advanced Materials,* vol. 25, pp. 2135-2139, 2013.

[29] D. Khodagholy, T. Doublet, M. Gurfinkel, P. Quilichini, E. Ismailova, P. Leleux, "Highly conformable conducting polymer electrodes for in vivo recordings," *Advanced Materials,* vol. 23, 2011.

[30] D. Khodagholy, J. N. Gelinas, T. Thesen, W. Doyle, O. Devinsky, G. G. Malliaras, "NeuroGrid: recording action potentials from the surface of the brain," *Nature neuroscience,* vol. 18, pp. 310-315, 2015.

[31] D. Khodagholy, J. N. Gelinas, Z. Zhao, M. Yeh, M. Long, J. D. Greenlee, "Organic electronics for high-resolution electrocorticography of the human brain," *Science Advances,* vol. 2, p. e1601027, 2016.

[32] M. Ganji, E. Kaestner, J. Hermiz, N. Rogers, A. Tanaka, D. Cleary, "Development and Translation of PEDOT: PSS Microelectrodes for Intraoperative Monitoring," *Advanced Functional Materials,* 2017.

[33] J. Rivnay, S. Inal, B. A. Collins, M. Sessolo, E. Stavrinidou, X. Strakosas, "Structural control of mixed ionic and electronic transport in conducting polymers," *Nature communications,* vol. 7, 2016.

[34] K. A. Ludwig, N. B. Langhals, M. D. Joseph, S. M. Richardson-Burns, J. L. Hendricks, and D. R. Kipke, "Poly (3, 4-ethylenedioxythiophene)(PEDOT) polymer coatings facilitate smaller neural recording electrodes," *Journal of neural engineering,* vol. 8, p. 014001, 2011.

[35] I. Uguz, M. Ganji, A. Hama, A. Tanaka, S. Inal, A. Youssef, "Autoclave Sterilization of PEDOT: PSS Electrophysiology Devices," *Advanced Healthcare Materials,* 2016.

[36] X. Cui and D. C. Martin, "Electrochemical deposition and characterization of poly (3, 4-ethylenedioxythiophene) on neural microelectrode arrays," *Sensors and Actuators B: Chemical,* vol. 89, pp. 92-102, 2003.

[37] X. T. Cui and D. D. Zhou, "Poly (3, 4-ethylenedioxythiophene) for chronic neural stimulation," *IEEE Transactions on Neural Systems and Rehabilitation Engineering,* vol. 15, pp. 502-508, 2007.

[38] M. Ganji, A. T. Elthakeb, A. Tanaka, V. Gilja, E. Halgren, and S. A. Dayeh, "Scaling Effects on the Electrochemical Performance of PEDOT, Au, and Pt for Electrocorticograpy Recording," *submitted* 2017.

Chapter 6

Monolithic and Scalable Au Nanorod Substrates Improve PEDOT–Metal Adhesion and Stability in Neural Electrodes

6.1 Introduction

In the past decade, conducting polymers (CPs) have gained substantial attention as the direct interfacing material between biomedical devices and neural tissue due to their superior electrochemical properties compared to conventional metals such as Au, Pt, and Ir.[1] In particular, poly(3,4-ethylenedioxythiophene):poly(styrenesul fonate) (PEDOT:PSS) has emerged as an outstanding material for neural interfaces and biomedical applications including recording and stimulating neural activity, neural regeneration, and therapeutic drug delivery.[1a,e,2] This is afforded with PEDOT:PSS due to several promising features such as low electrochemical impedance for high signal-to-noise ratio (SNR) recording, high charge injection capacity for safe and efficient stimulation, and compliant (soft) mechanical properties for conforming to biological tissue. Despite the superior properties, exploiting the full capability of CP coatings in chronic biomedical applications has been limited due to their weak adhesion and mechanical stability driven by i) lack of strong covalent bonds between coated polymer layers and underlying noble metal conductors[3] and ii) the volumetric expansion and contraction of polymer coatings in physiological media.[4] As a result of the poor adhesion, cracks in the CP films or complete delamination from the underlying metal conductors are often observed during 1) in vitro aging experiments, 2) chronic implants, 3)

prolonged charge injection, and 4) mechanical stresses driven by sterilization.[5] In vivo chronic implantation of PEDOT:PSS-coated electrodes resulted in a loss of conductivity/functionality of the device attributed to the mechanical failure of polymer coating.[3b,5b,6] Different groups have attempted to find a method of extending the operating lifetime of the polymer-based systems. Two approaches emerged to tackle this problem. The first approach is chemical in nature and utilizes an intermediate functionalized monolayer/ organic molecule between PEDOT and the underlying metal conductor through formation of covalent bonds between the intermediate layer and both sides, PEDOT and the underlying metal conductor. One such approach involves electrografting amine-functionalized EDOT[7] to stabilize PEDOT on metallic conductors which was subjected to 1 h of ultrasonication without significant cracking or delamination, whereas untreated PEDOT delaminated within seconds. However, cyclic voltammetry (CV) stability tests affected the treated PEDOT coating and the electrochemical impedance showed a significant degradation after 300 CV cycles.[8] The second approach is physical in nature and employs mechanical interlocking and more engaged surface area (roughened substrate) to anchor the coated CP to underlying metals. "Fuzzy gold" stabilization for polypyrrole (PPy)[9] and laser-roughened Pt anchoring for PEDOT/p-toluenesulfonate (pTS) and PEDOT/ClO4 are examples of the mechanical anchoring approach. When the latter was employed for PEDOT:PSS, severe delamination occurred upon biphasic pulsing (864 million pulses at 70 μC cm^{-2}) or steam sterilization.[5b] Recently, Boehler et al. demonstrated sputtered iridium oxide film (SIROF) as an exceptional adhesion promoter layer for electrodeposited PEDOT coatings on macroscale electrodes (500 μm diameter), resulting in polymer survival for over 10 000 CV cycles and 110 days under accelerated aging conditions at 60 °C.[10] The efficacy of this approach for microscale PEDOT-coated electrodes and for spin-cast PEDOT – used recently in recording for the surface of human cortex[11] – is yet to be assessed for

this technique. Here, we report an alternative approach to improve the adhesion of the polymer on underlying metal conductors, using a gold nanorod (Au-nr) layer. We conducted different electrochemical tests including CV, electrochemical impedance spectroscopy (EIS) along with morphological characterizations (optical, focused-ion beam (FIB), and scanning electron microscopy (SEM)) to fully characterize the fabricated electrodes and examine the PEDOT:PSS/Au-nr surface/interface. The Au-nr structure was integrated on top of the conventional Au electrodes, using a dealloying technique,[12] capable of enhancing the adhesion of spin-cast and electrodeposited PEDOT:PSS films. To benchmark the stability of modified PEDOT:PSS electrodes against conventional planar electrodes, we applied extensive CV stressing cycles (over 10 000) to validate the anchoring capability of the Au-nr layer. We hypothesize that the Au-nr interlocking layer prevents the delamination of PEDOT film under long-term reversible charge injections (cycling tests) where induced volumetric contraction/expansion of polymer film is possible as the result of electrostatic repulsions between fixed positive charges and exchange of cations, anions, and solvent molecules between the polymer and the solution.[13] The Au-nr layer stabilized the PEDOT:PSS/Au-nr interface for over 10 000 stressing CV cycles, affording at least 20-fold more cycling of coated polymer compared to that of conventional spin-cast PEDOT:PSS on planar Au macroelectrodes with the same diameter of 500 μm for which delamination occurred only after only 500 cycles. Additionally, we investigated the efficacy of the Au-nr films on the stability of 50 μm diameter electrodes, important for high spatial resolution in recording and stimulating electrodes. Within microscale, a 50 μm PEDOT:PSS/Au-nr electrode passed 8000 CV cycles without significant morphological change or electroactivity loss, yielding a tenfold improvement given the only 800 cycles' survival for PEDOT:PSS on planar Au. In addition, we observed a different degradation mechanism for spin-cast PEDOT:PSS compared to

electrodeposited PEDOT:PSS film under cycling stress that is not discussed in earlier literature. We found that under CV stress experiments, the spin-cast PEDOT:PSS film tends to delaminate from the metal substrate, exhibiting stronger cohesive polymer film strength than that of the polymer/metal interface, whereas electrodeposited PEDOT film tends to leach out via surface decomposition and gradual thinning rather than delaminating from the substrate. To simulate a 6 month semi chronic implant, accelerated aging tests (passive test) were performed to expose the electrodes to wetting environment over a long time (5 weeks) at 60 °C and longer survival of the coating was observed using the Au-nr structures. The adhesion-promoting effect of Au-nr layer was also validated in vivo where after 10 weeks chronic implant onto mouse barrel cortex, the PEDOT:PSS did not detach from the Au-nr substrate, in contrast to planar Au electrodes which were either partially or fully delaminated. In addition, the biocompatibility of PEDOT:PSS/Au-nr electrodes was verified through immunohistochemistry that showed no neuronal loss and minimal activation of astrocytes and microglia at the implant site.

6.2 Experimental Details

6.2.1 Device Fabrication

a) Spin-coated PEDOT:PSS based electrodes: The fabrication of the PEDOT:PSS device on planar Au (Au-pl) conductors is similar to previously established protocols and is identical to that of the of PEDOT:PSS devices on Au nanorod (Au-nr) conductors discussed here. Glass slides (Specialty Glass Products Inc.) or Si wafer were used as substrate carriers for deposition of parylene C layers. The glass or Si substrates first were cleaned with acetone/isopropanol (IPA)/deionized (DI) water/IPA, which was followed by ultrasonic agitation in IPA for 5 min. To facilitate detachment of the device after the process was completed, diluted Micro-90 (0.1%); an anti-adhesion layer, was spun-cast at 1500 rpm on the substrate. A first parylene C layer (≈1.9–2.5

μm) was deposited by chemical vapor deposition using a PDS 2010 Parylene coater system. Prior to metallization, metal lead patterns were defined using a Karl Suss MA6 mask aligner using NR9-3000 negative resist and subsequently developed. 15 nm Cr adhesion layer and 100 nm Au contact layer were then deposited using temescal BJD 1800 electron beam evaporator, and metal leads were defined by a lift-off process in acetone. Then, patterns of the electrode sites were defined using NR9-6000 negative resist and a Karl Suss MA6 mask aligner for exposure. A 15 nm/100 nm Cr/Au layer was sputtered followed by deposition of ~0.5 μm thick AuAg alloy using a co-sputtering technique performed at 400 W (RF) and 60 W (DC) powers for the co-deposition of Ag and Au, respectively. A lift-off process in acetone followed shortly after. To realize Au-nr film on electrode sites, de-alloying was performed in Nitric acid at 60 °C for 2 min. O_2 plasma (Oxford Plasmalab 80 RIE) was then applied for 2 min (150 W RF power) to activate the surface of parylene C for enhancing the adhesion of the subsequent encapsulating parylene C layer. A layer of ≈ 1.9–2.5 μm parylene C was then deposited and followed by coating another Micro 90 anti-adhesion layer; with slightly higher concentrated Micro-90 (1% as opposed to 0.1% for the first layer) to facilitate the separation of the subsequent layers. Then a third parylene-C layer was deposited as sacrificial layer. To define the patterns on electrode sites, a thick 2010 SU-8 photoresist layer was exposed and developed using Karl Suss MA6 mask aligner and SU8 developer. Prior to deposition of PEDOT:PSS film, O_2 plasma was used to etch the openings in the third and second parylene C layers. 20 mL aqueous dispersion of PEDOT:PSS (PH 1000 from Clevios) was mixed with ethylene glycol (5 mL), dodecylbenzene sulfonic acid (DBSA, 50 μL), and 1 wt% of (3-glycidyloxypropyl)trimethoxysilane (GOPS), and the solution was spun-cast at 650 rpm for 30 s and prebaked at 95 °C for 1 min. Then, to define the PEDOT:PSS film on top of Au-pl or Au-nr electrode sites, the sacrificial parylene C layer was mechanically peeled off. Finally, the devices

were cured at 140 °C for 1 h and then immersed in DI water to remove any Micro-90 residue from the device surface.

b) Electro-deposited PEDOT:PSS-based electrodes: First, Au-pl and Au-nr macro/microarrays were fabricated following a similar procedure to that of spin-coated PEDOT:PSS devices up to PEDOT:PSS coating step. At the final step, PEDOT:PSS film was electro-deposited rather spun-cast. Prior to the PEDOT:PSS electro-deposition, 20 CV cycles were performed on all channels within -0.6 to 0.6 V vs. Ag/AgCl in PBS as an electrochemical cleaning step. Then PEDOT:PSS was electro-deposited from 10 mM EDOT in 2.0 g/100mL NaPSS aqueous dispersion (both were purchased from Sigma-Aldrich) under potentiostatic conditions at a potential of 0.9 V vs. Ag/AgCl in a three electrode set up, i.e., Ag/AgCl electrode as a reference electrode, a large platinum electrode as a counter electrode, and the target microarray/macrodot arrays as the working electrode, at a constant temperature of 27 °C using a GAMRY interface 1000E. Polymerization was driven for 20 second at or below current density of 0.5 mA/cm^2 resulting in ~220 nm thick PEDOT:PSS film deposition on the electrode sits.

6.2.2 Device Characterization

The SEM images were acquired using an FEI SFEG ultra high resolution SEM at 5 kV accelerating voltage. To perform Focused-ion-beam (FIB) slicing FEI Scios DualBeam FIB/SEM system was used. GAMRY interface 1000E was used to perform EIS in 0.01M phosphate buffered saline (×1 PBS) solution, using a three electrode configuration, i.e. PEDOT:PSS electrodes as the working electrode, Ag/AgCl electrode as a reference electrode, a large platinum electrode as a counter electrode. 10 mV RMS sinusoidal signal with zero DC bias were applied and the frequency was swept from 1 Hz to 10 kHz. The stress testing was performed in terms of cyclic voltammetry under low current density, near equilibrium conditions in (1×) PBS solution, with the tested

electrode potential swept cyclically within the potential windows of -0.6 to 0.6 V relative to the Ag/AgCl electrode at constant scan rate of 100 mV s^{-1} with 5 mV potential steps.

6.2.3 Accelerated Aging Experiment

Devices were stored in PBS at 60 ˚C with a regular one-week period to take out from the solution for EIS measurements and optical microscopic inspection using Zeiss Axio fluorescence microscope.

6.2.4 Animal Procedure

All experimental procedures were performed in accordance with the guidelines established by the UCSD Institutional Animal Care and Use Committee (IACUC). We used 2 adult mice on a C57BL/6 background. The procedure for craniotomy over the left barrel cortex and glass window implantation was modified from a previously described procedure[26]. Briefly, dexamethasone was injected before surgery to prevent brain swelling. Mice were anesthetized with Ketamine (100 mg/kg) and Xylazine (10 mg/kg), and a single dose of Buprenorphine (0.05 mg/kg) was applied. A 3-mm diameter craniotomy with the center coordinates of A-P 2 mm and L-R 3 mm (relative to bregma) was performed, and an aluminum headpost was mounted over the other (right) hemisphere. After bone removal, the electrode array was placed on the dura mater, and the glass window assembly (made of three 3-mm coverslips and one 5-mm coverslip bonded together with optical adhesive) was fit within the exposure on top of the array. Then, the circumference of the glass window was sealed with dental acrylic. A combination of Sulfatrim and Ibuprofen was given via drinking water from one day before until five days after surgery.

To visualize the vasculature via two-photon imaging, 100 ul of 5 % (w/v) Alexa Fluor 680-dextran in PBS was injected intravenously. Two-photon images were obtained using an Ultima two-photon laser scanning microscopy system from Bruker Fluorescence Microscopy equipped with an

Optical Parametric Oscillator tuned to 1360 nm (Chameleon Compact OPO, Coherent) that was pumped by a Ti:Sapphire laser at 790 nm.[27] Alexa Fluor 680 was imaged through a 20x water immersion objective (UMPLFLN20XW, Olympus); fluorescence was detected with a cooled GaAsP detector (Hamamatsu, H7422P-40).

For histology, animals received a Pentobarbital (200 mg/kg) overdose and were transcardially perfused with Heparin-PBS followed by 4% Paraformaldehyde in PBS. H&E staining and immunohistochemistry were performed on 5-um paraffin sections according to standard procedures at the Moores Cancer Center Histology Core at UCSD.

6.2.5 Statistical Analysis

To normalize the presented data in Figure 6 (aging results), each representative impedance value for the week of 1, 2, 3, 4 and 5 was normalized to its initial value as measured before initiating the aging experiment using Matlab software. Averaged data (mean) and the corresponding standard deviation (SD) are presented in the form of (mean ± SD) and sample size of (n). The fits for the extracted EIS electrochemical components were carried out using custom-made fitting algorithm using Matlab.

6.3 Results and Discussions

6.3.1 Au Nanorods (Au-nr) Vs. Planar Au (Au-pl) Electrodes

PEDOT:PSS electrodes were fabricated according to published procedures utilizing a thin film of Cr/Au layer with 15 nm/100 nm thickness as metallic leads and conductors. The entire device is sandwiched in between 2 μm upper and 2 μm lower parylene C layers except where the PEDOT:PSS film is coated.[1b, 14] The Au-nr layer was selectively patterned in regions where PEDOT:PSS was to be coated. To realize the Au-nr film, a de-alloying process of the AuAg alloy and preferential etching of Ag[12a] was performed in a nitric acid solution as detailed in the

experimental section. To benchmark the electrochemical performance of Au-nr and planar Au (Au-pl) contacts, we prepared electrodes with 50 µm and 500 µm[15] diameters, which we refer to as micro and macro hereafter. **Figure 6.1a** and **Figure 6.1b** show the optical images of the fabricated Au-nr and Au-pl macro electrodes with their corresponding cross-sectional schematics, respectively. The darker color of Au-nr electrodes under optical imaging distinguishes them from Au-pl contacts due to light trapping in the nanoporous structure. EIS was performed to characterize and understand the Au-nr and Au-pl electrochemical properties. Measured EIS within the frequency range of 1 Hz to 10 kHz are shown in **Figure 6.1c** and **6.1d** which demonstrate lower magnitude for the electrochemical impedance of the Au-nr electrode for the whole frequency range compared to that of Au-pl contact. For Au-nr electrodes and at frequencies higher than 300 Hz, the impedance becomes limited with the series resistance Rs as deduced from the negligible dependence on frequency beyond 300 Hz and a rapid increase of the phase from -90° to 0°. At these frequencies, the reactance due to the large double layer capacitance is lower than R_s. The lower capacitance and higher reactance of the Au-pl electrode delays such transition by one decade of frequency up to 3 kHz. Cyclic voltammetry (CV) is the standard practice to gain insights into the electrochemical reactions, presence of electro-active elements, and stability of the electrode.[1d] Measured CVs of Au-nr and Au-pl electrodes between potential limits of -0.6 V and 0.6 V, in phosphate buffered saline (PBS) at 100 mV/s, are depicted in **Figure 6.1e**. As expected, the Au-nr contact exhibited larger charge storage capacity (CSC) equal to 3.08 mC/cm^2 compared to that of the Au-pl electrode (1.4 mC/cm^2) due to the larger double-layer charging capacity at the electrode/electrolyte interface. Earlier works reported -0.6 to 0.8 V (in reference to Ag/AgCl) scan window as the safe potential limits or water limit for CV cycling of common metal electrodes such as Pt and Ir.[1d] However, we found out that this typical water window (-0.6 to 0.8 V vs. Ag/AgCl)

is not suitable for cycling the Au-nr electrodes due to the emergence of a significant oxidation peak at approximately 0.7 V vs. Ag/AgCl (**Figure 6.1f**). To avoid the oxidation current peak as a potential degrading factor in our PEDOT:PSS stability tests, we restricted the CV cycling window to -0.6 – 0.6 V vs. Ag/AgCl for all CV experiments performed in this work.

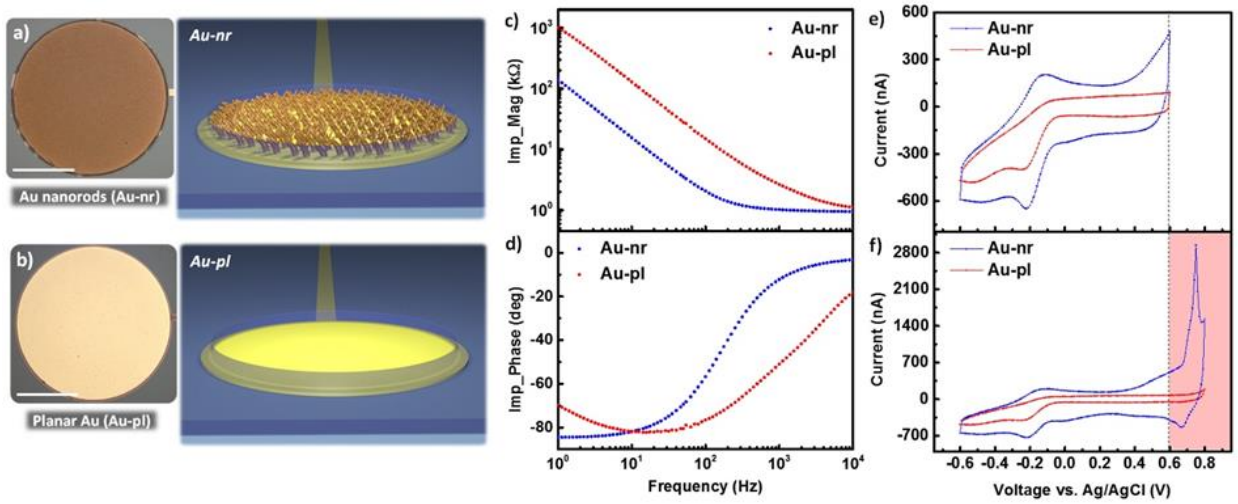

Figure 6.1 Au nanorods (Au-nr) vs. planar Au (Au-pl) electrodes: Top view optical image and corresponding cross-sectional schematic of (a) Au-nr and (b) Au-pl macro-electrodes with 500 µm diameter (scale bar, 200 µm). Measured (c) magnitude and (d) phase of the electrochemical impedance spectroscopy (EIS) of Au-nr (blue) and Au-pl (red) electrodes for the frequency range of 1 Hz to 10 kHz; showing enhanced electrochemical property of Au-nr compared to Au-pl electrode due to the larger interface capacitance (double-layer). (e) Measured cyclic voltammetry (CV) of Au-nr (blue) and Au-pl (red) electrodes within -0.6 to 0.6 V vs. Ag/AgCl potential limits; showing larger CV curve for Au-nr contact (larger CSC). (f) Measured cyclic voltammetry (CV) of Au-nr (blue) and Au-pl (red) electrodes within -0.6 to 0.8 V vs Ag/AgCl potential limits; demonstrating large oxidation current peak at around 0.7 V vs Ag/AgCl. Therefore, cycling potentials beyond 0.6 V (red colored regime) are excluded from stability tests to operate the electrodes within the safe electrochemical limits.

6.3.2 Structural and Morphological Characteristics of the PEDOT:PSS/Au-nr

Optical microscope pictures throughout the fabrication process are shown in **Figure 6.2**. For the fabrication of the PEDOT:PSS/Au-nr device, the AuAg alloy film was deposited selectively on electrode sites. A de-alloying step then follows to realize the Au-nr structures on sensing sites; sequence of metallic film definitions are shown in **Figure 6.2a**. Passivation layer deposition and

opening windows in parylene C above the electrode sites then follow and finally the micro-fabrication is completed with PEDOT:PSS deposition either through electro-deposition or spin-cast technique. Anisotropic conductive film (ACF) bonding was used to connect the device to commercial off the shelf ribbon cables that fit in the external characterization circuitry. The electrode arrays contain both macro and micro scaled electrodes which allowed us to investigate device stability for different diameters. In this stability study, only one macro size (D=500 μm) and micro size (D=50 μm) electrode were tested. The top view optical image of the patterned/de-alloyed Au-nr film on 50 μm diameter electrode is shown in **Figure 6.2c** along with an SEM image of Au-nr structure. After deposition of the parylene C passivation layer, openings on top of electrode sites were realized using oxygen plasma etching as shown in **Figure 6.2d** followed by PEDOT:PSS deposition using either spin-coating or electro-plating method. An optical microscope image of the spin coated PEDOT:PSS microelectrode using spin-cast processing is shown in **Figure 6.2e**. To confirm the structural integrity of the PEDOT:PSS/underlying Au-nr and Au substrate/parylene C interfaces, we performed focused-ion-beam (FIB) slicing at the center of the microdot of **Figure 6.2e**. The confinement of the PEDOT:PSS layer in the 3D Au-nr structure is demonstrated in the SEM image of Figure 2f highlighting the intimate contact between the different layers of the device.

The -0.6 to 0.6 V vs. Ag/AgCl CV cycling window discussed above was used to characterize the adhesion and mechanical stability of the PEDOT:PSS on Au-nr and Au-pl, at a scan rate of 0.1 V/s. The electrochemical impedance (1Hz – 10 kHz) and electrode surface alteration as determined by optical microscope imaging were monitored periodically during CV measurements to assess the adhesion and stability of the PEDOT:PSS coating on different underlying metal substrates. The PEDOT:PSS film was deposited potentiostatically on the Au-nr electrode with a 500 μm diameter.

Figure 3a shows the intact electrode prior to cycling, highlighting the uniform electrodeposited PEDOT:PSS film over the entire Au-nr electrode surface.

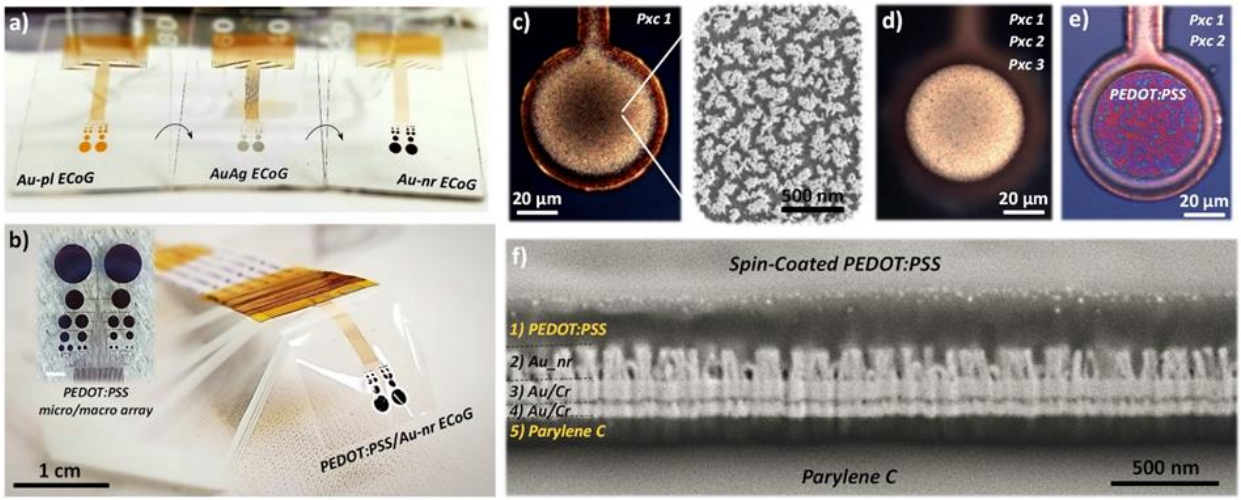

Figure 6.2 Structural and morphological characterization of the PEDOT:PSS/Au-nr electrophysiology device: (a) A picture of the neural probe on glass carrier substrate at different sequential steps of Cr/Au metallization, AuAg alloy deposition and Au-nr film formation using de-alloying technique, from left to the right, respectively. (b) A picture of the flexible/conformal PEDOT:PSS/Au-nr neural probe on parylene C released from glass substrate and bonded to ACF/ribbon cables to connect to the external characterization circuitry; the inset shows the macro/micro array layout including the 50 and 500 µm diameter electrodes assessed in this study (scale bar, 1mm). Fabrication flow of the 50 µm PEDOT:PSS/Au-nr electrode including (c) Au-nr adhesion layer definition on sensing site (adjacent top view SEM image shows morphology of the nano-structures of Au-nr film), (d) selective etching of the parylene C layers (abbreviated as pxc) on top of the metal contact and (e) deposition of the PEDOT:PSS layer using spin-coating/peeling-off technique. (f) Tilted view SEM image showing the cross-section of the stacked layers highlighting the intimate contact between the different layers of the device; sandwiched in between the parylene C and PEDOT:PSS films are the only electrochemical interfaces.

6.3.3 Stability Tests under Cycling Stress

Optical inspection of the same electrode of **Figure 6.3a** indicates the gradual change in the polymer color (colorimetric change) under CV stressing as shown in optical images of **Figure 6.3b**, **6.3c** and **6.3d** which correspond to 3,000, 7,000 and 11,000 CV cycles, respectively. This progressive color change can indicate over-oxidation of the PEDOT:PSS film which can occur during irreversible electrochemical oxidation reactions[10,16] rather than being related solely to the stability failure or detachment of the PEDOT:PSS coating. However, neither significant

delamination nor severe cuts across the electrode surface were observed over the entire cycling test period (over 10,000 cycles). To validate the stability of the interface and absence of delamination, we performed FIB slicing at the center of a reference macrodot that did not undergo any CV cycling (**Figure 6.3e**) and at the center of a macrodot shown in **Figure 6.3a-6.3d** after an 11,000 cycling tests (**Figure 6.3f**). The 45° tilted view SEM images indicate a slight thinning of the polymer thickness over the course of cycling/charge injection; nevertheless, the bulk of the PEDOT:PSS film was still retained within the 3-D nano-structure of the Au-nr conductor without any sign of delamination. The electrochemical impedance magnitude and phase of the PEDOT:PSS/Au-nr macro-electrode, as-fabricated and after being CV cycled for 1,000, 3,000, 5,000, 7,000, 10,000 and 11,000 cycles, are shown in **Figure 6.3g**. The measured EIS spectra were nearly identical for as-fabricated versus up to 10,000 CV cycles. A slight upward shift of the impedance traces below 40 Hz can be attributed to a slight decrease in the PEDOT:PSS thickness (color change in **Figure 6.3a-d** and additional transparency under electron beam on top of the Au-nr array in SEM **Figure 6.3e-f**) which reduces the capacitance and increases the electrode impedance. At and above 11,000 CV cycles, we observed an increase in the series resistance manifested by an up-shift of the impedance plateau at high frequencies as shown with the purple trace in **Figure 6.3g**. This result was counterintuitive because any morphological changes for the PEDOT:PSS, such as the thinning process illustrated in **Figure 6.3e** and **6.3f** should result in a change of the electrode capacitance or faradaic impedance. To investigate the origin of the increase in the series resistance, we inspected the overall device morphology and observed a partial dissolution of the Au metal lead as illustrated in the inset optical image of **Figure 6.3g**. This phenomenon of Au electrode dissolution was observed with multiple device experiments and is likely due to the local exposure of the Au surface during oxide formation/reduction as well as

oxygen evolution upon cycling voltammetry.[17] Therefore, to exclude the effect of metal lead dissolution from our PEDOT:PSS stability study, a maximum count of 10,000 CV cycles was set as the end point of the adhesion test protocol.

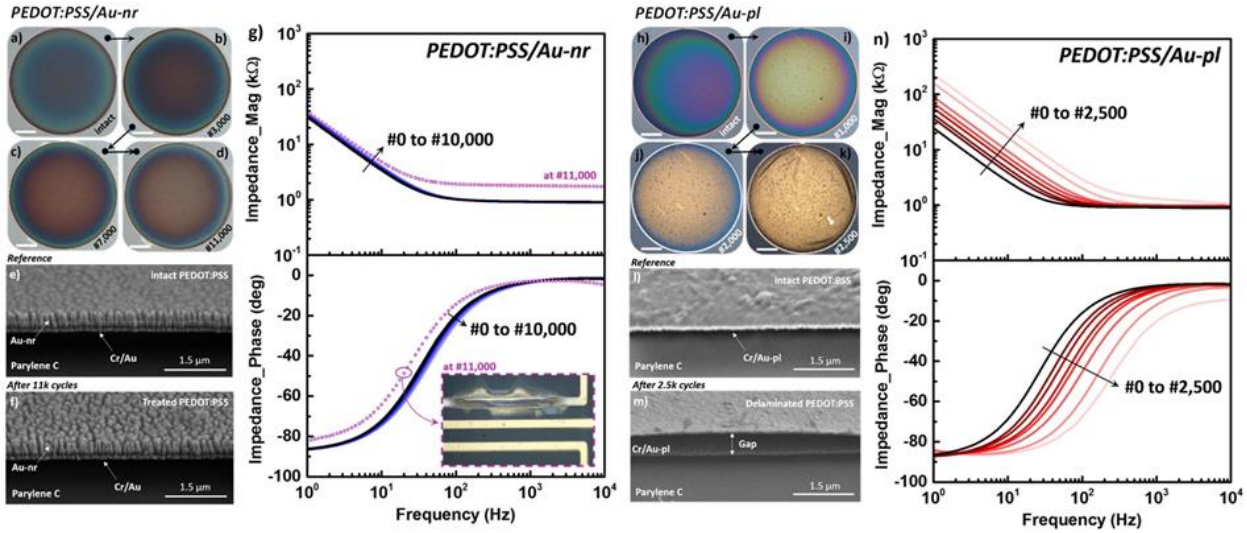

Figure 6.3 Electro-deposited PEDOT:PSS/Au-nr and PEDOT:PSS/Au-pl macro-electrode stability tests under cycling stress: Optical images of the same PEDOT:PSS/Au-nr macro dot (D= 500 µm) (a) as-fabricated and after sequential (b) 3,000, (c) 7,000 and (d) 11,000 CV cycles, highlighting the progressive colorimetric change of polymer coating (scale bar, 100 µm). (e) Tilted cross-sectional SEM images of the PEDOT:PSS coating on as fabricated Au-nr substrate. The PEDOT layer above the surface of the Au-nrs obstruct a clear view of the Au-nr tips. (f) Tilted cross-sectional SEM images of the PEDOT:PSS coating on Au-nr substrate after 11,000 cycles. The tips of the Au-nrs are sharper in (f) compared to (e) indicating slight thinning effect of cycling stress on polymer thickness while the bulk of the polymer film still is retained within the 3-D structure of the Au-nr film. (g) Impedance magnitude and phase spectra of the PEDOT:PSS coating on Au-nr substrate; as-deposited and CV cycled for 1,000, 3,000, 5,000, 7,000, 10,000 and 11,000 cycles, showing the nearly fixed EIS spectra up to 10,000 CV cycles. Significant electrochemical changes were measured (purple traces in EIS spectra) after 11,000 CV cycles at which metal leads failure was observed (inset). Optical images of the same PEDOT:PSS/Au-pl macro dot (D= 500 µm) (h) as-fabricated and after sequential (i) 1,000, (j) 2,000 and (k) 2,500 CV cycles, highlighting noticeable progressive colorimetric change of polymer coating under cycling stress (scale bar, 100 µm). Tilted view cross-sectional SEM images of PEDOT:PSS film on Au-pl substrate (l) as-deposited and (m) after 2,500 CV cycles, revealing a severe delamination of the PEDOT:PSS film from underlying metal substrate (indicated by the 'Gap'). (n) Impedance magnitude and phase spectra of the PEDOT:PSS coating on Au-pl substrate; as-deposited and after being CV cycled for 200, 500, 800, 1,200, 1,500, 2,000 and 2,500 cycles, showing noticeable impedance change, with an up to 10-fold (×10) increase in magnitude at 1 Hz after 2,500 CV cycles.

As a control experiment for the enhanced stability of PEDOT:PSS/Au-nr, PEDOT:PSS was also electro-deposited on planar Au conductors (PEDOT:PSS/Au-pl) with 500 µm diameter, as shown in **Figure 6.3h**. A similar color alteration of the polymer was observed across the PEDOT:PSS/Au-pl electrode surface over the course of cycling tests as shown in optical images **Figure 6.3i, j, k** after CV cycles of 1,000, 2,000 and 2,500 cycles, respectively. However, after

2,500 CV cycles PEDOT:PSS/Au-pl electrodes experienced a severe polymer film delamination near the electrode edge. For further examination, FIB slicing was performed on both a reference electrode that did not undergo CV cycling and the electrode of Figure 3k that underwent 2,500 CV cycles. The cross-section of the reference electrode in Figure 3l displayed an intact interface between the PEDOT and the underlying planar Au conductor. However, the cross-section of the 2,500 CV cycled electrode displayed a clear gap and detachment with the underlying Au conductor as shown in **Figure 6.3m**, and is in agreement with the wrinkled morphology observed in the optical image of **Figure 6.3k** that we associated with PEDOT delamination. Additionally, the electrode degradation under cyclic load for PEDOT:PSS/Au-nr is manifested in a progressive increase in the impedance magnitude and shift in impedance phase of **Figure 6.3n** with increasing cycling counts, in contrast to the nearly stable spectra of the PEDOT:PSS/Au-nr. The magnitude of the impedance at 1Hz increases by 10-fold after 2,500 CV cycles.

Another method for depositing PEDOT:PSS from solution is the spin-coating technique that offers monolithic integration and scalability benefits over electrodeposited PEDOT and has been recently used in high-density neural probe electrophysiology.[1b,11a,19] We characterized the stability of spin-cast PEDOT:PSS film on the 500 µm diameter conductor **Figure 6.4a** (see method section) in a similar experimental convention to electro-deposited PEDOT:PSS. **Figure 6.4b-6.4h** demonstrate a surface morphology change of the same PEDOT:PSS/Au-nr electrode at different CV cycles (up to 11,000 cycles). Similar to the electro-deposited PEDOT:PSS, progressive alteration of the PEDOT:PSS color was apparent under electrochemical stress by showing rapid changes during the first 3,000 cycles course (**Figure 6.4d**). It should be noted that after 7,000 cycles (**Figure 6.4f**), the contact interface between the PEDOT and the underlying Au-nr layer rearranges, presumably due to volumetric changes, resulting in strong color changes particularly

at the dot edges (see **Figure 6.4g-6.4h**). Despite the partial delamination of polymer coating, the magnitude and phase of the EIS spectra (**Figure 6.4l**) exhibit identical characteristics during the entire test period up to 10,000 CV cycles without noticeable electrochemical degradation, indicating a stable condition of spin-coated PEDOT:PSS/Au-nr macro-electrode under cycling stress. Similar to electro-deposited PEDOT:PSS/Au-nr contacts (**Figure 6.3g**), significant EIS change observed at or above 11,000 cycles, shown as purple traces in **Figure 6.4l**, were confirmed with inspection by optical microscope as the result of wiring failure rather than being related solely to the polymer stability. In contrast to the PEDOT:PSS/Au-nr electrode, the PEDOT:PSS/Au-pl contact (**Figure 6.4i**) showed delamination from the planar Au conductor starting from the electrode edges at only 500 CV cycles as shown in Figure 4j. PEDOT:PSS/Au-pl macro-electrode undergoes a full detachment from the substrate at 1,000 CV cycles (**Figure 6.4k**) as can also be observed with the noticeable impedance shifts in EIS spectra of **Figure 6.4m**. These results suggest at least 10-fold improvement in the adhesion of spin-coated PEDOT:PSS/Au-nr which endured 10,000 CV as discussed above. Electro-deposited PEDOT coating on Au-nr substrates (**Figure 6.3**) did show a slight EIS variation over the course of 10,000 CV cycles but no sign of film delamination from the substrate was observed. In contrast, spin-coated PEDOT film on Au-nr substrates (**Figure 6.4**) demonstrated partial film detachment due to cycling stress but fully stable electrochemical characteristics noted by measuring identical EIS spectra upon 10,000 CV cycles. From these experiments, we found that the adhesion of the PEDOT:PSS on Au-nr film is strongest with electro-deposition (**Figure 6.3a-f**) compared to spin-coating (**Figure 6.4a-h**). We also found that the electrodeposited PEDOT:PSS on Au-nr film underwent a slight thinning process that we associated with a slight reduction of the capacitance and increase in the impedance (**Figure 6.3g**). The fixed electrochemical impedance spectra for spin-cast PEDOT:PSS/Au-nr microelectrode

indicate absence of such thinning and stronger cohesive forces in the PEDOT film. We also found that the adhesion of electro-deposited PEDOT:PSS on planar Au conductors (**Figure 6.3h-k**) is stronger than that of spin-cast films (**Figure 6.4i-k**).

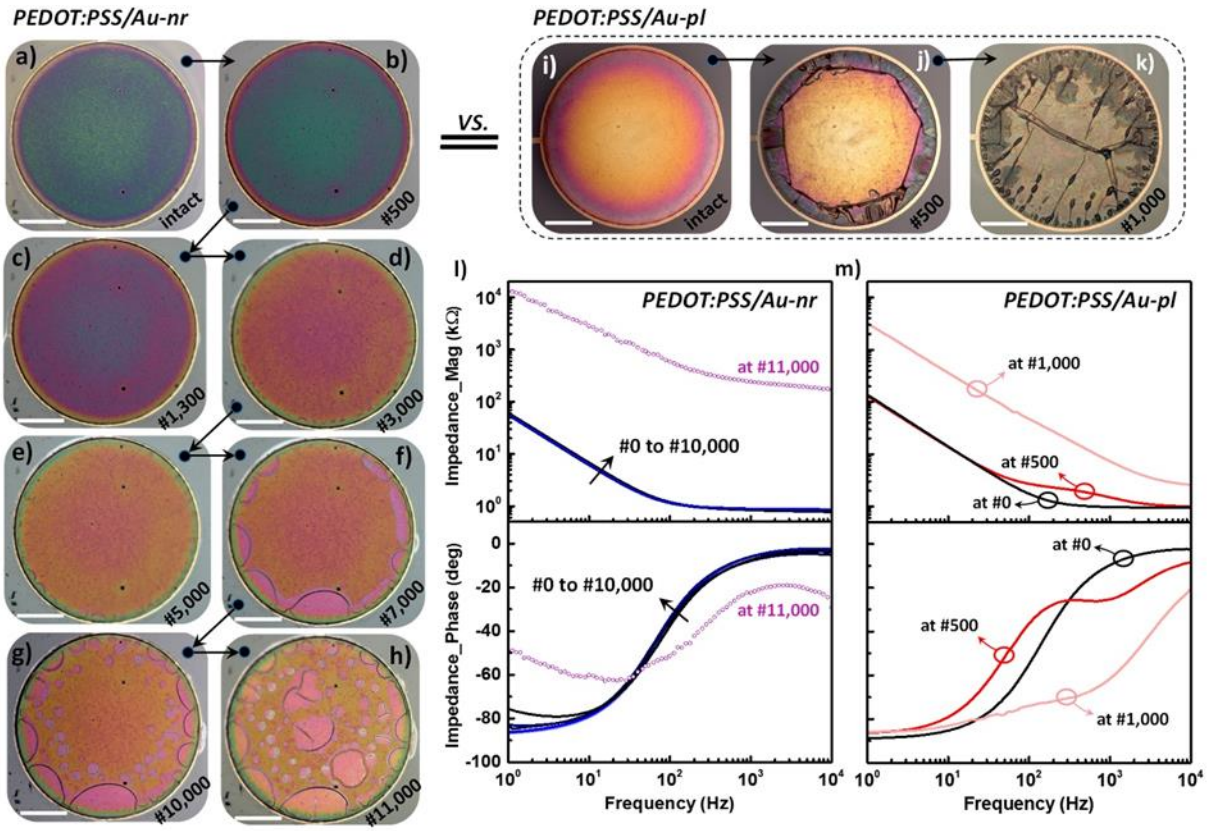

Figure 6.4 Spin- coated PEDOT:PSS/Au-nr and PEDOT:PSS/Au-pl macro-electrode stability tests under cycling stress: Optical images of the same spin-coated PEDOT:PSS/Au-nr macro dot (D= 500 µm) (a) as-fabricated and after sequential (b) 500 (c) 1,300 (d) 3,000 (e) 5,000 (f) 7,000 (g) 10,000 and (h) 11,000 CV cycles; highlighting the progressive colorimetric change of polymer coating along with partial PEDOT:PSS film delamination upon CV cycling, happens at or above 7,000 CV cycles. Optical images of the same spin-coated PEDOT:PSS/Au-pl macro dot (D= 500 µm) (i) as-fabricated and after sequential (j) 500 (k) 1,000 CV cycles demonstrating partial and complete PEDOT film delamination, respectively (scale bars are 125 µm). (l) The measured magnitude and phase impedance spectra of the PEDOT:PSS/Au-nr macro electrode at different cycling states; as-fabricated and CV cycled for 500, 1,300, 3,000, 5,000, 7,000, 10,000 and 11,000 cycles, which correspond to the left side optical images. The purple traces show the measured EIS spectra of electrode after 11,000 CV cycles, indicating a noticeable impedance change due to the wiring failure at that cycle count. (m) The measured magnitude and phase impedance spectra of the PEDOT:PSS/Au-pl macro-electrode as-fabricated (black) and CV cycled for 500 (dark-red) and 1,000 (light-red) cycles, demonstrating obvious impedance shifts due to the partial and complete PEDOT film delamination upon charge injection.

We have focused so far on large diameter (0.5mm) electrodes consistent with earlier studies on improving the adhesion strength and stability of PEDOT.[8, 10, 20] But microelectrodes are desired for advancing neurophysiological recordings both from the surface and the depth of brain tissue in a chronic setting.[11a, 21] Therefore, we evaluated the stability of PEDOT:PSS films on 50 µm

diameter Au-nr (**Figures 6.5a**) and Au-pl (**Figures 6.5i**) microelectrodes. For spin-cast PEDOT:PSS/Au-nr, the microelectrodes display an earlier onset of color change (>1000 cycles, **Figure 6.5c**) compared to the macroelectrodes (>3,000 cycles, **Figure 6.3c**). While this color change was notable but not dramatic for macroelectrodes (11,000 cycles, **Figure 6.3d**), a dramatic color change (>2,000 cycles, **Figure 6.5c-h**) and PEDOT delamination from the microelectrode edge (>5,000 cycles, **Figure 6.5e-h**) prevailed. Despite these morphological changes, the corresponding magnitude and phase of the EIS spectra measured after different CV cycling intervals (**Figure 6.5l**) did not indicate a significant electrochemical degradation of the electrode up to 8,000 cycles. However, at 9,000 CV cycles, a significant shift in EIS spectra was measured as illustrated with the purple traces in **Figure 6.5l**, which we attribute to wiring failure as we discussed above. On the other hand, PEDOT:PSS/Au-pl microelectrode exhibited a relatively compromised stability upon CV cycling that were evident from the ring-shape delamination in the optical images of **Figure 6.5j** and **6.5k** after only 400 and 800 CV cycles, respectively. In addition, significant electrochemical degradation is perceptible from the impedance magnitude and phase spectral shifts as shown in Figure 5m by dark-red (after 400 CV cycles) and light-red (after 800 CV cycles) traces. Nevertheless, the Au-nr anchoring layers also offer a stabilizing capability for microelectrodes by offering at least 10-fold enhanced durability for the PEDOT:PSS/Au-nr compared to PEDOT:PSS/Au-pl microelectrode. The mechanistic electrochemical studies discussed above elucidated the success of Au-nr conductors for stabilizing PEDOT:PSS under electrochemical stress. Another test that must be passed is the durability of the PEDOT:PSS in wet mediums that can be characterized with accelerated aging and in vivo experiments. We performed both types of experiments. Venkatraman and coworkers[20] have shown that PEDOT:PSS/Pt

macroelectrodes were stable after an accelerated aging test in PBS for 5 weeks whereas the microelectrodes experienced a significant degradation after four weeks.

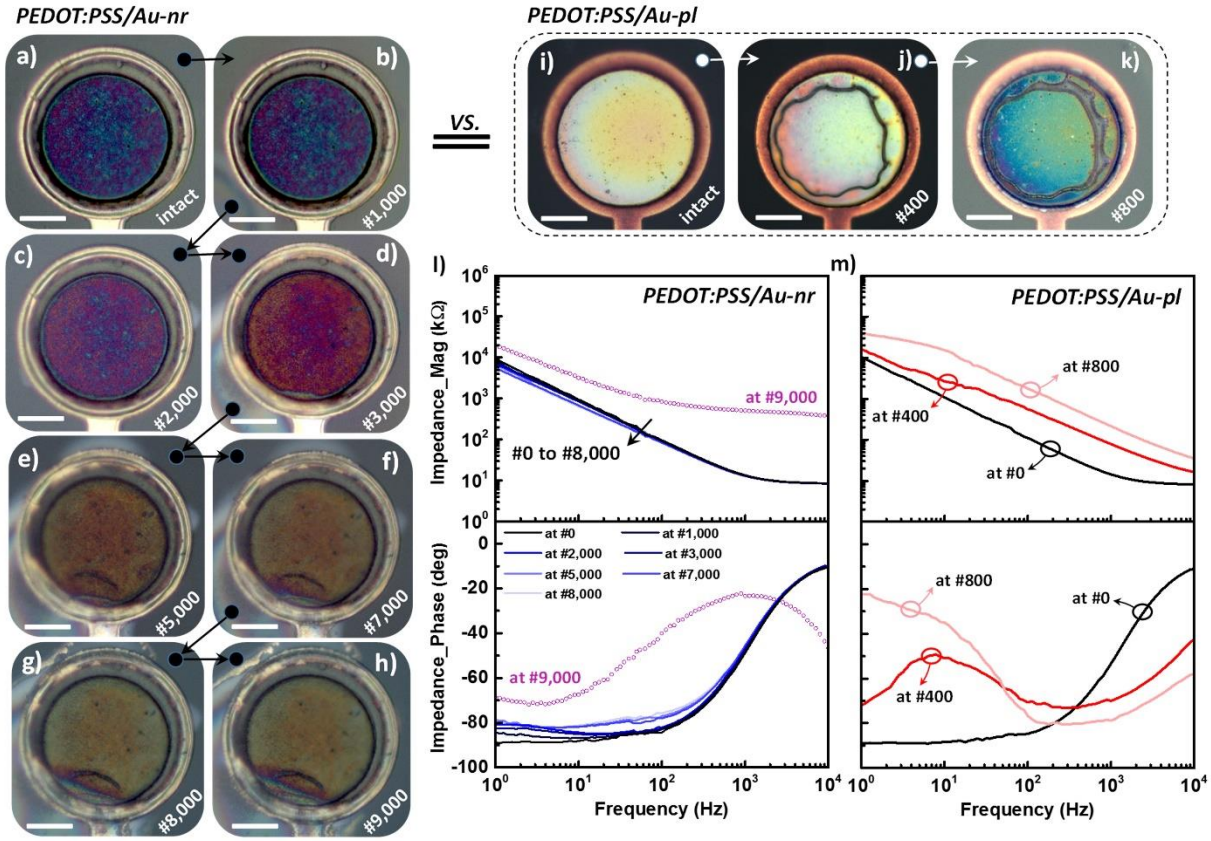

Figure 6.5 Spin-coated PEDOT:PSS/Au-nr and PEDOT:PSS/Au-pl microelectrode stability tests under cycling stress: Optical images of the same spin-coated PEDOT:PSS/Au-nr micro dot (D= 50 µm) (a) as-fabricated and after sequential (b) 1,000 (c) 2,000 (d) 3,000 (e) 5,000 (f) 7,000 (g) 8,000 and (h) 9,000 CV cycles, highlighting the progressive colorimetric change of polymer coating along with partial PEDOT:PSS film delamination upon CV cycling happens at or above 5,000 CV cycles. Optical images of the same spin-coated PEDOT:PSS/Au-pl micro dot (D= 50 µm) (i) as-fabricated and after sequential (j) 400 (k) 800 CV cycles demonstrating ring-shape PEDOT film delamination and its expansion, respectively (scale bars are 15 µm). (l) The measured magnitude and phase impedance spectra of the PEDOT:PSS/Au-nr microelectrode at different cycling states; as-fabricated and CV cycled for 1,000, 2,000, 3,000, 5,000, 7,000, 8,000 and 9,000 cycles, which correspond to the left side optical images. The purple traces show the measured EIS spectra of electrode after 9,000 CV cycles, indicating a noticeable impedance change due to the wiring failure at that cycle count. (m) The measured magnitude and phase impedance spectra of the PEDOT:PSS/Au-pl microelectrode as-fabricated (black) and after different cycling states of 400 (dark-red) and 800 (light-red) CV cycles, which demonstrate obvious impedance shifts due to the ring-shape PEDOT film delamination upon charge injection.

6.3.4 Accelerated Aging Stability Test

Given this and the interest in microelectrodes for electrophysiology applications, we performed accelerated aging experiments on microelectrode arrays with D=50µm that were prepared with spin-coated and electro-plated PEDOT:PSS on both Au-nr and Au-pl conductors (4 total devices). The four types of PEDOT:PSS devices were immersed into the PBS solution for 5 weeks at 60 °C. This temperature is recommended as a safe temperature for aging polymer films[13a,22] above which internal polymer film were reported to crack and exhibit unexpected effects that are beyond the scope of this study. Based on the Arrhenius Law, the equation (1) is used to estimate the simulated age upon accelerated aging temperature T. According to the ASTM international guidelines, the reference standard equation[20] provides an accelerated aging factor of 4.92 with respect to the body temperature (37 °C) resulting in equal simulated age of 25 weeks (~ 6 month chronic implants).

$$t_{37} = t_T \times 2^{(T-37)/10} \xrightarrow{@\ 60\ ^\circ C} t_{37} = t_{60} \times 2^{(60-37)/10} = 4.92 \times t_{60} \quad (1)$$

The results of the accelerating aging experiment are summarized in **Figure 6.6a** which shows the changes in the impedance magnitude normalized to values measured directly prior to aging for the four sets of PEDOT:PSS devices at three different frequencies of 10, 100 and 1,000 Hz. Each set of data in **Figure 6.6a** presents the average of normalized impedances of total channels per device type for PEDOT:PSS on (1) Au-nr spin-coated (Au-nr_SC, black), (2) Au-nr electro-deposited (Au-nr_ED, blue), (3) Au-pl spin-coated (Au-pl_SC, red) and (4) Au-pl electro-deposited (Au-pl_ED, green). Aging experiments were conducted with total functional channel counts of 25, 21, 26 and 23 per Au-nr_SC, Au-pl_SC, Au-nr_ED and Au-pl_ED PEDOT:PSS microelectrodes respectively as shown in **Figure 6.6b** (light blue columns). The average impedances (mean ± SD) at 1kHz for the Au-nr_SC, Au-pl_SC, Au-nr_ED and Au-pl_ED PEDOT:PSS microelectrodes were 13.05 ± 0.17 kΩ (n=21), 11.81 ± 1.13 kΩ (n=25), 9.72 ± 0.18

kΩ (n=26), and 9.58 ± 0.08 kΩ (n=23), respectively. We designated the microelectrode as nonfunctional if its 1 kHz impedance value exceeded a threshold impedance of 100 kΩ. The number of non-functional channels that exceeded the 100kΩ threshold are also plotted in **Figure 6.6b** as a function of aging time. The overall trends of impedance changes over the course of 5 weeks of accelerated aging indicate a stable impedance for the electro-deposited PEDOT:PSS on the Au-nr conductors (**Figure 6.6a**) with 2 non-functional channels out of 26 (92% survival, **Figure 6.6b**). The spin-cast PEDOT:PSS on Au-pl conductors degraded significantly where the impedances increased by over 18X (**Figure 6.6a**) and 19 channels became non-functional out of 25 (24% survival) after 5 weeks of accelerated aging time. The absence of covalent bonds at the interface of PEDOT/underlying metal deems the interface unstable in extended presence in wet media. The delamination behaviors are manifested in either partial or complete detachment from the Au-pl surface under accelerated aging as demonstrated in Figure 6c. In agreement with CV results, the Au-nr structure supported enhanced adhesion and mechanical stability for both spin-cast and electro-deposited PEDOT:PSS.

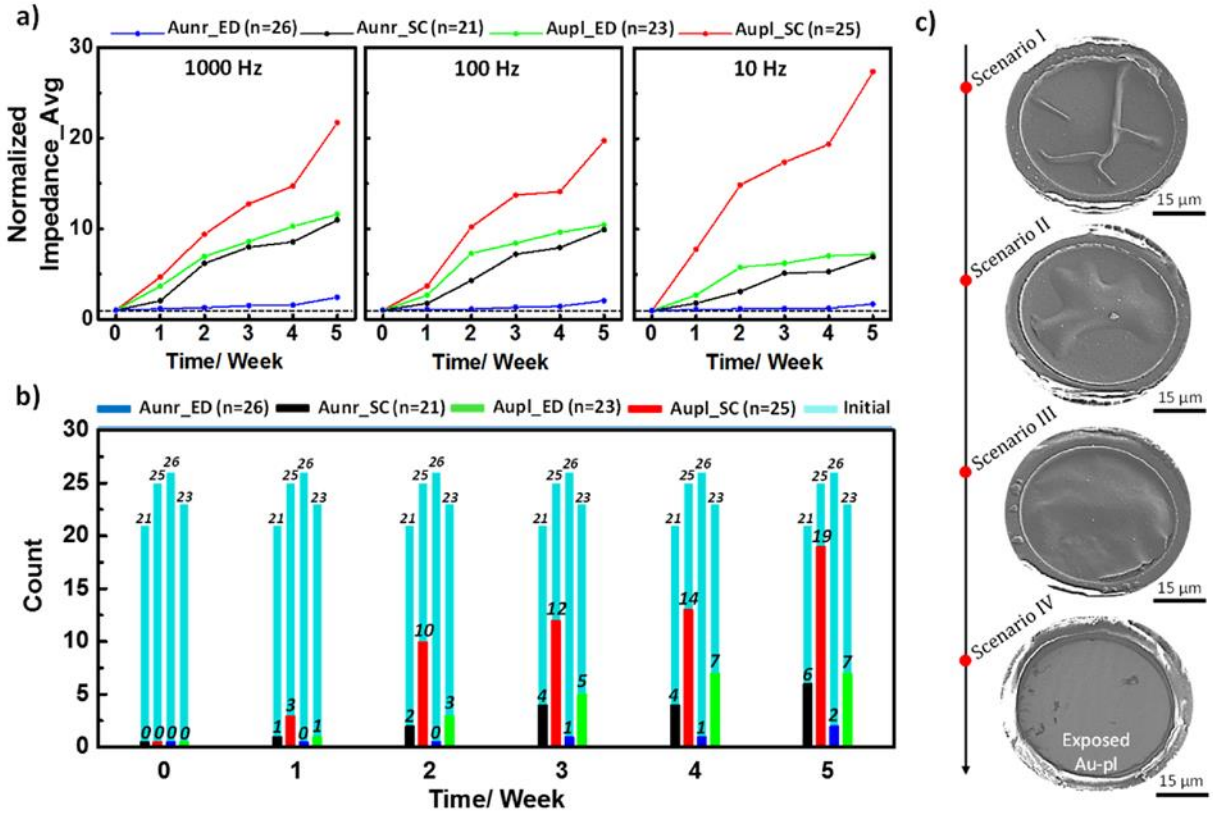

Figure 6.6 Accelerated aging results for spin-coated (SC) and electro-deposited (ED) PEDOT:PSS microelectrodes with Au-nr and Au-pl substrates: a) Normalized impedance average of different PEDOT:PSS-based microelectrodes; (1) spin-coated on Au-nr (Au-nr_SC, black), (2) electro-deposited on Au-nr (Au-nr_ED, blue), (3) spin-coated on Au-pl (Au-pl_SC, red) and (4) electro-deposited on Au-pl (Au-pl_ED, green), at 1000, 100 and 10 Hz frequencies as a function of accelerated aging period in BPB at 60 Co. b) Numbers of "non-functional" channels per device type; defined upon exceeding threshold impedance of 100 kΩ by microelectrodes 1kHz impedance value, as a function of accelerated aging period. Black, red, blue and green colors correspond to the Au-nr_SC, Au-pl_SC, Au-nr_ED and Au-pl_ED PEDOT:PSS based microelectrodes, respectively. The light-blue histograms present the total numbers of functional channels per device type at the beginning of the aging experiment. c) Different delamination behaviors of spin-coated PEDOT:PSS film ranging from partial delamination (Scenario I or II) to a full delamination (Scenario III) and detachment (Scenario IV) from the Au-pl substrate.

6.3.5 *In Vivo* Chronic Implant Stability Test

In different studies, PEDOT:PSS coating has been deployed as an electrode material where the electrodes were chronically implanted for electrophysiological recordings over the course of a month.[20,23] In most cases, the impedance of the electrodes increased significantly after the first week of implant due to either adverse effects of tissue inflammatory response on the electrode or

possible degradation of the PEDOT:PSS coating upon implant. In these studies, the quality, morphology, and adhesion/stability of the electrodes have not been reported. For spin-coated PEDOT:PSS electrodes, only two studies have reported the implantation of this type of electrodes with their corresponding stable and long-term action potential recording from the surface of the cortex for an implant period of less than 10 days.[11a,11b] The long term stability of the spin-coated PEDOT:PSS film was not reported. To translate our success in stabilizing PEDOT:PSS in benchtop electrochemical experiments to in vivo, we chronically implanted two sets of PEDOT microelectrodes including spin-cast (i) PEDOT:PSS/Au-nr and (ii) PEDOT:PSS/Au-pl onto mouse cerebral cortex for 10 weeks. For implantation, a craniotomy surgery was performed involving removal of the bone overlaying the barrel cortex while leaving the dura mater intact. The array was placed on top of the dura and covered with a glass "window" (**Figure 6.7a**). The window served a double purpose; first, it replaced the bone, second, it allowed visualizing the integrity of the brain tissue, including imaging of blood flow using single- and 2-photon microscopy (**Figure 6.7b**). After the implantation, the mouse was returned to its home cage and allowed to move freely in the cage for 10 weeks. After device explanation, FIB slicing and SEM Imaging were performed on the PEDOT arrays to examine the electrode morphology. **Figure 6.7c** demonstrates the tilted view SEM image of a explanted PEDOT:PSS/Au-nr microelectrode showing overall stable mechanical condition for spin-cast PEDOT film. To examine the PEDOT/metal interface, a FIB cut was performed at the electrode edge. The following cross-sectional SEM image at the FIB cut, shown in **Figure 6.7d**, reveals a tight confinement of PEDOT film within the 3D structure of the Au-nr film, preventing polymer film delamination. In contrast, conventional PEDOT:PSS film on Au-pl electrodes experienced significant morphological changes illustrated with either partial or full polymer delamination, as shown in SEM images of

the **Figure 6.7e** and Figure **6.7g** respectively. To verify the partial and full PEDOT film delamination on Au-pl electrodes, FIB cuts were performed at the electrodes edge. Cross-sectional SEM image, shown in **Figure 6.7f**, demonstrates retained (intact) polymer film on Au-pl substrate while PEDOT film delaminated at another electrode side as highlighted in **Figure 6.7e** by white dashed line. FIB cut also was performed at an electrode edge shown in **Figure 6.7g** which showed absence of PEDOT film as the worst PEDOT stability case. The Au-pl substrate exposure was perceptible upon continuous extension of metal substrate underneath parylene C passivation layer, shown in cross-sectional SEM image of **Figure 6.7h**. Indeed, full exposure of Au-pl underlying substrate indicates a PEDOT:PSS film delamination from the Au-pl substrate after the 10-week chronic implant. It should be noted that similar morphological changes or delamination of spin-coated PEDOT film from Au-pl substrate (**Figure 6.6c, 6.7e** and **6.7g**), observed in both in vivo and soaking tests, could correlate their degradation mechanism on polymer film.

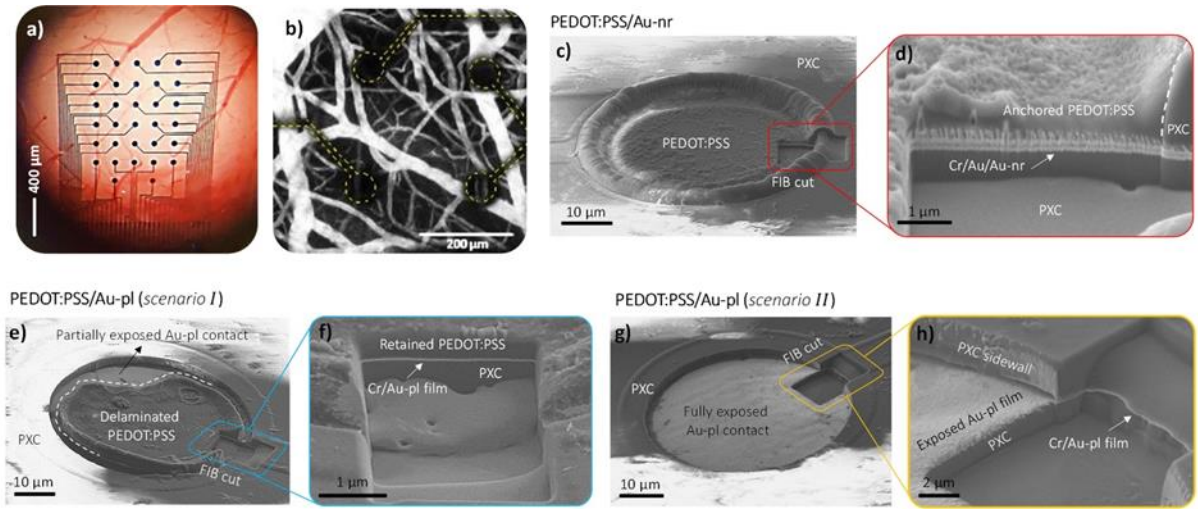

Figure 6.7 *In vivo* stability results after 10 weeks chronic implants for spin-coated PEDOT:PSS on Au-nr and Au-pl microelectrodes (D=50 µm): (a) Top view image of the chronically implanted PEDOT array on the mouse brain with a glass coverslip on top. (b) Maximum intensity projection of Alexa 680-Dextran labeled blood plasma below the PEDOT:PSS/Au-nr array (individual electrodes outlined with dashed yellow lines). Image shows vasculature up to 300 µm below the cortical surface. Data were acquired with 2-photon microscopy 9.5 weeks after implantation. (c) Tilted view (50 degree) SEM image of the explanted PEDOT:PSS/Au-nr microelectrode with sliced FIB cut, highlighted by red box. (d) Cross-sectional SEM image at the FIB cut section, showing a fully anchored PEDOT:PSS film within 3-D structure of Au-nr film. (e) Tilted view (50 degree) SEM image of the explanted PEDOT:PSS/Au-pl microelectrode (scenario I); sliced FIB cut is highlighted by blue box. Boundary of partially delaminated PEDOT:PSS and underlying Au-pl substrate is signified by white dashed line for ease of illustration. (f) Cross-sectional SEM image at the FIB cut section, showing the PEDOT:PSS/Au-pl film interface where PEDOT film is still attached on Au-pl substrate. (g) Tilted view (50 degree) SEM image of the explanted PEDOT:PSS/Au-pl microelectrode (scenario II), showing fully exposed Au-pl underlying substrate as the result of polymer delamination; sliced FIB cut is highlighted by yellow box. Extension of the Au-pl substrate underneath the parylene C passivation layer, shown in (h) cross-sectional SEM image at the FIB cut section, indicating fully delamination of the PEDOT:PSS film from Au-pl substrate upon chronic implant.

6.3.6 Post Implant Histological Analysis of Mouse Brain

Finally, to assess potentially aversive biological responses such as tissue inflammation beneath the implanted electrodes, we performed a histological evaluation 10 weeks after implantation. Therefore, hematoxylin and eosin (H&E) staining as well as immunohistochemical staining with antibodies that label neurons (NeuN), astrocytes (GFAP), and microglia (IBA1) were performed on brain slices. An overview of the H&E staining is shown in **Figure 6.8a**, including

an enlarged view of the cortex; location of the implantation site on the left hemisphere as well as the contralateral site (right hemisphere, no implant) for control, are highlighted. **Figure 6.8b** shows representative stainings of neurons, astrocytes and microglia of the (left) cortex underneath the implant and the contralateral (right) side. The staining with NeuN did not reveal any changes in neuronal density beneath the implant. In comparison to the contralateral hemisphere, the antibody staining of GFAP and IBA1 showed a 40-45% or 18-20% increase of astrocyte and microglia density, respectively. However, astrocyte and microglia densities are known to increase after craniotomy[24], therefore, they may not indicate a tissue reaction to the implant itself, but to the implantation procedure, in particular the craniotomy.

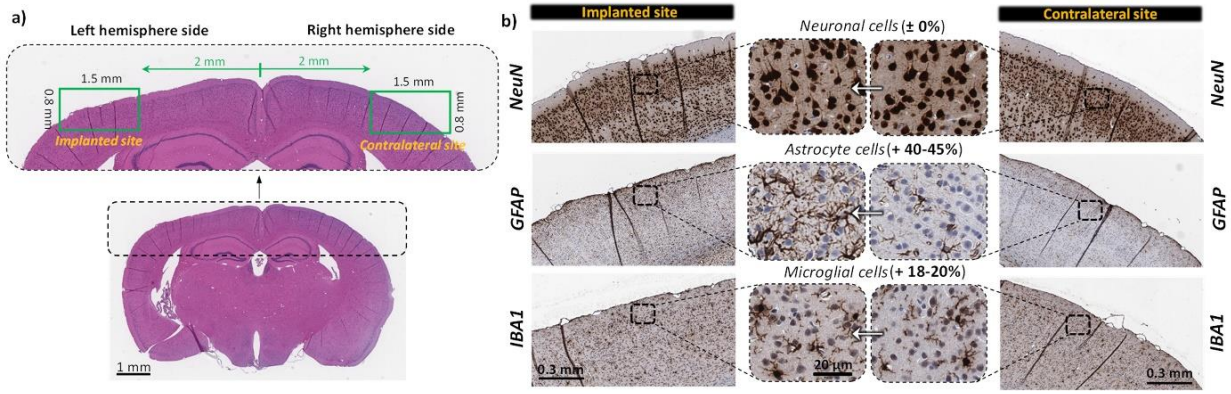

Figure 6.8 Histological analysis of mouse brain from an animal implanted with a PEDOT:PSS/Au-nr microelectrode array. The array was left for 10 weeks after implantation before tissue analysis was performed. (a) Image of a tissue section after hematoxylin/eosin (H&E) staining. Top, enlarged image of the cerebral cortex; the barrel cortex below the implant (implanted site, left green box) and the contralateral site (right green box), which serves as control, are highlighted. b) Magnified views of immunohistochemical staining of implanted and contralateral site (as indicated by green boxes in panel a) with NeuN antibodies to detect neurons (top), GFAP antibodies to detect astrocytes (middle), and IBA1 antibodies to detect microglia (bottom).

6.4 Conclusion

The biological applications of PEDOT:PSS materials are rapidly accelerating for in vitro diagnostics [11a, 25] and for in vivo electrophysiology [1b, 1c, 11a]. The adhesion and mechanical stability of PEDOT:PSS electrophysiology devices is imperative for their transition for chronic implants

and for neural stimulation. In this study, we introduced the fabrication and integration of the Au nanorod film (Au-nr) with standard PEDOT:PSS neural probe fabrication on flexible parylene C substrates to improve its adhesion and stability. By providing larger interface area and serving as a mechanical anchor for the PEDOT:PSS layers, an Au-nr adhesion layer improved the stability of the PEDOT:PSS based electrodes (both spin-casted and electro-deposited PEDOT:PSS devices), under both active CV stressing and passive accelerated aging experiments, contingent on polymer coating thicknesses studied in this work. The Au-nr adhesion layer demonstrated 10 fold stability improvement of PEDOT:PSS based electrodes compared to that of Au-pl substrates under CV stress for both macro and micro-scaled electrodes. Furthermore, 92% of electro-deposited PEDOT:PSS electrodes remained electro-actively functional after 5 weeks of accelerated aging experiments that is equivalent to ~ 6 month chronic implants. The adhesion-promoting effect of Au-nr film was verified under in vivo conditions where the PEDOT film was stabilized within the 3D structure of Au-nr film whereas coated polymer on Au-pl electrodes delaminated after a 10-week chronic implant. The adhesion improvement strategy reported here might also benefit other CP neural interface materials for chronic implants or neural stimulation applications where the long-term stability of the CP film is critical.

Chapter 6, in full, is a reprint of material as it appears in the following publication: M. Ganji, L. Hossain, A. Tanaka, M. Thunemann, E. Halgren, V. Gilja, A. Devor, S. A. Dayeh, "Monolithic and Scalable Au Nanorod Substrates Improve PEDOT–Metal Adhesion and Stability in Neural Electrodes," Advanced healthcare materials, vol. 7, p. 1800923, 2018. The dissertation author was the primary investigator and author of this material.

6.5 References

[1] a) R. Green, M. R. Abidian, *Advanced Materials* **2015**, 27, 7620; b) M. Ganji, E. Kaestner, J. Hermiz, N. Rogers, A. Tanaka, D. Cleary, S. H. Lee, J. Snider, M. Halgren, G. R. Cosgrove, *Advanced Functional Materials* **2018**, 28; c) J. Rivnay, S. Inal, A. Salleo, R. M. Owens, M. Berggren, G. G. Malliaras, *Nature Reviews Materials* **2018**, 3, 17086; d) S. F. Cogan, *Annu. Rev. Biomed. Eng.* **2008**, 10, 275; e) X. Cui, D. C. Martin, *Sensors and Actuators B: Chemical* **2003**, 89, 92.

[2] a) M. Ganji, S. Dayeh, presented at Meeting Abstracts **2017**; b) M. Ganji, A. Tanaka, V. Gilja, E. Halgren, S. A. Dayeh, *Advanced Functional Materials* **2017**, 27.

[3] a) S. G. Im, P. J. Yoo, P. T. Hammond, K. K. Gleason, *Advanced Materials* **2007**, 19, 2863; b) X. T. Cui, D. D. Zhou, *IEEE Transactions on Neural Systems and Rehabilitation Engineering* **2007**, 15, 502; c) R. Gerwig, K. Fuchsberger, B. Schroeppel, G. S. Link, G. Heusel, U. Kraushaar, W. Schuhmann, A. Stett, M. Stelzle, *Frontiers in neuroengineering* **2012**, 5, 8; d) E. M. Thaning, M. L. Asplund, T. A. Nyberg, O. W. Inganäs, H. von Holst, *Journal of Biomedical Materials Research Part B: Applied Biomaterials* **2010**, 93, 407; e) D. J. Ham, J. S. Lee, *Energies* **2009**, 2, 873.

[4] X. Chen, K.-Z. Xing, O. Inganäs, *Chemistry of materials* **1996**, 8, 2439.

[5] a) C.-K. Cho, W.-J. Hwang, K. Eun, S.-H. Choa, S.-I. Na, H.-K. Kim, *Solar Energy Materials and Solar Cells* **2011**, 95, 3269; b) R. A. Green, R. T. Hassarati, L. Bouchinet, C. S. Lee, G. L. Cheong, F. Y. Jin, C. W. Dodds, G. J. Suaning, L. A. Poole-Warren, N. H. Lovell, *Biomaterials* **2012**, 33, 5875; c) R. A. Green, N. H. Lovell, G. G. Wallace, L. A. Poole-Warren, *Biomaterials* **2008**, 29, 3393.

[6] X. Luo, C. L. Weaver, D. D. Zhou, R. Greenberg, X. T. Cui, *Biomaterials* **2011**, 32, 5551.

[7] B. Wei, J. Liu, L. Ouyang, C.-C. Kuo, D. C. Martin, *ACS applied materials & interfaces* **2015**, 7, 15388.

[8] L. Ouyang, B. Wei, C.-c. Kuo, S. Pathak, B. Farrell, D. C. Martin, *Science advances* **2017**, 3, e1600448.

[9] X. Cui, D. C. Martin, *Sensors and Actuators A: Physical* **2003**, 103, 384.

[10] C. Boehler, F. Oberueber, S. Schlabach, T. Stieglitz, M. Asplund, *ACS applied materials & interfaces* **2016**, 9, 189.

[11] a) D. Khodagholy, J. N. Gelinas, T. Thesen, W. Doyle, O. Devinsky, G. G. Malliaras, G. Buzsáki, *Nature neuroscience* **2015**, 18, 310; b) D. Khodagholy, J. N. Gelinas, G. Buzsáki, *Science* **2017**, 358, 369; c) J. Hermiz, N. Rogers, E. Kaestner, M. Ganji, D. Cleary, J. Snider, D. Barba, S. Dayeh, E. Halgren, V. Gilja, presented at Engineering in Medicine and Biology Society (EMBC), 2016 IEEE 38th Annual International Conference of the **2016**.

[12] a) J. Erlebacher, M. J. Aziz, A. Karma, N. Dimitrov, K. Sieradzki, *Nature* **2001**, 410, 450; b) E. Seker, Y. Berdichevsky, M. R. Begley, M. L. Reed, K. J. Staley, M. L. Yarmush, *Nanotechnology* **2010**, 21, 125504.

[13] a) J. Scheirs, *Compositional and failure analysis of polymers: a practical approach*, John Wiley & Sons, **2000**; b) T. Otero, I. Boyano, *The Journal of Physical Chemistry B* **2003**, 107, 6730; c) J. Heinze, B. A. Frontana-Uribe, S. Ludwigs, *Chemical Reviews* **2010**, 110, 4724.

[14] I. Uguz, M. Ganji, A. Hama, A. Tanaka, S. Inal, A. Youssef, R. M. Owens, P. P. Quilichini, A. Ghestem, C. Bernard, *Advanced healthcare materials* **2016**, 5, 3094.

[15] M. Ganji, A. T. Elthakeb, A. Tanaka, V. Gilja, E. Halgren, S. A. Dayeh, *Advanced Functional Materials* **2017**, 27.

[16] a) A. Giovannitti, K. J. Thorley, C. B. Nielsen, J. Li, M. J. Donahue, G. G. Malliaras, J. Rivnay, I. McCulloch, *Advanced Functional Materials* **2018**, 28, 1706325; b) B.-w. Park, L. Yang, E. M. Johansson, N. Vlachopoulos, A. Chams, C. Perruchot, M. Jouini, G. Boschloo, A. Hagfeldt, *The Journal of Physical Chemistry C* **2013**, 117, 22484.

[17] S. Cherevko, A. A. Topalov, A. R. Zeradjanin, I. Katsounaros, K. J. Mayrhofer, *Rsc Advances* **2013**, 3, 16516.

[18] K. Tybrandt, D. Khodagholy, B. Dielacher, F. Stauffer, A. F. Renz, G. Buzsáki, J. Vörös, *Advanced Materials* **2018**, 30, 1706520.

[19] J. Hermiz, N. Rogers, E. Kaestner, M. Ganji, D. R. Cleary, B. Carter, D. Barba, S. Dayeh, E. Halgren, V. Gilja, *NeuroImage* **2018**.

[20] S. Venkatraman, J. Hendricks, Z. A. King, A. J. Sereno, S. Richardson-Burns, D. Martin, J. M. Carmena, *IEEE Transactions on Neural Systems and Rehabilitation Engineering* **2011**, 19, 307.

[21] a) G. Malliaras, M. R. Abidian, *Advanced Materials* **2015**, 27, 7492; b) G. Buzsáki, *Nature neuroscience* **2004**, 7, 446.

[22] B. Rubehn, T. Stieglitz, *Biomaterials* **2010**, 31, 3449.

[23] a) T. D. Kozai, K. Catt, Z. Du, K. Na, O. Srivannavit, R.-U. Haque, J. Seymour, K. D. Wise, E. Yoon, X. T. Cui, *IEEE Trans. Biomed. Engineering* **2016**, 63, 111; b) T. D. Y. Kozai, N. B. Langhals, P. R. Patel, X. Deng, H. Zhang, K. L. Smith, J. Lahann, N. A. Kotov, D. R. Kipke, *Nature materials* **2012**, 11, 1065; c) K. A. Ludwig, J. D. Uram, J. Yang, D. C. Martin, D. R. Kipke, *Journal of neural engineering* **2006**, 3, 59; d) P. R. Patel, H. Zhang, M. T. Robbins, J. B. Nofar, S. P. Marshall, M. J. Kobylarek, T. D. Kozai, N. A. Kotov, C. A. Chestek, *Journal of neural engineering* **2016**, 13, 066002; e) K. A. Ludwig,

N. B. Langhals, M. D. Joseph, S. M. Richardson-Burns, J. L. Hendricks, D. R. Kipke, *Journal of neural engineering* **2011**, 8, 014001; f) A. Schander, H. Stemmann, E. Tolstosheeva, R. Roese, V. Biefeld, L. Kempen, A. Kreiter, W. Lang, *Sensors and Actuators A: Physical* **2016**, 247, 125.

[24] a) P. J. Drew, A. Y. Shih, J. D. Driscoll, P. M. Knutsen, P. Blinder, D. Davalos, K. Akassoglou, P. S. Tsai, D. Kleinfeld, *Nature methods* **2010**, 7, 981; b) R. D. Dorand, D. S. Barkauskas, T. A. Evans, A. Petrosiute, A. Y. Huang, *Intravital* **2014**, 3, e29728; c) D. Guo, J. Zou, N. Rensing, M. Wong, *PloS one* **2017**, 12, e0170005.

[25] a) F. Pires, Q. Ferreira, C. A. Rodrigues, J. Morgado, F. C. Ferreira, *Biochimica et Biophysica Acta (BBA)-General Subjects* **2015**, 1850, 1158; b) M. Sessolo, D. Khodagholy, J. Rivnay, F. Maddalena, M. Gleyzes, E. Steidl, B. Buisson, G. G. Malliaras, *Advanced Materials* **2013**, 25, 2135; c) J. Pas, C. Pitsalidis, D. A. Koutsouras, P. P. Quilichini, F. Santoro, B. Cui, L. Gallais, R. P. O'Connor, G. G. Malliaras, R. M. Owens, *Advanced Biosystems* **2018**, 2, 1700164.

[26] G. J. Goldey, D. K. Roumis, L. L. Glickfeld, A. M. Kerlin, R. C. Reid, V. Bonin, D. P. Schafer, M. L. Andermann, *Nature protocols* **2014**, 9, 2515.

[27] D. Kobat, M. E. Durst, N. Nishimura, A. W. Wong, C. B. Schaffer, C. Xu, *Opt Express* **2009**, 17, 13354.

Chapter 7

Selective Formation of Porous Pt Nanorods for Highly Electrochemically Efficient Neural Electrode Interfaces

7.1 Introduction

The unique physical properties of nanostructured materials led to enhanced electrochemical activity for a variety of applications for energy harvesting,[1] generation[2] and storage.[3] One-dimensional (1D) nanostructures are particularly attractive because they can offer large surface area, enhanced electric fields at their tips,[4] and the emergence of high-index crystalline facets at their circumference[5] which cumulatively facilitate electrochemical interactions. We utilize selective dealloying to develop 1D platinum nanorod arrays that are vertically aligned on top of metal leads in a process that is compatible with thin flexible films. We show that these PtNRs exhibit very low electrochemical impedances and high charge injection capacities at various length scales, are biocompatible, stable, scalable and suitable for efficient neurotechnologies. We utilize PtNR microelectrodes to demonstrate recording of brain activity with cellular resolution from the cortical surfaces in birds and monkeys. Significantly, strong modulation of surface recorded single unit activity by auditory stimuli is demonstrated in European Starling birds and of local field potentials from the visual cortex by light stimuli from monkeys. These developments pave the way for high fidelity and less invasive brain-machine interfaces and

could propel devices that operate on the principle of highly efficient electrochemical catalytic processes.

1D nanowire structures have been utilized in measuring intracellular activity from individual cells,[6-9] and the extracellular activity from in vitro cultured tissue[10] as well as in-vivo from intact retinal[11] and brain tissue.[12] Their incorporation into microelectrode arrays for the large-scale recording and stimulation of electrophysiological activity can significantly advance the performance of these devices compared to planar counterparts which are the gold standard in clinical practice. However, 1D nanostructures are mostly formed by vapor phase techniques that require high temperatures[13, 14] which are incompatible with flexible substrates. Solution growth methods are readily available to form 1D nanostructures[15] but their applicability to Platinum, the most known biocompatible material that is widely used in clinical practice, is yet to be demonstrated. 1D Pt nanostructures have been grown by electrochemical deposition in polycarbonate (PC) membranes,[16] in anodized aluminum oxide pores,[17] or dealloying of Pt containing metal compounds that usually resulted in PtNi,[18-20] PtAu,[21] or PtCo,[20,22] used mainly for fuel cell applications. But electrochemical methods do not lead to crystalline nanostructures nor to strong bonding to underlying metal leads (due to incorporation of electrochemical surfactants in the nanorods and at the nanorod-underlying electrode pad) and thus have weak physical strength similar to Pt-black. They are also problematic due to toxic ligand additives, metal elements and/or isotopes.

In this work, we report the fabrication of pure Pt nanorods (PtNRs) on thin and flexible parylene C substrates. This approach results in fabrication of nanostructured Pt film with outstanding electrochemical, mechanical properties, realized by selective chemical dissolution of Ag from PtAg alloy, without involving electrochemical surfactant nor cytotoxic ligands. We utilize

low-temperature selective dealloying to develop scalable and biocompatible 1D platinum nanorod (PtNR) arrays that exhibit superb electrochemical properties at various length scales for efficient neurotechnologies. PtNR arrays record brain activity with cellular resolution from the cortical surfaces in birds, mice, and non-human primates. Significantly, strong modulation of surface recorded single unit activity by auditory stimuli is demonstrated in European Starling birds, modulation of local field potentials in the visual cortex by light stimuli in a non-human primate, and as well as responses to electrical stimulation in mice. The ability of PtNRs to record behaviorally and physiologically relevant neuronal dynamics from the surface of the brain with high spectrotemporal resolution pave the way for less invasive brain-machine interfaces.

7.2 Experimental Details

7.2.1 Device Fabrication

The fabrication of the PEDOT:PSS and Pt devices is similar to previously established protocols [27-29]. For PtNRs, glass slides (Specialty Glass Products Inc.) or silicon wafers were used as substrate carriers for the thin parylene C layers. The substrates were first solvent cleaned by rinsing with acetone/isopropanol (IPA)/deionized (DI) water/IPA, then were subjected to ultrasonic agitation in IPA for 5 min, and were rinsed again with acetone/IPA/DI water/IPA. Diluted Micro-90 (0.1%), an anti-adhesion layer, was spun-cast at 1500 rpm on the substrate to facilitate the separation of the device after the device fabrication completed. A first parylene C layer (≈1.9–2.5 μm) was deposited by chemical vapor deposition using a PDS 2010 Parylene coater system. Metal lead patterns were defined and exposed using a Karl Suss MA6 mask aligner using NR9-3000 negative resist. Temescal BJD 1800 electron beam evaporator was used for the deposition of 15 nm Cr adhesion layer and 100 nm Au contact layer, and a lift-off process in acetone followed. Then patterns of the electrode sites were defined using NR9-6000 negative resist

and a Karl Suss MA6 mask aligner for exposure. A 15 nm/100 nm Cr/Pt layer was sputtered followed by deposition of ~0.5 μm thick AuAg alloy using a co-sputtering technique performed at 400 W (RF) and 50 W (DC) powers for co-deposition of Ag and Pt, respectively. A lift-off process in acetone followed shortly after. To realize PtNR film on electrode sites, de-alloying was performed in Nitric acid at 60 °C for 2 min. O2 plasma (Oxford Plasmalab 80 RIE) was then applied for 2 min (150 W RF power) to activate the surface of parylene C for enhancing the adhesion of the subsequent encapsulating parylene C layer. A layer of ≈ 1.9–2.5 μm parylene C was then deposited and followed by coating another Micro 90 anti-adhesion layer. This time, a slightly higher concentrated Micro-90 (1% as opposed to 0.1% for the first layer) was spun-cast at 650 rpm for 10 s on this second parylene C layer for ease of separation of the subsequent layers. A third parylene-C layer was then deposited to serve as a protector film for passivation layer during etching the electrode sites opening. Then a thick 2010 SU-8 photoresist was spun-cast and patterned, which was exposed and developed with SU-8 developer. O_2 plasma was used to etch the openings in the third and second parylene C layers. The third parylene C layer was then mechanically peeled off in all regions, resulting in exposure of fresh passivation layer (2nd PXC layer) and PtNR contacts as only interface materials. Finally, the devices were immersed in DI water, to remove any Micro-90 residue from the PtNRs and parylene C surface, where bonding to anisotropic conductive film (ACF) and commercial off the shelf ribbon cables, for external circuitry connection, completed the fabrication of PtNR electrophysiology devices.

7.2.2 Device Characterization

The devices were imaged using Axioscope Optical microscope and FEI SFEG ultra high-resolution SEM at 10 kV accelerating voltage. To reduce electron charging in the specimen, a 15 nm thick Ti layer was deposited on the back of the device and was electrically connected to the

stage of the system providing a runaway path for impinging electrons. To obtain the TEM images, focused ion beam (FIB) was used to create cross-sectional slices the microelectrodes. To prevent the sample from the damage by ion beam during the FIB milling process, the fabricated device is deposited with 1μm SiNx by Trion Orion III chemical vapor deposition (CVD) system. After that, the sample was coated with a 30nm Pt layer by e-beam evaporation to reduce the charging under electron and ion beams. The TEM sample lamellae was prepared with FIB (FEI Nova 600). The FIB and in-situ lift-off (INLO) process utilized here follow conventional procedures, in which a 30keV Ga beam was used for rough milling and reduced voltage (10keV) was used for fine milling. TEM characterization was carried out using a FEI Tecnai G(2) F30 S-Twin 300kV transmission electron microscope, equipped with Fischione Instruments high angle annular dark field (HAADF) and EDAX ECON energy-dispersion x-ray (EDX) detectors under scanning TEM (STEM) mode. Those experiments were performed at the Center for Integrated Nanotechnologies at Sandia National Laboratories.

EIS was performed using a GAMRY interface 1000E in 0.01 M phosphate buffer saline (×1 PBS) solution, using three electrodes configuration, i.e., Ag/AgCl electrode as a reference electrode, a large platinum electrode as a counter electrode, and the target micro/macrodot arrays as the working electrode. Sinusoidal signals with 10 mV RMS AC voltage and zero DC bias were applied and the frequency was swept from 1 Hz to 10 kHz. The cyclic voltammetry was performed under low current density, near equilibrium conditions in (1×) PBS solution, whereas tested electrode potential was swept cyclically between potential limits of -0.6 to 0.8 V vs. Ag/AgCl at constant scan rate of 200 mV s^{-1} with 10 mV potential steps. The CSCC and CSCA were calculated by time integral of the cathodal and anodal current density over a potential range of water electrolysis window for each material. To calculate the charge injection capacity, cathodal-first,

biphasic, charge-balanced current pulse were injected across working electrode and counter electrode while measuring working electrode's polarization potential with respect to Ag/AgCl reference electrode. The maximum cathodal excursion potential (E_{mc}) and anodal excursion potential (E_{ma}) were calculated as electrode potential versus Ag/AgCl (reference electrode) 10 μs after cathodal and anodal pulses ended. This period of interpulse delay is used to account for the voltage drop across the electrolyte and metal lead series resistance, resulting in an absolute polarized potential across electrode/electrolyte interface versus Ag/AgCl. Charge injection capacity was calculated as the injected charge (by multiplying stimulation current and pulse width) at which either E_{mc} reaches water reduction potential (cathodal limit) and/or E_{ma} reaches water oxidation potential (anodal limit). Water window limits are considered between −0.6 to 0.8 V for metallic electrodes (Pt and PtNR) and −0.9 to 0.6 V for organic electrodes (PEDOT:PSS), with respect to Ag/AgCl reference electrode. To maintain different inter-pulse potential (E_{ipp}) bias for each electrode materials, a net current flowed across the electrode/electrolyte interface with minute current magnitude (typically <10 nA) even for millimeter scale electrodes.

7.2.3 Electrophysiology Methods, Acquisition:

Bird Surgical Details and Recording Methods:

Preparatory surgeries were conducted either the day before or the day of electrophysiological recording. Animals were anesthetized with isoflurane (Baxter Healthcare). The birds were head-fixed in a stereotaxic device, and the scalp was dissected along the midline. A custom-built, metallic fixation pin was then attached to the caudal part of the bird's skull with dental cement.

On the days of recordings, an animal was anesthetized with 20% urethane (60–100 μl total; Sigma, St. Louis, MO) administered into the pectoral muscle in 20- to 30-μl aliquots at 30-min

intervals. The bird was placed in a sound-attenuating chamber, and its head was immobilized via the head-fixation pin.

These experiments were performed on two adult European starling song birds and two zebra finsh under a protocol approved by the Institutional Animal Care and Use Committee of the University of California, San Diego. A craniotomy and duratomy was performed over HVC following stereotaxic coordinates. The window was centered at 2.5mm lateral and was large enough to fit the surface micro-ECoG array. The hippocampus on top of HVC was removed by suction. To ensure intimate contact between the surface array and tissue, cerebral spinal fluid was removed from the surface of the brain by suction. The surface array was then placed on top of the brain using a micromanipulator (Narishige MO-10), and the depth probe was slowly lowered into the brain through one of the two via holes. Both hemispheres of the brain were used; whenever the brain tissue was visibly damaged by the procedure, the site was not further used for the experiment. Electrophysiological recordings from both the surface array and depth probe were performed simultaneously with the same data acquisition system, Intan RHD2000 from Intan Technologies (Los Angeles, CA). The Intan RHD2000 USB Controller was connected to a RHD2116 or RHD2132 headstage that was connected to the depth probe; a separate RHD2164 headstage was connected to a surface probe. The following adapter boards were used to connect the probe to the Intan headstage: a custom Flex Adapter31 for the surface probe and a Plexon (Dallas, TX) N2T A32-HST/32V adapter for the depth probe. Recordings were sampled at either 20kHz or 30kHz and data was acquired using either the Open Ephys GUI 32 or RHD2000 software provided by Intan. Default Intan filter settings were used with cutoffs set at 0.01 Hz and 7.5 kHz for data acquisition.

Stimuli were played using software written in Python, running on a single board computer (SBC) (Beaglebone Black). Synchronization with the recording system and later identification of the metadata of the stimuli was achieved by digital trigger pins and/or messages passed using the ZMQ library between the SBC and the Open Ephys recording software. To enable high precision of stimulus onset detection in the recordings, the stimuli were stereo, with one channel containing a 1-5 kHz waveform that was recorded by the Intan system at the same sampling rate as the neural data. (The software is available on: https://github.com/zekearneodo/ephysflow/tree/master/rig_tools) Spike sorting and clustering were performed using KiloSort software. Clusters then sorted into three groups, namely single unit (SUA), multi-unit (MUA), and 'noise', based on their refractory period. Clusters with little to no spikes 0 to 2ms from the previous spike considered single unit. Clusters contain many spikes with refractory period of less than 2ms considered multi-unit.

NHP Surgical Details and Recording Methods:

Experimental procedures on rhesus macaques were carried out according to the Guide to the Care and Use of Laboratory Animals. All efforts were made to minimize discomfort, and the Institutional Animal Care and Use Committee at the Massachusetts General Hospital monitored care and approved all procedures.

Intraoperative, intracranial neurophysiology recordings were acquired from two adult male rhesus macaques (Macaca mulatta, ages 11 and 14). Macaques were placed under general endotracheal anesthesia (isoflurane) and placed into a stereotactic frame (Kopf; Kujunga, CA). Craniotomies over the visual cortex were performed using standard anatomic landmarks, and cortex was carefully exposed. Using gyral anatomy and vasculature over V1 versus V4 (Figure 4), V1 and V4 areas were identified visually, and PtNR electrodes were placed over each region.

Signals were recorded using the ORH128 Intan Recording System as described previously30, similar to what was used in gathering the starling data. The data was acquired at 30 KHz and filtered by default Intan setting with cutoffs 0.01 Hz to 7.5 kHz. The majority of the data was acquired using OpenEphys acquisition graphic-user interface software31 (http://www.open-ephys.org/), with the impedance tests of the electrodes during the experiments carried out using the Intan RHD2000 software from Intan Technologies (Los Angeles, CA). Data was extracted and processed using MATLAB (Mathworks, Natick, MA).

For visual evoked potential experiments, an LED array comprised of white LEDs (Cree; Durham, NC) was placed over each closed eye and secured in place. A general anesthetic regimen of propofol and fentanyl was used briefly to facilitate the recording of visual evoked potentials. 20 or 40 ms full-field flashes at 1 Hz were delivered via TTL and computer-controlled software (LabView, National Instruments).

For electrical stimulation experiments, a monopolar platinum iridium microelectrode (10 KΩ, tip diameter: 2-3 um; PI2PT30.01A10; Microprobes Inc., Gaithersburg, MD) was affixed to a stereotaxic arm (Narishige; Amityville, NY) and lowered to the cortical surface under visual guidance, using an operating microscope. Pulses of varying amplitudes, frequency, and duration were subsequently applied. Electrical stimulation was delivered using a STG 2008 Multichannel Stimulator (Multi Channel Systems MCS GmbH, Reutlingen, Germany).

Mouse Surgical Details and Recording Methods:

The care and use of mice (2-6 months old; C57BL/6J; Jackson Laboratory, Bar Harbor, ME) followed all federal and institutional guidelines, and the Institutional Animal Care and Use Committees of the Massachusetts General Hospital. Mice were deeply anaesthetized with a cocktail of ketamine hydrochloride (100 mg/kg intraperitoneal injection) and xylazine (10 mg/kg

i.p. injection) prior to the start of surgery. Additional ketamine (1/10 initial dose) was supplemented every 30 min to maintain the plane of anesthesia.

Anesthetized mice were placed into a stereotaxic frame (Narishige, Japan) for the craniotomy as well as all subsequent testing. A heating blanket on the floor of the frame was used to maintain body temperature at 37°C. A craniotomy was performed on 4.5 mm x 4.5 mm area around the primary visual cortex (V1) defined by a stereotaxic coordinate33 (AP: -3.8, ML: -2 mm). After the skull was removed, the PtNR array was placed over the exposed visual cortex. Once the PtNR array was positioned on V1, neural signals were recorded using the ORH128 Intan Recording System. Similar to the recordings in NHPs, data was acquired at 30 KHz and filtered by the default Intan setting (cutoffs 0.01 Hz to 7.5 kHz). Data was extracted and processed using MATLAB.

In addition to the stereotaxic coordinate, the location of the array on the V1 was confirmed again by measuring visually-evoked potentials using full-field visual stimulation. Visual stimulation was presented from a monitor (HP ZR22w, Hewlett Packard, USA) placed 25 cm from the mouse with a viewing angle of 45° from the center of the monitor (toward the right eye of the mouse). The stimulus was delivered at least 30 times and the recording data from each trial were averaged. After confirming the array location, a monopolar stimulating electrode (10 KΩ; PI2PT30.01A10; Microprobes) was inserted into the visual cortex through the hole in the center of the PtNR array (Fig. S10d). Electrical stimulation consisted of a 200 µs, 10-30 µA cathodic first biphasic current pulse with no inter-phase-interval (i.e. 1 pulse was delivered every 3 seconds). Each electric stimulus was delivered 20 times and the recording data across trials were averaged.

7.2.5 Analysis and Statistical Methods

The spike waveforms are extracted from single unit clusters in Kilosort. The red waveforms are averages of 20 uniformly sampled spike snippets. The black scales on lower right of each waveforms indicates 50 μV amplitude. The interspike intervals (ISI) is the time between succeeding spikes of a neuron. The ISI histogram of spike waveforms shown in these figures indicate the distribution of the log of ISI which can be a visual tool to track violation of refractory period and differentiate single cells from multi-unit. Besides extracting waveforms from clusters, we can examine their quality and whether they are related to real neural cells or noise. One way to conduct this test is to monitor cell activity in response to stimulus with repeated trails. If a single unit response shows any stimulus locking property, this can be an indication of an isolated neuron. Figure 3e is an example of a recorded cell from surface of the brain with a stimulus locking response over 30 trails. The first row shows the spectrogram of 28 second bird own song stimulus. To create this spectrogram, bird song is converted to spectrograms by use of the MATLAB spectrogram function with parameters nfft=128, and Hanning window of nfft with 50% overlap. It contains 65 frequency bands in range 0-10KHz. Second row shows an example of one channel (Ch1) raw data in blue. The raw data contains both low and high frequency information. The green wave underneath is the high pass filtered (>300Hz) raw data and contains spikes. In the bottom the 30 trails average and raster plot of spike trains in response to 30 song trails have been shown. On the spectrogram plot, logarithm of power spectrum density (PSD) averaged over 65 frequency bands of spectrogram is shown in black. Underneath in black, average of 65 frequency bands of PSD is calculated for 5s stimulus. Local field potential recordings from non-human primates were extracted into MATLAB decimated to 1000 Hz. Voltage responses were averaged across trials of light flashes or pulses or trains of electrical stimulation.

7.3 Results and Discussions

7.3.1 Structural, Morphological and Electrochemical Characterization of PtNR Microelectrodes

We developed a method for fabrication of pure Pt nanorods (PtNRs) using selective chemical dissolution of Ag from a co-sputtered PtAg alloy on thin and flexible parylene C substrates (**Figure 7.1a-c**). The selective dissolution of metal alloys is known to result in nanoporous structures[22] and is optimized here (**Figure 7.2**) to result in 1D PtNRs as shown in the cross-sectional Transmission Electron Microscopy (TEM) images taken at the center of a PtNR microelectrode (**Figure 7.1d**). The height of the PtNRs can be adjusted with the deposition time of the co-sputtered PtAg alloy (**Figure 7.3**) and is chosen to be 300-400nm for this work; a height that is sufficient to provide both high electrochemical performance and mechanical stability. The high resolution TEM (HRTEM) images show that the PtNR is polycrystalline and porous (**Figure 7.1e**). The 1D porous structure (**Figure 7.1e**) provides large surface area and the sharp corners of atomic steps at grain interfaces (**Figure 7.1f**) lead to large dipoles that enhance electrochemical coupling and reactions. The fabrication process for incorporating the nanorods onto planar underlying metal leads is described in the Methods section and Supplementary Information (**Figure 7.4**).

The optical microscope images of several microelectrodes (**Figure 7.1b** and **Figure 7.1c**) and the scanning electron microscope (SEM) images indicate uniform distribution of the PtNRs across a single microelectrode (**Figure 7.1g**). The PtNRs are beveled below the passivating parylene C layer at about 2μm below the surface as shown in the cross-sectional SEM (**Figure 7.1h**) and tilted view SEM image (**Figure 7.1i**). This architecture significantly reduces the potential of PtNR damage due to shear forces that will be otherwise present if the PtNRs were to be fabricated on the device surface. The thin film fabrication process is of high-yield and uniformity, embodied in overlapping electrochemical impedance spectroscopy (EIS, **Figure 7.1j**),

cyclic voltammetry (CV, **Figure 7.1k**), and voltage transients (VTs, **Figure 7.1l**) spectra across 32 microelectrodes in an example device (**Figure 7.1b**). To demonstrate the biocompatibility and mechanical stability of PtNRs in vivo, we implanted the device in the mouse cortex (Methods section) for a period of 42 days followed by immunohistological staining (**Figure 7.5**) and examination of the explanted device by SEM (**Figure 7.1m**, **Figure 7.6**). Near normal neuronal and glial morphology and staining patterns were seen for implanted and contralateral non-implanted sites in two mice (**Figure 7.5**). Several PtNR microcontacts were further sectioned by focused ion beam (FIB) and their cross-section (**Figure 7.1n**, **Figure 7.6**) and showed intact PtNRs underneath the adsorbed tissue that remained on the microelectrode surface after explant. A higher magnification SEM image (**Figure 7.1o**) shows PtNR array morphology similar to that before implant (**Figure 7.1h-i**). Additionally, the compatibility of different sterilization techniques (Autoclave, ethylene oxide (ETO), STERRAD) with PtNR electrodes was validated (**Figure 7.8**). Over 90% of the microelectrodes were functional with a slightly increased impedance magnitude after sterilization but no morphological changes were observed, contrasting results we obtained on PEDOT:PSS with STERRAD sterilization.[23] These results demonstrate that PtNRs are biocompatible, robust and suitable for clinical translation.

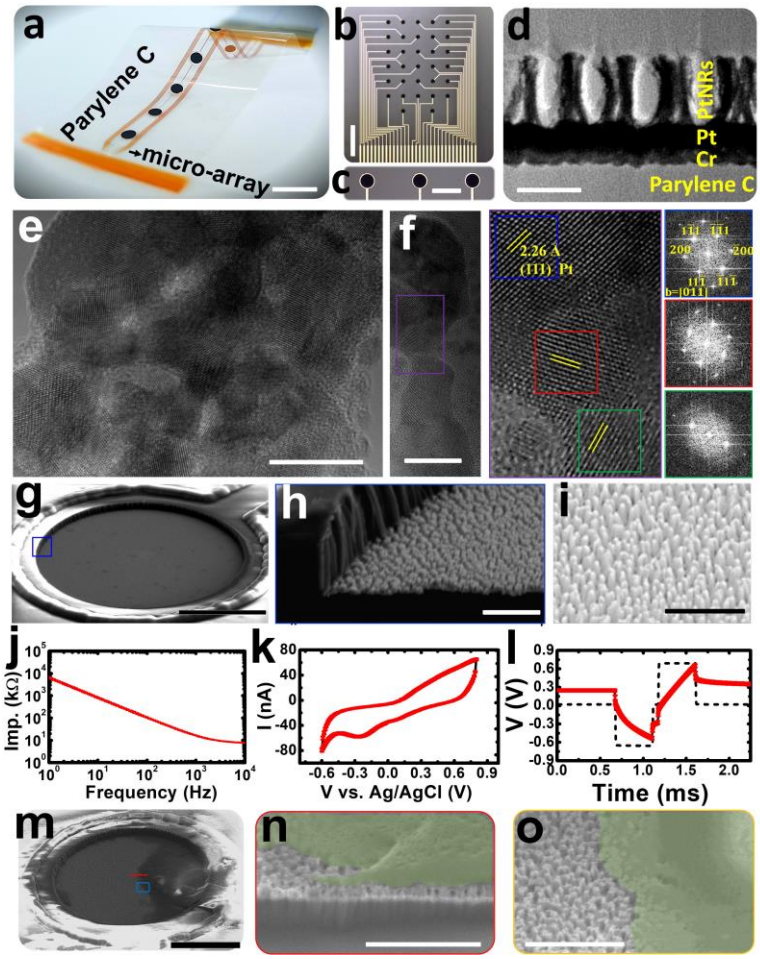

Figure 7.1 Structural, morphological and electrochemical characterization of PtNR microelectrodes: a) A picture of the fabricated electrophysiology PtNR device on thin film parylene C layer, showing the location of the PtNR microarray with 56 microelectrodes and 6 macro REF electrodes. Top view optical images of b) PtNR array with 32 microelectrodes and c) zoom-in images of 3 PtNR microelectrodes (D=50 µm). d) TEM image at the center of PtNR micro-electrode, showing the cross-section of the stacked layers highlighting intimate contact between the different layers of the device. High-resolution TEM image at the center (e) and tip (f) of PtNR showing porous polycrystalline structure. Inset is fast Fourier transform (FFT) of the crystal planes showing multiple rotated spots indicative of the polycrystalline nature of the PtNR. g-i) Tilted view SEM image of PtNR microelectrode (g) and cross-section (h) in the region highlighted with the black box in (g), and a zoom-in at the array center in (i). Average (black) and standard deviation (red) of measured electrochemical spectra for j) impedance, k) CV and l) voltage transients (injected bi-phasic current pulse I=5µA, PW=400µs) from 32 PtNR microelectrodes of the same device. m) Top view SEM image of one explanted PtNR microelectrode, showing partial coverage with biological tissue. n) Cross-sectional SEM image along red line in (m). o) tilted view zoom-in SEM image at the blue box in (m). Both (n) and (o) show similar PtNR morphology below tissue (n) and next to tissue (o). Scale markers are for a) 10 mm, b) 400 µm, c) 100 µm, d) 300 nm, e,f) 10 nm, g) 20 µm, h,i) 2 µm, m) 15 µm, n) 2 µm, o) 1 µm.

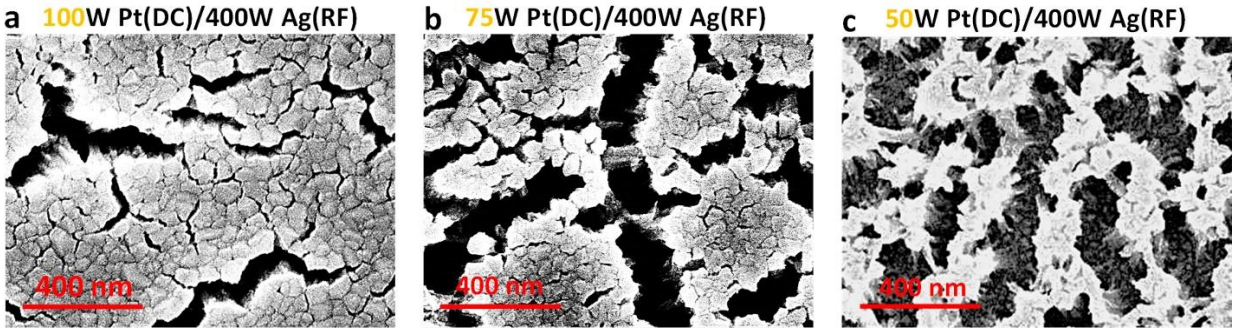

Figure 7.2 Structural optimization of PtNRs: SEM images of different nanostructured Pt films after chemical etching (de-alloying) using different Pt to Ag concentration ratios of a) 100W/ 400W b) 75W/ 400W and c) 50W/ 400W, resulting in different morphological characteristics.

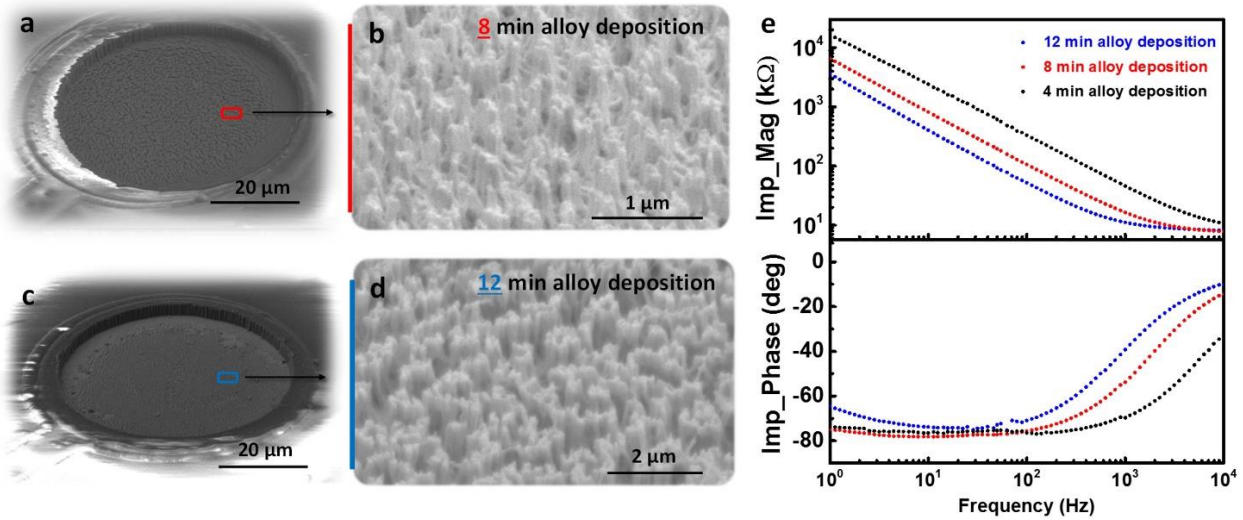

Figure 7.3 Effect of alloy deposition on the PtNR height: (a) Tilted view SEM image of PtNRs electrode with 8 min co-sputtering deposition, resulting in ~500 nm tall PtNRs (b). (c) Tilted view SEM image of PtNRs electrode with 16 min co-sputtering deposition, resulting in ~1 µm tall PtNRs (d). Electrochemical impedance spectroscopy of various PtNRs electrodes (D=50 µm) with different alloy deposition and PtNRs heights, resulting in different magnitude and phase impedance spectra.

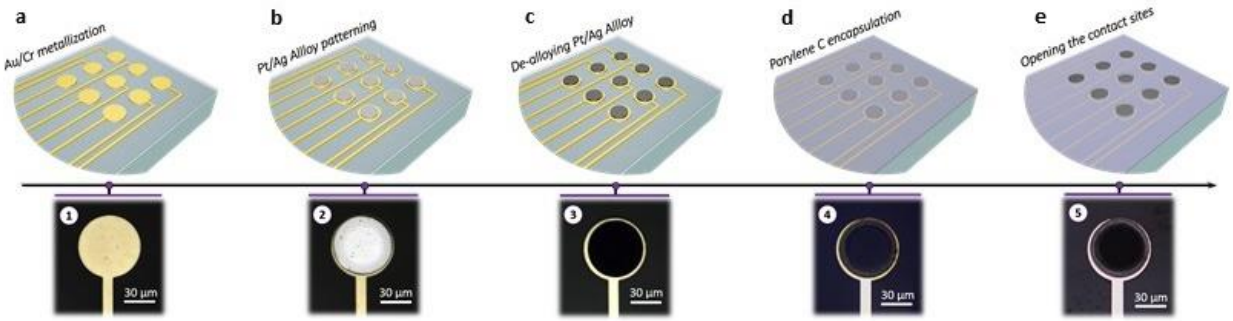

Figure 7.4 Fabrication flow of the PtNRs-based microelectrodes: a) Au/Cr contacts and leads metallization. b) Selective AgPt alloy deposition on sensing sites using co-sputtering deposition system c) selective PtNRs formation on electrode sites after chemical de-alloying in nitric acid at 60 C°. d) Deposition of second passivation parylene C layer. e) Selective oxygen plasma etching of parylene C layer on top of microcontacts and PtNR exposure.

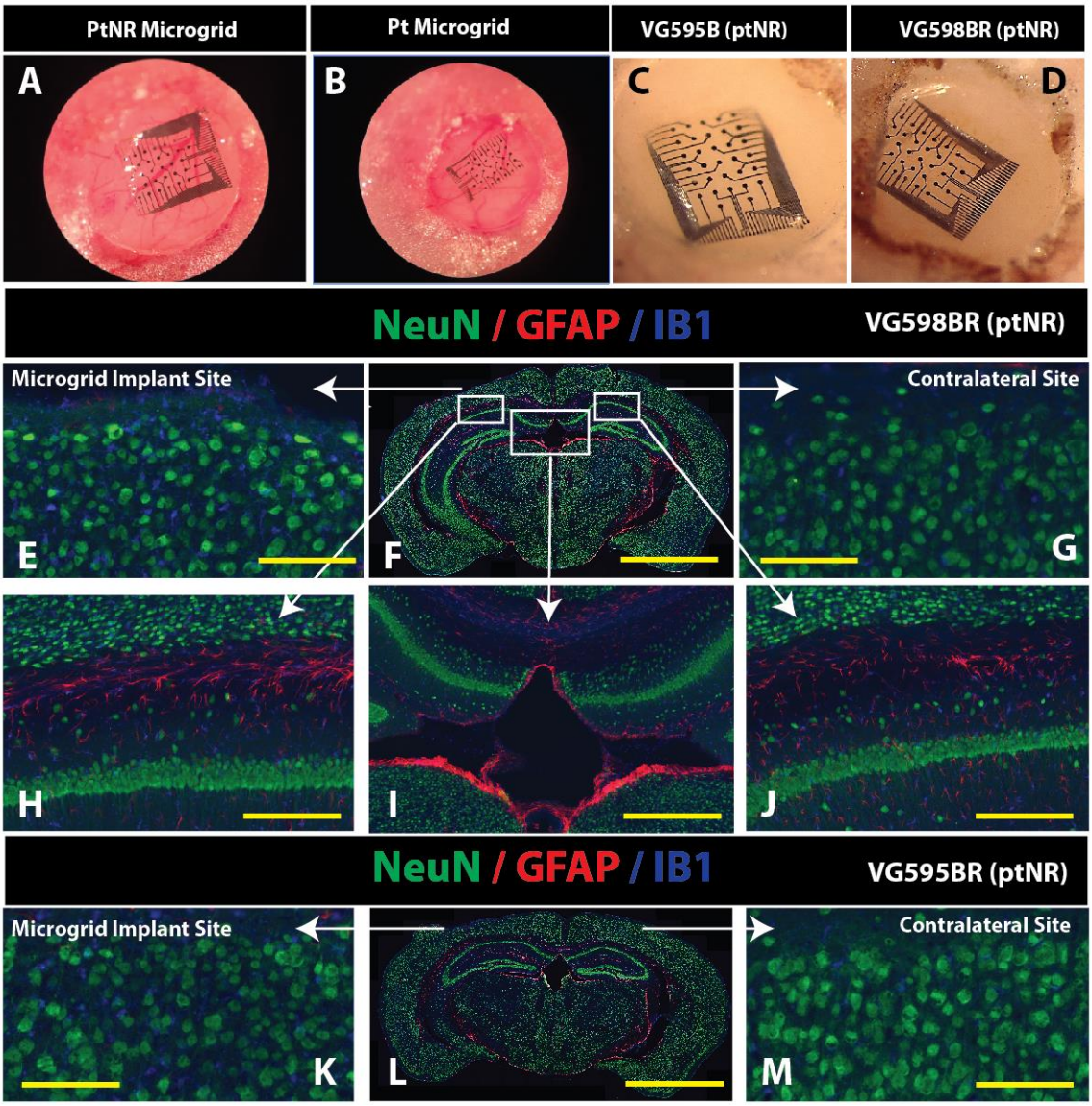

Figure 7.5 Biocompatibility and safety of cortical-surface PtNR microgrid implant in mice. In adult anesthetized mice a bur hole was drilled into skull and PtNR microgrid placed on the surface of motor cortex. Dura was cut-opened. After implants animals survived for 42 days and perfusion-fixed with 4% paraformaldehyde. (A, B) Intraoperative images taken just after placement of microgrid implants. (C,D) Images of cortical surface with implanted microgrid just after perfusion fixation. No fibrotic changes were seen. (E-M) Immunofluorescence images taken from coronal brain sections of two animals implanted with PtNR microgrids and stained with NeuN, GFAP and IB1 antibodies. Except of a slight indentation of the cortical surface at the site of microgrid implant near normal neuronal and glial morphology and staining pattern were seen when compared to contralateral non-implanted site. NeuN-stained neurons in cortical superficial layers as well as in hippocampal CA1 sector showed normal appearance with no detectable degeneration (comparing micogrid Implant Site vs. contralateral Site). Similarly, a comparable staining pattern for IB1 and GFAP were seen. Scale bars: E, G, K, M- 100 µm, F, L- 2 mm, I- 500 µm.

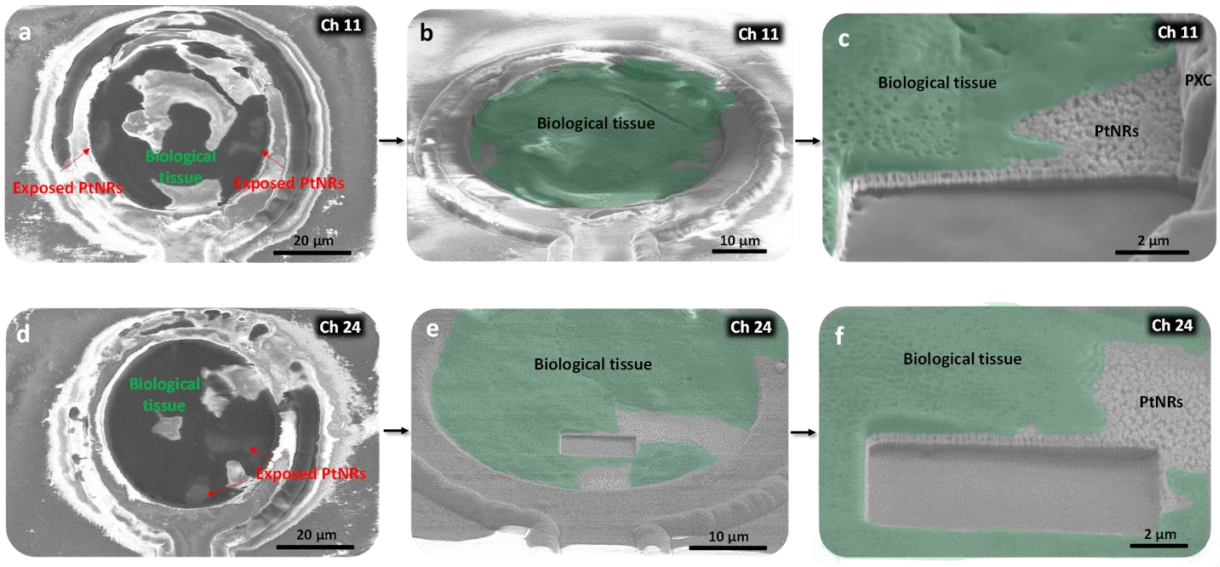

Figure 7.6 Examining PtNR morphology after 42 days implant in a mouse brain: Top view (a, d) and Titled view (b, e) SEM image of the ex-planted PtNR electrode (ch 11, ch 24). Cross-sectional SEM image (c, f) at sliced PtNR electrode surface, demonstrating a stable PtNRs film condition after ex-planation (42 days) with partial coverage with biological tissue.

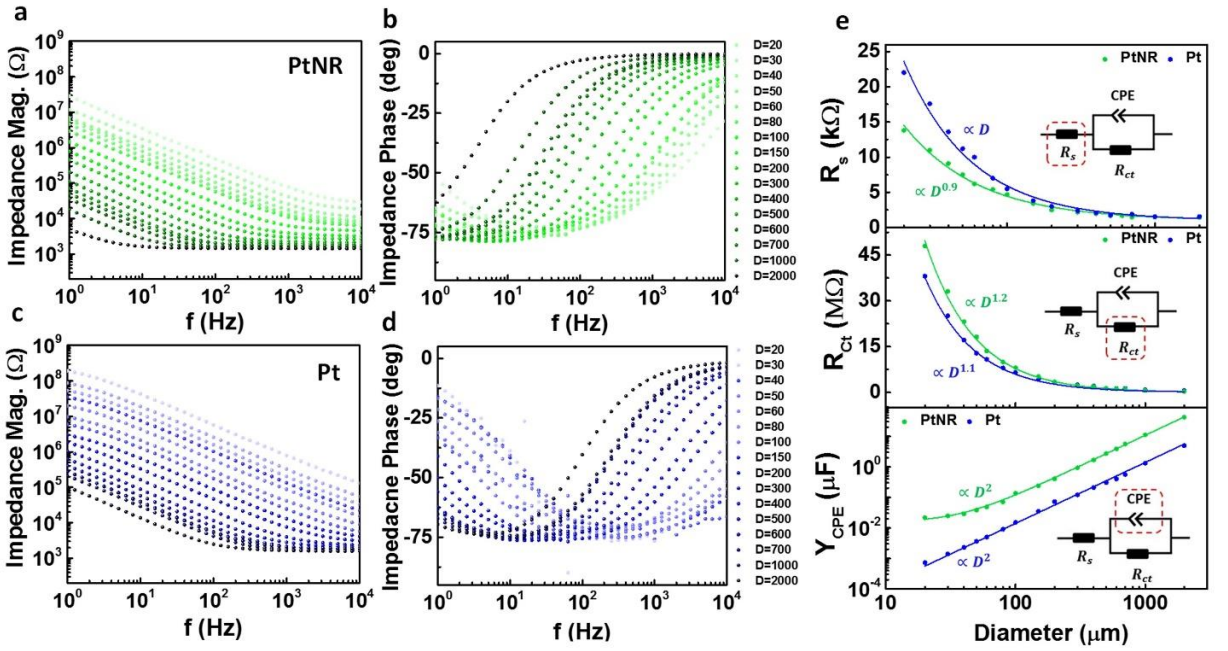

Figure 7.7 Electrochemical impedance measurements and analyses for Pt and PtNRs electrodes as a function of diameter: Electrochemical impedance magnitude and phase spectroscopy of PtNR (a and b) and Pt (c and d) electrodes with varying diameters ranging from 2,000 µm to 20 µm. e) Equivalent circuit model and corresponding small signal components of different small signal components (highlighted in red box in insets) for PtNR (blue) and Pt (green) electrodes.

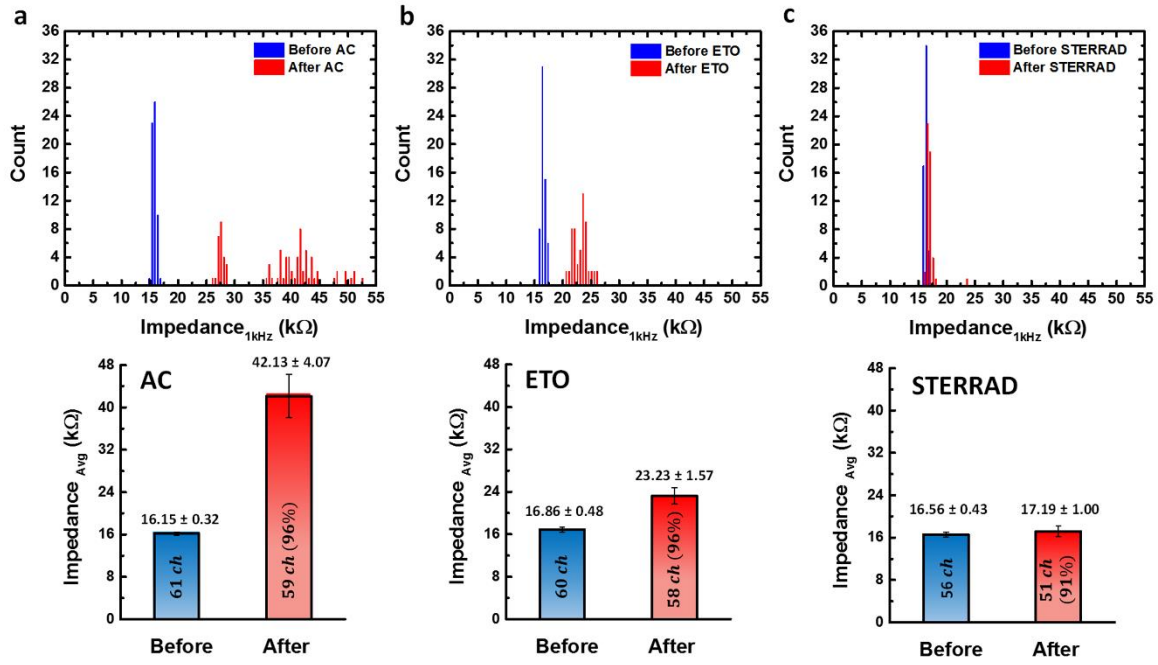

Figure 7.8 Sterilization effects on the PtNR electrode impedance: 1 kHz electrochemical impedance magnitude histogram of PtNR channels and corresponding statistics (AVG + STD) before (blue) and after (red) Autoclave (a), ETO (b) and STERRAD (c) sterilization techniques. EIS was first performed at UCSD, shipped to MGH for sterilization procedures, and then shipped back to UCSD for EIS measurements. Some channels were non-functional after receiving the devices back at UCSD likely due to failure at the ACF-ribbon/device interface, which was encountered even without devices undergoing the sterilization procedure.

Further highlighting the electrochemical performance and stability of the PtNR electrodes, PtNR electrode impedances at 1kHz in the diameter range of 20μm – 2mm are similar to those of PEDOT:PSS,[24] one of the most electrochemically efficient neural electrode materials, and were lower than those of activated planar Pt microelectrodes (**Figure 7.2a**). Activation of PtNRs and planar Pt electrodes is achieved by 10 cycles of cyclic voltammetry. At 1kHz, the impedance of PtNRs is 10X smaller than that of activated planar Pt microelectrodes at smaller diameters, whereas impedances of larger diameter microelectrodes become limited by their series resistances (**Figure 7.7**).[25] For a 56 microelectrode array with 50μm diameter per site, the electrode impedance at 1kHz for PtNRs is uniform (16.89 ± 0.47 kΩ) and is lower than the more variable impedances

(153.01 ± 24 kΩ) of similar-diameter activated Pt microelectrodes (**Figure 7.2b**). The 10Hz electrochemical impedance for PtNRs is also significantly lower than that of activated planar Pt microelectrodes and lower than that of PEDOT:PSS microelectrodes for all studied diameters (**Figure 7.2c**). The impedance values are also relatively uniform for a fixed 50 μm diameter (0.670 ± 0.025 MΩ) compared to activated planar Pt microelectrodes (8.95 ± 2.1 MΩ; Figure 2d). The low impedance of PtNR microelectrodes across frequencies is essential for the high fidelity recording of a broad range of brain activity such as local field potentials (ranging from ~0 to 300 Hz) to single and multi-unit activity >300Hz.[26]

It has also become increasingly important to be able to use microelectrodes in modulation of neural activity.[27] Stimulation capability is assessed by the charge injection capacity (CIC), the maximum amount of charge that can be injected through the electrode prior to building a potential across the electrode/electrolyte interface that can cause water hydrolysis (**Figure 7.2e**). For all diameters, PtNRs allow injection of higher currents and therefore permit higher CIC compared to PEDOT:PSS and activated planar Pt microelectrodes (**Figure 7.2f**). For a 20 μm diameter microelectrode, the CIC of PtNR is 4.4 $mC.cm^{-2}$ which is ~ 16 times larger than activated planar Pt (0.27 $mC.cm^{-2}$) with the same diameter. For the same current, the smaller voltage transients built across the PtNR/electrolyte interface lead to significantly smaller power dissipation per a single bi-phasic pulse (**Figure 7.2g**). This power can be as much as a quarter of that required to inject the same amount of charge across activated planar Pt microelectrodes (**Figure 7.2h**), and lower than that required for PEDOT:PSS microelectrodes. 100,000 biphasic current pulses effectively reduce the electrode impedance (21% reduction at 1 kHz; **Figure 7.2i**), presumably due to desorption of contaminants and H-plated on the electrode surface without influencing the structure of the PtNRs (as inferred from the SEM images in **Figure 7.2j**). The charge storage

capacity (CSC) deduced from the integrated area under the CV spectra (**Figure 7.2k**) demonstrate superior values that are 6 and 8 times larger than those of activated planar Pt and PEDOT:PSS microelectrodes, respectively, due to the high surface area of the PtNRs (**Figure 7.2l**). Overall, based on our quantitative assessments of the devices, the PtNR microelectrode system is a robust system for high performance, safe, and stable neural electrode interfaces.

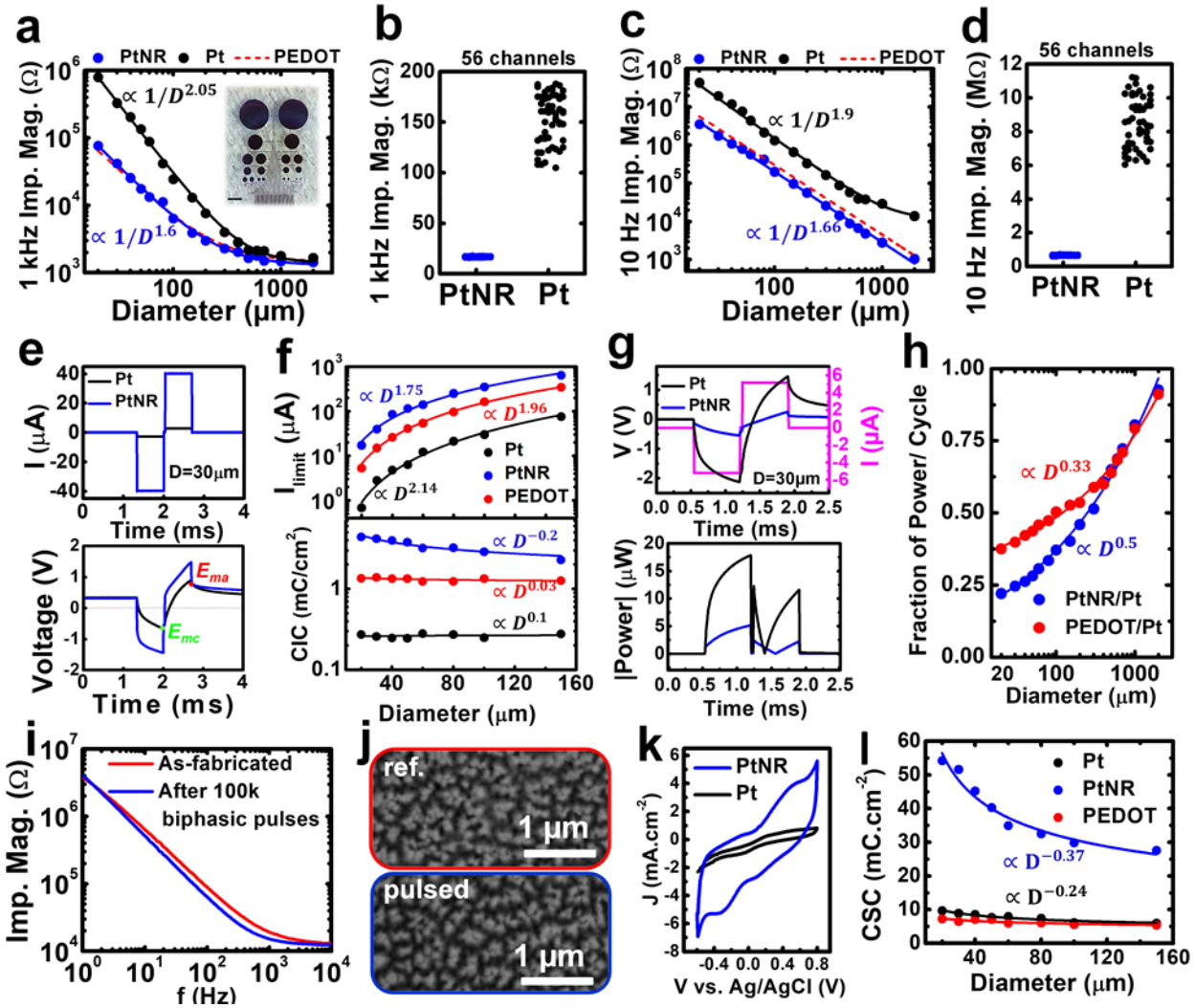

Figure 7.9 Electrochemical performance of PtNR vs. Pt and PEDOT:PSS microelectrodes: a) Measured and fitted values of electrochemical impedances of PtNR (blue), Pt (black) and PEDOT:PSSS (red-dashed) as a function of diameter at 1kHz (a) and 10Hz (c). Inset in (a) shows the variable diameter electrode layout. Scatter plot of 1kHz (b) and 10Hz (d) impedances for 56 PtNR and Pt channels with 50 μm diameter. e) Voltage transients in response to injected current (upper panel) for 30 μm diameter PtNR and Pt microelectrodes at their maximal (water hydrolysis) cathodal and the anodal potential limits. f) Measured and fitted values of current injection limits and charge injection capacities as a function of diameter. g) Measured voltage transients and calculated absolute power values of 30 μm diameter PtNR and Pt microelectrodes under the same charge injection (5 μA injected current). h) The ratio of power consumption/cycle of PtNR and PEDOT:PSS microelectrodes in reference to activated planar Pt microelectrodes as a function of electrode size. The circles represent experimental measurements and the lines are fits. i) Impedance spectra of a 50μm diameter PtNR microelectrode as-fabricated and after 100k biphasic current pulses (I=50 μA, PW=500 μs, f=100 Hz). j) Top view SEM images of PtNR on reference and 100k cycled microelectrode on the same array showing negligible morphological changes. k) CV responses (current densities) with 30 μm diameter PtNR and Pt microelectrodes. l) Charge storage capacities as a function of diameter showing superiority of PtNR microelectrodes.

7.3.2 Recording of Stimulus Modulated Single Unit Activities and local field Potential Dynamics with PtNRs

To demonstrate the superior neural recording capabilities of PtNR microelectrodes, we recorded from the auditory cortex in European starling birds (**Figure 7.10**) and from the visual cortex of a non-human primate (**Figure 7.15**). Similar to PEDOT:PSS microelectrodes,[24] we found PtNRs are capable of recording single units from the cortical surface in birds. When the electrode is implanted over the high vocal center (HVC) auditory region of the starling (**Figure 7.10a, 7.10b**), action potential waveforms, evident in the high pass filtered data (Supplementary Information; **Figure 7.11**) could then be clustered, which resulted in single unit waveforms with interspike intervaldistributions consistent with the published literature (ISI; **Figure 7.10c**). To confirm the presence of single unit action potentials, a depth electrode was inserted through the surface microarray, which allowed simultaneous recordings of surface and depth units (**Figure 7.12**). Significantly, we found stimulus-locked modulation of the single unit activity to auditory stimuli across multiple trials (30x) from the HVC, indicating coordinated single unit and population-level activity in birdsong experiments that can be measured from the surface of the brain (**Figure 7.10d**). The specific pattern of firing is observed from one example cell to the bird's own song, as demonstrated in the raw measured potentials, the high pass filtered (HPF) waveform, the trial averages, and the single unit raster plot from the 30 trials. Zooming in on a 5 second segment of the recording illustrates that this firing is correlated with the power of the auditory stimuli (**Figure 7.10e**). Recordings with PtNR microelectrodes are of high quality enabling us to extract low noise receptive fields (**Figure 7.11**) and correlation maps between surface and depth spikes (**Figure 7.12**) as well as among surface-recorded LFPs (**Figure 7.13**). The cellular resolution and responses of single units to relevant external stimuli highlight the potential for the use of thin PtNR microelectrodes in minimally invasive neuroprosthetic applications.

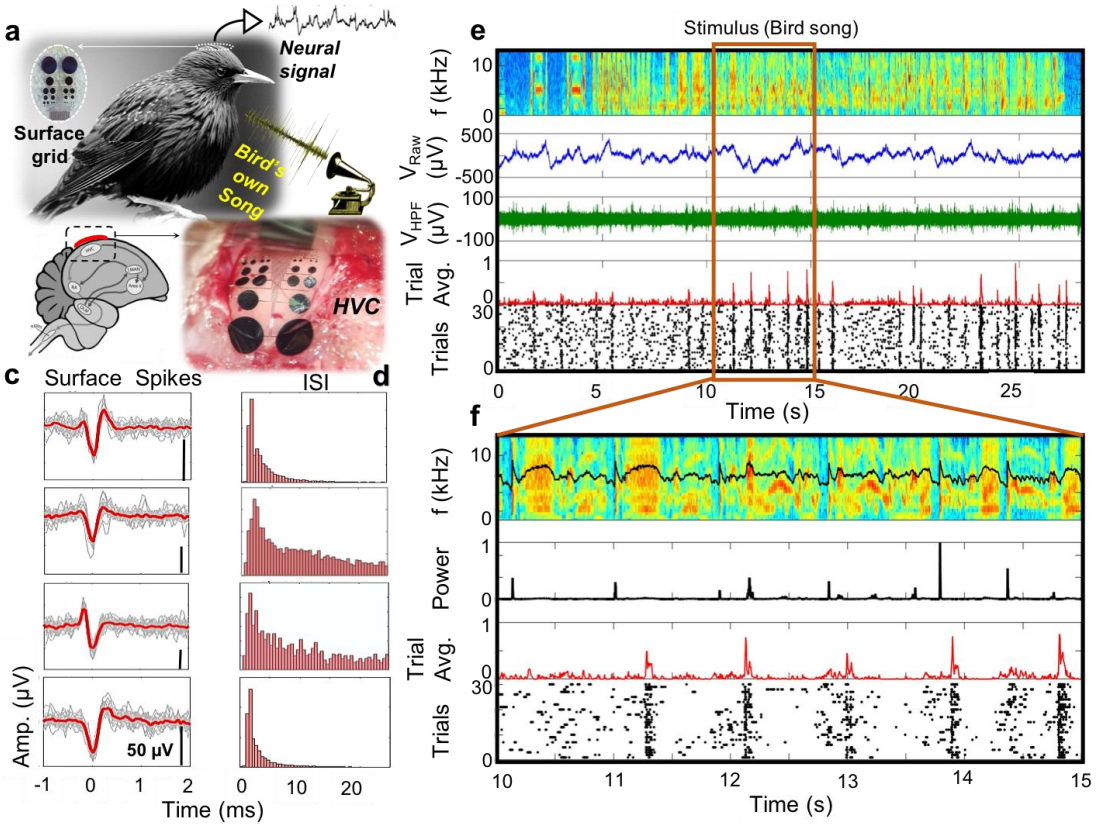

Figure 7.10 Recording of Stimulus Modulated Single Unit Activity with PtNRs in songbird experiments (N=2 Starling, N=2 Zebra Finch): a) Auditory stimuli in the form of bird song (e.g. bird own song) is played for European Starling bird under anesthesia and neural signals are recorded from HVC auditory area. b) Schematic of the songbird brain circuit and location of PtNR array implant in top of the HVC. c) Example of single unit surface spike waveforms and (d) their corresponding Inter-spike interval (ISI) histograms of waveforms. The red waveforms are averages of 20 uniformly sampled spike snippets. The black scales on lower right of each waveforms indicates 50 μV amplitude. e) Cell with stimulus driven neural response. First row demonstrates spectrogram of 28s stimulus (bird's own song). The color from blue to yellow indicate intensity of stimulus power from low to high. Second row displays a recorded raw signal (blue). Third row demonstrates same signal high pass filtered (>300 Hz) (green). Fourth row shows the trail average of 30 trail spike trains. Bottom row is a spike raster plot of a recorded single unit from the HVC surface for trails. f) Zoom in 5s of stimuli: First row shows spectrogram of 5s bird own song. The log of power spectrum density (PSD) averaged over 65 frequency bands is overlaid as a black line. Second row is the average of 65 frequency bands of PSD. Third row displays the trail average in red. Last row shows raster plot of 5s spike train in response to 30 trails showing modulated spiking across trials.

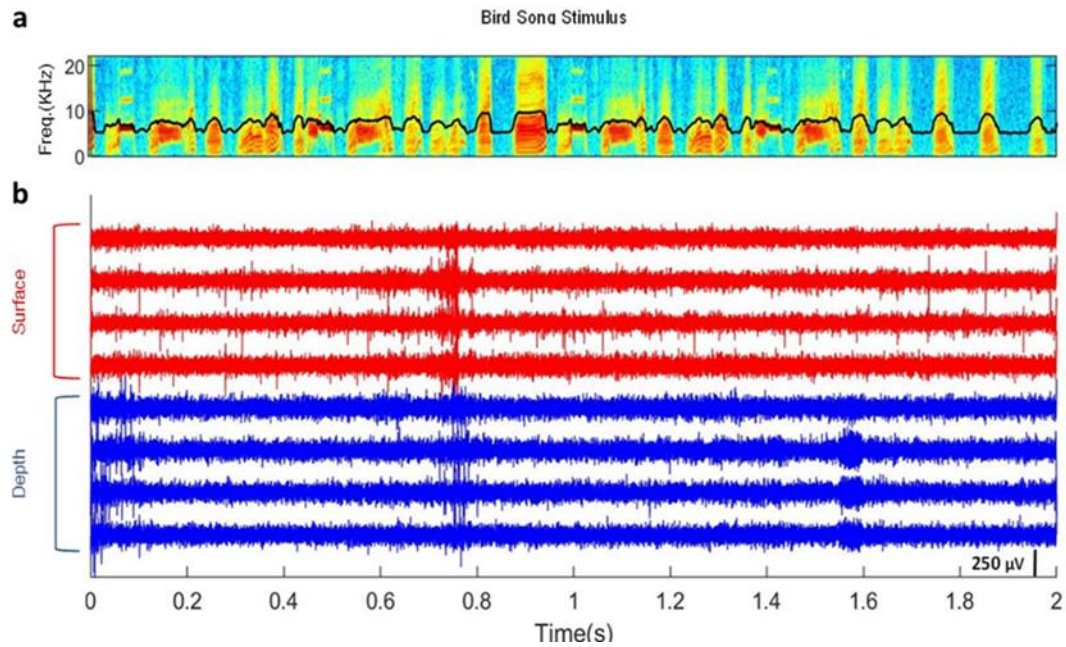

Figure 7.11 Example of recorded high pass filtered data from surface and depth electrodes: a) Spectrogram of the stimulus of a zebra finch song. The black waveform is the log of power spectrum density (PSD) averaged over 65 frequency bands of spectrogram. b) Eight high-pass filtered time series: Four recorded from surface electrodes in red and the other four are recorded from depth electrodes in blue. The black scale bar in bottom right indicates amplitude of 250µV.

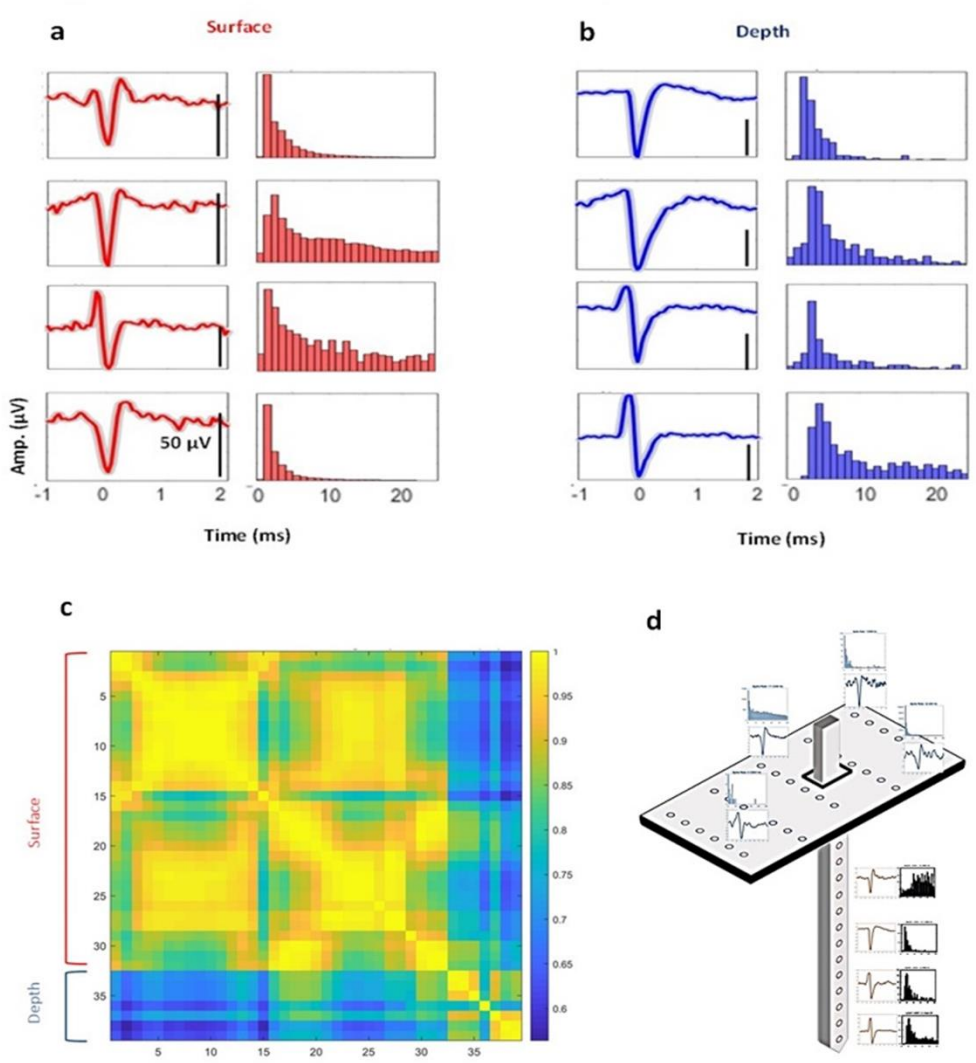

Figure 7.12 Examples of recorded single cell spike waveforms from surface and depth electrode: a) Single cells recorded spike waveforms from surface electrode. The red waveforms are averages of 20 sampled spike snippets and the scale black bar indicates 50μV in amplitude. Left column are waveforms corresponding inter-spike interval (ISI) histograms in red. b) Single cells recorded spike waveforms from depth electrode. The blue waveforms are averages of 20 sampled spike snippets. Left column demonstrates the waveforms corresponding inter-spike interval (ISI) histograms. c) Similarity map across 40 channels of LFP data from 32 surface electrodes and 8 depth electrodes. The 40 channels data first low pass filtered at 300 Hz to extract local field potential (LFP) waveforms then the correlation coefficient across the 40 channels LFP are calculated based on cross-correlation method. The color bar in right side indicates the most similarity between channels in bright yellow and less similarity in dark blue. This correlation matrix demonstrates high correlation between surface LFPs (r=0.8-1) as well as high correlation ibetween depth LFPs (r=0.8-1) but lower correlation among surface and depth LFPs (r=0.55-0.75). d) An illustration of spike waveforms and their spatial distribution as recorded from the surface and depth electrodes.

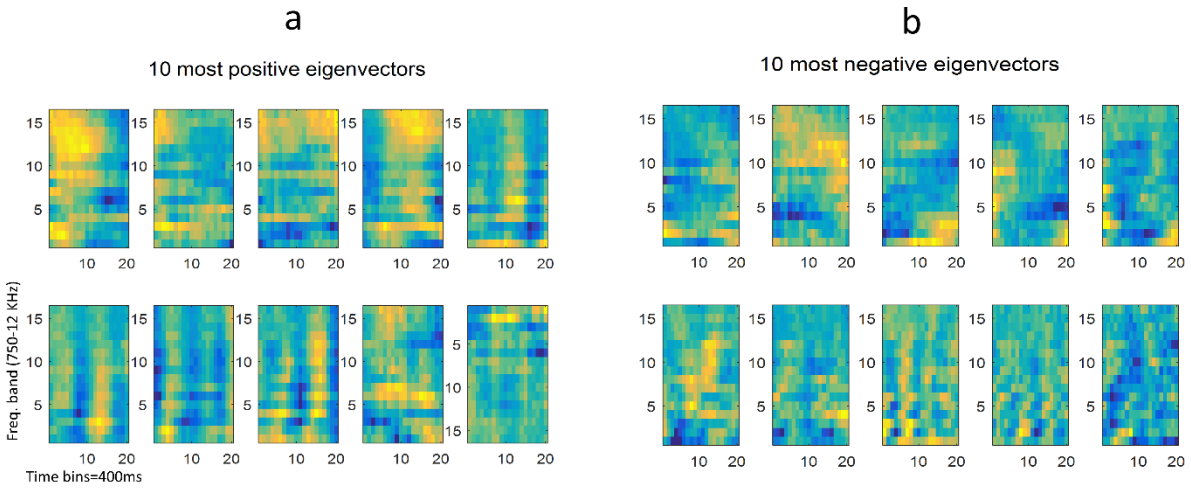

Figure 7.13 Examples of extracted CRFs from a cortical surface cell. a) 10 most significant facilitatory receptive fields of a single cell. b) 10 most significant excitatory receptive fields. This demonstrates that cells recorded with PtNR m microelectrodes are of high quality enabling us to extract low noise receptive fields from them.

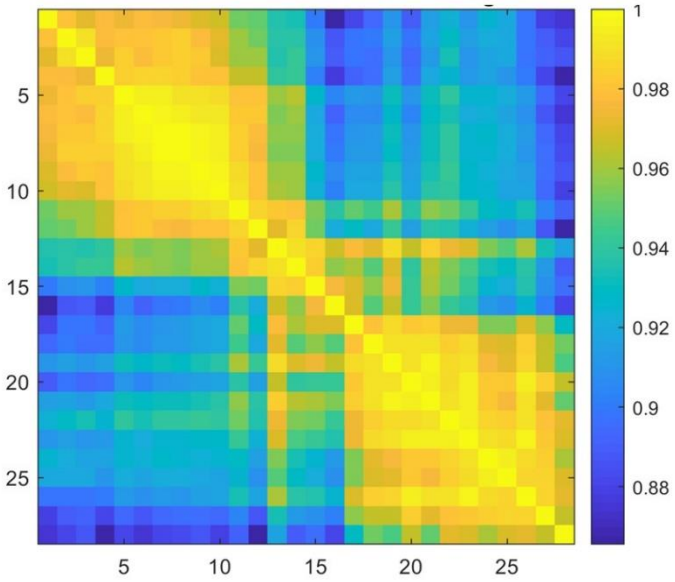

Figure 7.14 Similarity map across LFP data of 30 surface electrodes: 30 channels of data first low pass filtered at 300 freq. to extract local field potential (LFP) waveforms then the correlation coefficient across the 30 channels LFP are calculated based on cross-correlation method. The color bar in right side indicates the most similarity between channels (r=1) in bright yellow and less similarity in dark blue (r=0.8). This map shows similarity between LFP data of surface channels are high ranging from r=0.86 to 1.

To test how well the PtNR electrodes could detect behaviorally and physiologically relevant local field potential dynamics, we recorded neural responses in the primary visual cortex (V1) to

light flashes delivered to an anesthetized non-human primate (NHP; N=1; **Figure 7.15a-e**). We examined the average visual responses across a 2-column array of electrodes and found large visually evoked potential (VEP) responses 0.1 sec after either 20 or 40 ms duration light flashes (**Figure 7.15c-d**). The duration of the average VEPs were longer with the longer duration light flash, with a stronger response toward the end of the 2-column electrode array. We compared how well the PtNR electrodes recorded VEPs compared to a grid of conventional platinum (NeuroNexus, **Figure 7.15e**)) and found the responses were larger with the PtNR electrode, with significantly less noise as averaged across >20 trials per channel (**Figure 7.15d-e**). We also examined the neural response to electrical stimulation in the non-human primate and mouse cortex (**Figure 7.16**; NHP in Figure 7.15 is different to the NHP in Figure 7.16). Using lowered monopolar micro depth electrodes, we stimulated visual areas and recorded the neural responses using the PtNR electrodes.

We observed large voltage responses to trains (**Figure 7.16a**) and single pulses (**Figure 7.16e-f**) of stimulation which could be localized in time and space across a 2-column array as well as a circular array of PtNR electrodes (**Figure 7.16**e-f). electrodes, we stimulated visual areas and recorded the neural responses using the PtNR electrodes. We observed large voltage responses to trains (**Figure 7.16**a) and single pulses (**Figure 7.16**e-f) of stimulation which could be localized in time and space across a 2-column array as well as a circular array of PtNR electrodes (**Figure 7.16**e-f).

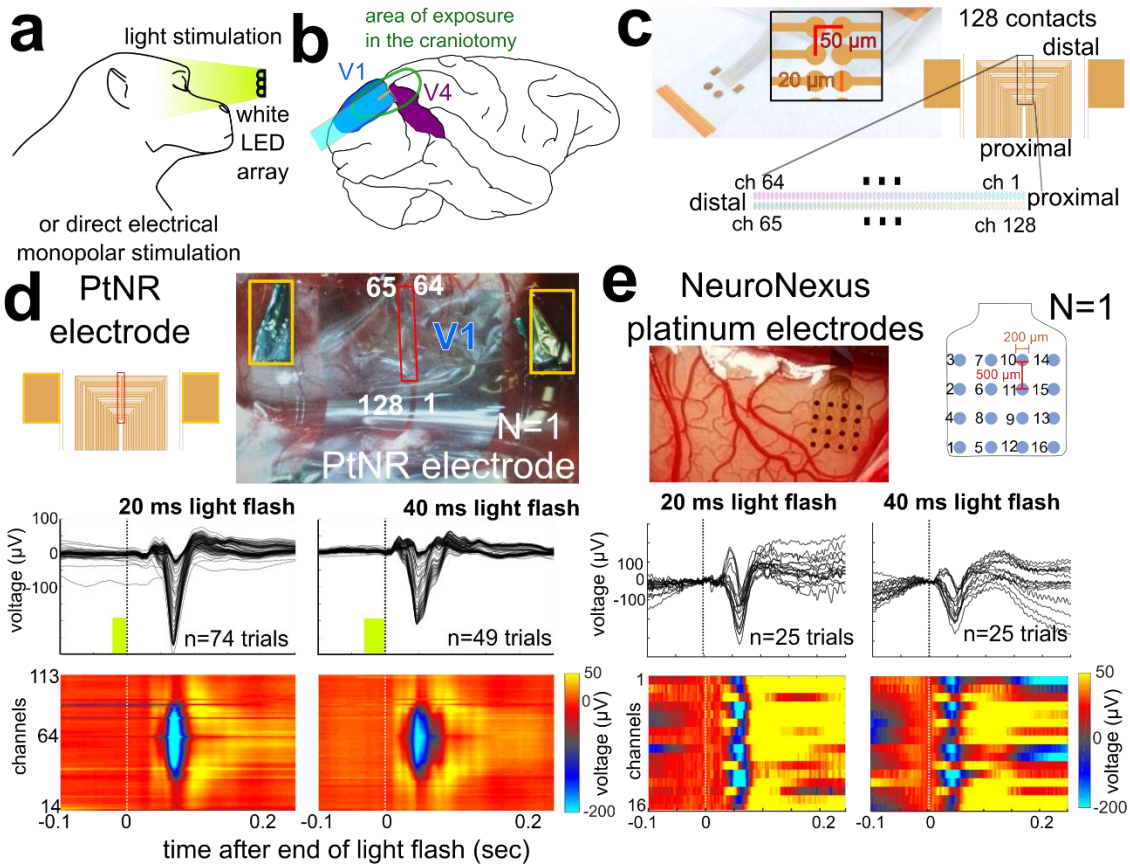

Figure 7.15 Recording of Stimulus Modulated local field potential dynamics with PtNRs in non-human primate experiments (N=1): a) Visual stimulation preparation involved an anesthetized non-human primates (NHPs). b) Schematic of the NHP and location of PtNR array implant in top of the primary visual cortex (V1). c) Electrode map which involves two columns of 64 channels. d) PtNR recording on the NHP V1 cortex with an average visually evoked response to 20 ms (left) and 40 ms (right) duration light flashes, viewed across channels as averages (top traces) and as viewed across the spatial map (bottom). e) Recording from V1 in the same cortex as (c) but with the platinum Neuronexus grid in the same area of V1 cortex.

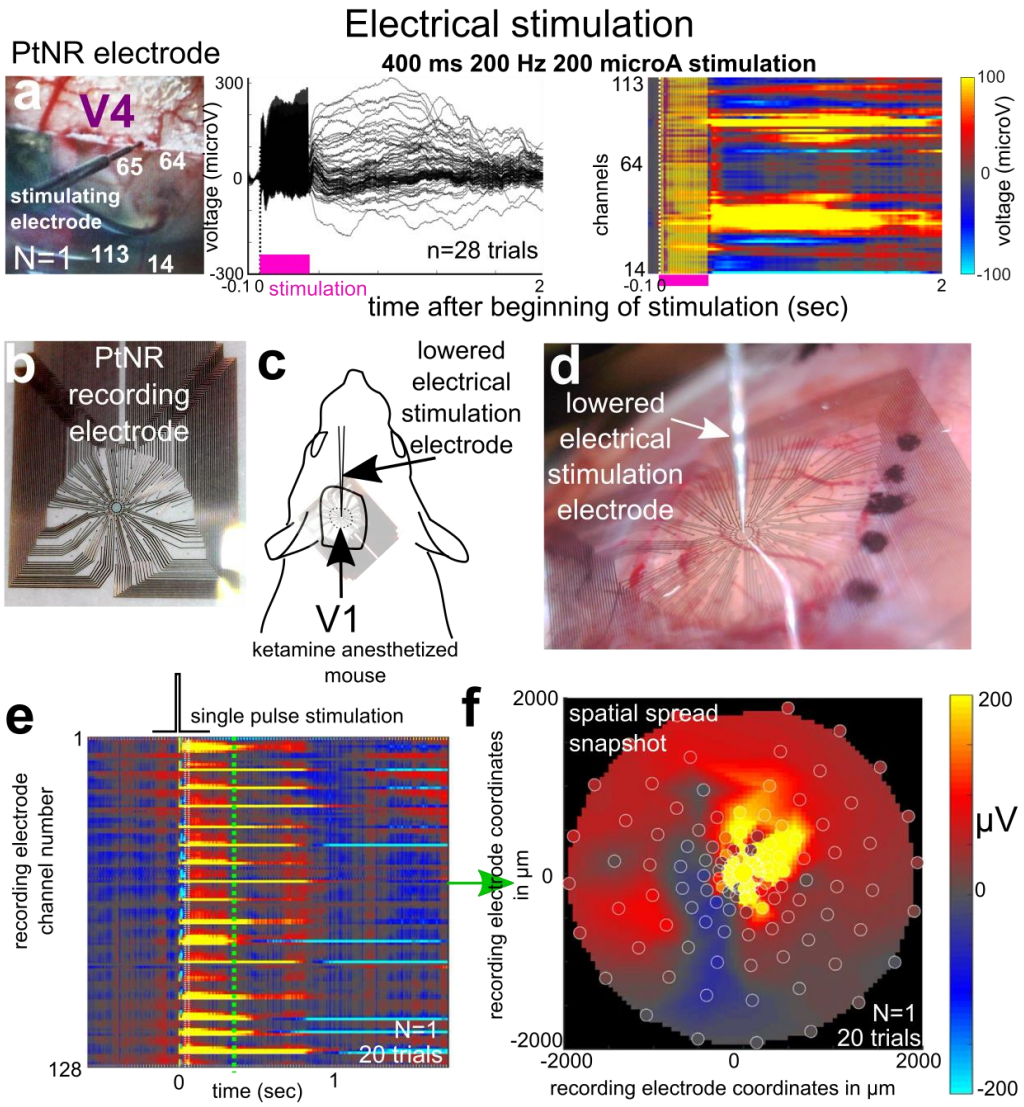

Figure 7.16 Recording of Stimulus Modulated local field potential dynamics with PtNRs in mouse experiments (N=1 NHP and N=1 mouse): a) Electrical stimulation responses to 400 ms train of 200 Hz 200 µA of stimulation near the PtNR array in V4 in a second NHP (left), with the average responses across channels showing responses up to 2 seconds after stimulation (middle) which are distributed across the array (right). b) Electrode map which involves concentric rings of electrode contacts. c) Electrical stimulation preparation involved a ketamine-anesthetized mouse. Schematic of the mouse and location of PtNR array implant in top of the primary visual cortex (V1) and d) an image of the preparation on the mouse cortex. e) PtNR recording on the mouse V1 with an average electrically-evoked response to a single pulse (30 µA) of monopolar electrical stimulation via the lowered depth electrode. Responses at the center of the PtNR array in V1, with the average responses across channels showing responses up to 2 seconds after stimulation (middle). f) These responses are distributed across the array as captured at a specific moment in time (green line in (e)). The map was interpolated across electrode sites as indicated by the circles on the array.

7.4 Conclusion

In summary, we developed a Pt-based biocompatible electrode system, PtNRs, whose electrochemical performance surpasses those of currently pursued electrode materials for neural interfaces. Across species, PtNRs microelectrodes are capable of recording detailed broadband neuronal activity with high spatiotemporal resolution in response to auditory, visual, and electrical stimulation. These results demonstrate the great potential for clinical translation evidenced by their excellent electrochemical properties, their biocompatibility and stability. In addition to high-quality neuronal recordings reported here, the excellent stimulation capability of PtNRs extend beyond cortical implants to applications for intervention with the spinal cord and peripheral nervous system.

Chapter 7, in full, is a reprint of material as it appears in the following submitted manuscript for publication: M. Ganji, A. C. Paulk, J. C. Yang, N. W. Vahidi, S. H. Lee, R. Liu, L. Hossain, E. M. Arneodo, M. Thunemann, M. Shigyo, A. Tanaka, S. B. Ryu, S. W. Lee, M. Marsala, A. Devor, D. Cleary, V. Gilja, T. Q. Gentner, S. I. Fried, E. Halgren, S. S. Cash, and S. A. Dayeh, " Selective Formation of Porous Pt Nanorods for Highly Electrochemically Efficient Neural Electrode Interfaces" Submitted to Nano Letters. The dissertation author was the primary investigator and author of this material.

7.5 References

[1] Z. L. Wang and J. Song, "Piezoelectric nanogenerators based on zinc oxide nanowire arrays," *Science*, vol. 312, pp. 242-246, 2006.

[2] C. Liu, J. Tang, H. M. Chen, B. Liu, and P. Yang, "A fully integrated nanosystem of semiconductor nanowires for direct solar water splitting," *Nano letters*, vol. 13, pp. 2989-2992, 2013.

[3] Y. Liu, X. H. Liu, B.-M. Nguyen, J. Yoo, J. P. Sullivan, S. T. Picraux, "Tailoring lithiation behavior by interface and bandgap engineering at the nanoscale," *Nano letters,* vol. 13, pp. 4876-4883, 2013.

[4] B. Tian, T. Cohen-Karni, Q. Qing, X. Duan, P. Xie, and C. M. Lieber, "Three-dimensional, flexible nanoscale field-effect transistors as localized bioprobes," *Science,* vol. 329, pp. 830-834, 2010.

[5] C. Xie, Z. Lin, L. Hanson, Y. Cui, and B. Cui, "Intracellular recording of action potentials by nanopillar electroporation," *Nature nanotechnology,* vol. 7, pp. 185-190, 2012.

[6] J. T. Robinson, M. Jorgolli, A. K. Shalek, M.-H. Yoon, R. S. Gertner, and H. Park, "Vertical nanowire electrode arrays as a scalable platform for intracellular interfacing to neuronal circuits," *Nature nanotechnology,* vol. 7, pp. 180-184, 2012.

[7] R. Liu, R. Chen, A. T. Elthakeb, S. H. Lee, S. Hinckley, M. L. Khraiche, "High density individually addressable nanowire arrays record intracellular activity from primary rodent and human stem cell derived neurons," *Nano letters,* vol. 17, pp. 2757-2764, 2017.

[8] X. Dai, W. Zhou, T. Gao, J. Liu, and C. M. Lieber, "Three-dimensional mapping and regulation of action potential propagation in nanoelectronics-innervated tissues," *Nature nanotechnology,* vol. 11, p. 776, 2016.

[9] G. Hong, T.-M. Fu, M. Qiao, R. D. Viveros, X. Yang, T. Zhou, "A method for single-neuron chronic recording from the retina in awake mice," *Science,* vol. 360, pp. 1447-1451, 2018.

[10] T.-M. Fu, G. Hong, R. D. Viveros, T. Zhou, and C. M. Lieber, "Highly scalable multichannel mesh electronics for stable chronic brain electrophysiology," *Proceedings of the National Academy of Sciences,* vol. 114, pp. E10046-E10055, 2017.

[11] R. Wagner and W. Ellis, "Vapor-liquid-solid mechanism of single crystal growth," *Applied Physics Letters,* vol. 4, pp. 89-90, 1964.

[12] G. Sun, J. Xu, and P. Harrowell, "The mechanism of the ultrafast crystal growth of pure metals from their melts," *Nature materials,* p. 1, 2018.

[13] L. E. Greene, B. D. Yuhas, M. Law, D. Zitoun, and P. Yang, "Solution-grown zinc oxide nanowires," *Inorganic chemistry,* vol. 45, pp. 7535-7543, 2006.

[14] D. Banerjee, S. H. Jo, and Z. F. Ren, "Enhanced field emission of ZnO nanowires," *Advanced Materials,* vol. 16, pp. 2028-2032, 2004.

[15] M. Shen, A. Han, X. Wang, Y. G. Ro, A. Kargar, Y. Lin, "Atomic scale analysis of the enhanced electro-and photo-catalytic activity in high-index faceted porous NiO nanowires," *Scientific reports,* vol. 5, p. 8557, 2015.

[16] C. Li, T. Sato, and Y. Yamauchi, "Electrochemical Synthesis of One-Dimensional Mesoporous Pt Nanorods Using the Assembly of Surfactant Micelles in Confined Space," *Angewandte Chemie International Edition,* vol. 52, pp. 8050-8053, 2013.

[17] L. Liu, E. Pippel, R. Scholz, and U. Gösele, "Nanoporous Pt− Co alloy nanowires: fabrication, characterization, and electrocatalytic properties," *Nano letters,* vol. 9, pp. 4352-4358, 2009.

[18] H. Li, A. Misra, J. K. Baldwin, and S. Picraux, "Synthesis and characterization of nanoporous Pt–Ni alloys," *Applied Physics Letters,* vol. 95, p. 201902, 2009.

[19] J.-L. Shui, J.-W. Zhang, and J. C. Li, "Making Pt-shell Pt 30 Ni 70 nanowires by mild dealloying and heat treatments with little Ni loss," *Journal of Materials Chemistry,* vol. 21, pp. 6225-6229, 2011.

[20] H.-J. Jin, X.-L. Wang, S. Parida, K. Wang, M. Seo, and J. r. Weissmüller, "Nanoporous Au− Pt alloys as large strain electrochemical actuators," *Nano letters,* vol. 10, pp. 187-194, 2009.

[21] S. Tominaka, T. Hayashi, Y. Nakamura, and T. Osaka, "Mesoporous PdCo sponge-like nanostructure synthesized by electrodeposition and dealloying for oxygen reduction reaction," *Journal of Materials Chemistry,* vol. 20, pp. 7175-7182, 2010.

[22] J. Erlebacher, M. J. Aziz, A. Karma, N. Dimitrov, and K. Sieradzki, "Evolution of nanoporosity in dealloying," *Nature,* vol. 410, pp. 450-453, 2001.

[23] I. Uguz, M. Ganji, A. Hama, A. Tanaka, S. Inal, A. Youssef, "Autoclave Sterilization of PEDOT: PSS Electrophysiology Devices," *Advanced Healthcare Materials,* 2016.

[24] D. Khodagholy, J. N. Gelinas, T. Thesen, W. Doyle, O. Devinsky, G. G. Malliaras, "NeuroGrid: recording action potentials from the surface of the brain," *Nature neuroscience,* vol. 18, pp. 310-315, 2015.

[25] M. Ganji, A. T. Elthakeb, A. Tanaka, V. Gilja, E. Halgren, and S. A. Dayeh, "Scaling Effects on the Electrochemical Performance of poly (3, 4-ethylenedioxythiophene (PEDOT), Au, and Pt for Electrocorticography Recording," *Advanced Functional Materials,* vol. 27, 2017.

[26] M. Ganji, A. T. Elthakeb, A. Tanaka, V. Gilja, E. Halgren, and S. A. Dayeh, "Scaling Effects on the Electrochemical Performance of poly (3, 4-ethylenedioxythiophene (PEDOT), Au, and Pt for Electrocorticography Recording," *Advanced Functional Materials,* vol. 27, p. 1703018, 2017.

[27] S. N. Flesher, J. L. Collinger, S. T. Foldes, J. M. Weiss, J. E. Downey, E. C. Tyler-Kabara, "Intracortical microstimulation of human somatosensory cortex," *Science translational medicine,* vol. 8, pp. 361ra141-361ra141, 2016.

[28] M. Ganji, E. Kaestner, J. Hermiz, N. Rogers, A. Tanaka, D. Cleary, "Development and Translation of PEDOT: PSS Microelectrodes for Intraoperative Monitoring," *Advanced Functional Materials,* vol. 28, 2018.

[29] M. Sessolo, D. Khodagholy, J. Rivnay, F. Maddalena, M. Gleyzes, E. Steidl., "Easy-to-fabricate conducting polymer microelectrode arrays," *Advanced Materials,* vol. 25, pp. 2135-2139, 2013.

[30] I. Uguz, M. Ganji, A. Hama, A. Tanaka, S. Inal, A. Youssef, "Autoclave sterilization of PEDOT: PSS electrophysiology devices," *Advanced healthcare materials,* vol. 5, pp. 3094-3098, 2016.

[31] J. Hermiz, N. Rogers, E. Kaestner, M. Ganji, D. Cleary, J. Snider, "A Clinic Compatible, Open Source Electrophysiology System," presented at the IEEE EMBC, Orlando, Florida, 2016.

[32] J. H. Siegle, A. C. López, Y. A. Patel, K. Abramov, S. Ohayon, and J. Voigts, "Open Ephys: an open-source, plugin-based platform for multichannel electrophysiology," *Journal of neural engineering,* vol. 14, p. 045003, 2017.

[33] G. Paxinos and K. B. J. Franklin, *The mouse brain in stereotaxic coordinates,* 2nd ed. San Diego: Academic Press, 2001.

Chapter 8

Summary

8.1 Summary of the thesis

As electrode development pushes towards decreasing contact size to increase spatial specificity, PEDOT:PSS contacts facilitate high SNR recordings and have a number of favorable characteristics. The spin-casting approach used in our fabrication provides a consistent electrochemical interface and insignificant morphological changes post-sterilization. This approach leads to a very high yield of functioning electrodes (>96%) with a narrow range of impedances. The EIS impedances for PEDOT:PSS are smaller than those for Pt which in turn results in lower noise power spectral density than those of Pt. This difference is significant because cognitive processes that are generally observed at low frequencies (theta, gamma, and low frequency oscillations) need to be measured with the lowest possible electrode noise. Additionally, important information about neuronal firing in the high-frequency bands has very small amplitudes, making it critical to maximize SNR.

Combining these reliably low impedances with several other favorable characteristics makes PEDOT:PSS a strong contender for leading the next generation of neural electrochemical interfaces. These additional characteristics include high charge injection capacity (safe/efficient stimulation)[1], compliant mechanical properties for mimicking the curvilinear brain tissue and to compensate brain micromotion in order to reduce tissue damage[2], and enhanced biocompatible electrode/tissue interfaces to minimize biofouling[3, 4]. With higher channel counts being achievable

via passive wiring or active multiplexing, PEDOT:PSS presents a great opportunity to achieve high-density, high-SNR arrays, with greatly increased spatial specificity.

In order to transition these technologies to the clinic, effective sterilization that renders the devices free of pathogenic agents needs to be demonstrated. Several methods exist for the sterilization of medical devices, relying on heat, chemicals or radiation to destroy potential pathogens. Among these, autoclaving is the most-frequently used. The device to be sterilized is placed in a chamber and exposed to high pressure steam typically at a temperature of 121 °C for several minutes. The simplicity of the procedure and low cost of the equipment make this method widely available among biology laboratories and clinics worldwide. As an important step prior to translation of PEDOT:PSS ECoG to clinic, we investigated the impact of sterilization methods on PEDOT:PSS microelectrodes and electrochemical transistors integrated on thin parylene supports. We show that devices inoculated with *E. coli* are effectively sterilized using autoclaving. The process does not alter appreciably the morphology of PEDOT:PSS films, while the electrical characteristics of microelectrodes and transistors show only minor degradation after exposure to steam. Sterrad sterilization, in contrast, causes large morphological changes in the PEDOT:PSS films and results in non-functional devices. The results show that autoclaving, which is readily available in most biological laboratories, is a viable sterilization method for PEDOT:PSS electrophysiology devices. This finding represents a significant step towards the widespread introduction of these devices to the clinical use.

However, to date, there is only one group who has demonstrated PEDOT:PSS utilization in intraoperative monitoring. Their pioneering work reported single units from a human brain and began to explore the spatial specificity capabilities of PEDOT:PSS devices[5]. Here we expanded on these efforts by thoroughly benchmarking PEDOT:PSS electrodes against clinical electrodes

and by demonstrating background, functional, and pathological recordings, the complete suite of mapping that is necessary for clinical translation of PEDOT:PSS into intraoperative monitoring for high fidelity electrophysiological recordings in human subjects. We reported the first evoked (stimulus-locked) cognitive activity with changes in amplitude across pial surface distances as small as 400 μm, potentially enabling basic neurophysiology studies at the scale of neural micro-circuitry.

Reduced contact size would permit higher resolution cortical recordings, but the effects of diameter on crucial recording and stimulation properties are poorly understood. In this thesis, we presented the first systematic study of scaling effects on the electrochemical properties of Pt and Au metallic and PEDOT:PSS organic electrodes. PEDOT:PSS exhibits better faradaic charge transfer and capacitive charge coupling than metal electrodes, and these characteristics lead to improved electrochemical performance and reduced noise at smaller electrode diameters. PEDOT:PSS coating reduced metallic electrodes impedance by up to 18X for diameters < 200 μm, but had no effect for millimeter scale contacts due to the dominance of series resistances. Therefore, the performance gains are especially significant at lower frequencies essential for recording cognitive and pathological activities. Additionally, the overall reduced noise of the PEDOT:PSS electrodes enable a lower noise floor for recording action-potentials. These results permit quantitative optimization of contact material and diameter for different ECoG applications.

The efficacy of electrical brain stimulation in combatting neurodegenerative diseases and initiating function is expected to be significantly enhanced with the development of smaller scale microstimulation electrodes and refined stimulation protocols. These benefits cannot be realized without a thorough understanding of scaling effects on electrochemical charge injection characteristics. In this work, we fabricated and characterized the electrochemical stimulation

capabilities of Au, Pt, PEDOT:PSS/Au, and PEDOT:PSS/Pt electrode arrays in the 20 μm - 2000 μm diameter range. We observed substantial enhancement in charge injection capacity up to 9.5X for PEDOT:PSS microelectrodes compared to metal ones and 88% lower required power for injecting the same charge density. These significant benefits are strongest for electrode diameters below 200μm. Detailed quantitative analyses were provided enabling optimization of charge injection capacity with potential bias, and symmetric and asymmetric pulse width engineering for all diameters. These systematic analyses informed the optimal design for chronic implants in regards of safety and clinically-effective stimulation protocols, ensure the longevity of the electrodes below critical electrochemical limits of stimulation, and demonstrate that the material choice and pulse design can lead to more energy efficiency stimulation protocols that are of critical importance for fully implanted devices.

Poly (3,4-ethylenenedioxythiophene) or PEDOT, is a promising candidate for next-generation neuronal electrode materials but its weak adhesion to underlying metallic conductors impedes its potential. We reported an effective method of mechanically anchoring the PEDOT within the Au nanorod (Au-nr) structure and demonstrate that it provides enhanced adhesion and overall PEDOT layer stability. We used cyclic voltammetry (CV) stress to investigate adhesion and stability of spin-cast and electro-deposited PEDOT. The Au nanorod (Au-nr) adhesion layer permitted 10,000 CV cycles of coated PEDOT film in phosphate buffered saline solution without delamination nor significant change of the electrochemical impedance whereas PEDOT coating film on planar Au electrodes delaminated at or below 1,000 cycles. Under CV stress, spin-cast PEDOT on planar Au delaminates, whereas electro-plated PEDOT on planar Au encounters surface leaching/decomposition. After 5 weeks of accelerated aging tests at 60 $^{\circ}$C, the electro-deposited PEDOT/Au-nr microelectrodes demonstrated a 92% channel survival compared to only

25% survival for spin-cast PEDOT on planar films. Furthermore, after a 10-week chronic implantation onto mouse barrel cortex PEDOT/Au-nr microelectrodes did not exhibit delamination nor morphological changes whereas the conventional PEDOT microelectrodes either partially or fully delaminated. Immunohistochemical evaluation demonstrated no or minimal response to the PEDOT implant.

The enhanced electrochemical activity of nanostructured materials are readily exploited in energy devices, [6, 7, 8] but their utility in scalable and human-compatible implantable neural interfaces can significantly advance the performance of clinical and research electrodes. We utilized low-temperature selective dealloying to develop scalable and biocompatible 1D platinum nanorod (PtNR) arrays that exhibit superb electrochemical properties at various length scales for high performance neurotechnologies. PtNR arrays recorded brain activity with cellular resolution from the cortical surfaces in birds, mice, and non-human primates. Significantly, strong modulation of surface recorded single unit activity by auditory stimuli is demonstrated in European Starling birds, modulation of local field potentials in the visual cortex by light stimuli in a non-human primate, and as well as responses to electrical stimulation in mice. PtNRs record behaviorally and physiologically relevant neuronal dynamics from the surface of the brain with high spatiotemporal resolution which paves the way for less invasive brain-machine interfaces.

8.2 References

[1] R. J. Vetter, J. C. Williams, J. F. Hetke, E. A. Nunamaker, D. R. Kipke, *IEEE transactions on biomedical engineering* **2004**, 51, 896.

[2] a) S. F. Cogan, *Annu. Rev. Biomed. Eng.* **2008**, 10, 275; b) D. R. Merrill, M. Bikson, J. G. Jefferys, *Journal of neuroscience methods* **2005**, 141, 171; c) V. S. Polikov, P. A. Tresco, W. M. Reichert, *Journal of neuroscience methods* **2005**, 148, 1.

[3] a) R. A. Green, R. T. Hassarati, J. A. Goding, S. Baek, N. H. Lovell, P. J. Martens, L. A. Poole-Warren, *Macromolecular bioscience* **2012**, 12, 494; b) M. R. Abidian, D. C. Martin, *Advanced Functional Materials* **2009**, 19, 573; c) S. F. Cogan, K. A. Ludwig, C. G. Welle, P. Takmakov, *Journal of neural engineering* **2016**, 13, 021001.

[4] a) N. G. Hatsopoulos, J. P. Donoghue, *Annual review of neuroscience* **2009**, 32, 249; b) C. E. Lagoa, J. Bartels, A. Baratt, G. Tseng, G. Clermont, M. P. Fink, T. R. Billiar, Y. Vodovotz, *Shock* **2006**, 26, 592.

[5] a) D. Khodagholy, J. N. Gelinas, T. Thesen, W. Doyle, O. Devinsky, G. G. Malliaras, G. Buzsáki, *Nature neuroscience* **2015**, 18, 310; b) D. Khodagholy, J. N. Gelinas, Z. Zhao, M. Yeh, M. Long, J. D. Greenlee, W. Doyle, O. Devinsky, G. Buzsáki, *Science Advances* **2016**, 2, e1601027.

[6] Wang, Z. L. & Song, J. Piezoelectric nanogenerators based on zinc oxide nanowire arrays. *Science* **312**, 242-246 (2006).

[7] Liu, C., Tang, J., Chen, H. M., Liu, B. & Yang, P. A fully integrated nanosystem of semiconductor nanowires for direct solar water splitting. *Nano letters* **13**, 2989-2992 (2013).

[8] Liu, Y. Tailoring lithiation behavior by interface and bandgap engineering at the nanoscale. *Nano letters* **13**, 4876-4883 (2013)